Additive manufacturing of 6061 and 7075 aluminium alloy with selective laser melting

Yingjie Li

THESE DE DOCTORAT DE L'ETABLISSEMENT UNIVERSITE BOURGOGNE FRANCHE-COMTE PREPAREE A l'UNIVERSITE DE TECHNOLOGIE DE BELFORT-MONTBELIARD

Ecole doctorale n^{o} 37

Sciences Physiques pour l'Ingénieur et Microtechniques – SPIM

Doctorat de Sciences pour l'Ingénieur

Par

Mr. Yingjie LI

Fabrication Additive des Alliages d'Aluminium 6061 et 7075 avec Fusion Laser Sélective

Thèse Soutenue à UTBM Site de Sévenans, le 25 septembre 2024

Composition du Jury:

Mr. BERTRAND Philippe	Professeur, L'École nationale d'ingénieurs de Saint-Étienne	President
Mr. JI Gang	Chargé de recherche (HDR), Université de Lille	Rapporteur
Mr. CHEROUAT Abel	Professeur, Université de technologie de Troyes	Rapporteur
Mr. KANG Nan	Maître de conférences (HDR), École Nationale Supérieure d'Arts et Métiers	Examinateur
Mr. LIAO Hanlin	Professeur, Université de technologie de Belfort-Montbéliard	Directeur de thèse

Acknowledgements

My PhD thesis was carried out at the University of Technology of Belfort-Montbéliard (UTBM), with the financial support from the China Scholarship Council (CSC).

Completing this doctoral dissertation has been a challenging and rewarding journey, and I would not have been able to accomplish it without the support, encouragement, and guidance of many individuals. I would like to take this opportunity to express my sincere gratitude to all those who have helped me along the way.

First and foremost, I would like to express my deepest appreciation to my advisor, Professor Hanlin Liao, for his unwavering support, insightful guidance, and continuous encouragement throughout my research. His expertise, patience, and constructive feedback have been invaluable, and I am incredibly grateful for his mentorship. I would also like to express all my thanks to my co-supervisor Dr. Shuohong Gao (Institute of New Materials, Guangdong Academy of Sciences, Chian), for providing all kinds of assistance and technical guidance throughout all this work.

I am also deeply indebted to the members of my dissertation committee, Professor Gang JI, Professor Abel Cherouat , and Professor Bertrand Philippe, and Professor Nan KANG for their valuable time, insightful comments, and constructive criticism, which have greatly improved the quality of this dissertation.

Many thanks to the members of our ICB-LERMPS laboratory: Mr. Zhoukun Shi, Mrs. Xinge Jiang, and others, for their assistance with my PhD work.

A very special thank you goes to my family, especially my parents, my brother Mr. Xin LI and my wife Mrs. Yuanping ZHONG, for their unconditional love, patience, and encouragement throughout this journey. Their belief in me has been a constant source of strength and motivation.

Thank you all for your support and encouragement.

General Introduction

After more than 20 years of development, metal additive manufacturing (AM) technology has become one of the most prominent and rapidly advancing technologies in advanced manufacturing. This technology has garnered significant attention in metal manufacturing due to its ability to overcome many of the limitations faced by traditional manufacturing techniques. For example, it facilitates the production of complex shapes and customized structures with ease, while also meeting the requirements for lightweight design without compromising strength and structural integrity. Fundamentally, this technology is distinctly different from traditional manufacturing techniques such as casting, forging, extrusion, and machining. These methods can utilize layer-by-layer additive manufacturing, often referred to as 3D printing of metals, where components are built up point by point and layer by layer. This technique offers unparalleled freedom in manufacturing complex-shaped parts, allowing the use of non-traditional manufacturing methods to achieve high precision and control without the need for additional machining.

Aluminum alloys are the second most widely used metal after steel, with an annual usage growth rate of approximately 6%. This growth is primarily due to the alloy's low density, being one-third lighter than steel, its corrosion resistance, and its excellent overall physical and chemical properties. Currently, around 80% of aluminum alloy applications are in structural alloys for deformation products, mainly produced through rolling, extrusion, or forging. With the continuous advancement of SLM technology, research into aluminum alloys using the SLM process has also been deepening. In recent years, the additive manufacturing of aluminum alloys has gained increased attention. Currently, printable aluminum alloys are primarily limited to near-eutectic Al-Si alloys. Al-Si alloys are characterized by excellent fluidity, high thermal conductivity, low thermal expansion coefficient, and superior castability, owing to their relatively narrow solidification range. Therefore, in SLM manufacturing, sub-eutectic Al-Si (7-12 wt%)-Mg (>1 wt%) alloys such as AlSi7Mg, AlSi10Mg, and AlSi12Mg are predominantly used. Strength is a crucial indicator for aluminum alloys, which is why there is relatively less research on using SLM to produce medium- and high-strength aluminum alloys, such as the 2xxx 6xxx, and 7xxx series. Importantly, these heat-treatable aluminum alloys, including 2xxx, 6xxx, and 7xxx can achieve increased strength and beneficial corrosion resistance after heat treatment, making them particularly suitable for applications in the aerospace and automotive industries. However, due to the relatively wide solidification range of these aluminum alloys, they

are prone to cracking during the solidification process.

To date, research activities on the SLM of aluminum alloys remain limited compared to other alloys. Numerous factors constrain the printing of aluminum alloys, such as the tendency of the powder to form oxides, low absorption of common laser wavelengths by aluminum alloys, and high thermal conductivity of the material. Particularly, the high thermal conductivity and low laser energy absorption of aluminum alloys necessitate higher energy input to achieve powder melting. However, this also results in uneven vaporization of the alloy components, as elements like Zn and Mg with higher vapor pressures tend to vaporize first. This leads to inconsistencies in the final printed parts.

To address the aforementioned limitations, we can use green lasers, which have a shorter wavelength compared to traditional infrared lasers, as the laser source. Aluminum alloys have a higher absorption rate for green lasers. This higher absorption rate means that the powder can be melted with lower energy density, thereby reducing the evaporation of low melting point elements and enhancing the performance of the aluminum alloy. Additionally, the introduction of transition elements or modified particles can act as heterogeneous nucleation sites during solidification, inducing significant grain refinement and suppressing cracking. This thesis is chiefly organized into five chapters, as follows:

Chapter 1 provides a brief introduction to several additive AM technologies, with a focus on the characteristics and advantages of SLM technology and the common materials used. This includes a detailed overview of recent research progress on aluminum alloys in the SLM process and the challenges encountered. Finally, the principles behind the issues arising during the printing process are discussed, based on the research of relevant scholars, leading to the presentation of the purpose and objectives of this study.

Chapter 2 Characterization of raw materials and printed parts using appropriate equipment involves several key steps. First, an introduction to the raw materials is provided, followed by an explanation of the SLM system, including printing equipment, its operational principles, and process parameters. Analysis of the printed parts' microstructure and mechanical properties is conducted, followed by characterization of how heat treatment affects their performance.

Chapter 3 investigated the microstructure and mechanical properties of parts printed using SLM technology with Al6061 and Al6061 alloyed with varying amounts of titanium(Ti) particles. Initially, powders of 6061 alloy and different amounts of Ti particles were mechanically mixed, followed by morphology and phase analysis of the mixed powders. Subsequently, process parameters were optimized to identify the best

conditions, and crack-free samples were prepared for analysis of microstructure, composition, and mechanical properties. The evolution of microstructure after heat treatment and its impact on mechanical properties, particularly the tensile performance of 6061+Ti, were also studied. Finally, a novel approach using Ti particle modification of Al6061 was proposed to prepare crack-free samples using green laser equipment. The enhancement mechanism was elucidated, and the mechanical properties were investigated accordingly.

Chapter 4 Based on the results from the previous chapter, it is evident that adding Ti particles enhanced the performance of Al6061 and produced crack-free samples. Therefore, in this chapter, we investigate high-strength aluminum alloy Al7075. First, submicron Ti particles were added in different proportions to create reinforced 70Al75 composite powder, which was prepared through mechanical mixing. Then, using green laser equipment, we studied the process parameters' effects on the microstructure and hardness of the printed parts from the mixed powders, optimized the parameters to produce crack-free samples, and examined the impact of varying Ti particle content on the microstructure, phase composition, and mechanical properties. To further improve the mechanical properties, T6 heat treatment was applied. The results showed a significant increase in strength and elongation compared to unmodified Al7075. The tensile strength of the heat-treated samples improved, though the elongation decreased. Based on observations of the microstructure and composition, the mechanism by which Ti particles inhibit cracking in Al7075 was proposed. Finally, the reinforcement mechanisms and fracture mechanisms of the Ti/Al7075 composites were discussed.

Chapter 5 Submicron TiC and SiC particles were used to modify Al7075 powder, creating a novel mixed powder for manufacturing using green laser equipment. X-ray diffraction (XRD), scanning electron microscopy (SEM), and electron backscatter diffraction (EBSD) were employed to study the effects of different amounts of TiC/SiC particles on the microstructural evolution. The relative density and microhardness of Al7075 and the composite materials were evaluated. Additionally, preliminary studies on the tensile properties of both the as-printed and heat-treated samples were conducted. Through experimental results and microstructural observations, the fracture mechanisms were analyzed, providing a new approach for using SLM to prepare high-hardness, crack-free Al7075.

Finally, the conclusions and perspectives for future work are presented.

Content

List of Figures

List of Tables

Chapter 1 Bibliography

Additive Manufacturing (AM) is a process of creating objects by adding material layer by layer. Selective Laser Melting (SLM) is a common technique within AM, which uses a high-energy laser beam to selectively melt metal powder and build parts layer by layer. The characteristics of the SLM process include the ability to produce complex geometries and fine features, suitability for various metal materials, and the high density and superior performance of the manufactured parts. Aluminum alloys are among the commonly used metals, and recent years have seen extensive research on their application in the SLM process. However, typical medium-strength aluminum alloy 6061 and high-strength 7075 aluminum alloy often exhibit defects such as hot cracking, porosity, and composition loss during the SLM process, which adversely affect their mechanical properties. Reducing defects in the printing process of medium and high-strength aluminum alloys has thus become a research focus. Recent studies have shown that optimizing process parameters and modifying aluminum alloy powders can reduce defects or eliminate cracks, thereby improving performance. Compared to traditional infrared lasers, green lasers have shorter wavelengths, which are better absorbed by non-ferrous metals and aluminum alloys, resulting in better powder melting and fewer defects during the printing process.

In this chapter, we first introduce some common processes in additive manufacturing and provide a detailed description of the SLM process and its characteristics. Then, we briefly discuss some materials used in the SLM process. Following this, we focus on the types of aluminum alloys and the development of aluminum alloys in the SLM process. Additionally, we cover the formation of cracks during printing and the principles for eliminating cracks, as well as the impact of infrared and green lasers on the process. Finally, we present the main objectives and originality of this work.

1.1 Introduction advanced additive manufacturing technology

1.1.1 Electron beam melting (EBM)

Electron beam melting (EBM) is an additive manufacturing technology that uses an electron beam to melt metal powders in a vacuum chamber, layer by layer, to create three-dimensional (3D) objects. [1]. The schematic is as follows Figure 1.1

Principles of EBM: EBM is a powder bed fusion process that uses an electron beam to melt metal powders layer by layer. The process begins with a thin layer of

metal powder spread over a built platform in a vacuum chamber, the vacuum environment has a very important influence on the processed materials [3, 4]. An electron beam is then directed at the powder, selectively melting and fusing the particles to create a solid layer. The build platform is lowered, another layer of powder is spread on top of the previous layer, and the process is repeated until the object is complete. The use of an electron beam allows for precise control of the energy input, resulting in a highly localized melting process. [5, 6]

Materials used in EBM and Applications: EBM is typically used to process metals with high melting points, such as titanium, cobalt-chrome, and nickel-based alloys. [7, 8] The use of these materials makes EBM well-suited for producing parts for aerospace, medical, and other high-performance applications. The powders used in EBM must be highly pure, with a consistent size and shape to ensure uniform melting and solidification [9, 10]. EBM has several advantages over other additive manufacturing technologies, including high accuracy, fast build times, and the ability to produce complex geometries. EBM is also capable of producing parts with high density and strength, which makes it suitable for producing high-performance components used in aerospace and medical applications. EBM has some limitations, including the need for a vacuum environment, which can limit the size of the parts that can be produced. At the same time, it involves the challenges of craftsmanship, such as dimensional accuracy and surface finish. The process is also limited to processing certain materials, and the equipment and process can be expensive c[11, 7].

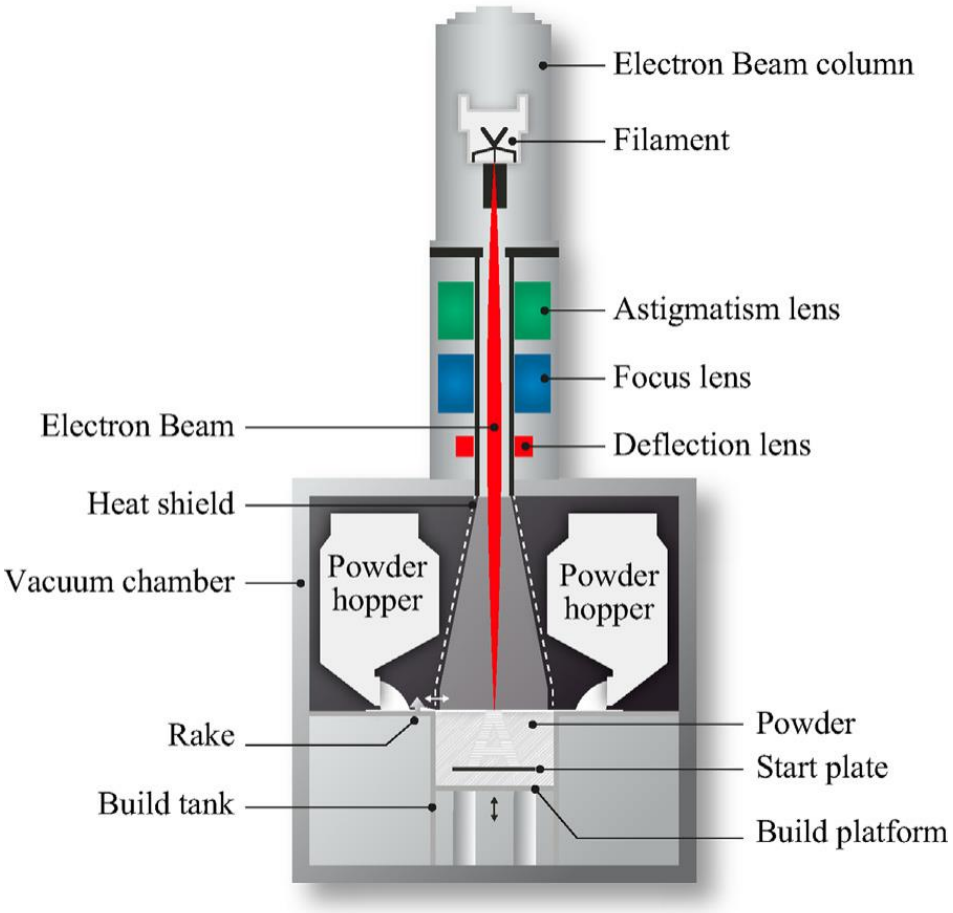

Fig 1.1 Schematic EBM system[2]

1.1.2 Binder Jetting(BJ)

Binder Jetting is an additive manufacturing process that involves depositing layers of powder material and bonding them together using a liquid binding agent. It is a highly versatile process that can be used with a wide range of materials and is capable of producing parts with complex geometries, low-cost and high-printing efficiency [22].

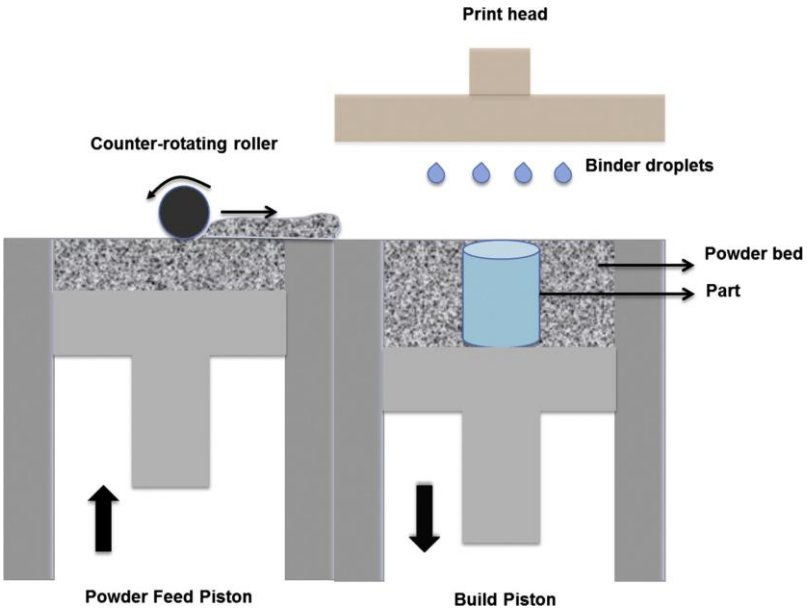

Fig 1.2 Schematic of the Binder Jetting process[23]

Process Description: The BJ process starts by spreading a thin layer of powder material on a build platform. A print head then moves over the powder and deposits the binding agent in the desired pattern. The binding agent bonds the powder particles together and creates a solid layer. The platform is then lowered, and a new layer of powder is spread on top of the previous one. The process is repeated layer by layer until the part is complete [24]. Schematic diagram of process principle as Figure1.2 B.J has several advantages over other additive manufacturing processes. One of the main advantages is the ability to use a wide range of materials, including metals, ceramics, and polymers. This makes it a highly versatile process that can be used for various applications. Another advantage is the ability to produce parts with complex geometries, including internal features that cannot be produced using traditional manufacturing methods. In addition, BJ is a high-speed process that can produce parts quickly and at a relatively low cost. Despite its many advantages, BJ has some limitations. One of the main limitations is the quality of the parts produced. The parts are not as strong as those made using traditional manufacturing methods, and the surface finish is not as good [25, 26]. In addition, BJ technology remains a significant challenge, because of the hazardous and difficult-to-remove nature of the typically employed phenolic solvent-based binder, Therefore, it has a great impact on human health and the quality of parts [27, 28].

Binder Jetting has many potential applications in a wide range of industries, For example, Figure1.3 applications in electrochemical energy storage [29], electronic devices [30], biomedicine [31], and renewable bio-based materials [32].

Fig 1.3 Parts produced by BJ: (a) turbine component, SS 420 infiltrated with bronze (b) mold insert from X190CrVMo20 tool steel, SS 316L; and (d) wrench, SS 420[33]. (e,g)3D printed parts showing the capability of binder jetting in the food industry[34]; (f) binder jetted reflector antenna from SS 316 infiltrated with copper[35]; and (h)a shell structure sand mold[36]. process

1.1.3 Selective laser sintering (SLS)

Selective Laser Sintering (SLS) is an additive manufacturing process that uses a laser to sinter a powdered material, typically nylon or polyamide, into a solid 3D structure based on a 3D model [37]. SLS has been a popular choice for engineers and manufacturers for decades due to its low cost per part, high productivity, and established materials, making the technology ideal for a range of applications. Figure1.4 schematically illustrates the SLS manufacturing process, Selective Laser Sintering starts with a powdered material being spread over a build platform. The laser then scans the powder, melting it together in a predetermined pattern, building layer by layer to create the desired 3D object. After each layer is complete, a new layer of powder is spread over the top, and the process is repeated. Once the build is complete, the object is removed from the build platform and cleaned of any excess powder [38].

SLS involves selectively fusing powdered material, such as nylon or polyamide, using a laser to build up a 3D object layer by layer. One of the key advantages of SLS is its ability to produce highly complex, customized designs that may be difficult or impossible to create using traditional manufacturing methods. SLS has a wide range of applications, including rapid prototyping, product design and development, and aerospace, automotive, medical, and dental industries [39, 40]. it can use a wide range of materials, including nylon, polycarbonate, plastics, ceramics, metals, and even glass[41].SLS has a low cost per part and no requirement for support structures since the unsintered powder provides support during the build and can be used to produce

A large number of parts quickly, making it ideal for high-volume manufacturing [42]. However, there are some limitations to the technology, including the need for post-processing to remove excess powder and achieve the desired surface finish, Postprocessing treatments are necessary to improve the surface quality, as well as the relatively high cost of SLS printers and materials [43].

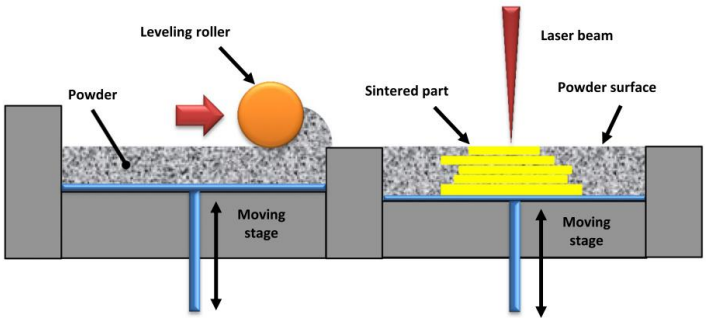

Fig 1.4 Schematic of the Selective Laser Sintering process[38]

1.1.4 Selective laser melting (SLM)

SLM and SLS are both additive manufacturing processes used for 3D printing, there is no difference between SLM and SLS in terms of process setup and mechanisms. 1.1. Introduction advanced additive manufacturing technology but they differ in their approach to creating parts. SLS only sinters-or partially melts-the powder, For SLM, it melts powder using a high-power laser to create a solid metal object [13, 44].

The SLM machine then uses a computer-controlled laser to selectively melt and fuse the powder particles together, layer by layer, following the cross-sectional shape of each layer as defined in the 3D model. The laser is directed by a mirror or other optical system to the specific locations where the material needs to be melted and fused, based on the information from the digital model.

After each layer is melted and fused, the build platform moves down by a small distance, and a new layer of powder is spread over the previous layer. The laser then fuses the new layer to the previous one, and the process repeats until the entire object is built up layer by layer. As the object is built up layer by layer, the remaining powder provides support for the parts of the object that are being printed. Once the printing is complete, the object is removed from the build platform and the remaining powder is brushed or blown away. The finished object can then be post-processed as required, such as polishing, machining, or coating [45, 46].

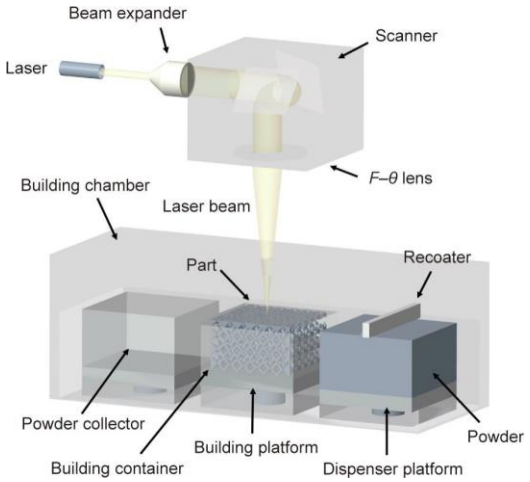

Fig 1.5 Schematic of the SLM process[44]

SLM process parameters refer to the various settings and variables that can be adjusted to optimize the SLM process, Figure 1.6 provides an illustration of these process parameters commonly studied of SLM, including laser power, scanning speed, hatch spacing, and layer thickness.

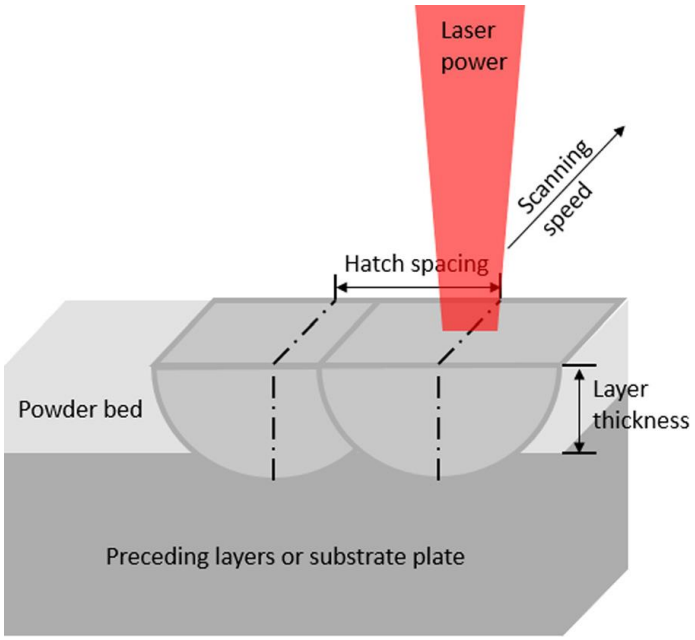

Fig 1.6 Schematic of SLM process parameters: laser power, scan ning speed, hatch spacing, and layer thickness[46]

Laser power: The amount of energy delivered to the powder bed by the laser. Increasing the laser power can increase the melting rate, but it can also lead to more thermal stresses and distortion. The researchers found that increasing the laser power can completely melt the powder, fill the pores under the action of capillary force, and improve the density [47].

Scanning speed: The speed at which the laser moves over the powder bed.

Increasing the scanning speed can reduce printing time, but it can also decrease the melting efficiency and affect part quality. Ruidi et al. [48] have reported that scan speed affects melt pool continuity.

Hatch spacing: The distance between adjacent scan lines. Decreasing the hatch spacing can improve surface finish and resolution, but it can also increase printing time. The smaller the hatch spacing, the greater the internal stress and the greater the temperature gradient, which will easily lead to warping and deformation of the molded part [49].

Layer thickness: The thickness of each layer of the part. Increasing the layer thickness can reduce printing time, but it can also affect the part quality and surface finish. Gusarov et al. 50] through research found that the thickness of the powder will affect the absorption rate of the laser, and the total laser energy absorbed in the layer increases with the increase of its thickness; Tolochko et al.[51] explained that increasing the layer thickness will lead to increased balling processes, which reduces the dimensional accuracy and surface roughness.

In addition, the temperature of the powder bed [52], the scanning strategy [53], the size and distribution of powder particles[54], and the pressure of the printing chamber[55] also have an impact on the printing process.

1.1.4.1 Advantages of Selective laser melting technology

SLM is a metal 3D printing technology that offers several advantages over traditional manufacturing techniques. Some of the advantages of SLM include [46, 56]:

1. Design freedom: SLM allows for the creation of complex geometries that are difficult or impossible to produce using traditional manufacturing techniques. This design freedom enables the production of parts with improved functionality and reduced weight.

2. Reduced material waste: SLM is an additive manufacturing process, meaning that parts are built layer by layer using only the necessary material. This reduces material waste and minimizes the environmental impact of manufacturing.

3. Rapid prototyping: SLM enables rapid prototyping, allowing for the quick and cost- effective production of prototypes for testing and validation. This helps to accelerate the design process and reduce time to market.

4. Improved part quality: SLM produces parts with high accuracy and excellent mechanical properties. This enables the production of high-quality parts with consistent properties and surface finish.

5. Customization and personalization: SLM enables the production of customized and personalized parts, making it well-suited for medical and dental applications, such

as the production of implants and prosthetics.

6. Reduced tooling costs: SLM eliminates the need for costly tooling, such as molds and dies, which can result in significant cost savings. In summary, SLM offers numerous advantages over traditional manufacturing techniques, including design freedom, reduced material waste, rapid prototyping, improved part quality, customization, and personalization, and reduced tooling costs. These advantages make SLM an attractive option for a wide range of applications, from aerospace and automotive to medical and dental [57, 58].

1.2 Materials of selective laser melting

SLM is an increasingly popular manufacturing technology that enables the production of complex and highly customized parts from various materials. Five main types of materials are involved in most SLM research: Steel and iron-based materials [59], titanium alloy [60], nickel-Based Alloy[61], magnesium[62], and aluminum alloy[63]. As the research progresses, many other metals, copper, and ceramics, have also been studied by SLM [64-66]. We will introduce the related research on aluminum alloy in detail in the next chapter. The following chapter introduces the above-mentioned materials, The research on various materials through the SLM process has yielded significant results and encountered certain challenges.

Research on 316L stainless steel in SLM processes primarily focuses on optimizing process parameters for the best printing quality, examining the effects of various pre-treatments and post-treatments, and evaluating fatigue performance and corrosion cracking behavior. Some studies also explore adding elements or compounds to improve performance and quality [67-70]. In the case of the Ti64 alloy, research indicates that scanning speed significantly affects the alloy's density, followed by laser power. Both low and high energy densities result in increased porosity. Process parameters influence the microstructure, roughness, densification, and microhardness of SLMed Ti6Al4V parts. Higher scanning speeds decrease tensile strength and lead to unmelted powders on fracture surfaces [71, 72]. SLM-built IN718 parts exhibit different microstructures compared to conventionally manufactured components due to the rapid melting and solidification during the process. Key differences include fine columnar grain structures oriented in the build direction, and variations in phase composition and anisotropy. The rapid solidification can create a supersaturated γ matrix with different precipitate distributions, sometimes forming nano-sized precipitates that enhance material strength. Research frequently focuses on how adjusting process parameters affects part structure and performance. Heat treatments are used to modify microstructures, reduce residual stress, and strengthen materials [73,

74]. Inconel 718, a nickel-based alloy, benefits significantly from heat treatments that enhance its properties. For example, post-heat treatment transforms columnar grain structures into characteristic cellular structures, improving tensile strength when combined with optimized process parameters [75]. Magnesium, due to its high affinity for oxygen, forms a ductile oxide layer during the SLM process, weakening the bonding between powder particles and leading to defects. Magnesium's narrow temperature range between melting and boiling points makes it prone to evaporation under high laser power, causing rough surface textures and susceptibility to porosity and thermal cracking [76-78].

1.3 Aluminum-based alloys

Aluminum alloys are celebrated for their lightweight yet strong nature, boasting excel lent corrosion resistance and a high strength-to-weight ratio. This makes them ideal for critical applications in the aerospace industry, where they are extensively used in the construction of aircraft structures and components. In the automotive sector, these alloys contribute to weight reduction, enhancing fuel efficiency and reducing emissions. Aluminum's superior thermal and electrical conductivity also makes it suitable for heat sinks in electronics and electrical transmission lines. In construction, aluminum alloys are favored for their durability and resistance to environmental conditions, often used in window frames, doors, and structural components. These versatile and sustainable properties ensure aluminum alloys remain a material of choice across various industries.

1.3.1 Types of Aluminum Alloys and Their Applications

Aluminum alloys are categorized into several series, each defined by specific alloying elements that confer distinct properties and applications:

1. 1000 Series (Pure Aluminum):Key Element: Primarily aluminum (99% purity or higher). Properties: High electrical and thermal conductivity, excellent corrosion resistance, highly ductile. Uses: Electrical wiring, food and chemical handling, reflective surfaces.

2. 2000 Series (Aluminum-Copper Alloys):Key Element: Copper. Properties: High strength, good machinability, less corrosion-resistant than other alloys. Uses: Aerospace components, military equipment, structural applications.

3. 3000 Series (Aluminum-Manganese Alloys):Key Element: Manganese. Proper ties: Moderate strength, good workability, weldability, and corrosion resistance. Uses: Cooking utensils, radiators, roofing, and air-conditioning units.

4. 4000 Series (Aluminum-Silicon Alloys): Key Element: Silicon. Properties: Low melting point, good fluidity, moderate strength. Uses: Welding rods and brazing alloys,

automotive parts.

5. 5000 Series (Aluminum-Magnesium Alloys): Key Element: Magnesium. Proper ties: Good strength, excellent corrosion resistance, especially in marine environments. Uses: Shipbuilding, transport vehicles, bridges, storage tanks.

6. 6000 Series (Aluminum-Magnesium-Silicon Alloys): Key Element: Magnesium and silicon. Properties: Balance of strength and ductility, good corrosion resistance, easily extruded. Uses: Structural applications, automotive industry, architecture, railway cars.

7. 7000 Series (Aluminum-Zinc Alloys): Key Element: Zinc. Properties: Highest strength among aluminum alloys, good fatigue resistance. Uses: Aerospace industry, military applications, high-performance applications.

8. 8000 Series (Other Elements): Key Element: Other elements (e.g., iron, lithium). Properties: Specific properties depending on added elements. Uses: Specialized applications, like conductors (Al-Fe), and aerospace (Al-Li).

Each series of aluminum alloys offers a unique set of characteristics suitable for different applications, balancing factors such as strength, ductility, conductivity, and corrosion resistance. The choice of an aluminum alloy for a specific application depends on the requirements of strength, weight, corrosion resistance, machinability, and other factors [79, 80]. High-strength wrought aluminum alloys, such as the 2xxx series (Al-Cu-Mg-based), 7xxx series (Al-Zn-Mg-based), and 8xxx series (Al-Li-based), are highly sought after for structural applications in the aircraft, aerospace, and defense industries [81, 82]. The 5xxx series (Al-Mg-based alloys), known for their moderate to high strength, are extensively used in storage and marine applications. The 6xxx series (Al-Mg-Si-based alloys), with their moderately high strength, are commonly employed in heat transfer applications and serve as structural materials in the auto motive industry. Additionally, Al-Si-based cast alloys are particularly favored for use in internal combustion engines within the automotive sector [82].

1.3.2 Recent developments of Al-based alloys for SLM

Aluminum alloys, esteemed as quintessential lightweight materials, have garnered immense demand across aerospace, automotive, and high-speed train industries, owing to their exceptional physical attributes. These include high specific strength and commendable damage tolerance [83]. In light of their contribution to structural weight minimization and efficient utilization of metal resources, aluminum alloys processed by SLM have become a focal point of extensive research. The current research on SLM of aluminum alloys can be broadly divided into two categories, one that focuses on relatively easy-to-print AlSiMg alloys, mainly including AlSi10Mg, AlSi12[84], and

another that deals with difficult-to-print aluminum alloys, such as the 2xxx series (Al-Cu alloys) and the 7xxx series (Al-Zn-Mg alloys)[85]. Below, we will introduce the relevant research and advancements in these two types of aluminum alloys.

1.3.2.1 SLM of Al-Si alloys

To date, most of the printable traditional aluminum alloys are close to eutectic aluminum-silicon-based alloys, such as AlSi10Mg [86], Al12Si [87], and AlSi9Mg [88]. According to the aluminum-silicon binary phase diagram shown in Figure1.7, the eutectic point contains 12.6 wt.% silicon. Consequently, aluminum-silicon alloys with near-eutectic compositions possess lower liquidus line temperatures and a narrower solidification range, offering better fluidity than most aluminum alloys. The increased silicon content enhances their laser absorbance [89]. These superior characteristics make them more amenable to SLM processing, facilitating the suppression of cracking behaviors and contributing to it being the most widespread and mature in the field, especially AlSi10Mg, Next, we will focus on discussing the SLM research related to AlSi10Mg.

Firstly, there is the study of the process, which examined how different laser powers, scanning speeds, and laser beam diameters affect the size of the SLM melt pool. the

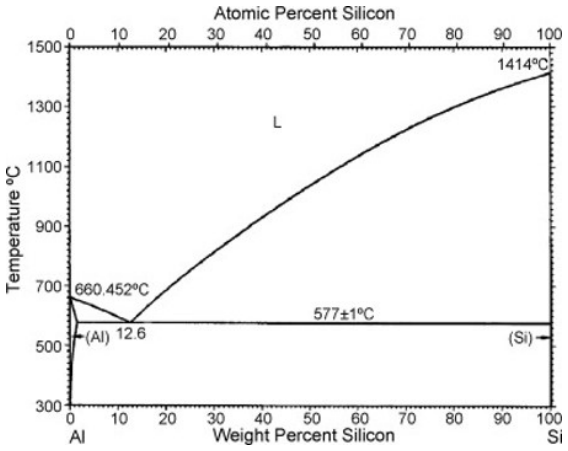

Fig 1.7 Al-Si binary phase diagram [90]

length, width, and depth of the melt pool all increase with higher laser power and slower scanning speeds, with the most notable change being in the length. However, excessively high energy density might cause spattering, adversely affecting the forming quality [91]. As the laser beam diameter increases, the length of the melt pool slightly decreases, while the width and depth remain largely unchanged [92].

The formation of solidification microstructures during the SLM process depends on the temperature gradient (G) and cooling rate (R). The grain size is primarily determined by the cooling rate, with a higher rate facilitating grain refinement. Changes

in the key solidification parameter, the temperature gradient to cooling rate ratio (G/R), alter the growth morphology of the melt pool microstructure. As G/R gradually decreases, the microstructure transitions from cellular to columnar to equiaxed grains. The solidification environment of the SLM melt pool is highly complex and variable, influenced by the thermodynamic behavior of the melt pool. This results in high temperature gradients and cooling rates, thereby affecting the material's forming process, morphology, microstructure, and properties. In SLM samples, there is typically a periodic microstructure and grain orientation along the stacking direction [93]. Typical solidification microstructures in the melt pool are shown in Figure 12 [94-96]: Figure 1.8(a) shows columnar and equiaxed grains with columnar grains epitaxially growing and oriented towards the heat source scanning direction; Figure 1.8(b) shows predominantly columnar grains growing perpendicularly to the solidification front depicted by the yellow dashed line in the image. Liu et al. [97] used Electron Backscatter Diffraction (EBSD) to study the effect of laser power on the grain morphology and texture of AlSi10Mg alloy in SLM, finding that the formation of equiaxed grains is due to nucleation at the melt pool boundaries and the transition from columnar to equiaxed grains. This study provides new insights into the formation of the melt pool eutectic Si phase and the distribution of grain structures in different regions.

During the SLM process of aluminum alloys, different regions of the melt pool exhibit varied solidification behaviors. The bottom of the melt pool, where the temperature gradient is the highest, typically shows epitaxial growth of columnar grains in the overlaying layer, growing perpendicularly to the laser scanning direction. The surface of the melt pool, on the other hand, demonstrates heterogeneous nucleation of equiaxed grains, with a transition from columnar to equiaxed grains occurring at the top of the melt pool [95,96].

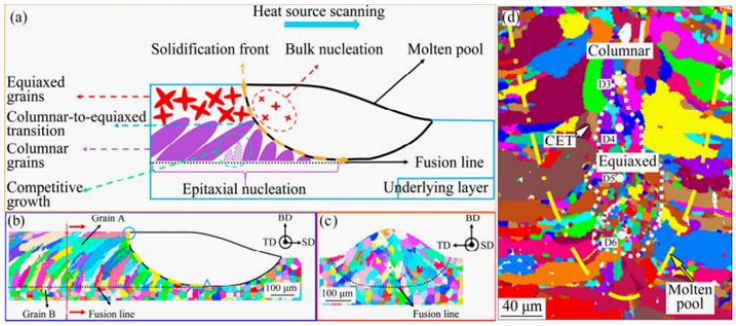

Fig 1.8 (a) Solidification behavior along the scanning direction, (b)Grain structure simulation along the scanning direction, (c)Grain structure simulation along the stacking direction, (d) EBSD analysis of grain structure along the stacking direction [95,96]

During the SLM process, the powder's flowability impacts its ability to spread uniformly. Additionally, rapid solidification following the laser beam's melting of the

surface can lead to high viscosity melt pools, which may cause issues such as balling, cracking, and porosity, severely affecting mechanical properties. Therefore, it is necessary to optimize parameters to improve density. Zou et al. [98] used AlSi10Mg powder with an average particle size of 26.53μm, selecting three different laser powers (140 W, 160 W, and 180 W) and three different scanning speeds (800, 1000, 1200 mm/s) to study the impact of laser energy density on the densification of AlSi10Mg material. They found that within a certain range, the density is positively correlated with the laser energy density, with the highest density reaching 99%. The variation curve is shown in Figure1.9 (a b). At the same power, the density of the formed parts decreases with an increase in laser scanning speed; at the same rate, the density increases with an increase in laser power. The impact of scanning speed on density is shown in Figure 1.9 (c d); within a certain range of scanning speeds, increasing the speed improves density, but beyond a critical value, the density decreases. Similarly, with a fixed scanning speed, increasing the laser power raises the alloy's density, but too high a laser power can produce defects, thereby reducing density. Trevisan et al [99]. prepared AlSi10Mg alloy using SLM, achieving an average density of 99.6%, with the process parameters and density optimization chart shown in Figure1.9 (e). Maamoun et al. [100] studied the effect of process parameters on the quality of SLM aluminum alloy parts. Under a constant layer thickness of 30 um, they optimized the AlSi10Mg metalworking parameters (laser power, scanning speed, hatch spacing), ultimately achieving a sample density of 99.7%.

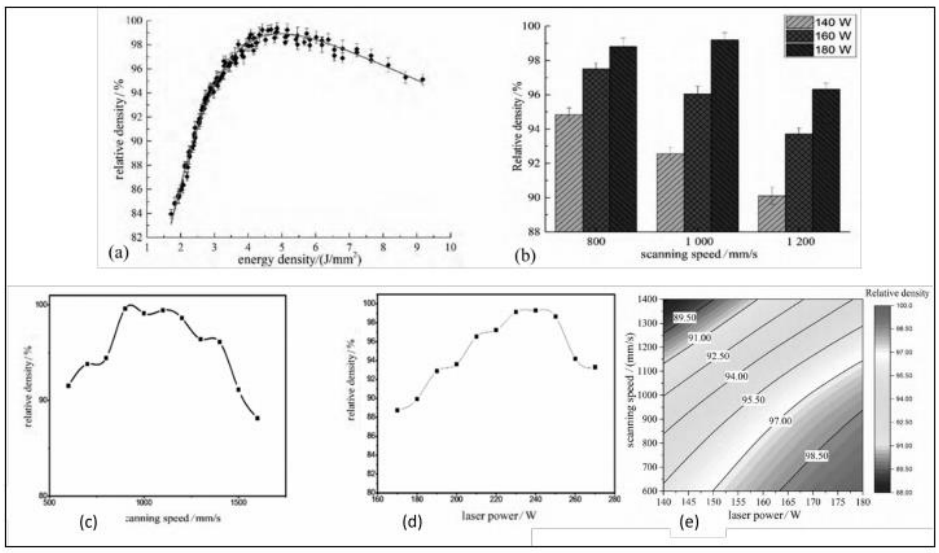

Fig 1.9 (a)density and energy density change curves, and (b) the relationship between different speeds, different powers, and den- sity[134]. (c d) The effect of laser scan speed and laser power on the relative density of SLM AlSi10Mg (P=220 W)[135]. (e)Relationship between SLM parameters and relative density of al loys[136]

In recent years, the addition of nanoparticles to aluminum-based materials has been a key focus in SLM research. The uniform distribution of nanoparticles in aluminum-based composites can effectively improve their ductility. Incorporating nano-sized reinforcing particles can increase the nucleation rate of o-Al crystals, ensuring that the reinforcing particles are uniformly distributed within the matrix grains and at grain boundaries. This distribution alters the solid-liquid interface, thereby influencing microstructure evolution, and ultimately achieving the goal of grain refinement [101].

In SLM formed composites, the use of nanoparticles as a reinforcing phase is beneficial due to their lattice compatibility with the Al matrix, acting as grain refiners. While SiC is a commonly used reinforcing phase in aluminum-based composites, TiB2 possesses superior physical properties and application prospects compared to SiC. TiB2 particles with a diameter of 50 nm can be used for grain refinement, enhancing hardness, plasticity, and tensile strength. Despite the high cost of nano-sized TiB2, it can significantly reduce the porosity of SLM composites [102], and also act as a dispersion strengthening phase and heterogeneous nucleating agent [103,104].

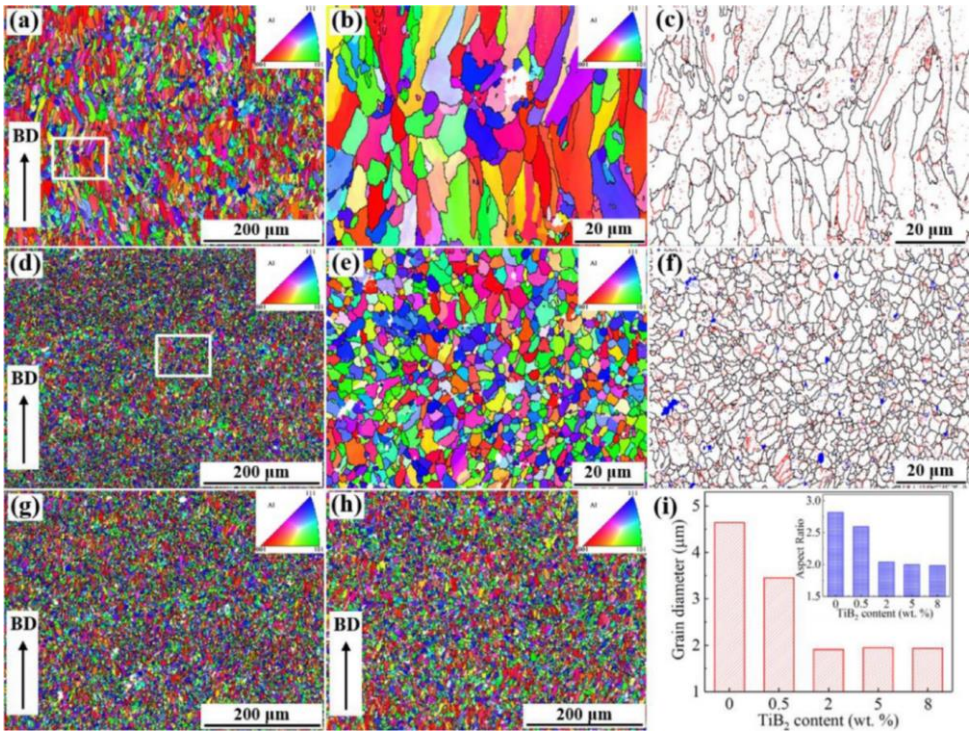

Fig 1.10 The microstructures observed from the side view of SLMed x%TiB2/AlSi10Mg composites: (a-c)0.5%, (d-f)2%,(g)5%, (h)8%, (f) the variation of average grain diameter with different TiB2 particle contents, and the inset is the corresponding grain aspect ratio evolution[105]

Xi et al. [106] studied the effect of TiB2 content on the microstructure formation and grain refinement of SLM-fabricated AlSi10Mg/TiB2 composites. They found that

as the TiB2 content increased from 1% to 5%, the average size of the composite material decreased from 6.32 to 1.55μm. At relatively high TiB2 contents, a fine equiaxed crystal structure was observed. Thijs et al. [107] Analyzed the microstructure of SLM-fabricated AlSi10Mg alloy using EBSD, the microstructure along the heat flow direction consisted of columnar grains, while perpendicular to the forming direction, it was equiaxed. Xiao et al. [105] studied 2 wt.% nano-TiB2 reinforced AlSi10Mg composite materials. As illustrated in Figures1.10, at a laser power of 250 W and a scanning speed of 1300 mm/s, the microstructure of the alloy and different contents of TiB2/AlSi10Mg composites are shown. EBSD images reveal that the microstructure of SLM AlSi10Mg alloy is primarily composed of coarse columnar grains growing towards the center of the melt pool. Figure1.10(b) indicates that the microstructure in the center of the melt pool shows epitaxial growth. However, at the melt pool boundaries, the grains are mostly fine equiaxed crystals with random orientations. The coarse columnar crystals of TiB2/AlSi10Mg are refined and transformed into equiaxed grains. With the increasing content of TiB2, grains continue to refine and transition to equiaxed grains. When the TiB2 content reaches 2%, the melt pool structure gradually disappears, as shown in Figure 1.10(e), indicating that the introduction of TiB2 promotes the transformation from columnar to equiaxed grains while refining the microstructure.

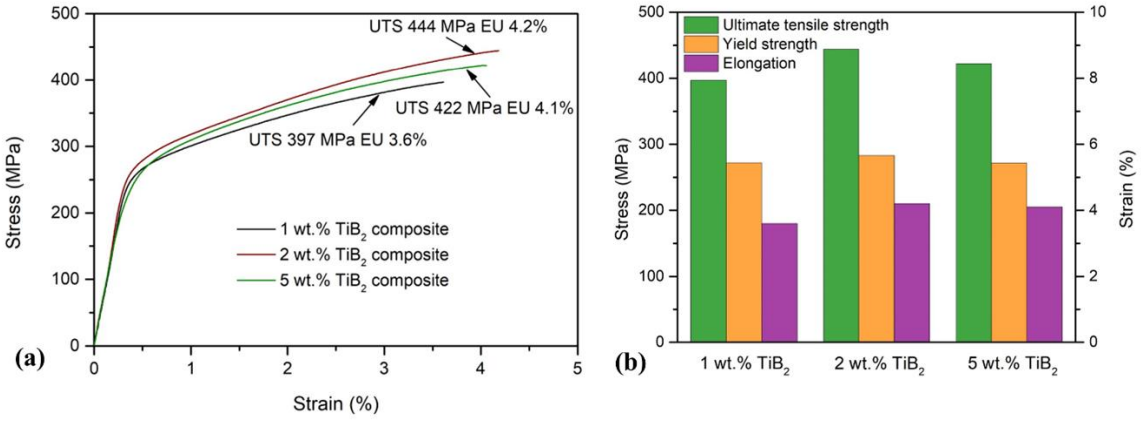

Fig 1.11 (a)TiB2 particles reinforced tensile stress-strain curve of Al Si10Mg composite, (b) tensile strength, yield strength and elon gation[108]

LI et al[108]investigated the impact of adding a small quantity of TiB2 ceramic particles (mass fraction of 1%) on the microstructural properties of Selective Laser Melted AlSi10Mg alloy. Compared to the AlSi10Mg alloy, the particle-reinforced aluminum based composite material exhibited more stable hardness distribution, along with improved tensile strength, yield strength, and elongation. Xi et al [106]. fabricated TiB2/AlSi10Mg composite materials using SLM technology and analyzed the

fabrication quality, grain refinement, and mechanical properties. They found that when 2wt% TiB2 was added to the composite material, it exhibited higher microhardness (≈127 HV), tensile strength (≈444 MPa), and yield strength, As shown in Figure1.11.

1.3.2.2 SLM of high-strength aluminum alloys

As SLM technology continues to advance, research into high strength and medium-strength aluminum alloys is delving deeper. Series 2 and Series 7 aluminum alloys, known for their high strength and favorable heat treatment characteristics, are increasingly gaining attention for applications in demanding fields like aerospace [109]. Additionally, Series 6 aluminum alloys, while having lower strength, exhibit excellent overall performance, including good weldability, machinability, and corrosion resistance. This makes them highly suitable for widespread applications in the automotive and construction industries [110]. With SLM technology, these high strength and medium-strength aluminum alloys can be used to fabricate lighter, more intricate structural components, thereby improving efficiency and performance.

Currently, the challenge of SLM processes for high-strength or precipitation-hardened Al alloys (2xxx, 6xxx, and 7xxx series) is their susceptibility to hot tear during the final stages of solidification when the alloys are in the mushy state, leading in an impairment to the mechanical properties of the printed component [81, 111].

Table 1.1 The chemical compositions (% by weight) of the previous aluminum alloys before (powder) and after laser melting [112]

2017A	Si%	Fe%	Cu%	Mn%	Mg%	
Before	0.56	0.40	4.0	0.57	0.72	
After	0.58	0.50	3.9	0.61	0.48	

7075	Si%	Fe%	Cu%	Mn%	Mg%	
Before	0.081	0.25	1.4	0.054	2.6	
After	0.11	0.27	1.5	0.057	2.1	

7020	Si%	Fe%	Cu%	Mn%	Mg%	
Before	0.077	0.29	0.16	0.29	1.3	
After	0.13	0.31	0.17	0.30	1.0	

6061	Si%	Fe%	Cu%	Mn%	Mg%	
Before	0.57	0.26	0.32	0.032	1.2	
After	0.60	0.26	0.29	0.030	1.0	

5083	Si%	Fe%	Cu%	Mn%	Mg%	
Before	0.14	0.25	0.032	0.60	3.8	

Qi et al. [111] investigated the relationship between the melting pattern and crack formation in 7075. They studied the effects of scanning speed and defocus distance on the transition of melting patterns during laser selective melting of Al7075 powder. Three types of cracks appear in sequence with the melting mode: nearly straight-line cracks parallel to the building orientation (conduction mode), disorderly distributed short cracks (transition mode), and short cracks mainly forming at the top and bottom layers of the samples (keyhole mode) , In keyhole mode, the irregular orientation of the grain due to fluctuations in the flow field and multiple re-melting can reduce cracking but cannot completely prevent it. T. Kaufmann et al. [113]. attempted to study the fabrication of AW7075 using the SLM process. They were able to prepare samples with a high relative density. However, even with a preheating of the base plate at 200°C, they were unable to eliminate the occurrence of cracks. Mauduit et al. [148]observed differences in the chemical composition of 7075 alloys before and after SLM processing, noting a significant reduction in elemental content, with zinc (Zn) experiencing a 30% loss and magnesium (Mg) a 19% loss, as shown in the following table 1.1. This depletion of Zn and Mg elements could potentially weaken the mechanical properties of 7075 alloy, as these constituents are crucial in providing solid solution strengthening and precipitation hardening effects through the formation of MgZn2 phases.

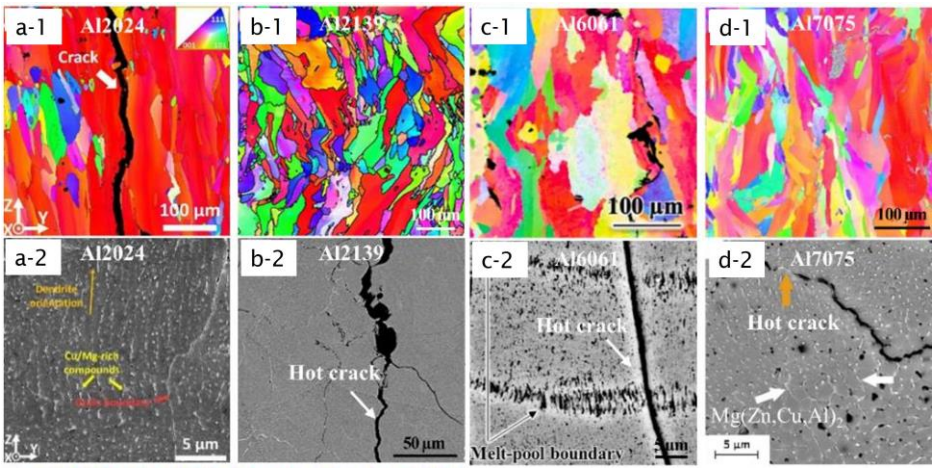

Fig 1.12 SLM-processed Al-based alloys. The representative microstructure of SLM-processed (a-1, a-2)Al2024 [114], (b-1, b-2) A12139[115], (g-1, g-2)Al6061[116], and (h-1, h-2)A17075 [117,118]

Several studies have investigated the 2xxx series aluminum alloys (e.g., 2219, 2618) for additive manufacturing through the optimization of process parameters. These parameters mainly focus on laser power, scanning speed, hatch spacing, layer thick ness, and preheating temperature. It was found that laser power and scanning speed significantly affect crack formation. Thermal cracking decreases with increased laser power and reduced scanning speed. However, cracks still occur even with a preheated substrate at 200-400 °C [119, 120]. Ahuja et al [121]. described the processing of 2xxx series aluminum alloys and observed an increase in relative density when manufacturing small cubic samples with support structures. They prepared samples with a relative density of 99.96%, attributing this mainly to the reduced thermal trans fer between the sample and the build platform when the cross-sectional area of the support is relatively small compared to the surface of the cubic sample. They also noted that the relative density is not directly correlated with the volumetric energy density [122]. Fulcher et al [123]. earlier indicated that the cracking in 6061 is related to its high thermal expansion coefficient and the wide melting range of the material. Uddin successfully prepared crack-free pure 6061 samples by preheating the powder bed to 500°C. The resulting tensile yield strength, ultimate strength, and elongation values were respectively 60 MPa, 130 MPa, and 15% [124].

Figure 1.12 demonstrates the occurrence of hot cracks in L-PBF processed aluminum alloys, including the 2xxx series (Al2024, Al2139) [114, 115], 6xxx series (Al6061)[152], and 7xxx series (Al7075)[117, 118]. These cracks predominantly appear along the boundaries of columnar grains.

1.4 Challenges in SLM manufacturing of high-strength aluminum alloys

1.4.1 Solidification cracking and Mitigation remedies

From the previous description, we understand that hot cracking or hot tearing, especially solidification cracking, is a primary challenge in the SLM processing of high strength aluminum-based alloys. Therefore, a fundamental understanding of the principles behind crack formation is crucial for ensuring the successful development of high-strength aluminum alloys without cracks.

Solidification cracks, also known as hot cracks or solid-state cracks, are a type of crack that forms during the transition of materials from a liquid to a solid state. These cracks are primarily caused by uneven shrinkage and thermal stress within the material [125, 126]. Solidification cracks typically appear along grain boundaries, and the surfaces of these cracks often display a dendritic morphology[127], As presented in Figure1.13. They are frequently partially covered with eutectic phases, indicating poor backfilling by the liquid in the final stages of solidification. The tearing observed on the eutectic surfaces suggests that the mushy zone lacks sufficient strength [128].

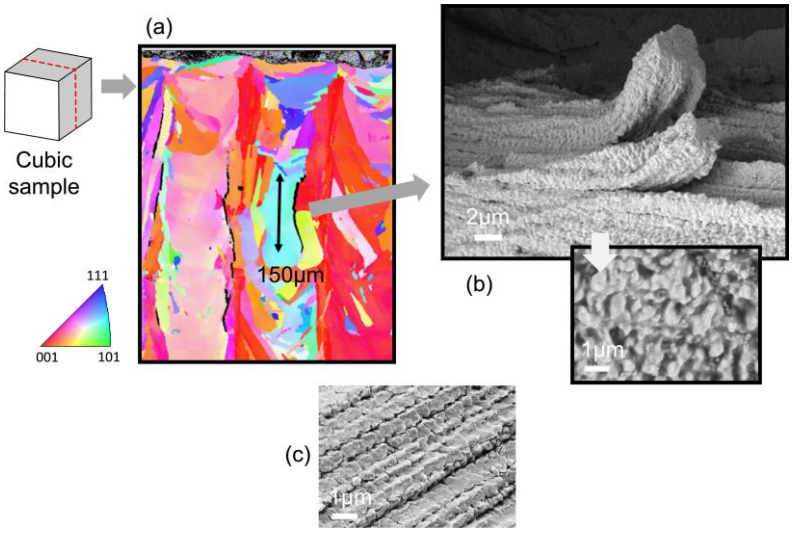

Fig 1.13 Solidification cracking of an Inconel 738 sample pro-cessed by SLM: Microscopic vertical cracks along the grain boundaries, and dendritic microstructures visible on the surface of the cracks [127]

The solidification process of alloys is complex and critical. Unlike pure metals, the solidification of alloys occurs within a specific temperature range. The proportion of different elements affects the temperatures at which solidification starts and ends. The solidification temperature range is defined as the difference between the temperatures of the liquidus and solidus lines. During the SLM process, due to the high thermal gradient and the rapid development of the solid-liquid interface, columnar

crystals are formed, with primary columnar dendrites preferentially growing parallel [109, 128, 129].

Figure1.14 illustrates that solidification progresses through various phases as the solid fraction (fs) incrementally rises. Initially, during solidification, only a small proportion of the liquid phase forms solid particles/phases, known as the slurry zone, where crack formation is unlikely due to adequate liquid metal flow. As solidification advances, a coherency fraction solid/liquid typically between 0.5- 0.8 is attained. Here, dendritic grains begin interconnecting, creating a mushy zone. In this zone, material strength is compromised due to a thin liquid film at the grain boundaries, a result of micro segregation. The permeability significantly decreases as the intertwined dendritic structure restricts liquid backfilling. In this region, solidification cracking is prone to occur due to tensile stresses/strains caused by solidification shrinkage and thermal contraction. Consequently, the temperature interval between the coherency point and the rigidity point is known as the brittle temperature range (BTR) or vulnerable temperature range[130, 131]. As the solid fraction fs further escalates to approximately 0.9-0.99, extensive dendritic bridging takes place. Beyond the rigidity fraction, a robust solid framework forms, providing adequate mechanical strength to withstand cracking and facilitating stress distribution across larger distances [126]. The susceptibility to solidification cracking, traditionally evaluated using the solidification temperature range (the difference between liquidus and solidus temperatures), is a critical factor in materials science. Materials with a wider solidification temperature range tend to have an elongated mushy zone and are more prone to solidification cracking. A prolonged mushy zone implies increased shrinkage strain/stress. Additionally, the challenge of liquid backfilling during the final stages of solidification becomes more pronounced for materials with long channels across a broad temperature range [132, 126]. Analysis of Al-based alloys' solidification paths, based on the classic Scheil-Gulliver model, reveals that alloys like Al2024, Al6061, and Al7075, with broad solidification temperature ranges (132 K, 140 K, and 177 K respectively), are vulnerable to solidification cracking during SLM. In contrast, AlSi7Mg, AlSi10Mg, and AlSil2 alloys, having narrower ranges (55 K, 36 K, and 4 K respectively), demonstrate better processability and greater resistance to hot cracking in SLM processing. However, this parameter fails to account for the absence of solidification cracking in AlSi0.5 and its occurrence in AlSi1 and AlSi2, as Al-Si0.5 exhibits a broader range (81 K) compared to AlSi1 (78 K) and AlSi2 (72 K). Therefore, still more comprehensive indices that consider the complex mechanisms of hot cracking are needed for a more accurate assessment of solidification cracking susceptibility [128, 133].

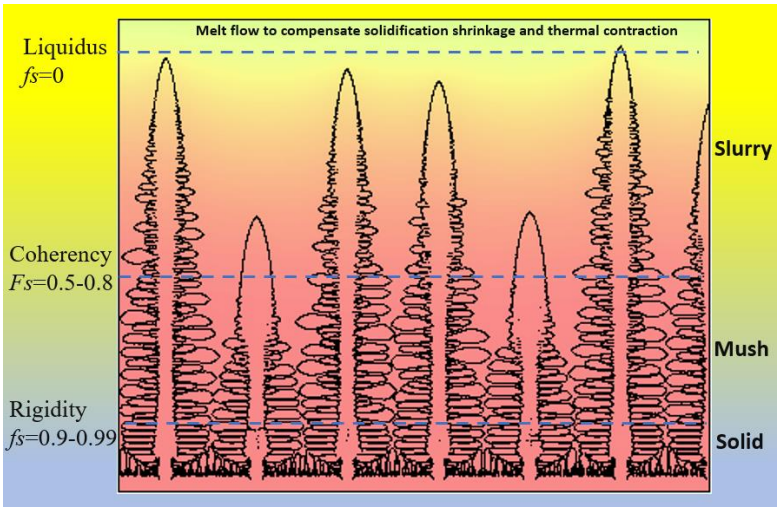

Fig 1.14 Schematic Diagram of the Principle of Solidification Cracking.

The current main strategies to reduce solidification cracking, in addition to adopting appropriate process parameters such as scanning strategy [134]and heating the substrate [135], include two widely accepted approaches to enhance the hot-cracking resistance of traditional high-strength aluminum by modifying the alloy composition: improving liquid flowability and grain refinement through the introduction of nucleants.

The first approach is eutectic modification. This is often achieved by adding certain elements or compounds to the alloy during the manufacturing process, which leads to changes in the way the different phases of the material solidify and interact with each other, Eutectic phases located at grain boundaries, particularly those with high angles, significantly impact solidification cracking. This influence stems from their role in the liquid backfilling capability during the final stages of solidification and in determining the strength of the mushy zone. The strategic positioning of these eutectic phases at the grain boundaries is a key factor in how they affect the material's behavior during solidification [136].

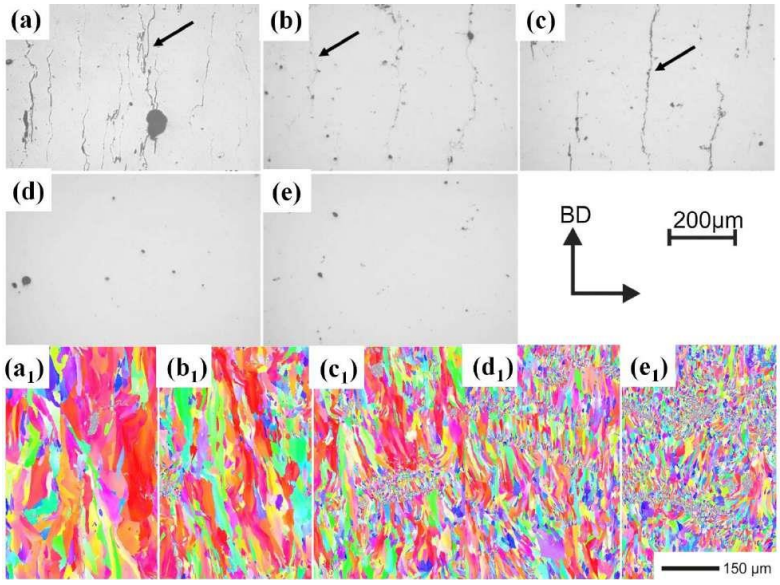

Fig 1.15 Cross-section morphology and EBSD results of LPBF processed Al7075 samples with different content of Si: (a and al) Al7075, (b and b1) 7075+1%Si, (c and c1)7075+2%Si, (d and d1) 7075+3%Si, (e and e1)7075+4%Si [137]

Montero Sistiaga et al. [137] reported that adding 3-4% silicon significantly enhances the processability of the Al7075 alloy, thus effectively alleviating solidification cracking. Introducing Si into Al7075 leads to the formation of more eutectic forming phases in the final stages of solidification, such as Si and Mg2Si,. In the L-PBF process, the addition of Si to 7075 aluminum alloy reduces the melting temperature by 17°C, lowers the solidification temperature range, and improves the flowability of the melt in the final solidification stage [138]. Compared to Al7075 alloy with 0-2wt% Si, the crack-free Al7075 alloy with 3-4wt% Si exhibits a more refined microstructure, with fine equiaxed grains at the melt pool boundary and fine columnar particles within the melt pool. The hardness of the built and aged Al7075+4wt% Si alloy is approximately 171 HV, comparable to that of wrought Al7075-T6 alloy (175 HV). Otaniet al. [139] found that increasing the silicon content in the Al7075 effectively reduced voids and cracks. Additionally, Zhou et al. [138] demonstrated that adding both 4wt% Si and 2wt% TiB2 to an Al-Zn-Mg-Cu alloy facilitated the creation of crack-free Al7xxx series alloys, characterized by a fully equiaxed microstructure. The L-PBF-processed composite alloy exhibited an ultimate tensile strength (UTS) of about 556 MPa and an elongation (EL) of approximately 4.0% after T6 treatment, showcasing enhanced strength and ductility compared to alloys with only Si or TiB2 additions. From the above discussion, it can be observed that the modification of Al-Cu-Mg and Al-Zn-Mg-Cu alloys with Si can enhance the hot-cracking resistance.

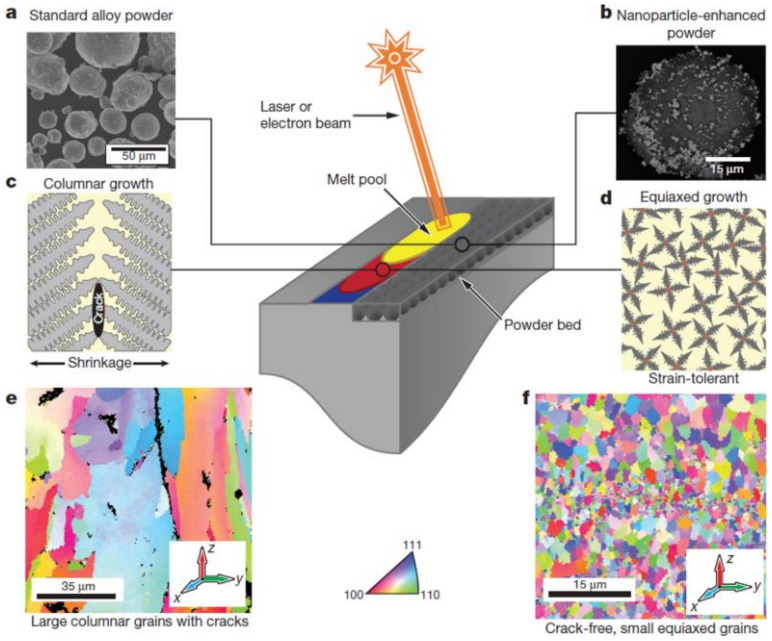

Fig 1.16 Conventional Al7075 powder feedstock and Al7075 powder functionalized with nanoparticles grain refinement schematic comparison[109]

The second approach involves grain refinement. This is achieved by introducing grain refiners to promote heterogeneous nucleation or by adding solutes that offer a high growth restriction factor [140]. Through research, we can discover introduction of nanoparticle nucleants, which manage solidification during additive manufacturing, can address certain challenges. The selection of these nucleants was based on crystallographic criteria, and they were incorporated into the powders of 7075 and 6061 series aluminum alloys. Post-nucleant functionalization, it was observed that these high-strength aluminum alloys, previously deemed unsuitable for additive manufacturing, could be effectively processed using SLM. The outcome was the formation of crack-free, equiaxed (with grains having nearly similar dimensions in length, width, and height), and fine-grained microstructures. The following Figure 1.17 is a chematic comparison showing the transformation of 7075 from coarse columnar crystals to equiaxed crystals after the addition of grain refining particles. These microstructures led to the attainment of material strengths on par with wrought materials[109, 141].

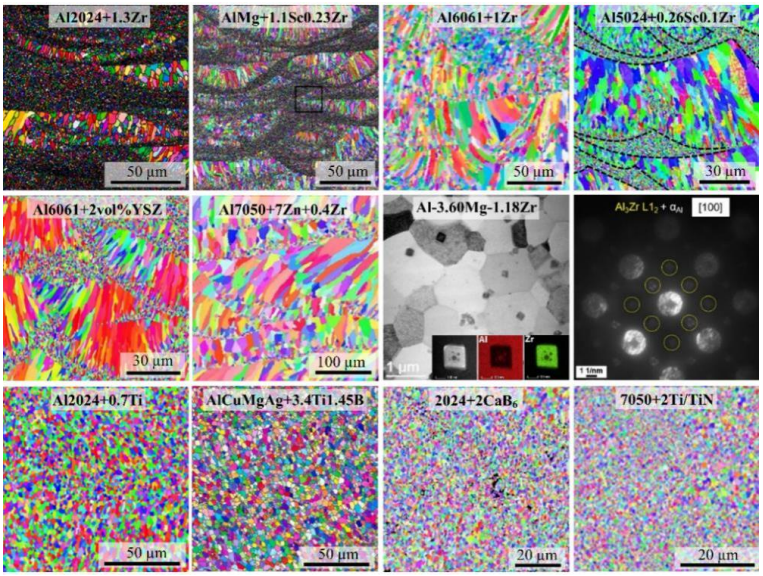

Fig 1.17 Microstructure of L-PBF-processed Al-based alloys con-taining transition elements or ceramic particles.[142-145,116,109]

In another study by Martin and colleagues, AA6061 and AA7075 powders were coated with zirconium (Zr) nanoparticles to demonstrate crack-free SLM manufacturing of functionalized materials [145]. Their findings indicated that components made from AA6061 and AA7075 powders functionalized with Zr nanoparticles were crack-free, displaying a uniform equiaxed grain structure with grain sizes around 5µm. The suppression of crack formation and the refined equiaxed morphology were attributed to the numerous nucleation sites provided by the introduction of Zr nanoparticles. Zhang et al [146] also discovered that the use of zirconium (Zr), which forms Al3Zr particles with aluminum in the melt pool, leads to notable grain refinement and a reduction in hot tearing during the SLM process of 2xxx alloys. These Al3Zr particles act as heterogeneous nucleation sites. Similarly, Opprecht et al. [147] incorporated 2 vol% of Yttrium Stabilized Zirconia (YSZ) in 6061 aluminum alloy, leads to significant grain refinement. The originally coarse columnar microstructure, with grains averaging around 100 um in length, transformed a finer, mixed structure of both columnar and equiaxed grains. This resulted in the columnar grains being less than 10 um in length and the equiaxed grains being smaller than 1 um. This refinement in microstructure was due to the in-situ reaction of YSZ with liquid aluminum during SLM. This reaction generated MgAl2O4 and Al3Zr particles, serving as heterogeneous nucleation sites for the a-Al phase.

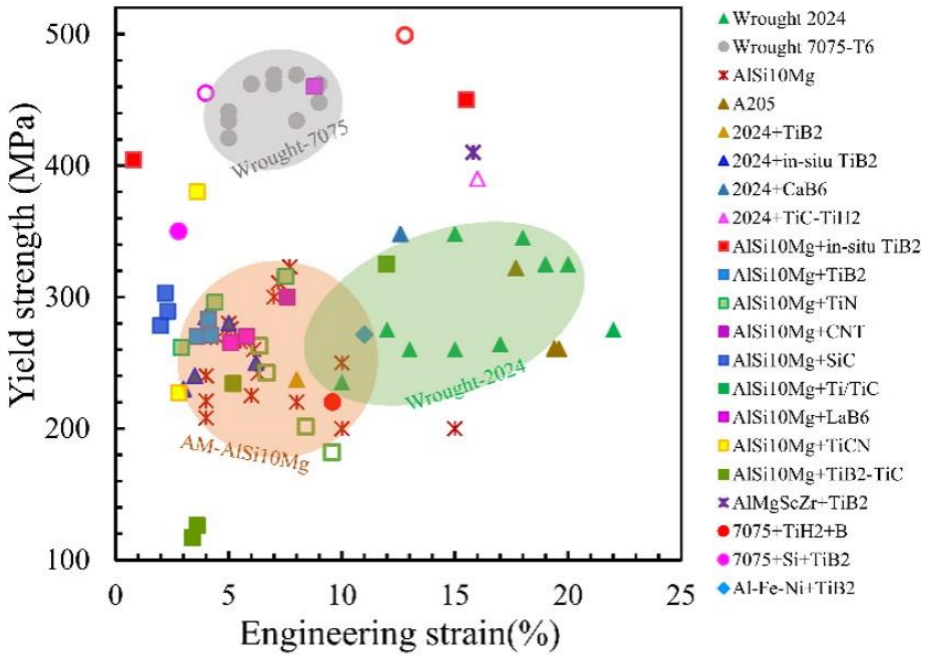

Fig 1.18 Summary of the comparison between engineering yield strength and engineering strain in newly developed Al-based compos- ites.[141-145, 148- 152]

This process was key to achieving a crack-free SLM production of Al6061. Moreover, the incorporation of a small number of transition elements (X), such as Zr, Sc, and Ta, in high-strength Al-based alloys, has been recognized as an effective way to inhibit hot cracking during L-PBF processing by forming a typical bi-modal columnar-equiaxed microstructure, as shown in Figure1.19. The development of a bi-modal microstructure arises primarily due to the favored formation of the primary Al3X phase at the boundaries of the melt pool. This facilitates heterogeneous nucleation and equiaxed growth of the a-Al phase. Concurrently, in the center of the melt pool, the solute trapping of transition elements within the Al solid solution is encouraged by both the rapid growth rate and the substantial cooling rate. Moreover, the addition of ceramic particles like TiB2 [152], TiC[153], TiN[140], and CaB6 [154] into high-strength Al based alloys leads to the formation of a completely equiaxed microstructure. This is attributed to the even dispersion of ceramic particles, which aids in the production of crack-free components via SLM. Optimal grain refiners are characterized by their high melting points, superior thermal stability, effective wettability in Al melts, and minimal lattice mismatch with the a-Al lattice.

The SLM process's high-temperature melting and dynamic characteristics of melt pool flow offer substantial benefits in producing high-strength Al-based metal matrix composites. These methods encompass the addition of ex-situ ceramic reinforcing particles into the initial powder as a powder mixture[154, 155, 156] the synthesis of reinforcing particles using an in-situ technique during powder production[152 157, 158,

159], and the formation of reinforcing particles during SLM via in-situ reactions among reactive particles like Ti/B4C, TiH2/B, and Al melts.[160-162]. Figure 1.18 presents a summary of the relationship between engineering yield strength and engineering strain in recently developed Al-based composites. Numerous Al-based composites, including AlSi10Mg reinforced with LaB6, TiN, TiB2, and CNTs, exhibit marginally improved mechanical properties relative to AMed AlSi10Mg alloys [163, 141 155]. The Al7075 alloy, treated with inoculation of 0.8 wt% TiH2 and 0.16 wt% B, can be processed into crack-free alloys using L-PBF. This process results in a yield strength (YS) of 220 MPa, an ultimate tensile strength (UTS) of 368 MPa, and an elongation (EL) of 9.6% in the as-built condition. Post a T6 heat treatment, the (TiH2+B)/Al7075 composite achieves a YS of 499 MPa, a UTS of 582 MPa, and an EL of 12.8%, surpassing the performance of wrought Al7075 alloy in T6 condition [162].

1.4.2 Alloy element evaporation

Given the involvement of high-energy density lasers in the SLM process, elements within aluminum alloys such as zinc, magnesium, and copper, which possess relatively lower boiling points, are prone to volatilization. This phenomenon of elemental evaporation not only leads to an uneven distribution of material composition but also significantly diminishes the mechanical properties of the aluminum alloy, notably its strength and toughness.

Magnesium (Mg) and Zinc (Zn) are two pivotal alloying elements in aluminum alloys, The evaporation temperature of Mg is approximately 1090C, while for Zn, it is about 907C, exerting a significant influence on their properties[164, 165]. Magnesium, being a lightweight metal, when incorporated into aluminum alloys, markedly enhances the alloy's strength without appreciably increasing its weight. This effect is particularly pronounced in heat-treatable aluminum alloys, such as the Mg2Si phase in 6061 aluminum alloy[166]. In contrast, the primary strengthening phase in 7075 aluminum alloy is MgZn2 These elements manifest as fine precipitates within the aluminum matrix[167, 168]. The uniform dispersion of these fine precipitates throughout the alloy's lattice structure significantly elevates the strength and hardness of the alloy, demonstrating their essential role in augmenting the mechanical properties of aluminum alloys.

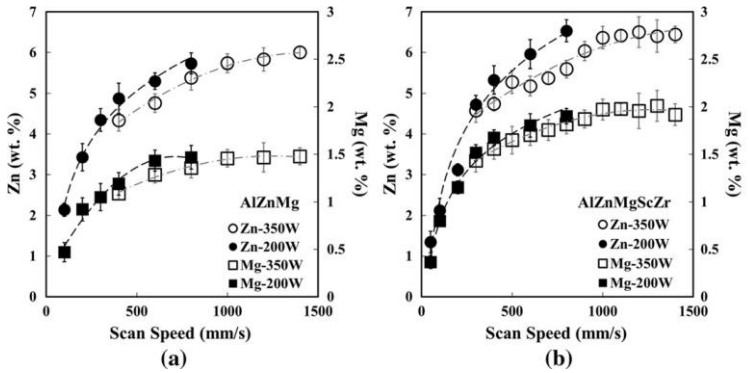

Fig 1.19 The concentration of Zn and Mg in the as-built(a) Al-Zn-Mg and(b)Al-Zn-Mg-Sc-Zr[205]

Magnesium (Mg) and Zinc (Zn) are two pivotal alloying elements in aluminum alloys, The evaporation temperature of Mg is approximately 1090C, while for Zn, it is about 907C, exerting a significant influence on their properties[164 ,165]. Magnesium, being a lightweight metal, when incorporated into aluminum alloys, markedly enhances the alloy's strength without appreciably increasing its weight. This effect is particularly pronounced in heat-treatable aluminum alloys, such as the Mg2Si phase in 6061 aluminum alloy[166]. In contrast, the primary strengthening phase in 7075 aluminum alloy is MgZn2 These elements manifest as fine precipitates within the aluminum matrix[167, 168]. The uniform dispersion of these fine precipitates throughout the alloy's lattice structure significantly elevates the strength and hardness of the alloy, demonstrating their essential role in augmenting the mechanical properties of aluminum alloys.

Martin et al[109]. attempted to print conventional AA7075, achieving a predominantly equiaxed fine-grain structure with no cracks by incorporating 1 vol% of hydrogen stabilized zirconium (ZrH2) nanoparticles. After undergoing solution treatment and aging, the alloy's T6 yield strength reached 325-373 MPa. This strength level, although substantial, was below the anticipated strength, attributed to the loss of 25% Zn and 32% Mg during the printing process. Zhou et al [133]. researched various SLM processing parameters for the Al-6Zn-2Mg alloy and discovered that all tested combinations of laser power and speed resulted in the elemental loss. As illustrated in Figure1.19, the loss of Zn and Mg significantly increased as the laser speed decreased. Mauduit et al [148]. [7] prepared various aluminum alloy samples through the SLM process, including 2017A, 7075, 7020, 6061, among others. They observed losses of magnesium (Mg) and zinc (Zn) in these alloys. As demonstrated in the accompanying table 1.2, the Mg loss in the 2017A aluminum alloy reached as high as 33%, while the minimum loss of Mg in other alloys was close to 17%. In the 7xxx series alloys, the loss of Zn was around 30%. This significant loss is attributed to the fact that Zn has a

lower evaporation temperature compared to Mg.

Table 1.2 The concentration of Zn and Mg in the as-built [169]

Alloys	2017A	7075	7020	6061	5083	AlMg14	AlSi10Mg
Reduction in amount of Mg (%)	33	19	23	17	29	34	57
Reduction in amount of Zn （%）	-	3	30	-	-	-	-

Generally, metal alloys suitable for SLM need to meet three basic physical properties: high laser absorptivity, low thermal conductivity, and absence of low boiling point volatile elements. SLM-processed aluminum alloys often struggle to meet this criteria [157]. This could be due to the lower melting point of aluminum alloys and insufficient laser absorption by aluminum powder [96]. Aluminum and copper alloys both have low absorption rates for traditional 1064 nm infrared lasers, approximately 7% and 5% respectively [170]. Under low power of infrared lasers, heat does not accumulate easily, making it difficult for the powder to melt. At high power densities, however, keyhole formation occurs, leading to issues like particle and droplet spatter, compositional instability, and ultimately resulting in defects such as porosity, cracks, and lack of fusion [171, 172]. Copper and aluminum alloys demonstrate significantly higher absorption rates for 450 nm blue lasers, reaching approximately 65% and 14.5%, respectively. For green laser around 515 nm, copper still shows a high absorption rate of about 40%. Professor Tsukamoto's team [173], through exploring blue-light equipment, successfully fabricated pure copper cladding layers free of porosity and cracks. Similarly, Domine et al [174]. utilized green-light SLM equipment to create high-quality pure copper parts, presenting a new approach for using these novel laser technologies to print materials that exhibit low absorption rates under traditional infrared laser.

1.5 Conclusion

This chapter, through a comprehensive review of a substantial amount of literature, has revealed the challenges encountered in the SLM process, especially for medium to high strength aluminum alloys during the printing process. It summarizes the countermeasures and strategies into several aspects, ensuring the successful development of medium to high strength aluminum alloy processes and new materials via the SLM technique.

In the SLM process, medium-strength aluminum alloys like 6061 and high-

strength aluminum alloys such as 2024 and 7075 face two primary challenges. The first challenge pertains to crack formation, which is intricately linked to the material's solidification process. The thermal cracking sensitivity of an alloy is directly proportional to the disparity in its solidification temperatures; greater discrepancies lead to a higher propensity for cracking. Solidification cracking typically occurs during the mushy zone phase, a stage characterized by columnar dendritic growth impeding the backfill of liquid. A more extensive temperature gradient indicates an elongated mushy zone, thereby increasing the likelihood of crack formation. This can be mitigated by introducing nucleating agents to refine the grain structure, transforming columnar crystals into equiaxed crystals or forming eutectic phases, thus lowering the solidification temperature and enhancing the fluidity of the liquid phase. The loss of low melting point elements is another difficulty faced by high-strength aluminum alloys in the SLM process. There is limited research on improving performance by increasing the powder's absorption rate. For instance, copper exhibits poor printability under infrared laser, but significant improvements have been made under green laser with higher absorption rates. Utilizing shorter laser wavelengths to print materials with low absorption rates provides a novel approach for fabricating high-strength aluminum alloys.

1.6 Objectives and motivations of this study

As previously mentioned, most research on medium-strength 6061 and high-strength 7075 aluminum alloys in the SLM process has focused on exploring the process and modifying the materials. However, there has been limited research on enhancing the absorption rate of these materials, which naturally have a low absorption rate for infrared laser, and on developing processes and properties under short-wavelength lasers. Drawing inspiration from the increased absorption rate of copper under green laser, which resulted in better part fabrication, this paper investigates the performance of 6061 and 7075 aluminum alloys and their titanium particle modified materials printed with green laser. This research offers a new perspective for fabricating high-strength aluminum alloys.

1. The study explores 6061 aluminum powder and its variants with 1wt%, 2wt%, and 4wt% Ti particles, focusing on their process parameters, microstructural morphology, mechanical properties, and heat treatment strengthening mechanisms under green laser printing conditions.

2. The research involves fabricating high-strength 7075 aluminum alloy samples using green laser SLM equipment, incorporating different concentrations of Ti particles and TiC/SiC particles (1wt%, 2wt%, and 4wt%). The study focuses on analyzing the

process parameters, microstructural morphology, mechanical properties, and the performance of these materials after heat treatment.

References

[1] C. Korner, "Additive manufacturing of metallic components by selective electron beam melting—a review," International Materials Reviews, vol. 61, no. 5, pp.361-377,2016.

[2] M. Galati and L. Iuliano, "A literature review of powder-based electron beam melting focusing on numerical simulations," Additive Manufacturing, vol. 19, pp.1-20,2018.

[3] M. Kahnert, S. Lutzmann, and M. Zaeh, "Layer formations in electron beam sintering," in 2007 International Solid Freeform Fabrication Symposium, 2007. [4] M. Sigl, S. Lutzmann, and M. Zaeh, "Transient physical effects in electron beam sintering," in 2006 International Solid Freeform Fabrication Symposium, 2006.

[5] L. E. Murr et al., "Microstructural architecture, microstructures, and mechanical properties for a nickel-base superalloy fabricated by electron beam melting," Metallurgical and Materials Transactions A, vol. 42, pp. 3491-3508, 2011.

[6] M. Larsson, U. Lindhe, and O. Harrysson, "Rapid manufacturing with electron beam melting (ebm) a manufacturing revolution?" In 2003 International Solid Freeform Fabrication Symposium, 2003.

[7] S. Biamino et al., "Electron beam melting of ti-48al-2cr-2nb alloy: Microstructure and mechanical properties investigation," Intermetallics, vol. 19, no. 6, pp.776-781,2011.

[8] X. Tan et al., "Graded microstructure and mechanical properties of additive manufactured ti-6al-4v via electron beam melting," Acta Materialia, vol. 97, pp.1-16,2015.

[9] P. Heinl, L. Miller, C. Korner, R. F. Singer, and F. A. Miller, "Cellular ti-6al 4v structures with interconnected macro porosity for bone implants fabricated by selective electron beam melting," Acta biomaterialia, vol. 4, no. 5, pp. 1536 1544,2008.

[10] L. E. Murr et al, "Characterization of titanium aluminide alloy components fabricated by additive manufacturing using electron beam melting," Acta materialia, vol. 58, no. 5, pp. 1887-1894, 2010.

[11] J. Parthasarathy, B. Starly, S. Raman, and A. Christensen, "Mechanical evaluation of porous titanium (ti6al4v) structures with electron beam melting (ebm)," Journal of the mechanical behavior of biomedical materials, vol. 3, no.3, pp.249-259, 2010.

[12] K. O. Abdulrahman, E. T. Akinlabi, R. M. Mahamood, S. Pityana, and M. Tlotleng, "Laser metal deposition of titanium aluminide composites: A review," Materials Today: Proceedings, vol. 5, no. 9, pp. 19738-19 746, 2018.

[13] D. D. Gu, W. Meiners, K. Wissenbach, and R. Poprawe, "Laser additive manufacturing of metallic components: Materials, processes and mechanisms," International materials reviews, vol. 57, no. 3, pp. 133-164,2012.

[14] X. Zhang, C. Li, M. Zheng, Z. Ye, X. Yang, and J. Gu, "Anisotropic tensile behavior of ti-47al-2cr-2nb alloy fabricated by direct laser deposition," Additive Manufacturing, vol. 32, p.101087,2020.

[15] P. N. Sibisi, A. Popoola, N. K. Arthur, and S. L. Pityana, "Review on direct metal laser deposition manufacturing technology for the ti-6al-4v alloy," The International Journal of Advanced Manufacturing Technology, vol. 107, pp.1163-1178,2020.

[16] A. Singh, A. Ramakrishnan, and G. Dinda, "Fabrication of al-11.2 si components by direct laser metal deposition for automotive applications," Journal of Welding and Joining, vol. 35, no. 4, pp. 67-73, 2017.

17] T. Abioye, A. Medrano-Tellez, P. Farayibi, and P. Oke, "Laser metal deposition of multi-track walls of 308lsi stainless steel," Materials and Manufacturing Processes, vol. 32, no. 14, pp. 1660-1666, 2017.

[18] M. Moradi, A. Hasani, Z. M. Beiranvand, and A. Ashoori, "Additive manufacturing of stellite 6 superalloy by direct laser metal deposition-part 2: Effects of scanning pattern and laser power reduction in differrent layers," Optics 8 Laser Technology, vol. 131, p. 106455, 2020.

[19] M. R. Hajideh and M. Farahani, "Direct laser metal deposition cladding of in718 on din 1.2714 tool steel reinforced by the sic nanoparticles," Journal of Materials Research and Technology, 2023.

[20] I. Tabernero, A. Lamikiz, S. Martiénez, E. Ukar, and J. Figueras, "Evaluation of the mechanical properties of inconel 718 components built by laser cladding," International Journal of Machine Tools and Manufacture, vol. 51, no. 6,pp. 465-470, 2011.

[21] K. Shah, I. ul Haq, A. Khan, S. A. Shah, M. Khan, and A. J. Pinkerton, "Parametric study of development of inconel-steel functionally graded materials by laser direct metal deposition," Materials Design (1980-2015), vol. 54, pp.531-538,2014.

[22] J. Cai, B. Zhang, and X. Qu, "Microstructure evolution and mechanical be havior of ss316l alloy fabricated by a non-toxic and low residue binder jetting process," Applied Surface Science, p. 156589, 2023.

[23] P. Nandwana, A. M. Elliott, D. Siddel, A. Merriman, W. H. Peter, and S. S. Babu, "Powder bed binder jet 3d printing of Inconel 718: Densification, microstructural evolution and challenges," Current Opinion in Solid State and Materials Science, vol. 21, no. 4, pp. 207-218, 2017.

[24] K. Yuvaraj, A. M. Ismail, P. Nagarajan, and S. Vigneshwaran, "Design and fabrication of gypsum prototypes based on binder jetting technology," Materials Today: Proceedings, vol. 45, pp. 3085-3090, 2021.

[25] A. Mostafaei et al., "Binder jet 3d printing-process parameters, materials, properties, modeling, and challenges," Progress in Materials Science, vol. 119, p.100707,2021.

[26] B. Utela, D. Storti, R. Anderson, and M. Ganter, "A review of process development steps for new material systems in three dimensional printing (3dp)," Journal of Manufacturing Processes, vol. 10, no. 2, pp. 96-104, 2008.

[27] Y. Mao, J. Li, W. Li, D. Cai, and Q. Wei, "Binder jetting additive manufacturing of 3161 stainless-steel green parts with high strength and low binder content: Binder preparation and process optimization," Journal of Materials Processing Technology, vol. 291, p. 117020, 2021.

[28] X. Lv, F. Ye, L. Cheng, S. Fan, and Y. Liu, "Binder jetting of ceramics: Powders, binders, printing parameters, equipment, and post-treatment," Ceramics International, vol. 45, no. 10, pp. 12609-12624, 2019.

[29] F. Zhang et al., "3d printing technologies for electrochemical energy storage," Nano Energy, vol. 40, pp. 418-431,2017.

[30] S. Gaytan et al., "Fabrication of barium titanate by binder jetting additive manufacturing technology," Ceramics International, vol. 41, no. 5, pp. 6610 6619,2015.

[31] J. Suwanprateeb and R. Chumnanklang, "Three-dimensional printing of porous polyethylene structure using water-based binders," Journal of Biomedical Materials Research Part B: Applied Biomaterials: An Official Journal of The Society for Biomaterials, The Japanese

Society for Biomaterials, and The Australian Society for Biomaterials and the Korean Society for Biomaterials, vol. 78, no. 1, pp. 138-145, 2006.

[32] H. Zeidler, D. Klemm, F. Bottger-Hiller, S. Fritsch, M. J. Le Guen, and S. Singamneni, "3d printing of biodegradable parts using renewable biobased materials," Procedia Manufacturing, vol. 21, pp. 117-124, 2018.

[33] S. Wieland and F. Petzoldt, "Binder jet 3d-printing for metal additive manufacturing: Applications and innovative approaches," in CFI Ceram. Forum Int. 93,2016, E26-E30.

[34] S. Holland, T. Foster, and C. Tuck, "Creation of food structures through binder jetting," in Fundamentals of 3D food printing and applications, Elsevier, 2019, pp.257-288.

[35] E. A. Rojas-Nastrucci, J. T. Nussbaum, N. B. Crane, and T. M. Weller, "Ka band characterization of binder jetting for 3-d printing of metallic rectangular waveguide circuits and antennas," IEEE Transactions on Microwave Theory and Techniques, vol. 65, no. 9, pp. 3099-3108, 2017.

[36] H. Shangguan, J. Kang, C. Deng, J. Yi, Y. Hu, and T. Huang, "3d-printed rib enforced shell and mold for aluminum castings," The International Journal of Advanced Manufacturing Technology, vol. 96, pp. 2175-2182, 2018.

[37] J.-P. Kruth, P. Mercelis, J. Van Vaerenbergh, L. Froyen, and M. Rombouts, "Binding mechanisms in selective laser sintering and selective laser melting," Rapid prototyping journal, 2005.

[38] R. D. Farahani, D. Therriault, M. Dubé, S. Bodkhe, and M. Mahdavi, "Additive manufacturing of multifunctional nanocomposites and composites," 2018.

[39] F. Paolucci, M. van Mook, L. Govaert, and G. Peters, "Influence of post condensation on the crystallization kinetics of pal2: From virgin to reused powder,"Polymer, vol. 175, pp. 161-170, 2019.

[40] W. Gao et al., "The status, challenges, and future of additive manufacturing in engineering," Computer-Aided Design, vol. 69, pp. 65-89, 2015.

[41] J.-P. Kruth, X. Wang, T. Laoui, and L. Froyen, "Lasers and materials in selective laser sintering," Assembly Automation, vol. 23, no. 4, pp. 357-371, 2003.

[42] S. Riza, S. Masood, and C. Wen, "Laser-assisted additive manufacturing for metallic biomedical scaffolds," Comprehensive Materials Processing, vol. 10, pp.285-301,2014.

[43] K. S. Munir, Y. Li, and C. Wen, "Metallic scaffolds manufactured by selective laser melting for biomedical applications," in Metallic Foam Bone, Elsevier, 2017,pp.1-23.

[44] B. Nagarajan, Z. Hu, X. Song, W. Zhai, and J. Wei, "Development of micro selective laser melting: The state of the art and future perspectives," Engineering, vol. 5, no. 4, pp. 702-720, 2019.

[45] C. K. Chua and K. F. Leong, 3D Printing and additive manufacturing: Principles and applications (with companion media pack)-of rapid prototyping. World Scientific Publishing Company, 2014.

[46] C. Y. Yap et al., "Review of selective laser melting: Materials and applications," Applied physics reviews, vol. 2, no. 4, p. 041101, 2015.

[47] I. Yadroitsev, P. Bertrand, and I. Smurov, "Parametric analysis of the selective laser melting process," Applied surface science, vol. 253, no. 19, pp. 8064-8069, 2007.

[48] R. Li, J. Liu, Y. Shi, L. Wang, and W. Jiang, "Balling behavior of stainless steel and nickel powder during selective laser melting process," The International Journal of Advanced Manufacturing Technology, vol. 59, pp. 1025-1035, 2012.

[49] M. Balbaa, S. Mekhiel, M. Elbestawi, and J. McIsaac, "On selective laser melting of inconel 718: Densification, surface roughness, and residual stresses," Materials Design, vol. 193, p. 108818, 2020.

[50] A. Gusarov and J.-P. Kruth, "Modelling of radiation transfer in metallic powders at laser treatment," International Journal of Heat and Mass Transfer, vol.48, no. 16, pp. 3423-3434,2005.

[51] N. K. Tolochko et al., "Balling processes during selective laser treatment of powders," Rapid prototyping journal, 2004.

[52] X. Shi, S. Ma, C. Liu, and Q. Wu, "Parameter optimization for ti-47al-2cr 2nb in selective laser melting based on geometric characteristics of single scan tracks," Optics Laser Technology, vol. 90, pp. 71-79, 2017.

[53] H. Jia, H. Sun, H. Wang, Y. Wu, and H. Wang, "Scanning strategy in selective laser melting (slm): A review," The International Journal of Advanced Manufacturing Technology, vol. 113, pp. 2413-2435, 2021.

[54] A. B. Spierings, N. Herres, and G. Levy, "Influence of the particle size distribution on surface quality and mechanical properties in am steel parts," Rapid Prototyping Journal, vol. 17, no. 3, pp. 195-202, 2011.

[55] P. Bidare, I. Bitharas, R. Ward, M. M. Attallah, and A. J. Moore, "Laser powder bed fusion in high-pressure atmospheres," Int. J. Adv. Manuf. Technol, vol.99, no.1-4,pp.543-555,2018.

[56] J. Gunasekaran, P. Sevvel, and I. J. Solomon, "Metallic materials fabrication by selective laser melting: A review," Materials Today: Proceedings, vol. 37, pp.252-256,2021.

[57] I. Yadroitsev, P. Krakhmalev, and I. Yadroitsava, "Selective laser melting of ti6al4v alloy for biomedical applications: Temperature monitoring and microstructural evolution," Journal of Alloys and Compounds, vol. 583, pp. 404 409,2014.

[58] R. Mertens, S. Dadbakhsh, J. Van Humbeeck, and J.-P. Kruth, "Application of base plate preheating during selective laser melting," Procedia Chirp, vol. 74, pp.5-11,2018.

[59] J. Suryawanshi, K. Prashanth, and U. Ramamurty, "Mechanical behavior of selective laser melted 316l stainless steel," Materials Science and Engineering: A, vol. 696, pp. 113-121, 2017.

[60] S. Sui et al., "The influence of laves phases on the room temperature tensile properties of Inconel 718 fabricated by powder feeding laser additive manufacturing," Acta Materialia, vol. 164, pp. 413-427, 2019.

[61] Z. Xie, Y. Dai, X. Ou, S. Ni, and M. Song, "Effects of selective laser melting build orientations on the microstructure and tensile performance of ti-6al-4v alloy," Materials Science and Engineering: A, vol. 776, p. 139001, 2020.

[62] C. Ng, M. Savalani, H. C. Man, and I. Gibson, "Layer manufacturing of mag nesium and its alloy structures for future applications," Virtual and physical prototyping, vol. 5, no. 1, pp. 13-19, 2010.

[63] A. Aversa et al., "New aluminum alloys specifically designed for laser powder bed fusion: A review," Materials, vol. 12, no. 7, p. 1007, 2019.

[64] Popovich A, Sufiiarov V, Polozov I, et al. Microstructure and mechanical properties of additive manufactured copper alloy[J]. Materials Letters, 2016, 179: 38-41.

[65]Yan X, Chang C, Dong D, et al. Microstructure and mechanical properties of pure copper manufactured by selective laser melting[J]. Materials Science and Engineering: A, 2020, 789: 139615.

[66]Yeong W, Yap C Y, Mapar M, et al. State-of-the-art review on selective laser melting of ceramics[J]. High value manufacturing: advanced research in virtual and rapid prototyping, 2013, 1: 65-70.

[67] J. Cherry, H. Davies, S. Mehmood, N. Lavery, S. Brown, and J. Sienz, "Investigation into the effect of process parameters on microstructural and physical properties of 316l stainless

steel parts by selective laser melting," The International Journal of Advanced Manufacturing Technology, vol. 76, pp. 869-879, 2015.

[68] D. Kong et al., "Mechanical properties and corrosion behavior of selective laser melted 3161 stainless steel after different heat treatment processes," Journal of Materials Science Technology, vol. 35, no. 7, pp. 1499-1507, 2019.

[69] M. Laleh, A. E. Hughes, W. Xu, P. Cizek, and M. Y. Tan, "Unanticipated dras tic decline in pitting corrosion resistance of additively manufactured 316l stain- less steel after high-temperature post-processing," Corrosion Science, vol. 165, p.108412,2020.

[70] X. Yin et al., "Effect of tungsten particles on microstructure and properties of 316 1 stainless steel manufactured by selective laser melting," Journal of Manufacturing Processes, vol. 68, pp. 210-221, 2021.

[71] G. Kasperovich, J. Haubrich, J. Gussone, and G. Requena, "Correlation be tween porosity and processing parameters in tial6v4 produced by selective laser melting," Materials Design, vol. 105, pp. 160-170, 2016.

[72] B. Song, S. Dong, B. Zhang, H. Liao, and C. Coddet, "Effects of processing parameters on microstructure and mechanical property of selective laser melted ti6al4v,"Materials Design, vol. 35, pp. 120-125, 2012.

[73] Y. Kok et al., "Anisotropy and heterogeneity of microstructure and mechanical properties in metal additive manufacturing: A critical review," Materials Design,vol.139,pp.565-586,2018.

[74] Y. M. Wang et al., "Additively manufactured hierarchical stainless steels with high strength and ductility," Nature materials, vol. 17, no. 1, pp. 63-71, 2018.

[75] M. Ni, S. Liu, C. Chen, R. Li, X. Zhang, and K. Zhou, "Effect of heat treatment on the microstructural evolution of a precipitation-hardened superalloy produced by selective laser melting," Materials Science and Engineering: A, vol. 748, pp. 275-285, 2019.

[76] M. Salehi, S. Maleksaeedi, H. Farnoush, M. L. S. Nai, G. K. Meenakshisundaram, and M. Gupta, "An investigation into interaction between magnesium powder and ar gas: Implications for selective laser melting of magnesium," Powder Technology, vol. 333, pp. 252-261, 2018.

[77] D. Lide, "Properties of elements and inorganic compounds," C'RC' Handbook of Chemistry and Physics on CD-ROM, 2002.

[78] A. Pawlak, M. Rosienkiewicz, and E. Chlebus, "Design of experiments approach in az31 powder selective laser melting process optimization," Archives of Civil and Mechanical Engineering, vol. 17, pp. 9-18, 2017.

[79] A. Aversa et al., "New aluminum alloys specifically designed for laser powder bed fusion: A review," Materials, vol. 12, no. 7, p. 1007, 2019.

[80] Y. Qi, H. Zhang, X. Nie, Z. Hu, H. Zhu, and X. Zeng, "A high strength al-li alloy produced by laser powder bed fusion: Densification, microstructure, and mechanical properties," Additive Manufacturing, vol. 35, p. 101 346, 2020. [116] P. A. Rometsch, Y. Zhu, X. Wu, and A. Huang, "Review of high-strength aluminium alloys for additive manufacturing by laser powder bed fusion," Materials Design, vol. 219, p. 110779, 2022.

[81] N. T. Aboulkhair, M. Simonelli, L. Parry, I. Ashcroft, C. Tuck, and R. Hague, "3d printing of aluminium alloys: Additive manufacturing of aluminium alloys using selective laser melting," Progress in materials science, vol. 106, p. 100 578, 2019.

[82] M. S. Kenevisi, Y. Yu, and F. Lin, "A review on additive manufacturing of al-cu (2xxx) aluminium alloys, processes and defects," Materials Science and Technology, vol. 37, no. 9, pp. 805-829, 2021.

[83] H. Zhang, H. Zhu, T. Qi, Z. Hu, and X. Zeng, "Selective laser melting of high strength al-cu-mg alloys: Processing, microstructure and mechanical proper- ties," Materials Science and Engineering: A, vol. 656, pp. 47-54, 2016.

[84] Y. Weng, L. Ding, Z. Jia, and Q. Liu, "Effect of combined addition of ag and cu on the precipitation behavior for an al-mg-si alloy," Materials Characterization, vol. 171, p.110 736,2021.

[85] T. Marlaud, A. Deschamps, F. Bley, W. Lefebvre, and B. Baroux, "Influence of alloy composition and heat treatment on precipitate composition in al-zn mg-cu alloys," Acta Materialia, vol. 58, no. 1, pp. 248-260, 2010.

[86] J. Praneeth, S. Venkatesh, and L. S. Krishna, "Process parameters influence on mechanical properties of alsi10mg by slm," Materials Today: Proceedings, 2023.

[87] K. Prashanth, S. Scudino, and J. Eckert, "Defining the tensile properties of al-12si parts produced by selective laser melting," Acta Materialia, vol. 126, pp.25-35,2017.

[88] N. Kang, P. Coddet, L. Dembinski, H. Liao, and C. Coddet, "Microstructure and strength analysis of eutectic al-si alloy in-situ manufactured using selective laser melting from elemental powder mixture," Journal of Alloys and Com pounds, vol. 691, pp. 316-322, 2017.

[89] K. Kempen, L. Thijs, E. Yasa, M. Badrossamay, W. Verheecke, and J.-P. Kruth, "Process optimization and microstructural analysis for selective laser melting of alsil0mg," in 2011 International Solid Freeform Fabrication Sympo- sium, University of Texas at Austin, 2011.

[90] W.-Y. Li, C. Zhang, X. Guo, G. Zhang, H. Liao, and C. Coddet, "Deposition characteristics of al-12si alloy coating fabricated by cold spraying with relatively large powder particles," Applied surface science, vol. 253, no. 17, pp.7124-7130,2007.

[91] P. Bidare, I. Bitharas, R. Ward, M. Attallah, and A. J. Moore, "Fluid and particle dynamics in laser powder bed fusion," Acta Materialia, vol. 142, pp. 107 120,2018.

[92] I. Yadroitsev, A. Gusarov, I. Yadroitsava, and I. Smurov, "Single track formation in selective laser melting of metal powders," Journal of Materials Processing Technology, vol. 210, no. 12, pp. 1624-1631, 2010.

[93] H. Rao, S. Giet, K. Yang, X. Wu, and C. H. Davies, "The influence of processing parameters on aluminium alloy a357 manufactured by selective laser melting,' Materials Design, vol. 109, pp. 334-346, 2016.

[94] S. Chen, G. Guillemot, and C.-A. Gandin, "Three-dimensional cellular automaton finite element modeling of solidification grain structures for arc-welding processes," Acta materialia, vol. 115, pp. 448-467, 2016.

[95] X. Li and W. Tan, "Numerical investigation of effects of nucleation mechanisms on grain structure in metal additive manufacturing," Computational Materials Science, vol. 153, pp. 159-169, 2018.

[96] S. Liu, H. Zhu, G. Peng, J. Yin, and X. Zeng, "Microstructure prediction of selective laser melting alsi10mg using finite element analysis," Materials Design, vol. 142, pp. 319-328, 2018.

[97] X. Liu, C. Zhao, X. Zhou, Z. Shen, and W. Liu, "Microstructure of selective laser melted alsi10mg alloy," Materials 8 Design, vol. 168, p. 107677, 2019.

[98] Y. ZOU, Z. WEI, and Jun DU, "Alsi10mg the influence and optimization of process parameters on the density in laser selective melting of alsi10mg," Laser Application, vol. 36, no. 6, pp. 656-662, 2016.

[99] F. Trevisan et al., "On the selective laser melting (SLM) of the alsi10mg alloy: Process, microstructure, and mechanical properties," Materials, vol. 10, no. 1, p.76,2017.

[100] A. H. Maamoun, Y. F. Xue, M. A. Elbestawi, and S. C. Veldhuis, "Effect of selective laser melting process parameters on the quality of al alloy parts: Pow der characterization, density, surface roughness, and dimensional accuracy,' Materials, vol. 11, no. 12, p. 2343, 2018.

[101] M. Chen et al., "Novel composite powders with uniform tib2 nano-particle distribution for 3d printing," Applied Sciences, vol. 7, no. 3, p. 250, 2017.

[102] P. Wang et al., "A review of particulate-reinforced aluminum matrix composites fabricated by selective laser melting," Trans. Nonferrous Met. Soc. China, vol. 30, no. 8, pp. 2001-2034, 2020.

[103] M. Chao, H.-c. Cui, F.-g. Lu, and X.-h. Tang, "Evolution behavior of tib2 particles during laser welding on aluminum metal matrix composites reinforced with particles," Transactions of Nonferrous Metals Society of China, vol. 23, no. 6, pp. 1543-1548, 2013.

[104] T. Quested, A. L. Greer, and P. Cooper, "The variable potency of tib2 nucleant particles in the grain refinement of aluminium by al-ti-b additions," in Materials Science Forum, Trans Tech Publ, vol. 396, 2002, pp. 53-58.

[105] Y. Xiao et al., "Enhancing strength and ductility of alsi10mg fabricated by selective laser melting by tib2 nanoparticles," Journal of Materials Science U Technology, vol. 109, pp. 254-266, 2022.

[106] L. Xi, D. Gu, S. Guo, R. Wang, K. Ding, and K. G. Prashanth, "Grain refinement in laser manufactured al-based composites with tib2 ceramic," Journal of materials research and technology, vol. 9, no. 3, pp. 2611-2622, 2020.

[107] L. Thijs, K. Kempen, J.-P. Kruth, and J. Van Humbeeck, "Fine-structured aluminium products with controllable texture by selective laser melting of pre alloyed alsi10mg powder," Acta Materialia, vol. 61, no. 5, pp. 1809-1819, 2013.

[108] I. Brodova, O. Chikova, A. Petrova, and A. Merkushev, "Structure formation and properties of eutectic silumin obtained using selective laser melting,"

Physics of Metals and Metallography, vol. 120, pp. 1109-1114, 2019.

[109] J. H. Martin, B. D. Yahata, J. M. Hundley, J. A. Mayer, T. A. Schaedler, and T. M. Pollock, "3d printing of high-strength aluminium alloys," Nature, vol.549, no.7672, pp. 365-369,2017.

[110] D. Lassance, D. Fabregue, F. Delannay, and T. Pardoen, "Micromechanics of room and high temperature fracture in 6xxx al alloys," Progress in materials science, vol. 52, no. 1, pp. 62-129,2007.

[111] T. Qi, H. Zhu, H. Zhang, J. Yin, L. Ke, and X. Zeng, "Selective laser melting of al7050 powder: Melting mode transition and comparison of the characteristics between the keyhole and conduction mode," Materials Design, vol. 135, pp.257-266,2017.

[112] A. Mauduit, S. Pillot, H. Gransac, et al., "Study of the suitability of aluminum alloys for additive manufacturing by laser powder bed fusion," UPB Sci. Bull. Ser. B Chem. Mater. Sci, vol. 79, pp. 219-238,2017.

[113] N. Kaufmann, M. Imran, T. M. Wischeropp, C. Emmelmann, S. Siddique, and F. Walther, "Influence of process parameters on the quality of aluminium alloy en aw 7075 using selective laser melting (SLM)," Physics Procedia, vol. 83, pp. 918-926, 2016.

[114] Q. Tan et al., "Inoculation treatment of an additively manufactured 2024 aluminium alloy with titanium nanoparticles," Acta Materialia, vol. 196, pp. 1-16, 2020.

[115] J. H. K. Tan, S. L. Sing, and W. Y. Yeong, "Microstructure modelling for metallic additive manufacturing: A review," Virtual and Physical Prototyping, vol.15,no.1,pp.87-105,2020.

[116] C. Bohm, M. Werz, and S. Weihe, "Practical approach to eliminate solidification cracks by supplementing almg4. 5mn0. 7 with alsi10mg powder in laser powder bed fusion," Materials, vol. 15, no. 2, p. 572, 2022.

[117] A. Mehta et al., "Additive manufacturing and mechanical properties of the dense and crack free zr-modified aluminum alloy 6061 fabricated by the laser powder bed fusion," Additive Manufacturing, vol. 41, p. 101966, 2021.

[118] W. Stopyra, K. Gruber, I. Smolina, T. Kurzynowski, and B. Kuznicka, "Laser powder bed fusion of aa7075 alloy: Influence of process parameters on porosity and hot cracking," Additive Manufacturing, vol. 35, p. 101270, 2020.

[119] D. Koutny et al., "Influence of scanning strategies on processing of aluminum alloy en aw 2618 using selective laser melting," Materials, vol. 11, no. 2, p. 298, 2018.

[120] Z. Hu, X. Nie, Y. Qi, H. Zhang, and H. Zhu, "Cracking criterion for high strength al-cu alloys fabricated by selective laser melting," Additive Manufacturing, vol. 37, p. 101 709, 2021.

[121] B. Ahuja, M. Karg, K. Y. Nagulin, and M. Schmidt, "Fabrication and characterization of high strength al-cu alloys processed using laser beam melting in metal powder bed," Physics Procedia, vol. 56, pp. 135-146, 2014.

[122] M. Karg, B. Ahuja, S. Kuryntsev, A. Gorunov, and M. Schmidt, "Processability of high strength aluminum-copper alloys aw-2022 and 2024 by laser beam melting in powder bed," in 2014 International Solid Freeform Fabrication Symposium, University of Texas at Austin, 2014.

[123] B. A. Fulcher, D. K. Leigh, and T. J. Watt, "Comparison of alsi10mg and al 6061 processed through dmls," in 2014 International Solid Freeform Fabrication Symposium, University of Texas at Austin, 2014.

[124] S. Z. Uddin, L. E. Murr, C. A. Terrazas, P. Morton, D. A. Roberson, and R. B. Wicker, "Processing and characterization of crack-free aluminum 6061 using high-temperature heating in laser powder bed fusion additive manufacturing," Additive Manufacturing, vol. 22, pp. 405-415,2018.

[125] S. Kou, "A criterion for cracking during solidification," Acta Materialia, vol. 88, pp.366-374,2015.

[126] J. Lippold, T. Bollinghaus, and C. E. Cross, Hot cracking phenomena in welds III. Springer Science & Business Media, 2011.

[127] D. Grange, J. Bartout, B. Macquaire, and C. Colin, "Processing a non-weldable nickel-base superalloy by selective laser melting: Role of the shape and size of the melt pools on solidification cracking," Materialia, vol. 12, p. 100686, 2020.

[128] Y. Li, H. Li, L. Katgerman, Q. Du, J. Zhang, and L. Zhuang, "Recent advances in hot tearing during casting of aluminium alloys," Progress in Materials Science, vol. 117, p. 100741, 2021.

[129] M. E. Glicksman, Principles of solidification: an introduction to modern casting and crystal growth concepts. Springer Science & Business Media, 2010.

[130] T. Clyne and D. GJ, "The influence of composition on solidification cracking susceptibility in binary alloy systems," 1981.

[131] M. Rappaz, J. .-. Drezet, and M. Gremaud, "A new hot-tearing criterion," Metallurgical and materials transactions A, vol. 30, pp. 449-455, 1999.

[132] T. Boellinghaus, J. C. Lippold, and C. E. Cross, Cracking phenomena in welds IV. Springer, 2016.

[133] S. Kou, "A simple index for predicting the susceptibility to solidification crack ing," Weld. J, vol. 94, no. 12, pp. 374-388, 2015.

[134] S. Catchpole-Smith, N. Aboulkhair, L. Parry, C. Tuck, I. A. Ashcroft, and A. Clare, "Fractal scan strategies for selective laser melting of 'unweldable'nickel superalloys," Additive Manufacturing, vol. 15, pp. 113-122, 2017.

[135] K. Prashanth et al., "Production of high strength al85nd8ni5co2 alloy by selective laser melting," Additive Manufacturing, vol. 6, pp. 1-5, 2015.

[136] J. Liu, H. P. Duarte, and S. Kou, "Evidence of back diffusion reducing cracking during solidification," Acta Materialia, vol. 122, pp. 47-59, 2017.

[137] M. L. Montero-Sistiaga et al., "Changing the alloy composition of al7075 for better processability by selective laser melting," Journal of Materials Processing Technology, vol. 238, pp. 437-445, 2016.

[138] S. Zhou, Y. Su, H. Wang, J. Enz, T. Ebel, and M. Yan, "Selective laser melting additive manufacturing of 7xxx series al-zn-mg-cu alloy: Cracking elimination by co-incorporation of si and tib2," Additive Manufacturing, vol. 36, p. 101458, 2020.

[139] Y. Otani and S. Sasaki, "Effects of the addition of silicon to 7075 aluminum alloy on microstructure, mechanical properties, and selective laser melting processability," Materials Science and Engineering: A, vol. 777, p. 139079, 2020.

[140] X. Li, G. Li, M.-X. Zhang, and Q. Zhu, "Novel approach to additively manufacture high-strength al alloys by laser powder bed fusion through addition of hybrid grain refiners," Additive Manufacturing, vol. 48, p. 102400, 2021.

[141] Q. Tan et al., "A novel method to 3d-print fine-grained alsi10mg alloy with isotropic properties via inoculation with lab6 nanoparticles," Additive Manufacturing, vol. 32, p. 101034, 2020.

[142] R. Mertens, L. Baert, K. Vanmeensel, and B. Van Hooreweder, "Laser powder bed fusion of high strength aluminum," Material Design & Processing Communications, vol. 3, no. 5, e161, 2021.

[143] J. R. Croteau et al., "Microstructure and mechanical properties of al-mg-zr alloys processed by selective laser melting," Acta Materialia, vol. 153, pp. 35 44,2018.

[144] Y. Wang, X. Lin, N. Kang, Z. Wang, Y. Liu, and W. Huang, "Influence of post heat treatment on the microstructure and mechanical properties of al-cu-mg-zr alloy manufactured by selective laser melting," Journal of Materials Science Technology, vol. 111, pp. 35-48, 2022.

[145] K. V. Yang, Y. Shi, F. Palm, X. Wu, and P. Rometsch, "Columnar to equiaxed transition in al-mg (-sc)-zr alloys produced by selective laser melting," Scripta Materialia, vol. 145, pp. 113-117, 2018.

[146] H. Zhang, H. Zhu, X. Nie, J. Yin, Z. Hu, and X. Zeng, "Effect of zirconium addition on crack, microstructure and mechanical behavior of selective laser melted al-cu-mg alloy," Scripta Materialia, vol. 134, pp. 6-10, 2017.

[147] M. Opprecht, J.-P. Garandet, G. Roux, C. Flament, and M. Soulier, "A solution to the hot cracking problem for aluminium alloys manufactured by laser beam melting,"Acta Materialia, vol. 197, pp. 40-53, 2020.

[148] A. B209-14, Standard specification for aluminum and aluminum-alloy sheet and plate,2014.

[149] J. Wang et al., "Selective laser melting of high-strength tib2/almgsczr compos ites: Microstructure, tensile deformation behavior, and mechanical properties," Journal of Materials Research and Technology, vol. 16, pp. 786-800, 2022.

[150] H. Ding et al., "Effect of in-situ tib2 particles on microstructure and mechanical properties of al-fe-ni manufactured by selective laser melting," Materials Science and Engineering: A, vol. 845, p. 143065, 2022.

[151] L. Wang, X. Jiang, M. Guo, X. Zhu, and B. Yan, "Characterization of structural properties for alsil0mg alloys fabricated by selective laser melting," Materials Science and Technology, vol. 33, no. 18, pp. 2274-2282, 2017.

[152] M. Ghoncheh et al., "On the microstructure and solidification behavior of new generation additively manufactured al-cu-mg-ag-ti-b alloys," Additive Manufacturing, vol. 37, p. 101724, 2021.

[153] E. Zhuravlev et al., "Assessment of alznmgcu alloy powder modification for crack-free laser powder bed fusion by differential fast scanning calorimetry," Materials Design, vol. 204, p. 109677, 2021.

[154] P. Mair et al., "Laser powder bed fusion of nano-cab6 decorated 2024 aluminum alloy," Journal of Alloys and Compounds, vol. 863, p. 158 714, 2021.

[155] C. Gao, W. Wu, J. Shi, Z. Xiao, and A. Akbarzadeh, "Simultaneous enhancement of strength, ductility, and hardness of tin/alsi10mg nanocomposites via selective laser melting," Additive Manufacturing, vol. 34, p. 101378, 2020.

[156] C. Gao, Z. Liu, Z. Xiao, W. Zhang, K. Wong, and A. Akbarzadeh, "Effect of heat treatment on slm-fabricated tin/alsi10mg composites: Microstructural evolution and mechanical properties," Journal of Alloys and Compounds, vol. 853, p.156722,2021.

[157] X. P. Li et al., "Selective laser melting of nano-tib2 decorated alsi10mg alloy with high fracture strength and ductility," Acta Materialia, vol. 129, pp. 183 193,2017.

[1] T.85 Sun et al., "The role of in-situ nano-tib2 particles in improving the print ability of no castable 2024al alloy," Materials Research Letters, vol. 10, no. 10, pp.656-665,2022.

[159] P. Mair, L. Kaserer, J. Braun, N. Weinberger, I. Letofsky-Papst, and G. Leicht fried, "Microstructure and mechanical properties of a tib2-modified al-cu alloy processed by laser powder-bed fusion," Materials Science and Engineering: A, vol. 799, p. 140 209, 2021.

[160] J. Yi, X. Zhang, J. H. Rao, J. Xiao, and Y. Jiang, "In-situ chemical re action mechanism and non-equilibrium microstructural evolution of (tib2+ tic)/alsil0mg composites prepared by slm-cs processing," Journal of Alloys and Compounds, vol. 857, p. 157 553, 2021.

[161] X. Liu, Y. Liu, Z. Zhou, K. Wang, Q. Zhan, and X. Xiao, "Grain refinement and crack inhibition of selective laser melted aa2024 aluminum alloy via inoculation with tic-tih2," Materials Science and Engineering: A, vol. 813, p. 141 171, 2021.

[162] B. Huang, Y. Liu, Z. Zhou, W. Cheng, and X. Liu, "Selective laser melting of 7075 aluminum alloy inoculated by al-ti-b: Grain refinement and superior mechanical properties," Vacuum, vol. 200, p. 111 030, 2022.

[163] L. Jiang et al., "Preparation and mechanical properties of cnts-alsi10mg composite fabricated via selective laser melting," Materials Science and Engineering: A, vol. 734, pp. 171-177, 2018.

[164] E. L. Rooy, "Introduction to aluminum and aluminum alloys," 1990. [201] F. Campbell, "Aluminum alloys," Lightweight Materials: Understanding the Basics, Ohio: ASM International, p. 34, 2012.

[165] F. Campbell, "Aluminum alloys," Lightweight Materials: Understanding the Basics, Ohio:ASM International, p. 34,2012.

[166] E. Linardi, R. Haddad, and L. Lanzani, "Stability analysis of the mg2si phase in aa 6061 aluminum alloy," Procedia Materials Science, vol. 1, pp. 550-557, 2012.

[167] Y. Zhang et al., "Effect of aging time on precipitation of mgzn2 and microstructure and properties of 7075 aluminum alloy," Journal of Materials Engineering and Performance, pp. 1-11, 2023.

[168] H. B. Yang, M. N. Li, H. Y. Bu, and X. Lu, "Effects of alloying elements on the amounts of mgzn2 and s-al2cumg phase in 7075 aluminum alloy," Journal of Micromechanics and Molecular Physics, vol. 5, no. 02, p. 2050003, 2020.

[169] L. Zhou et al., "Process-dependent composition, microstructure, and printability of al-zn-mg and al-zn-mg-sc-zr alloys manufactured by laser powder bed fusion," Metallurgical and Materials Tran1sactions A, vol. 51, no. 6, pp. 3215 3227,2020.

[170] E. W. Spisz, Solar absorptances and spectral reflectances of 12 metals for temperatures ranging from 300 to 500 K. National Aeronautics and Space Administration, 1969.

[171] Z. Wan, H.-P. Wang, J. Li, J. Solomon, N. Chen, and B. Carlson, "Effect of beam oscillation frequency on spattering in remote laser stitch welding of thin-gage zinc-coated steel with keyhole penetration," Journal of Materials Processing Technology, vol. 302, p. 117 482, 2022.

[172] W. Zhang et al., "Interfacial characteristics and mechanical properties of additive manufacturing martensite stainless steel on the cu-cr alloy substrate by directed energy deposition," Journal of Materials Science Technology, vol. 90, pp.121-132,2021.

[173] T. Hara et al., "Pure copper layer formation on pure copper substrate using multi-beam laser cladding system with blue diode lasers," Applied Physics A, vol. 126, pp. 1-6, 2020.

[174] A. Domine, C. Verdy, C. Penaud, L. Vitu, N. Fenineche, and L. Dembinski, "Selective laser melting (slm) of pure copper using 515-nm green laser: From single track analysis to mechanical and electrical characterization," The Inter- national Journal of Advanced Manufacturing Technology, pp. 1-12, 2023.

Chapter 2 Materials characterization and experimental techniques

2.1 Characterization of the raw materials

In this work, 6061Al and 7075Al pre-alloy powders were used as the raw materials respectively. The Ti powder with a particle seize of 1~20 um was used as reinforced particle. The shape, morphology, and chemical composition of the powder were characterized by scanning electron microscopy (SEM JEOL-5900 LV, Japan), equipped with energy-dispersive X-ray spectroscopy (EDS) .The particle size distributions of the powders were measured by a laser diffraction powder sizer (Mastersizer 2000, Malvern Instruments Ltd., UK) which is displayed in Figure 2.1. Besides, the overview and representative magnified morphology of the used metallurgical powder were presented.

Fig 2.1 Laser diffraction powder sizer

As can be seen in Figure 2.2 the 6061Al and 7075Al powder particles were mainly spherical and near-spherical in shape, without satellite particles on the surface. That is an important characteristic of excellent flowability which meets exactly the requirement during the SLM process. The particle size distributions are concentered on 35um. The results of EDS characterization are agreed with the chemical composition that is listed in

Table 2.1.

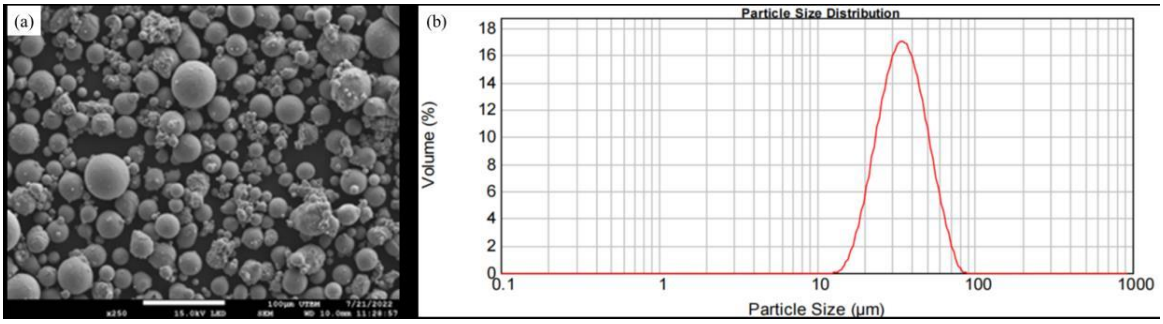

Fig 2.2 Characterization of 6061Al powder (a) morphology (b) particle size distribution

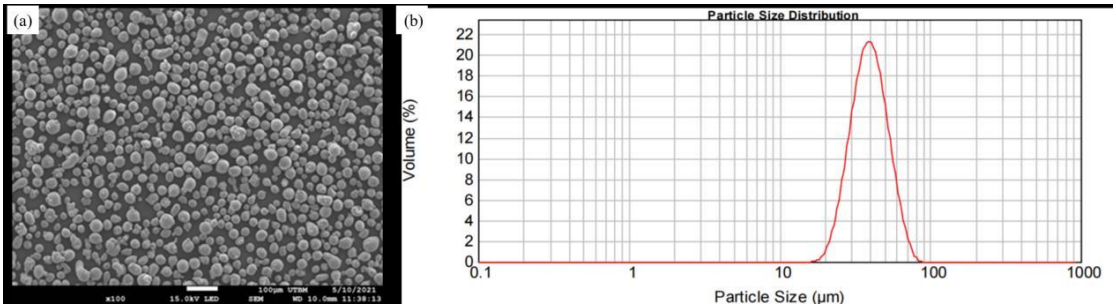

Fig 2.3 Characterization of 7075Al powder (a) morphology (b) particle size distribution

Table 2.1 The nominal composition of the powders

	Nominal composition (wt.%)			
Alloy	AI	Zn	Mg	Cu
6061A1	Bal			
7075AI	Bal	5.0±0.07	2.5±0.05	1.7±0.08

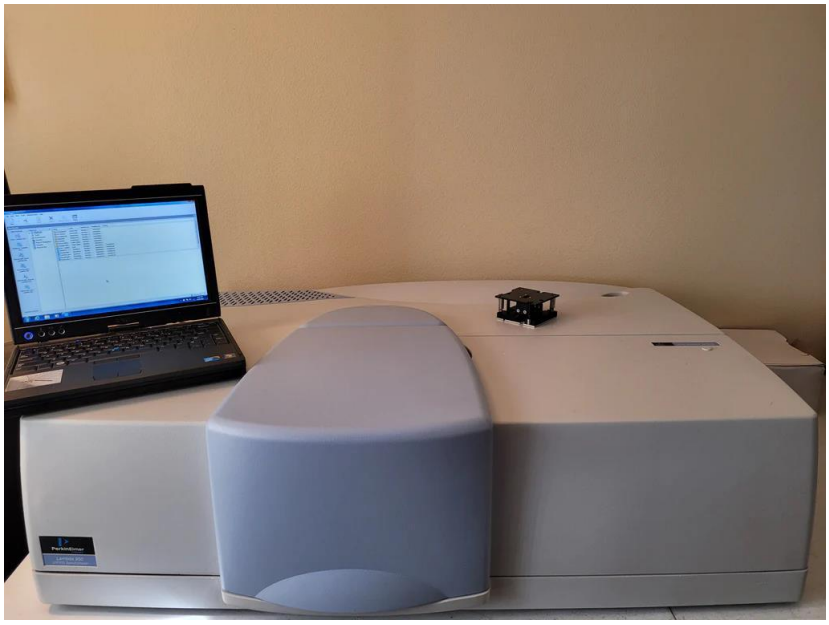

Fig 2.4 The Perkin Elmer Lambda 950 High-Performance UV/Vis/NIR Spectrophotometer

The process of testing the reflectance of powder using the Perkin Elmer Lambda 950 High Performance UV/Vis/NIR Spectrophotometer (as show in involves several steps. Firstly, the spectrophotometer is calibrated and set up according to the manufacturer's specifications for reflectance measurements. The powder sample is then prepared, typically by pressing it into a uniform layer or using a suitable holder to ensure a consistent and reproducible surface for measurement. The sample is placed in the spectrophotometer, and the instrument measures the intensity of light reflected from the powder at various wavelengths across the UV, visible, and NIR spectrum. The data is collected and analyzed to determine the reflectance properties of the powder.

2.2 The SLM system

2.2.1 Introduce to the utilized machine

A series of specimens were prepared using a selective laser melting machine truprint 1000 (TRUMPF, Germany). It is equipped with an green laser. The maximum power is 400W. The photos of this machine and working chamber are exhibited in Figure 2.5. It employs a hopper of feedstock powder. The chamber can be filled with argon. The gas circulation system can discharge the splashed powder or dregs to the side. The platform can be moved up and down by motor control. The oxygen content can be kept below 0.1 vol.% using neutral gas (such as argon) controlled by a sensor to avoid material oxidation during manufacturing. In this work, the aluminum alloy was used as a platform for manufacturing.

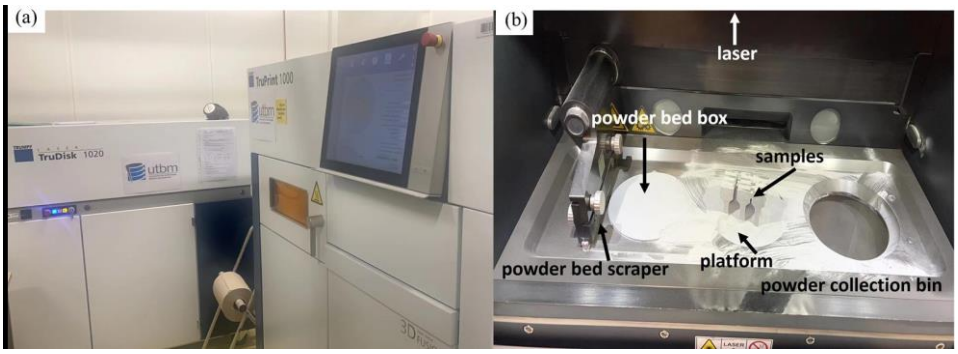

Fig 2.5 (a) The utilized SLM system, (b) working chamber

2.2.2 Working principle and main processing parameters

Before starting all the works, the 3D design software was used to design the building models, then, the models were imported into the SLM computer system for slicing and setting parameters. In the system of truprint 1000, the laser beam (with a laser power) expose (exposure in a time at a level of ~μs) and scan rapidly (with a scanning speed) with the designed strategy, which was controlled by the computer, Figure 2.6 (a) is a picture of SLM manufacturing process. As shown in Figure 2.6 (b), the distance between each laser track is hatch distance. When the first layer powder was selectively melted fully, the platform could be dropped a height to spreading the second powder, the value of the height is layer thickness. The processing parameters can be set in the computer system.

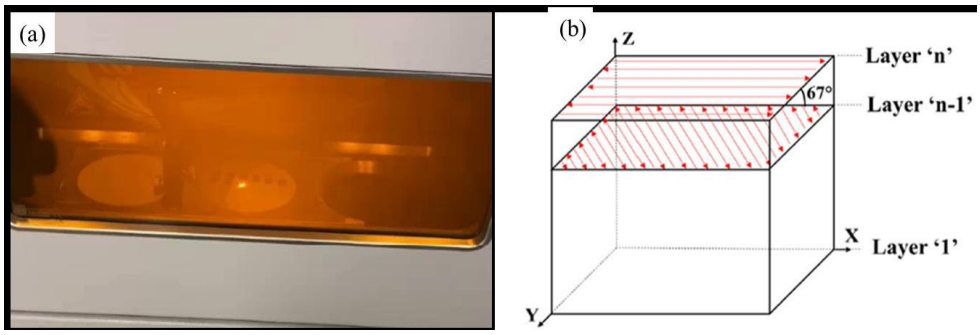

Fig 2.6 (a)SLM manufacturing process, (b)Schematic diagram of scanning strategy and parameters

2.3 Materials characterization

2.3.1 Top surface morphology and porosity analysis

The cubic SLM samples (show in Figure 2.7) were embedded in resin, polished, and then etched. As shown in Figure 2.8 (a), an optical microscope was used to obtain optical micrographics by an optical microscope (OM, Nikon, Japan) and observe the defects distributions. The porosity was determined from the OM micrographs by an image analysis method. Each sample was analyzed with a minimum of five optical micrographs at different areas alternatively via the image processing software ImageJ.

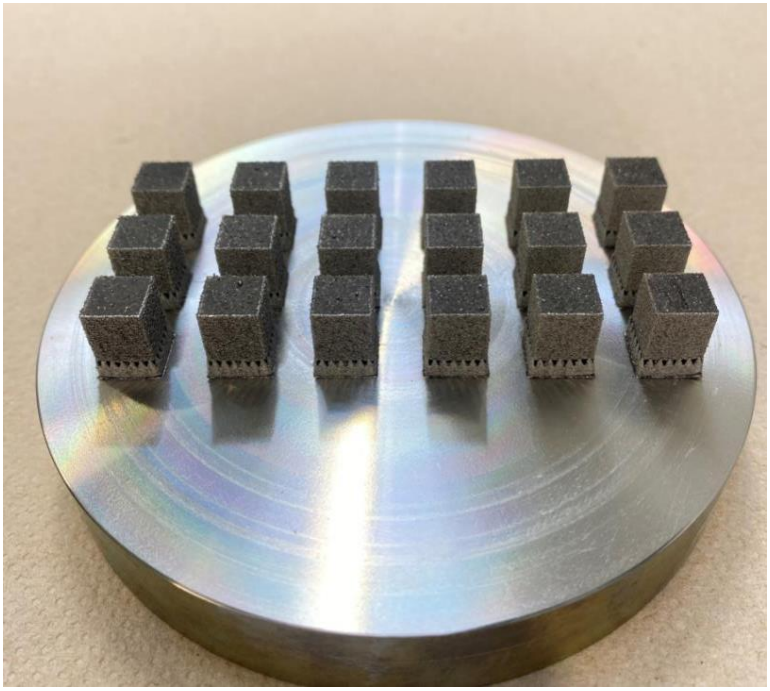

Fig 2.7 The cubic SLM samples

2.3.2 Microstructural characterization

To clearly observe the microstructure, specimens were polished and etched at room temperature using a solution with 95 mL H2O+2.5 mL HNO3 +1.5 mL HC+1.0 mL HF for 10~20 s, then, were observed by SEM system (Figure 2.8 (b), equipped with an EDS unit. Grain size and crystallographic orientations of SLM specimens were observed by A scanning electron microscope (SEM), equipped with both electron backscattered diffraction (EBSD) and energy dispersive X-ray spectroscopy (EDS) (EDAX-TSL) with a step size of 0.15 um and analyzed using Channel 5 software. Samples for EBSD characterization were prepared by mechanical polishing and final surface iron milling. The SEM micrographs and EDS analyses were taken at an accelerating voltage of 15 keV. EBSD analysis were performed along their longitudinal direction at a scanning step size of 0.3 μm. A critical misorientation angle of 10 was applied to identify grain boundaries.

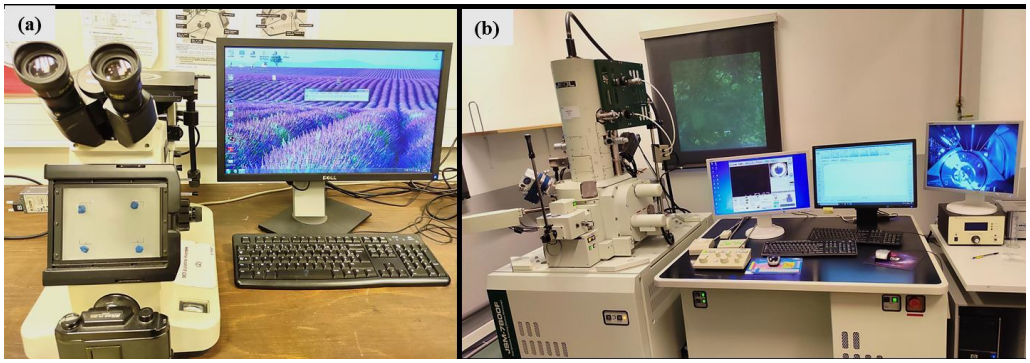

Fig 2.8 (a) The optical microscope and (b)scanning electron microscopy

2.3.3 Phase analysis

Fig 2.9 The X-Ray diffractometer

The XRD analyses were performed on an X-Ray diffractometer (XRD-6100, Shimadzu Co. Ltd., Japan), as presented in Figure 2.9, operating at 40 kV/40 mA and using Cu Kα radiation (λ=0.15406 nm). 20 scans were performed between 30 and 110 with a scan speed of 5° • min-1.

2.4 Post heat treatment

As shown in Figure 2.10, to study the effect of heat treatment on the microstructures and mechanical properties, the SLM samples were performed in a box-type furnace using a furnace (OTF 1200X-80) under Argon protective atmosphere to prevent the samples from oxidation. The T6 heat treatment process is as follows: First, the material is heated at a rate of 5℃/min to 470℃ and held for 1 hour under a protective argon atmosphere, then rapidly removed and quenched in water. Second, the material is heated at a rate of ℃/min to 120℃ and directly maintained at this temperature for 24 hours under a protective argon atmosphere, followed by cooling in air.

Fig 2.10 Home-made furnace (PMDM-LERMPS)

2.5 Measurement and study of mechanical properties

2.5.1 Microhardness

The Vickers hardness measurements were carried out using a microhardness tester (Leiz-Wetzlar, Germany) at a condition with a load of 100 g and an indentation time of 25 s. To ensure accuracy, the average value of the hardness was recorded by 10 measurements.

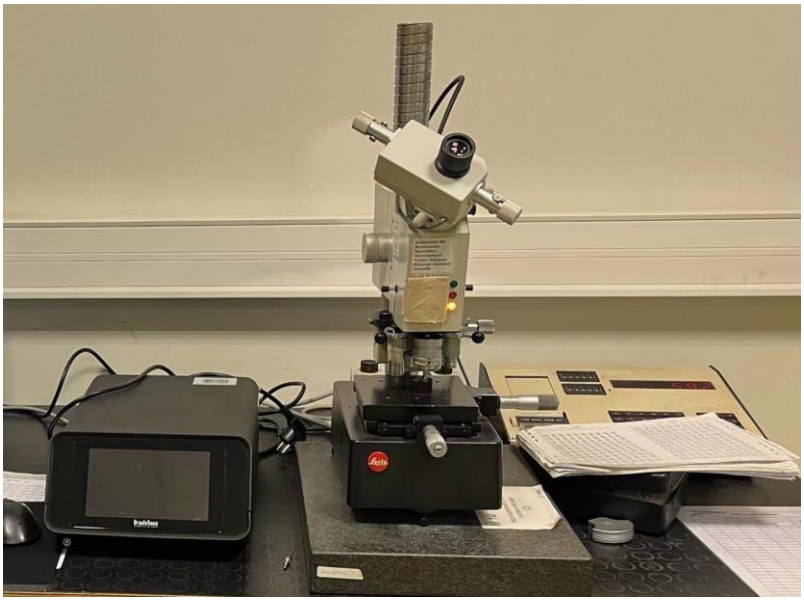

Fig 2.11 The microhardness tester

2.5.2 Tensile test

The tensile samples were fabricated parallel to the platform and removed from the platform along the XY plane, as depicted in Figure 2.12 (a). Macro morphology of the polished tensile samples with a gauge length of 55 mm, a width of 16 mm, and a thickness of 4 mm for mechanical properties test were shown in Figure 2.12 (c). Tensile tests were carried out at room temperature according to the ASTM E 8M standard at a displacement rate of 1 mm/min [7]. The morphology of tensile testing equipment was displayed in Figure 2.12 (b). Mechanical properties including ultimate tensile strength (UTS), yield strength (YS), and fracture strain were read directly from the INSTRON tensile tester. The elongation at break (EL) was measured based on the guidance of the ASTM E 111 standard. The strain-to-failure was evaluated through strain gauges and electronic extensometers with a range of 10 mm that were mounted on the gauge section of the test samples. For each experimental group, three samples were tested, and the averaged values were calculated. The fracture morphologies of the tensile samples were then observed and investigated using SEM.

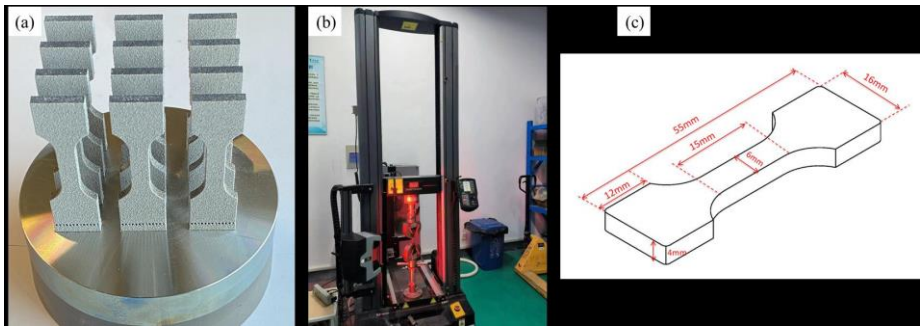

Fig 2.12 (a) The tensile samples; (b) static tensile test machine (c) polished SLMed samples for tensile test

References

[1] I. ISO, ASTM 52921: 2013. Standard Terminology for Additive Manufacturing--Coordinate Systems and Test Methodologies, International Organization for Standardization: Geneva, Switzerland, (2013).

[2] G. Hilton, IEC Magnetic Materials 60404-Part 6: Methods of measurement of the magnetic properties of magnetically soft metallic and powder materials at frequencies in the range 20 Hz to kHz by the use of ring specimens, (2003).

[3] H. Tiismus, A. Kallaste, A. Belahcen, M. Tarraste, T. Vaimann, A. Rassolkin, B. Asad, P Shams Ghahfarokhi, AC Magnetic Loss Reduction of SLM Processed Fe-Si for Additive Manufacturing of Electrical Machines, Energies, 14(2021)1241.

[4] S. Tumanski, Handbook of magnetic measurements, CRC press, 2016.

[5] A. Plotkowski, K. Carver, F. List, J. Pries, Z. Li, A.M. Rossy, D. Leonard, Design and performance of an additively manufactured high-Si transformer core, Mater. Des., 194 (2020) 108894.

[6] I.I.E. Commission, Magnetic materials-Part 4: Methods of measurement of dc magnetic roperties of magnetically soft materials, in, IEC, 2000.

[7]A. E8, ASTM E8/E8M standard test methods for tension testing of metallic materials 1, Annu. B. ASTM Stand., 4 (2010)1-27.

Chapter 3 Study on Selective Laser Melting of 6061 Aluminum Alloys Modified with Titanium

The manufacturing of AA6061 Aluminum alloy Selective Laser Melting (SLM) faces significant challenges, such as hot cracking and the evaporation of volatile elements such as Mg and Si. To address these problems, this chapter proposes a method that focuses on introducing Titanium (Ti) phases to reduce the occurrence of hot cracking in AA6061 during SLM. Ti (wt%1~4%) was added to the original feedstocks to test their strengthening effects and explain the strengthening mechanism. The use of a green laser source with a shorter wavelength (515 nm) compared to that of a red laser source (605~700 nm) enables a lower energy density and a lower loss of Mg and Si. Thus, better mechanical properties can be achieved. The mechanics behind grain refinement and hot cracking mitigation in the Ti-modified AA6061 alloy are explained. An investigation was conducted to examine the heat treatment response of the alloy that was developed.

3.1 Introduction

Laser-based powder bed fusion (LPBF), commonly referred to as Selective Laser Melting (SLM), is an additive manufacturing method that utilizes a laser as the energy source. This approach enables the production of intricate metal components by consolidating powder layers using additive processes [1]. Compared to traditional subtractive manufacturing methods, additive manufacturing (AM) provides inherent benefits for producing medium-low quantities of products. This is because AM can create customized and intricate components as a single piece without requiring costly molds or tooling [2]. In addition, the steep temperature gradients and rapid cooling rates applied during SLM improved the mechanical performance of the 3D-printed components. The increased strength of the metals treated with SLM is attributed to the presence of supersaturated solid solutions and nonequilibrium phases, as well as their improved solidification microstructures with high dislocation densities [3]. In aluminum alloys produced using SLM, strength can be enhanced through precipitation during subsequent heat treatment. These aluminum alloys, namely, those in the 2xxx, 6xxx, and 7xxx series, acquire their mechanical strength via the production of precipitates during post-heat treatments. This phenomenon is especially intriguing.

AA 6061 is a heat-treatable alloy that contains silicon (Si) and magnesium (Mg)

as its primary alloying constituents. AA6061 is extensively used in the aerospace and automobile industries because of its exceptional strength-to-weight ratio, resilience to corrosion, and simplicity of traditional manufacturing [4]. For example, AA6061 is capable of extrusion, rolling, forging, and casting processes. Various assembly techniques, including riveting, welding, brazing, soldering, and adhesive bonding, are also applicable to AA6061 . In contrast, the use of SLM AM fabrication for AA6061 enhances the benefits of the material by optimizing the topology, mesh structure, thin features, internal features, and other characteristics that may be challenging to obtain using traditional manufacturing methods [5,6]. Consequently, AA6061 has garnered interest from the additive manufacturing sector. The processing of AA6061 utilizing SLM has been challenging due to the high susceptibility of the material to cracking during solidification [7,8]. The welding literature extensively discusses the phenomenon of solidification cracking in Al-Si-Mg alloy systems [9–11]. Valuable knowledge about the parameters that influence crack development in SLM may be derived from these discussions. After analysing solidification cracking in welds, Cross [12] determined that several metallurgical factors contribute to this phenomenon. These factors include the significant difference between the solidus and liquidus temperatures (solidification range) of an alloy, the hindrance of liquid transport to the shrinkage area caused by a complex dendritic network in the mushy zone, and the absence of eutectic points for a specific alloy. Furthermore, the surface tension of the liquid metal influences the occurrence of solidification cracking by influencing the wetting behaviour of grain boundaries and the flow of liquid metal between dendrites.

Pellini [13] introduced a strain theory to explain solidification cracking from a mechanical perspective. This theory suggests that a liquid metal film may rupture when it is subjected to excessive strain, which is dictated by the cooling rate of the weld and the range of solidification. While there is ongoing discussion among researchers about the nucleation and spread of solidification cracking in welding, the prevailing approach for welding AA6061 products is to use filler metals derived from silicon-rich 4000 series aluminium alloys or magnesium-rich 5000 series aluminium alloys. Kou [14] noted that the use of filler material decreased the heat gradient in the molten zone during solidification, potentially alleviating the issue of cracking during welding. Additional techniques, such as preheating the base materials [15] and using backing strips, have also been examined. Following reference, preheating was accomplished during the pulsed laser welding procedure by injecting an additional continuous wave laser beam. Preheating led to decreased cracking in autogenous bead-on-plate welding of a 6000 series alloy, namely, 6016 (not AA6061). The backing strip technique [16] was shown

to be effective for autogenous welding of aluminium alloys in the 5000 series. However, crack-free autogenous welding was not successful for an aluminium alloy in the 6000 series. Based on the welding literature, it can be inferred that the range of solidification and the pace at which the liquid metal cools (also known as the solidification rate) are the primary parameters that determine the occurrence of solidification cracking. The research also indicated that the use of filler materials and preheating of the weld zone have effectively been utilized in welding to prevent cracking.

To date, there have been very limited successful reports on the use of SLM processing to produce crack-free AA6061. For example, Louvis et al. [17] documented the occurrence of delamination and a low relative density (89.5%) when AA6061 was manufactured using SLM. These authors attributed these difficulties to the creation of an oxide film. It was contended that the aluminium oxide film had a greater melting point than the precursor powder. Instead of undergoing melting, the oxide layer disintegrates inside the molten pool, disrupting the bonding between two successive layers and resulting in delamination. A separate investigation determined that the propensity of the first powders to absorb oxygen was recognized as a significant element contributing to the separation of the layers [5]. In addition to the problems related to delamination, it has been shown that AA6061 is especially prone to cracking when manufactured using SLM. For instance, Fulcher et al. [8] showed that the occurrence of cracks during SLM processing of AA6061 was strongly correlated with the high coefficient of thermal expansion and wide melting range of the material. Loh and colleagues [18,] examined the thermo-processing characteristics of laser powder bed fusion on AA6061. These studies have shown that crack development and growth occur across several grains [19]. To overcome some of the challenges associated with the SLM processing of AA6061, several approaches have been investigated. Robert et al. [7] conducted a study on the manufacture of an unalloyed combination of aluminium (Al) and silicon (Si) powders using SLM. The proportions of the powders used were the same as those used for nominal AA6061. During the solidification process of AA6061, the occurrence of incongruent solidification within a temperature range of 80 K may lead to hot tearing, which in turn causes the creation of cracks. Robert and his colleagues anticipated achieving a more harmonious solidification process by specifically melting just the aluminum and enclosing the unmelted silicon particles inside the aluminum matrix. This method mitigated fractures in the microstructure but did not completely eradicate cracking. Furthermore, a composition that lacks all the alloying components found in AA6061 is a fundamentally distinct precursor material in comparison to a pre-alloyed powder. In addition, the research did not provide any

information on the mechanical characteristics of the manufactured components that could be compared to the attributes of AA6061 in its original form.

Martin et al. studied AA6061 and AA7075 powders coated with zirconium hydride (ZrH2) nanoparticles. The purpose of this study was to showcase the manufacture of the functionalized material using SLM without encountering any cracking issues [20]. Their findings demonstrated that the components produced utilizing Zr nanoparticle-modified AA6061 and AA7075 powders were free from cracks and that they displayed consistent equiaxed grains with an estimated grain size of around 5 μm. The prevention of fracture development and the production of fine equiaxed morphologies were attributed to the presence of many nucleation sites introduced by the Zr nanoparticles. While the research did not provide information on the mechanical characteristics of functionalized AA6061, it did demonstrate that the mechanical properties of functionalized AA7075 fell within the acceptable range for identical wrought alloys in the T6 state. Notwithstanding these findings, the incorporation of external entities, such as Zr, into AA6061 and AA7075 alloys requires modified materials to undergo requalification and certification for aerospace and other vital applications. In addition, the functionalization of precursor powders with Zr nanoparticles necessitates an extra step using an electrostatic assembly approach, which may result in increased processing expenses. Based on the above analysis, it is evident that the prior approaches using SLM have not been successful at producing components made of pre-alloyed and unmodified AA6061 powder that are both crack free and almost completely dense while also possessing appropriate mechanical characteristics. Adding Ti to AA6061 alloys via SLM can improve the quality of laser welding. A study used ternary Ti3AlC2 powder to enhance the laser welding of 6061 Al alloys [27]. The addition of Ti3AlC2 powder increased the width and stability of the molten pool, which helped to inhibit the formation of defects such as pores, spatter, rugged surfaces, sagging, and undercutting. The reaction products of the Ti3AlC2 powders, including Ti3AlxC2, TiAl3, and TiC, impeded the growth of dendrites and could serve as nucleating agents, resulting in the formation of massive isometric crystals and dispersed precipitates. This refinement strengthening and dispersion strengthening could impede the extension of deformation and compensate for the influence of uneven melting loss of alloying elements, leading to an increase in and uniformity of the weld hardness from 53.1 HV 0.2 to 74.9 HV 0.2 [21]. However, it is important to note that the specific process parameters, blend ratio, and other factors can significantly influence the results. Therefore, careful optimization and control of these factors are crucial for successful application of this method.

In this work, a different ratio of Ti was added to the powder bed to process crack-free and nearly fully dense AA6061 parts via SLM. Additionally, instead of a red laser, a green laser was used to lower the energy density, decrease the loss of Mg and Si and further enhance the mechanical properties. The results showed that an increased percentage of Ti added to the powder bed decreased the pace at which the material solidified, resulting in a more uniform solidification process and preventing the occurrence of hot tearing. The micrographs clearly showed a lack of melt pools and melt tracks, which are often observed during SLM processing. The following passage provides a more comprehensive account of the experimental methods and findings that illustrate the successful production of crack-free AA6061 via the use of SLM with the addition of Ti.

3.2 **Materials and experimental methods**

3.2.1. Powder production and characterization

AA6061 powder, which was mixed with Ti micro-scale particles from Sichuan Huomosi Industrial Technology Co., Ltd., was used as the raw material for printing components utilizing the TruPrint 1000 additive manufacturing system. The particle size was measured by a laser diffraction powder sizer (Mastersizer 2000, Malvern Instruments Ltd., UK) and found to be 15-60 μm, 1-5 μm, and 1-10 μm for AA7075 and Ti, respectively. A novel green laser configuration was used in this study. The wavelengths of the green laser and fibre laser (normally used) are different, and the corresponding absorption rates are also different. The absorption rate of green light is better. An aluminum alloy can be printed with lower energy, which reduces the evaporation of Mg and Si in AA6061 (see Fig. 1). The optimized processing parameters were a laser energy of 300 W, a scanning speed of 800 mm/s, and an energy density of 78.1 J/mm^3.

To characterize and analyse the properties, the samples were ground using SiC papers up to a 1200 grit size. They were then polished using 200-proof anhydrous ethanol and a 0.05 μm alumina polishing slurry. Tensile testing was performed using an INSTRON 5967 electronic universal testing machine, with a nominal strain rate of 0.001 mm/mm per second. Following tensile testing, the fracture surfaces were analysed using scanning electron microscopy (SEM). A scanning electron microscope (SEM, German ZEISS Sigma 300) was used, the gold spray target was used, the electron gun was a Schottky field emission electron gun, and the resolution was 1.0 nm.

The SEM instrument was equipped with an energy dispersive spectrometer (EDS, Smartedx). Additionally, SEM-equipped electron backscatter diffraction (EBSD, Oxford Nordlys max3) was used. The gold coating was sprayed with Quorum SC7620 for 45 seconds before SEM observation. The Vickers hardness measurements were carried out by means of a microhardness tester (Leiz-Wetzlar, Germany) at different locations on the XY and XZ planes. The test was performed at a load of 100 g and an indentation time of 25 s, and the process was repeated 10 times to ensure accuracy.

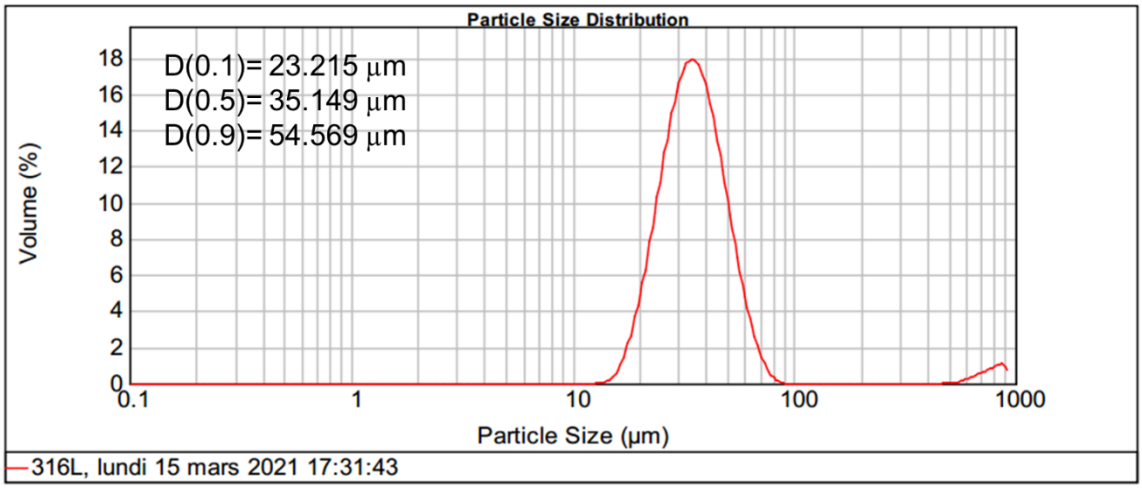

Fig 3.1 AA6061 particle size

The AA 6061 particle size distribution can be detected and is illustrated in Fig. 3.1. The average size of the power was 35.15 µm.

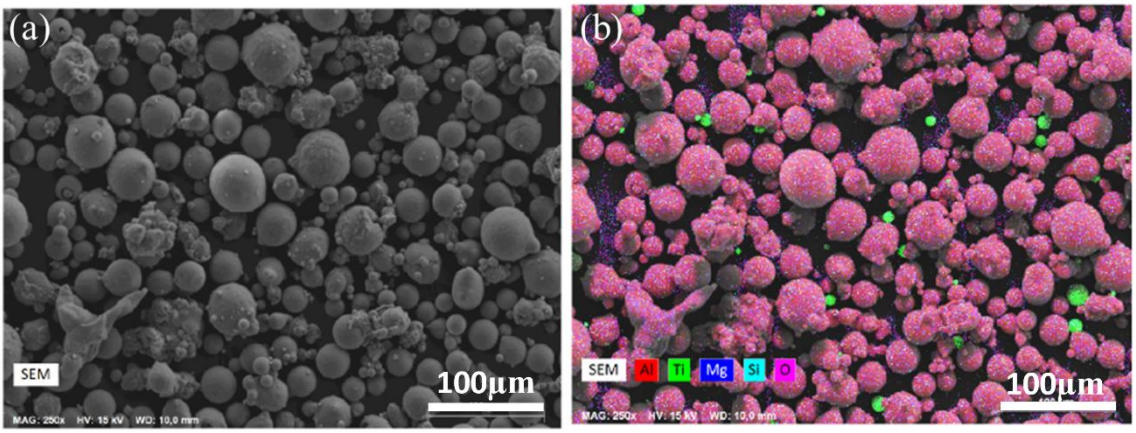

Fig 3.2 Powder morphology and element distribution

Fig. 3.2 shows the morphology and elemental distribution of the mixed AA 6061 +1% Ti powder. AA6061 and TiC powder were distributed in a uniform distribution after ball milling, and basically no Ti was present on the surface of the Al particles.

3.2.2 Green laser

Green lasers and Fiber lasers are both used in various applications, but they have different characteristics and are suited for different tasks [22]. Aluminum alloys absorb infrared laser (typically above 800 nanometres) to a limited extent because their absorption efficiency for visible light is relatively low. Aluminum alloys absorb green laser (532 nanometres) more effectively. They have higher absorption efficiency for green laser, which can efficiently convert into heat energy, thereby enhancing melting efficiency and processing speed.

It is important to note that the specific use case and material being used can significantly influence which type of laser is most suitable. Therefore, careful consideration of these factors is crucial when choosing between a green laser and a fiber laser.

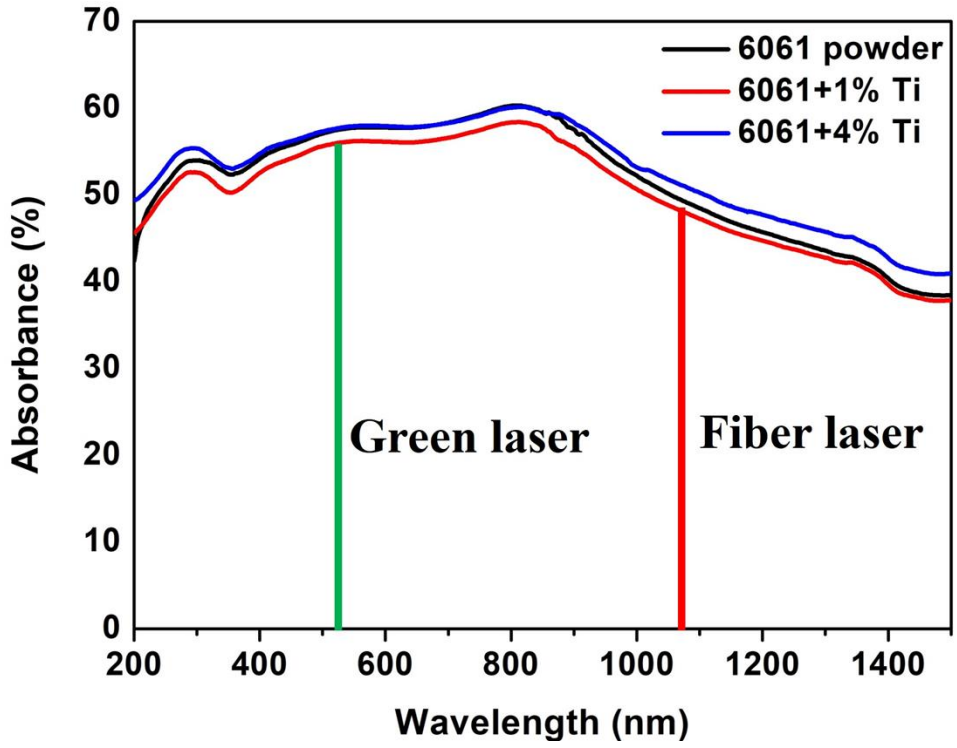

Fig 3.3 Green laser and Fiber laser comparison

As shown in Fig. 3.3, for the 6061 powder, 6061+1%Ti, and 6061+4%Ti powders, the absorbance was much greater for the green laser than for the fiber laser. These advantages can be exploited to manufacture additional solid SLM parts without increasing the energy density.

3.2.3 Experimental details

The SLM tests were conducted using self-designed equipment that was outfitted with a 1 kW green laser. Cuboid samples measuring 8 × 8 × 8 mm^3 were created to optimize the processing parameters and characterize the microstructure. The samples were produced utilizing varying laser powers (ranging from 200 to 300 W) and scan velocities (ranging from 400 to 1800 mm/s). The layer thickness was set at a constant value of 30 μm. The linear energy density (LED) is defined as follows:

$$Ed = \frac{P}{Vht}, (3.1)$$

where P represents the laser power, h represents the hatch spacing (0.12 mm), the laser spot diameter is 0.2 mm, v represents the scan speed, and t represents the slice thickness (0.04 mm). Here, as shown in Fig. 3.4(a), the scan rotation remains at 67° between two subsequent layers. For instance, the first layer is 0°, the second layer is 67°, and the third layer is 134° relative to the first layer. The scanning pattering rotation setting eliminates the thermal effects accumulated at each layer and impacts the part's properties. After the SLM manufacturing, cubes 8 × 8 × 8 mm^3 were cut into standard tensile strength test dimensions, as illustrated in Fig. 3.4(b).

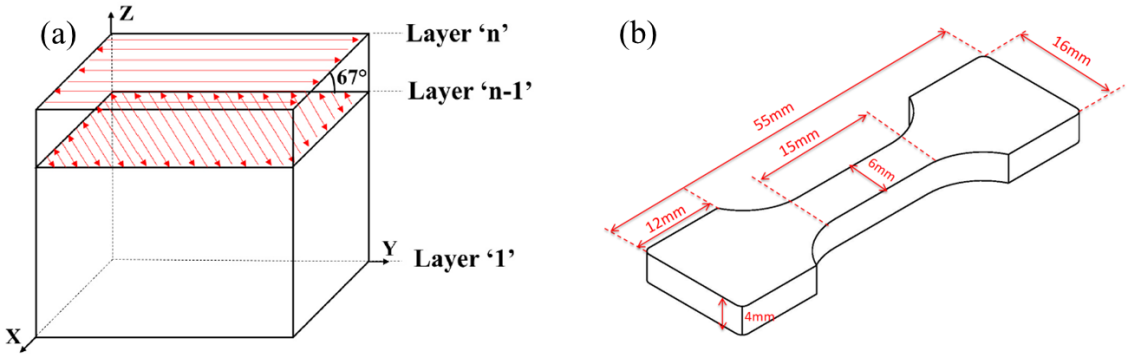

Fig 3.4 (a) Printing strategy and (b) sample size of the printed parts for tensile testing.

As mentioned, the laser power and scanning velocity were selected as the parameters for optimizing the SLM experiment. 18 experiments with varying parameters are listed in Table 3.1. The energy density can be calculated by Eq. 3.1.

Table 3.1 Experimental parameters

	P	V	Ed
	(W)	(mm/s)	(J/mm^3)

1	200	1200	34.7
2		1000	41.7
3		800	52.1
4		666	62.5
5		533	78.1
6		400	104.1
7	250	1500	34.7
8		1250	41.7
9		1000	52.1
10		833	62.5
11		666	78.1
12		500	104.1
13	300	1800	34.7
14		1500	41.7
15		1200	52.1
16		1000	62.5
17		800	78.1
18		600	104.1

3.3 Results and materials characterization

3.3.1 Microstructure observation

After the SLM experiments following the various parameters listed in Table 3.1, AA6061 and AA6061+Ti were characterized, and the as-built microstructure of AA6061is shown in Fig. 3.5.

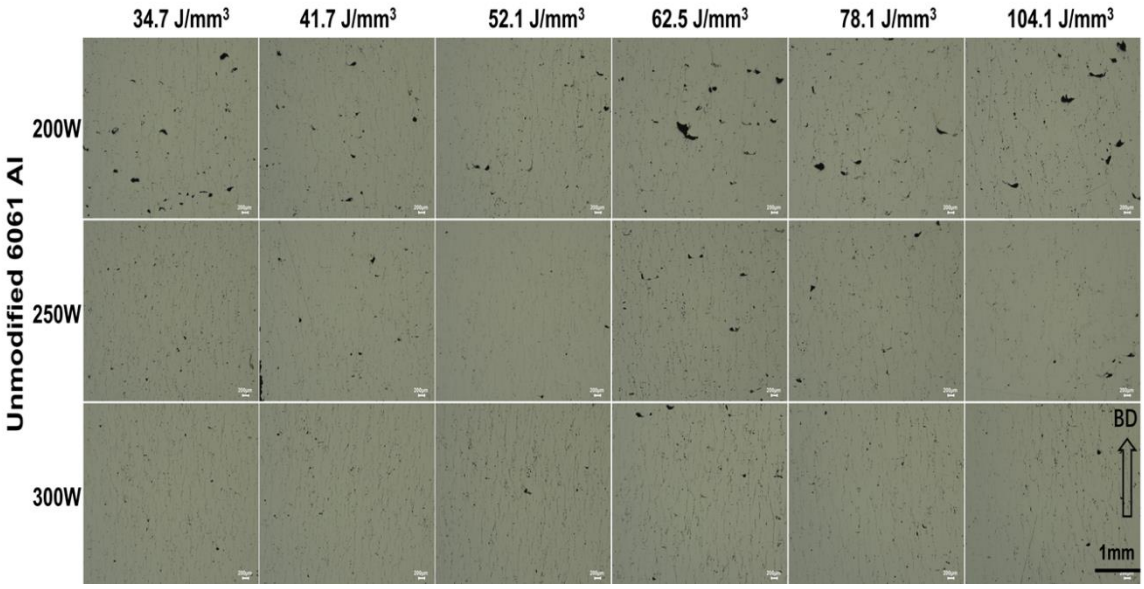

Fig 3.5 AA6061 microstructure observation

Fig. 3.6 shows the AA6061 sample, which contains not only pores but also a large number of cracks. Additionally, from the SEM photo, we can visually observe macroscopic structural changes, under 200 W, pores and cracks are distributed randomly. With increasing power from 200 to 300 W, the number of pores and cracks decreases. With increasing energy density from 34.7 to 104.1 (J/mm^3), the number of pores and cracks increase, these changes can be observed intuitively and directly.

Unaltered AA6061, which contains significant amounts of Si and Mg as primary alloying elements, is an Al-Si-Mg-based alloy. The current study revealed that the original AA6061 has inadequate printability and buildability. The AlSi10Mg alloy, commonly known as an Al-Si-Mg-based alloy, has exceptional LPBF printability/buildability [23]. AA6061 and AlSi10Mg have comparable magnesium (Mg) contents, ranging from 0.8-1.2 wt% and 0.2-0.45 wt%, respectively. However, they vary significantly in silicon (Si) content. AA6061 has only 0.4-0.8 wt% Si, whereas AlSi10Mg contains 9-11 wt% Si. The exceptional printability of AlSi10Mg is often ascribed to its high melt flowability, small shrinkage, and limited solidification range, which are characteristics commonly observed in alloys with a near-eutectic composition . Thus, Al-Si-based alloys with compositions close to eutectic are often compatible with power bed fusion-based additive manufacturing (AM) methods [24]. AA6061 has the highest sensitivity to solidification cracking compared to other commercially available aluminium alloys.

For overcome thermal crack problem, the addition of Ti powder in AA6061 powder was tried.

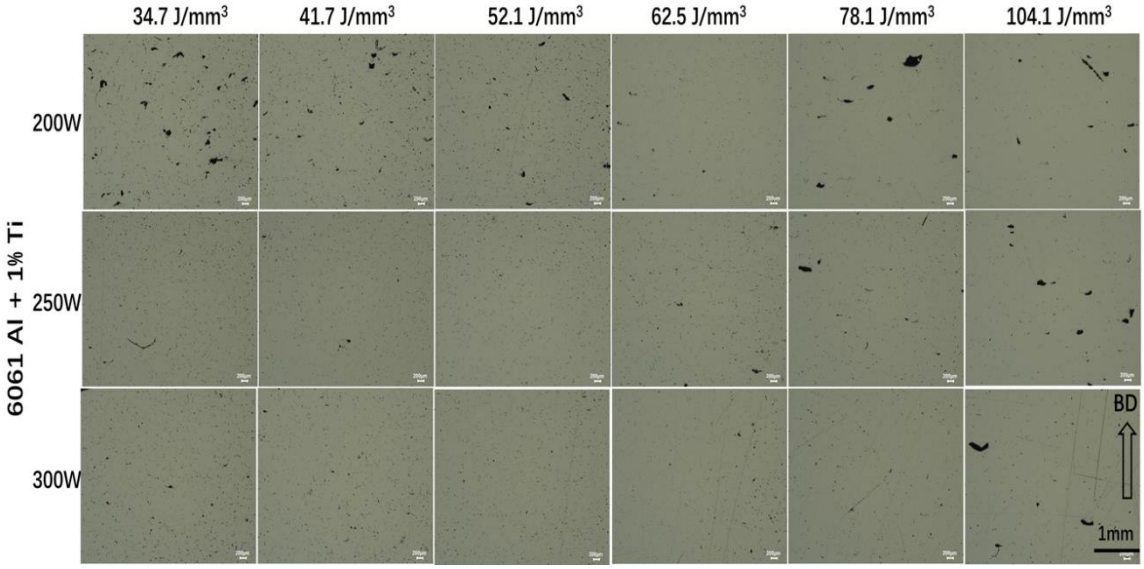

Fig 3.6 AA6061+1% Ti microstructure observation

The microstructure of the as-built AA6061+1%Ti alloy is shown in Fig. 3.6. The pores and cracks are significantly improved compared to those in the original AA6061 sample. Similarly, under 200 W of energy, pores and cracks are distributed randomly. With increasing power from 200 to 300 W, the number of pores and cracks decreases. With increasing energy density from 34.7 to 104.1 (J/mm^3), the number of pores and cracks increase, these changes can be observed intuitively and directly too.

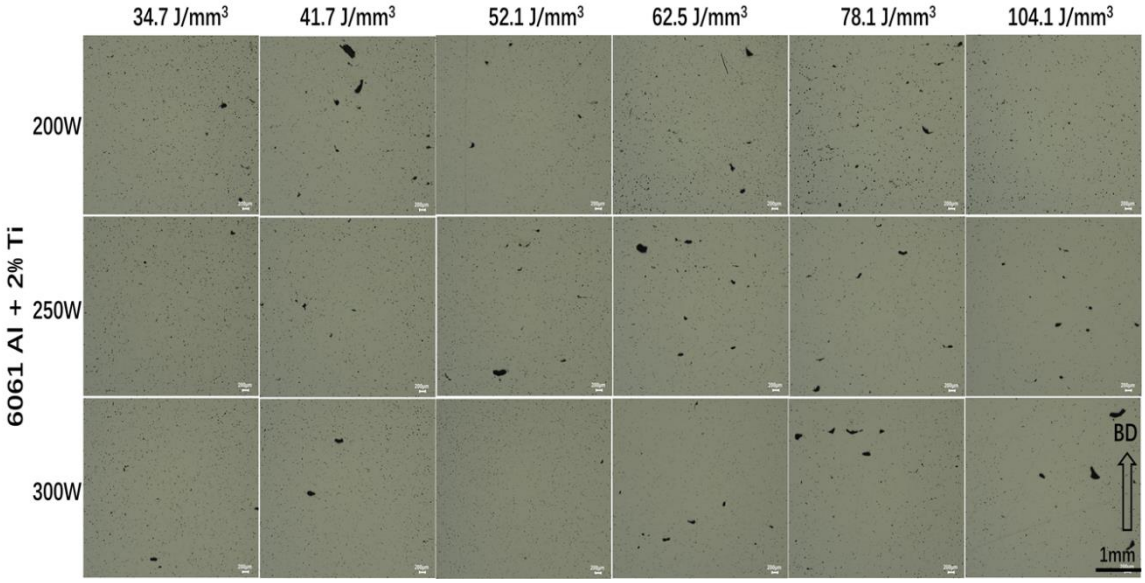

Fig 3.7 AA6061+2% Ti microstructure observation

The microstructure of the as-built AA6061+2%Ti alloy is shown in Fig. 3.7. The pores and cracks are significantly improved compared to those in the original AA6061

sample. Similarly, under 200 W, pores and cracks are distributed randomly. With increasing power from 200 to 300 W, the number of cracks decreases. With increasing energy density from 34.7 to 104.1 (J/mm^3), the number of cracks increases. No cracks can be found under the 2% Ti addition due to the strengthening effects.

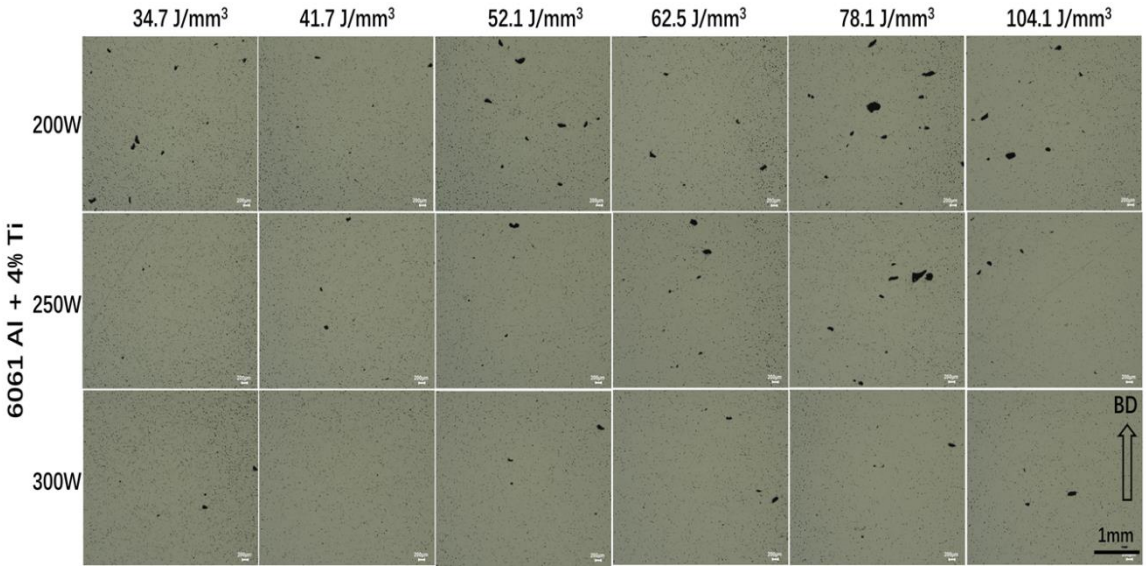

Fig 3.8 AA6061+4% Ti microstructure observation

The microstructure of the as-built AA6061+4%Ti alloy is shown in Fig. 3.8. The pores and cracks are significantly improved compared to those in the original AA6061 sample. Similarly, under 200 W, pores and cracks are distributed randomly. With increasing power from 200 to 300 W, the number of cracks decreases. With increasing energy density from 34.7 to 104.1 (J/mm^3), the number of cracks increases. No cracks can be found under the 4% Ti addition due to the strengthening effects.

3.3.2 Elemental distribution

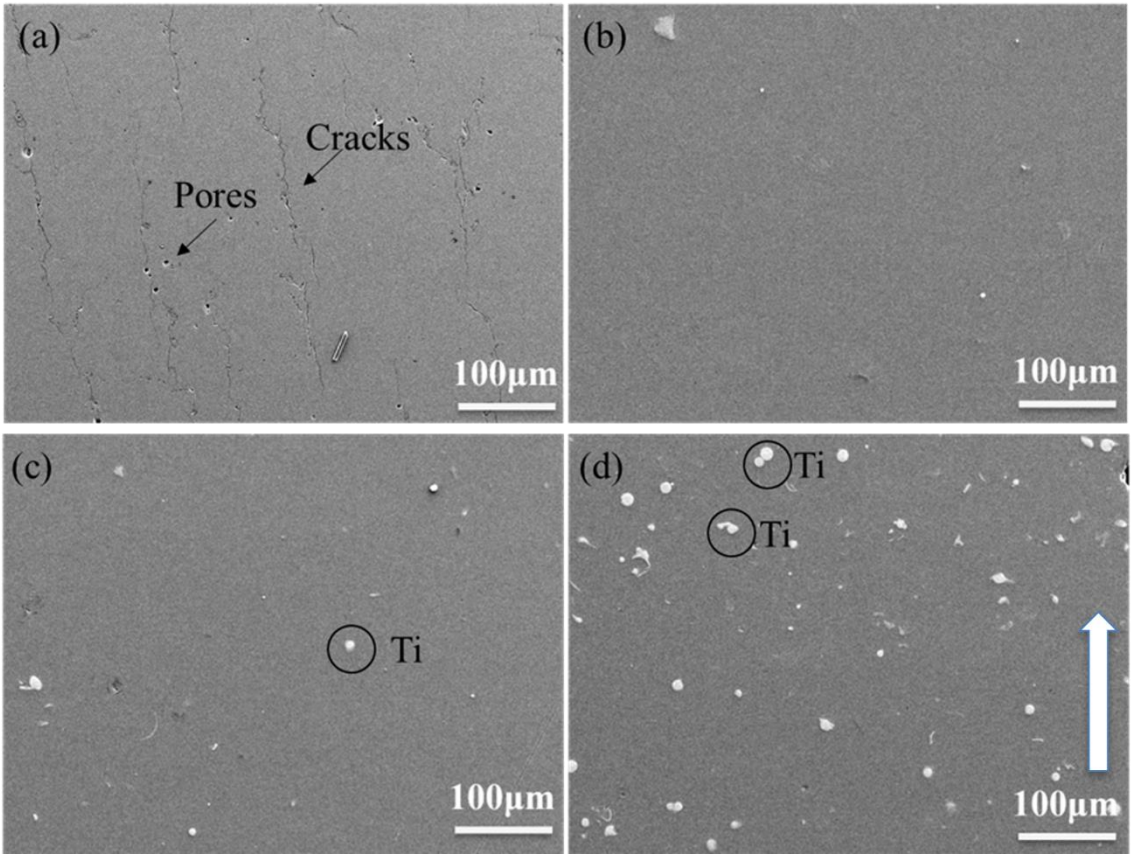

Fig 3.9 (a) AA6061, (b) AA6061+1%Ti, (c) AA6061+2%Ti, (d) AA6061+4%Ti.

Fig. 3.9 shows the Cross-section morphology of the manufactured AA6061 and mixed powder. As mentioned above, cracks and pores are generated during the manufacturing of AA 6061 powder due to stress release and solidification. The presence of spherical pores suggested that the pores may have been created by the entrapment of process gas, the release of gas from the metal powder, or the intrinsic porosity of the metal powder during the atomization process. The micrographs exhibit the existence of crescent-shaped melt pools and the formation of bands in the melt tracks. The presence of melt pools and melt tracks is a common characteristic observed in microstructures created with SLM in several material systems [25].

With increasing Ti concentration, cracks and pores can be eliminated. Free-crack and free-pore surface manufacturing can be seen accompanied by some unmelted Ti particles on the surface. The pores became trapped at the bottom of the deep melt pool and remained there after solidification. As the scanning speed increased, which resulted in a decreased energy density, the melting process gradually shifted from the keyhole

mode to the conduction mode, leading to a decrease in the number of pores. Nevertheless, the material experienced the formation of solidification fissures and exhibited a higher density as the scan speed increased. Solidification cracking occurs as a result of the rupture of the liquid film that forms during the last phase of solidification and is caused by thermal stress. The presence of extensive columnar grains in the AA6061 alloy renders it prone to solidification cracking. Cracks resulting from solidification were observed. Additionally, irregularly shaped pores were discovered when the scanning speed was high, indicating insufficient fusion caused by low energy densities. Melted Ti particles can better merge with AA6061 particles during melting and compensate for pores and cracks during the process. These unmilted particles can be detected in Fig. 3.10.

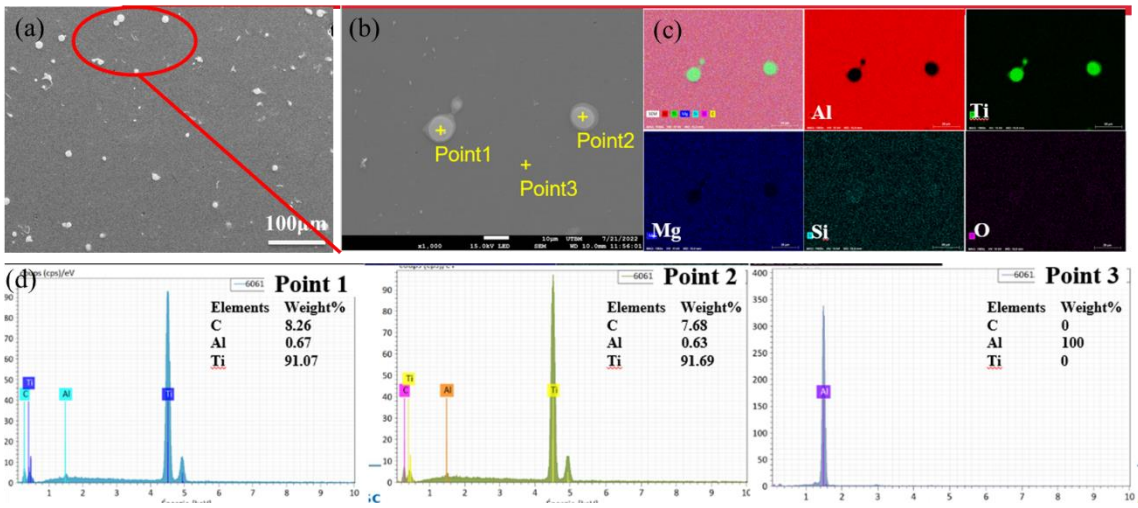

Fig 3.10 AA6061+4%Ti element distribution (a) SEM image, (b) enlarged image from (a) a high resolution, (c) EDS element distribution, and (d) element distribution weight ratio.

Fig. 3.10(a,b) shows the Ti particle distribution in a high-resolution image. AA6061 exhibited extensive cracking. However, adding Ti particles to AA6061 completely inhibited cracking. A significant amount of residual titanium particles was found in the samples in Fig. 3.10(c), as indicated by the EDX elemental distribution. Ti was mainly located at the Ti additions, and Ti was not melted within the AA6061 alloy. Fig. 3.10(d) shows Points 1 to 3, representing the positions of the Ti particles and the Al substrate, respectively. This indicates that the strengthening mechanism of Ti additions should be precipitation strengthening [26]. Precipitates can enhance the critical resolved shear stress (CRSS) needed for dislocations to move along crystallographic planes. The strengthening effect depends on the geometric characteristics of the precipitates and the interaction mechanisms between the dislocations and precipitates. Typically, small and well-aligned particles are susceptible

to being sheared by dislocations, while larger partially or poorly aligned precipitates are avoided by dislocations, resulting in the formation of dislocation loops around them and hindering dislocation movement [26].

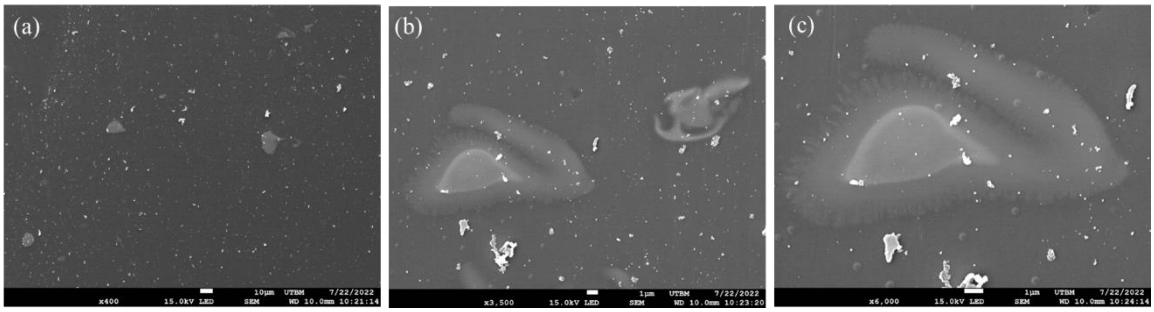

Fig 3.11 Cross-section morphology and elemental distribution of Ti particles: (a) surface morphology after AM, (b) two kinds of particle interfaces on the surface, and (c) merged interface of Ti and the AA6061 substrate.

From section 3.11 (a-b), it can be observed that Ti particles, apart from exhibiting a spherical shell structure, also possess other irregular morphologies. The Ti particles are composed of a pure Ti core surrounded by a TiAl compound shell. Some particles had distinct interfaces between the AA 6061 substrate and strengthened Ti particles, while some surfaces at the interface of the AA6061 and Ti particles had unclear and merged interfaces. The gradually changing color in Fig. 3.11(c) indicates that some melting or alloy formation may have occurred. For a better understanding of the interface reaction, element detection was employed at the particle inside and at the particle interface.

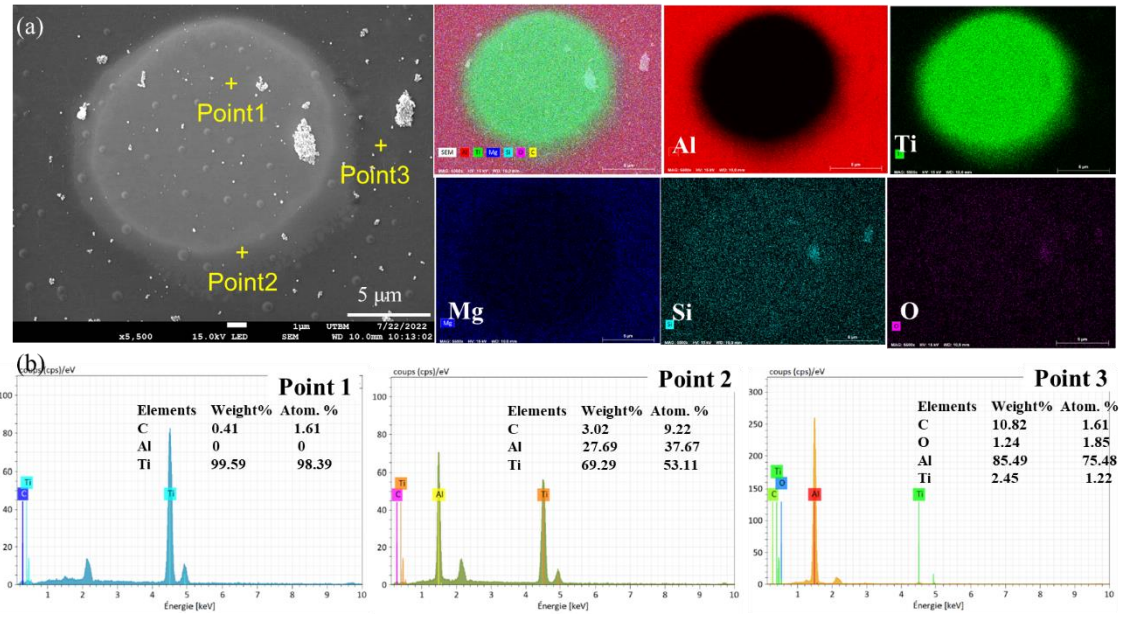

Fig 3.12 Cross-section morphology and elemental distribution of Ti particles

Fig. 3.12 shows the surface morphology and elemental distribution of the Ti particles after additive manufacturing. The circular shell structure is composed of a pure Ti inner core and a TiAl compound outer shell. Point 1 indicates the inside position of the Ti particle, and Points 2 and 3 show the interval positions of the AA6061+Ti and pure AA 6061 positions, respectively. Fig. 3.12(b) shows the elemental distribution at Points 1 to 3 for the different Ti particle positions. The formation of TiAl alloys strengthens the bonding strength of the particles by eliminating pores and cracks, which means that eutectic bonding and melting occurred at the interface between the Ti and AA6061. This performance also suggested that the AA6061+Ti mixed parts strengthened by alloying with AlTi formed.

3.3.3 Density

The investigation involved measuring the relative density of AA6061 cube coupons that were produced using various scan speeds and laser power settings as part of the process parameter development study. The density measurements of 72 specimens are presented in Table 3.2. Among these specimens, under each Ti concentration, 18 were produced using 200 W, 250 W, and 300 W, respectively. Overall, the samples produced with a higher Ti concentration (4%) exhibited a higher relative density than did the samples without Ti particles. The cube coupons produced under 250 W, 1000 mm/s, and 1% Ti addition had a maximum relative density of 99.11%. For some parameter sets, the densities of the cube specimens made with 2% and 4% stacking were similar. However, the samples created without induction heating had cracks, making this comparison meaningless.

The relationships for different additions of Ti under different powers can be seen in Fig.3.14.

The optimal parameters are 250 W and 1000 mm/s. Adding Ti can significantly inhibit the formation of thermal cracks and increase the relative density within a wide processing window.

Table 3.2 relative density of different samples.

	200							250						300
1000	800	666	533	400	1500	1250	1000	833	666	500	1800	1500	1200	100
97.6	98.1	97.0	97.5	96.6	97.7	97.9	98.5	97.2	97.6	97.9	97.8	97.8	97.3	97.
97.2	97.7	99.0	98.4	98.9	98.0	98.6	99.1	98.9	98.7	98.7	97.9	98.2	98.7	98.
97.0	97.6	97.1	97.0	98.1	97.5	97.8	97.6	97.6	98.3	98.7	97.6	97.6	98.2	98.
98.6	97.9	98.1	97.8	97.9	98.7	98.6	98.7	98.3	98.1	98.4	98.4	98.9	98.7	98.

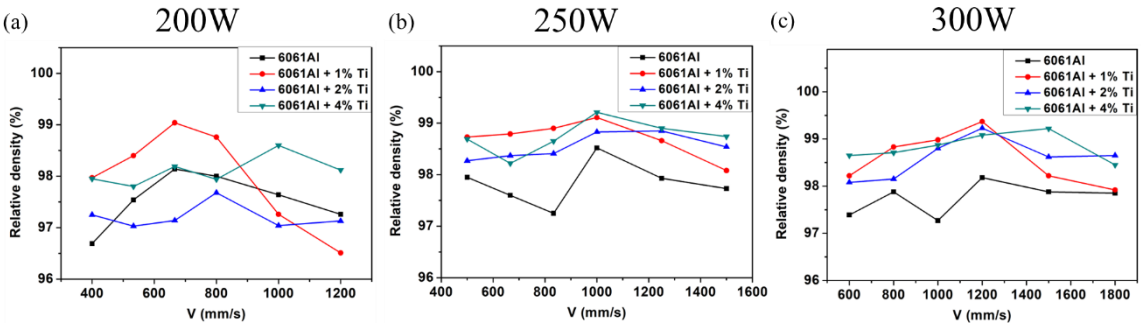

Fig 3.13 Relative density of the As-built samples (a) 200 W, (b) 250 W, and (c) 300 W.

As shown in Fig. 3.13, for the A6061 as-built sample, the relative density is relatively high at 1000 mm/s and 250 W and at 666 mm/s and 200 W. The samples annealed at 300 W have a relatively low density due to the higher energy from the laser and melting pool. For the AA6061+1%Ti addition condition, 250 W and 1000 mm/s have the optimized density, which means that low and high energy as well as velocity worsen the density. For the AA6061+2%Ti addition condition, 300 W and 1000 mm/s achieved the best density. For the AA6061+4%Ti addition condition, 300 W and 1500 mm/s achieved the best density. These high Ti addition conditions indicate that a higher laser energy is needed to achieve the highest density. With increasing Ti addition, the optimized velocity increases from 500 mm/s to 1500 mm/s, which also suggests the energy requirement for the processing window.

3.3.4 Element concentration

To better understand the variation in the properties and mechanism of Ti addition, the EDS results for 6061Al + 1%Ti are listed in Table 3.3. According to other published studies, the Mg content decreases during the printing process. Our results showed that the loss of Mg was greatly reduced. The green laser employed in this study greatly improved the element loss during the SLM process. Additionally, the addition of Ti may protect against Mg and Si loss, which suggests that Ti is effective at improving sample performance.

Table 3.3 Chemical compositions of the powder and the optimized as-built 6061Al + 1% Ti mixture

Laser type	Sample	Al	Mg	Si	Ti/Zr	Reference
Green laser	6061Al powder	97.31±0.2	1.00±0.1	0.77±0.1	0	This work
	6061Al+1%Ti	97.03±0.2	1.03±0.2	0.72±0.2	0.89±0.3	This work
	6061Al powder	95.45	0.82	1.06	1.14	Acta 2020-Grenoble [1]
	6061Al+2%YSZ	95.58	0.55	1.09	1.19	
Fiber laser	6061Al powder	-	1.14	0.78	-	AM2021-USA [2]
	6061Al+1%Zr powder	-	0.96	0.69	0.99	
	6061Al+1%Zr As-built	-	0.8	0.47	0.92	

1. Fig. 3.14 shows the elemental concentrations of Mg, Si, and Ti in the as-built samples. Without the addition of Ti, the concentration of Mg decreases with increasing scanning speed, from 1.0 to 0.65. With the addition of Ti, the concentration of Mg decreases slightly with increasing scanning speed, from 1.0 to 0.95. Additionally, the Si content decreases less with increasing scanning speed, from 0.7 at the beginning to 0.6 at the end. The concentration of Ti increases slightly with increasing scanning speed. Hence, the added Ti particles were not completely melted, and some remained. The addition of Ti may have

an inhibitory effect on the loss of Mg, which means that the addition of Ti can protect against Mg loss from the SLM process. The addition of Ti particles may help suppress the evaporation of Mg elements. During the SLM process, high temperatures can cause Mg to evaporate easily due to its relatively low melting and boiling points. However, the high melting point and high thermal conductivity of Ti can, to some extent, reduce the local temperature peaks, thereby decreasing the evaporation loss of Mg.

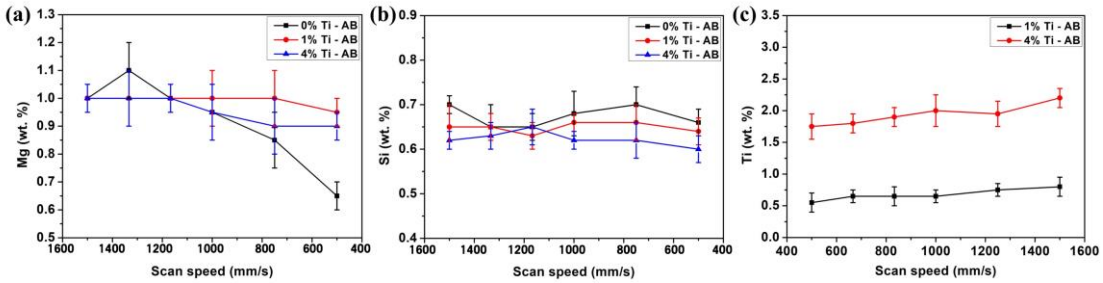

Fig 3.14 Element concentrations of the as-built samples: (a) Mg, (b) Si, and (c) Ti.

3.3.5 Microstructure evolution EBSD observation

Additive manufacturing is a quick solidification process that involves a high cooling rate, and after SLM, samples may have different microstructures due to differences in processing conditions and Ti additions. The microstructural evolution of the as-built AA6061 and Ti addition samples can be observed via EBSD, as shown in Fig. 3.15.

Table 3.4 Processing parameters for the EBSD results

Samples	Velocity (mm/s)	P (W)
AA6061 AA6061+1%Ti AA6061+2%Ti AA6061+4%Ti	1000	250

The specimens that were analysed underwent processing using the procedure parameters specified in Table 3.4. The colors denote distinct grain orientations. The

alignment of all the photos was determined based on their building direction (BD).

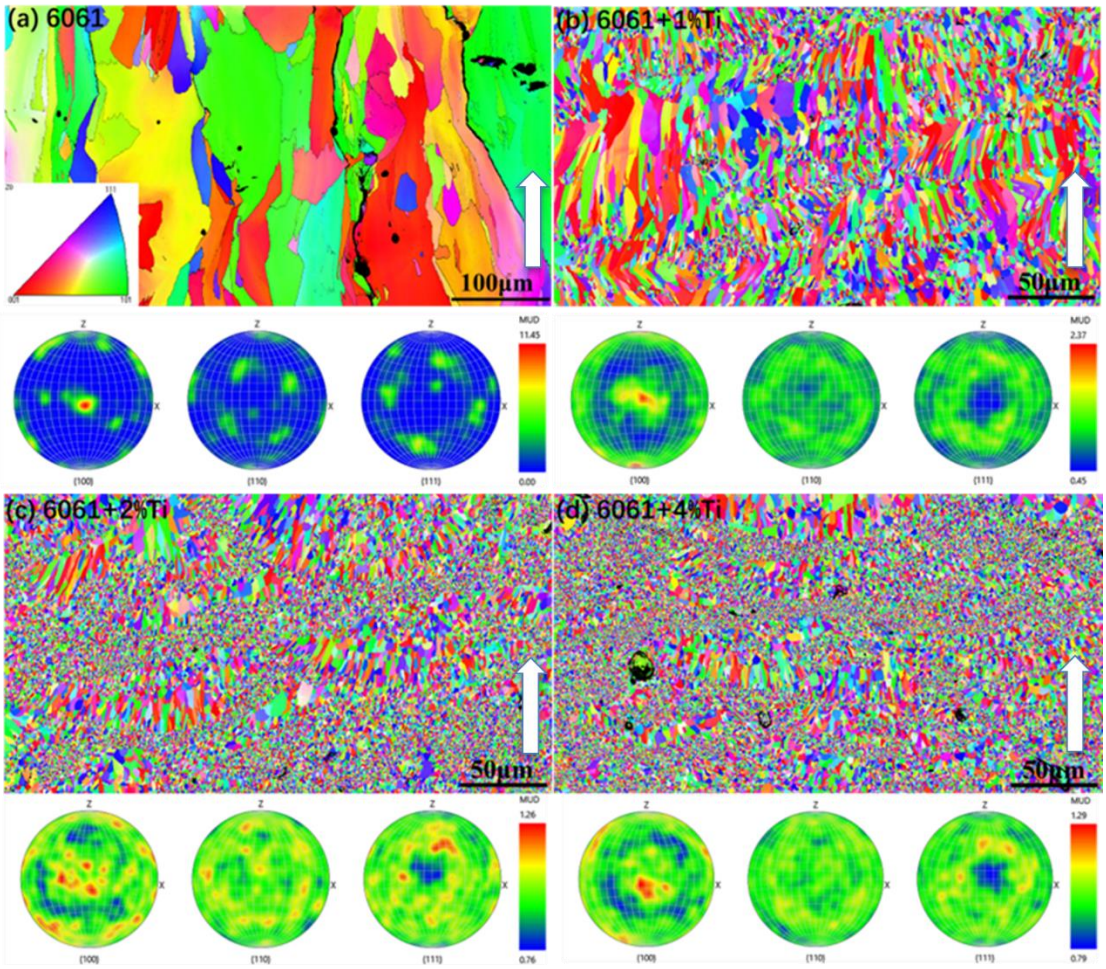

Fig 3.15 EBSD results of the (a) as-built AA6061 sample, (b) AA6061+1% Ti sample, (c) AA6061+2% Ti sample, and (d) AA6061+4% Ti sample.

Fig. 3.16 shows that the grain size and grain distribution increase with increasing Ti concentration. When the Ti addition increases from 0 to 4%, the grain size sharply decreases. The grains exhibit a parallel growth pattern in the direction of the construction. The grains in the base alloy have lengths ranging from 57 to 2 μm. No borders of the melt pool are observable, as indicated in Fig. 3.15. The grains exhibit multilayer growth. The EBSD data indicated that the base alloy possesses elongated grains, which may contribute to a heightened susceptibility to solidification cracking. The addition of Ti to the AA6061 alloy results in a significant improvement in grain refinement. The Al alloy undergoes grain refining by the process of heterogeneous nucleation on the Al_xTi_y nuclei, which serve as the major pro-peritectic phase during solidification. EBSD analysis allows for the calculation of the grain diameter and area fraction of these grains. The Al_xTi_y alloy exhibited a crystal structure that was

comparable to that of Al, resulting in a minimal lattice misfit. This characteristic contributes to a low energy barrier for Al nucleation. The high cooling rate inherent in SLM leads to the creation of Al_xTi_y particles with an alloy crystal structure, which is advantageous for heterogeneous nucleation and grain refining[27-28]. Fig. 3.15 illustrates that grain refinement is significantly more noticeable in the vicinity of the margins of the melt pool.

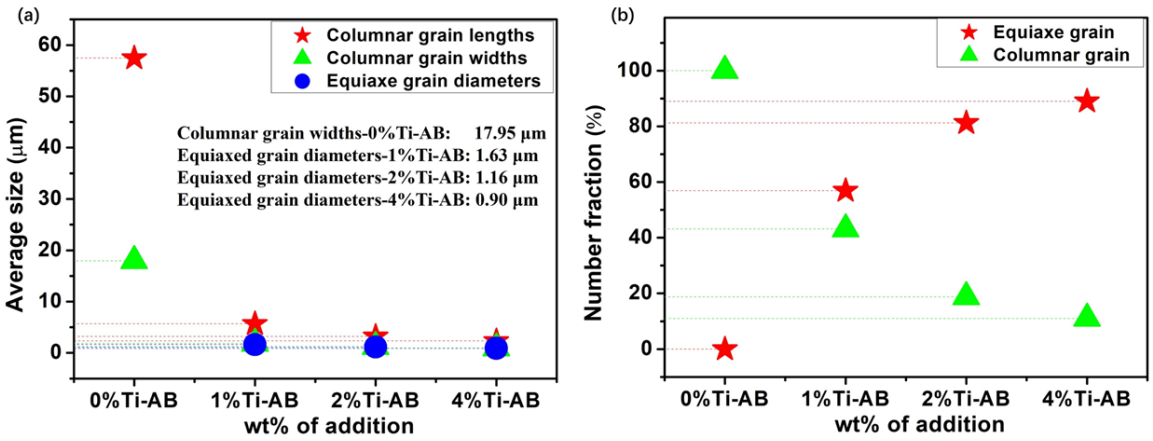

Fig 3.16 Average grain size of the as-built samples.

As mentioned above, under the same processing conditions, the average grain size sharply decreases with increasing Ti addition. The grain sizes of the columnar and equiaxed grains decrease with increasing Ti content. The proportion of equiaxed crystals increases with increasing Ti content from 0% to 90%. With decreasing diameter, the shape of the columnar grains gradually changes to that of equiaxed grains, which suggests that grain refinement strengthens the density of the samples. Additionally, the number fraction of columnar grains gradually decreases, supporting that the equiaxed grains increase, indicating that the finer equiaxed grains increase the strength. Adding Ti to the alloy increases the proportion of alloying elements that dissolve in the molten metal. This, in turn, limits the expansion of the grains and encourages the formation of smaller grains. Grain refinement greatly reduces the occurrence of solidification cracks. Additional research has shown that the use of grain refiners, such as the Ti used here, in base alloys can effectively decrease the occurrence of solidification fractures [29,30].

Additionally, with increasing Ti addition, the polar image shows an even grain orientation. For the AA6061 sample, the grain direction points to the {100]}due to the microstructure mainly illustrating columnar grains in the EBSD map. However, more equiaxed grains can be observed with increasing Ti addition, which verifies the even polarity of the map without certain grain directions. For the 6061Al samples, coarse

columnar grains and hot cracks and a fiber texture along the BD direction. For the 6061Al+1%Ti sample, the number of fine equiaxed grains and columnar grains and the texture intensity decreased to 2.37. For the 6061Al+2%Ti sample, there are finer equiaxed grains and columnar grains, and the maximum intensity of the texture is 1.26. For 6061Al+4%Ti, there are finer equiaxed grains and few columnar grains, and the maximum intensity of the texture is 1.29. The grain directions were tested separately and evenly for better refinement performance.

The grains observed in this study were columnar in shape and extended over at least two to three layers of melted material. This indicates that the grains grew epitaxially during consecutive melting cycles. The size of these elongated grains would not be sufficient to handle the stretching forces that occur during blocked shrinking. Furthermore, due to the restricted ability of the mushy zone to deform under stress, these tensile forces cause the mushy melt to separate or rupture during the last phases of solidification, leading to the formation of fractures. Moreover, tiny grains (1-2 μm) can be found at the grain boundaries, indicating that recrystallization occurred during the SLM process. This behavior occurs when the Ti particles are added and becomes more significant when the Ti addition is increased, which suggests the single-solvent recrystallization mechanism. Usually, the combination of "compound A" and "impurity B" is dissolved in a minimal quantity of heated solvent to completely dissolve the mixture, resulting in a saturated solution [31]. Subsequently, the solution was permitted to cool. As the temperature of the solution decreases, the solubility of the compounds in the solution decreases as well. As a consequence, the intended chemical precipitates (recrystallizes) out of the solution. As the rate of cooling decreases, the size of the crystals increases. Here, compound A represents AA6061 particles, and impurity B represents Ti particles.

The solubility product of the contaminant Ti additions should not be surpassed at any temperature in an ideal scenario. Under those circumstances, the solid crystals will be composed solely of pure AA6061 particles, while all the impurities will remain dissolved in the solution. The solid crystals are gathered by filtration, while the liquid that passes through the filter is discarded. When the solubility product of the impurity is surpassed, a portion of the impurities will precipitate together. However, because of the comparatively low amount of impurities, the concentration of impurities in the precipitated crystals will be lower than the concentration in the original solid. Iterative recrystallization will yield a more refined crystalline precipitate [32]. The purity was assessed following each recrystallization through the measurement of the melting point,

as impurities tend to decrease the melting point. NMR spectroscopy can also be employed to assess the degree of contamination. Repeated recrystallization leads to a decrease in the amount of material because compound A has some solubility. The process of crystallization necessitates an initial step, such as the introduction of a "seed" crystal. In the laboratory, a tiny piece of glass, created by scraping the side of the glass recrystallization vessel, can serve as the core for crystal growth. Effective recrystallization relies on identifying the appropriate solvent. Typically, this involves a blend of foresight/experience and experimentation. The solubilities of the compounds increase with increasing temperature and decrease with decreasing temperature. The method of hot filtration is employed to eliminate any insoluble impurities [33].

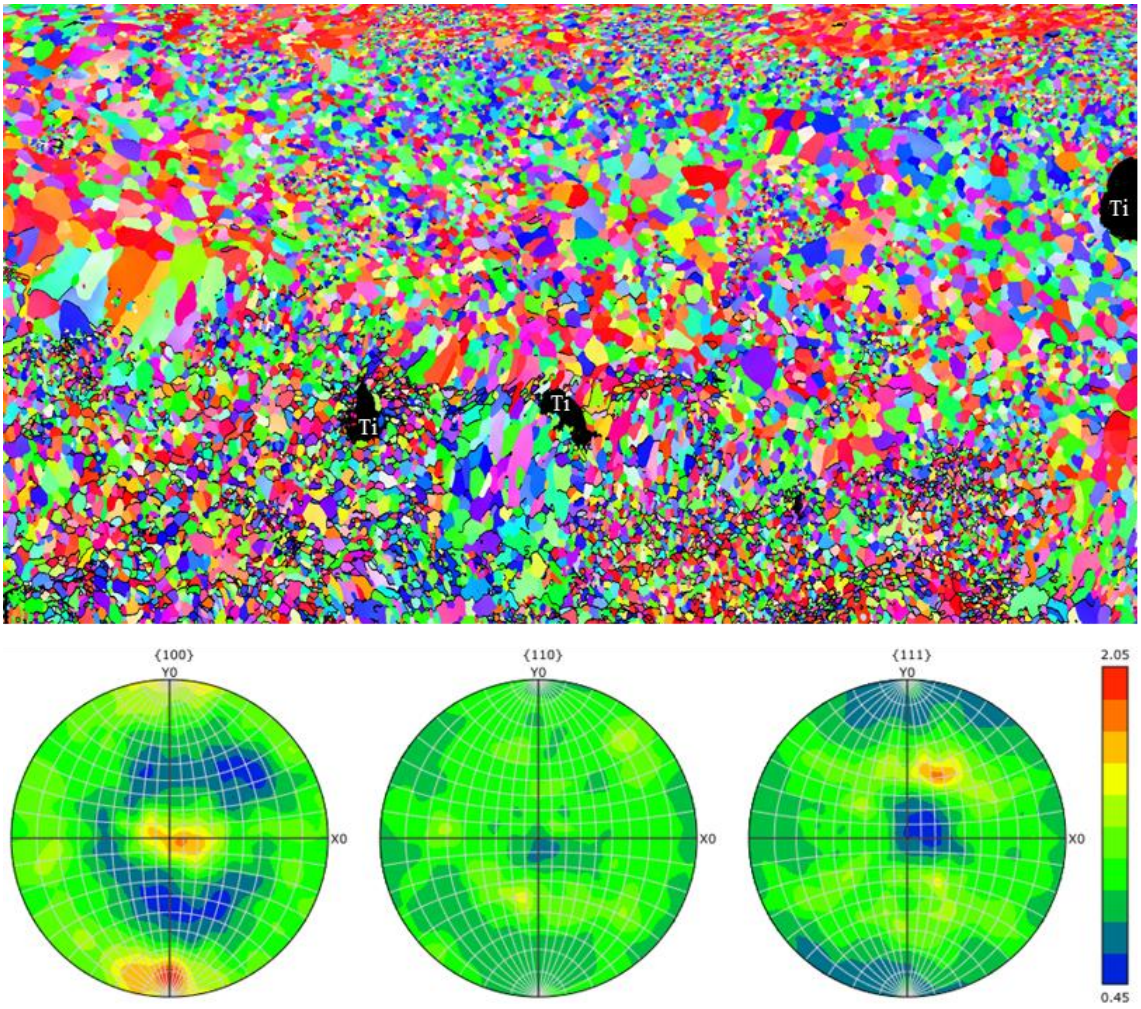

Fig 3.17 EBSD map of the as-built AA6061+1%Ti-XY sample

Fig. 3.17 shows the EBSD map of the as-built AA6061+1%Ti-XY sample. The EBSD image in the 6061Al+1%Ti-XY direction and the polar map. Fine equiaxed grains and columnar grains can be observed, and the maximum intensity of the texture

is 2.05. The strong intensity of the local texture in the {111} plane is attributed to the relatively large grains. Additionally, the black areas are the residual Ti particles. Very tiny grains can be found surrounding the Ti particles, which indicates the occurrence of the single-solvent recrystallization behavior mentioned above. The refined grains were not evenly separated in the mapping but were mainly distributed at the larger grain boundaries, which also explains the recrystallization. Typically, smaller equiaxed grains were found close to the edges of the melted area, while longer columnar grains were found inside the melted area. It is possible that the Al_xTi_y phases were created inside the melt pool and contributed to the improvement in the grain structure within the melt pools. However, in the interior of the melt pool, the number density and effectiveness of these nucleates may be reduced since most of the Ti would be trapped in the Al solid solution as a result of an accelerated solidification process. This study also showed that the solidification microstructure has a significant impact on the ability to build/print SLM Al alloys. The addition of Ti alloy resulted in grain refinement, which prevented the formation of lengthy liquid channels along the large columnar grain boundaries during solidification. As a result, the likelihood of cracks occurring was reduced.

3.3.6 Microstructure evolution and TEM observation

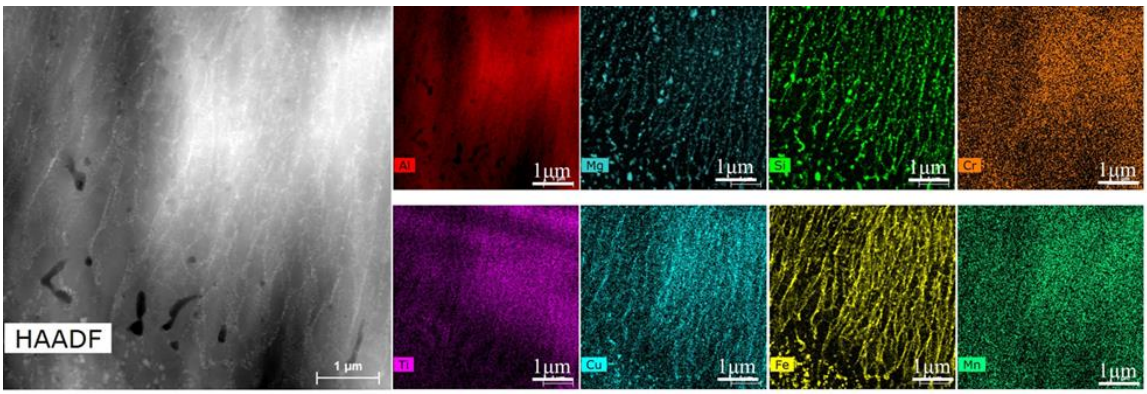

Fig 3.18 HAADF STEM image of the as-built columnar grains of the AA 6061+1%Ti sample

Fig. 3.18 shows the HAADF scanning TEM (STEM) micrograph of the as-built columnar grains. The TEM sample was obtained from an area characterized by the presence of tiny, equiaxed grains located at the perimeter of the melt pool. The distribution of significant elements, namely, Al, Mg, Si, Cr, Ti, Cu, Mn, and Fe, within the specified region. Irregularly shaped intermetallic particles, ranging from 50 to 120 nm in size, were predominantly detected near the grain boundaries. Based on XEDS mapping, it is probable that the phases discovered in AA6061 [34-35] are Al6 (Mn, Fe) or Mg_2Si, which are commonly observed. The presence of magnesium-rich oxide

particles was sporadically detected [36]. A high-angle annular dark-field scanning transmission electron microscopy (HAADF STEM) image was obtained from the inside of the equiaxed grains. Fe, Si, Mg, and Cu phase particles were detected within the Al grains via XEDS mapping. The particles exhibited a cuboidal morphology with an edge length just below 80 nm.

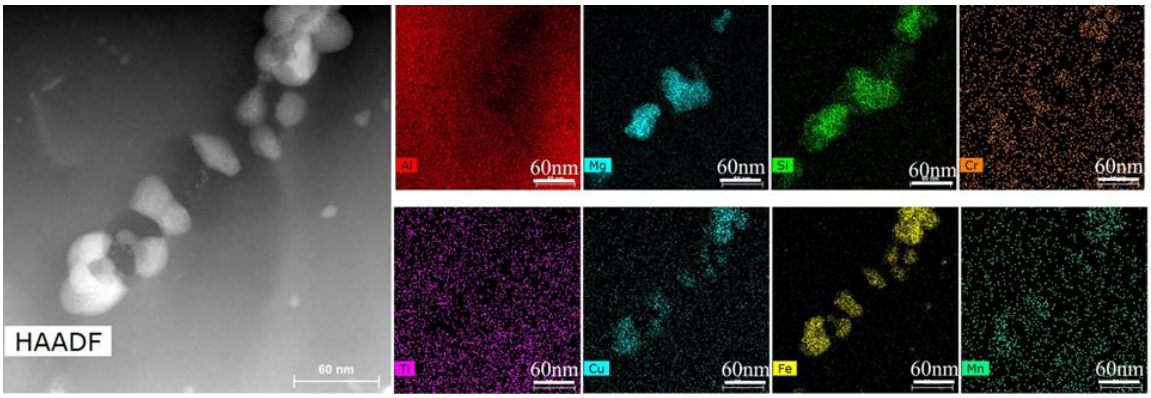

Fig 3.19 HAADF STEM map of as-built columnar grains of black and white particles of the AA 6061+1%Ti sample

Fig. 3.19 shows the HAADF STEM map of the as-built columnar grains of black and white particles from the AA 6061+1%Ti samples. There are precipitated phases at the grain boundaries (GBs) of the columnar crystals. The black particles may be Mg_2Si, and the white particles may be Cu_xFe_y compounds, which means that the unmelted Mg_2Si and Cu_xFe_y compounds were mainly distributed at the GBs. All the elements were mainly distributed inside the grains, which indicated that during the SLM process, impurity metallic elements (Mg, Cu, and Fe), impurity nonmetal elements, and Si generated compounds when the processing temperature exceeded the melting point. For the elements that did not melt, their trends accumulated at the GB to form metallic dissolved solid matter. For a better understanding of the formation of these elements, TEM is needed.

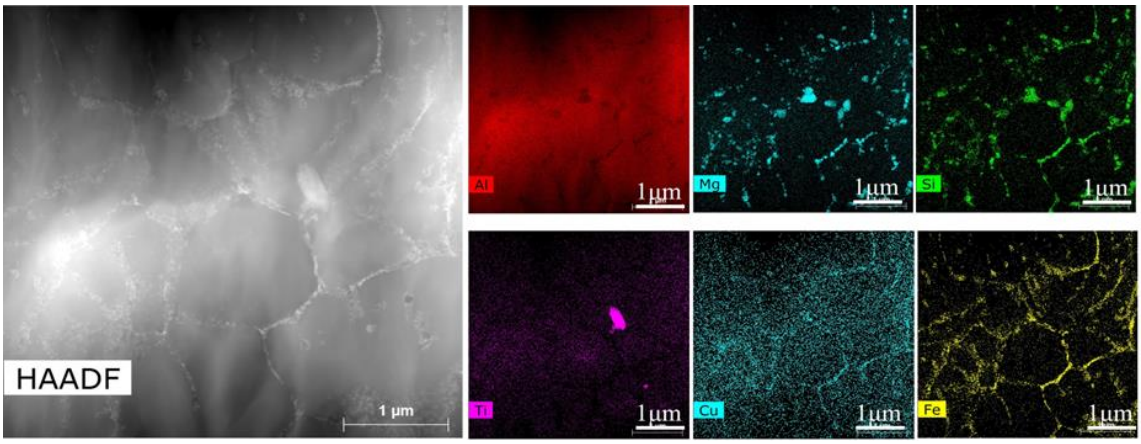

Fig 3.20 HAADF STEM map of as-built equiaxed grains of black and white particles of the AA 6061+1%Ti sample

Similarly, the HAADF STEM map of the as-built equiaxed grains of black and white particles in the AA 6061+1%Ti sample is shown in Fig. 3.20. Mg, Si, Cu, and Fe were mainly distributed at the GBs. Additionally, one Ti grain can be detected at the GB as an additional phase.

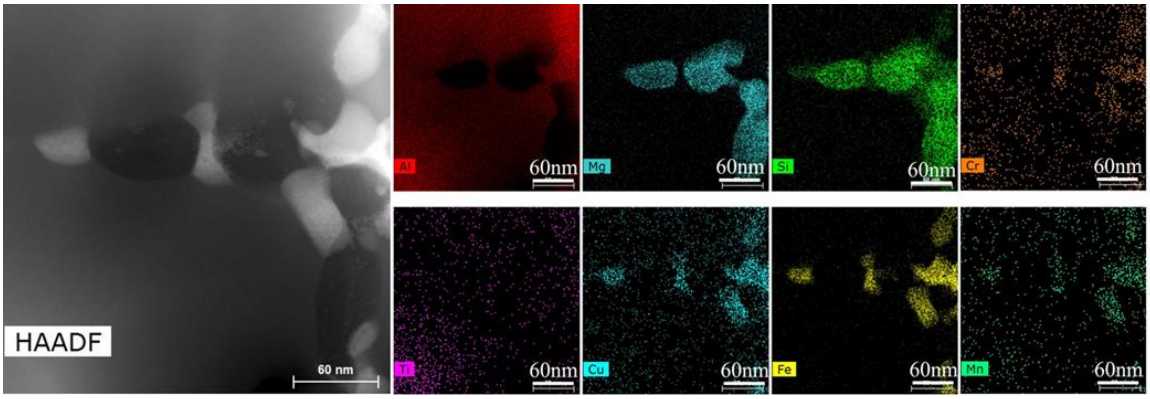

Fig 3.21 HAADF STEM map of as-built equiaxed grains of black and white particles of the AA 6061+1%Ti sample

Similarly, precipitates form at the grain boundaries of the equiaxed grains. The black particles may be Mg_2Si, and the white particles may be Cu_xFe_y compounds. These results are the same as those shown in Fig. 3.21 HAADF STEM map of as-built columnar grains of black and white particles from the AA 6061+1%Ti samples, which indicated that Mg2Si and Cu_xFe_y compounds always formed at the GBs, and their formation mechanism needs to be explored via TEM.

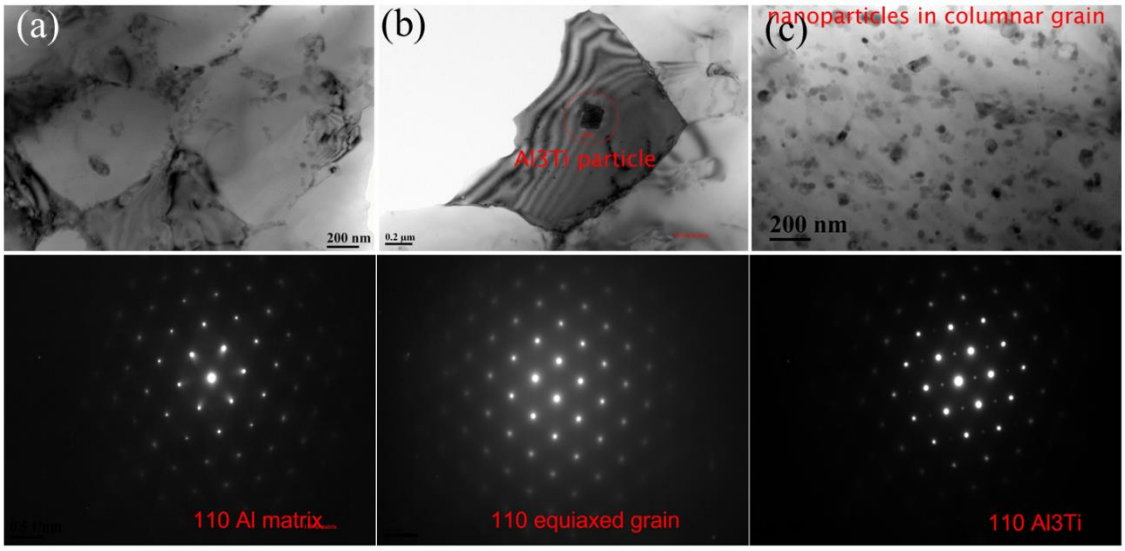

Fig 3.22 TEM images of as-built 6061Al + 1% Ti: (a) equiaxed crystals, (b) Al3Ti particles found inside equiaxed grains, and (c) Al3Ti particles found inside columnar grains.

To gain a deeper and more comprehensive understanding of the formation mechanism of Al-Ti compounds, Figure 3.22 presents the detailed TEM (Transmission Electron Microscopy) results for the 6061 aluminum alloy with the addition of 1% Ti particles. As illustrated in Figure 3.22(a), the sample exhibits equiaxed crystals, within which small black grains are clearly visible, either embedded within the grains themselves or positioned around the grain boundaries (GB). Upon closer examination, one of these black grains was specifically identified as an Al_3Ti particle, as highlighted in Figure 3.22(b). These nano-sized Al_3Ti particles are not only present within the equiaxed crystals but are also observed within the columnar grains, indicating their widespread formation throughout the microstructure. Further analysis of the crystal lattice reveals that the aluminum matrix, including both the equiaxed grains and the coherent Al_3Ti particles, predominantly exhibits a <110> crystal orientation. During the solidification process of untreated AA6061 alloy, the formation of columnar grains is observed, with these grains aligning their orientation along the thermal gradient, particularly in the <110> direction. In the final stages of solidification, solute segregation plays a significant role, leading to the grain boundaries being occupied by a liquid film and low-melting-point intermetallic compounds, further influencing the microstructural evolution.

3.3.7 Mechanical performance

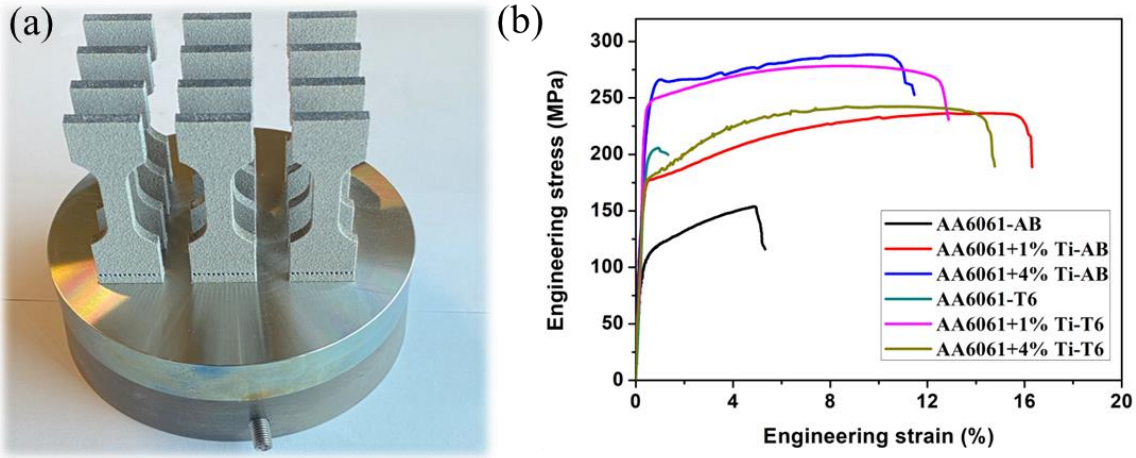

Fig 3.23 Mechanical performance of the (a) tensile test samples and (b) engineering stress–strain curve

Fig. 3.23 illustrates the mechanical performance of the AA6061 samples and various Ti addition samples. The tensile test parameters included crosshead velocity (1 mm/min) and T6 heat treatment: solution treatment at 530 ℃ for 5 h, water quenching, and aging at 175 ℃ for 9 h. The detailed data is shown in the table 3.5 below.

Table 3.5 The results of the tensile properties of as-built and heat-treated samples

Sample	Condition	Ys0.2(MPa)	UTS(MPa)	El(%)
6061	As-built	109.0±2.4	150.5±3.7	4.8±0.4
6061+1Ti	As-built	176.0±2.8	234.8±1.5	15.1±1.4
6061+4Ti	As-built	249.3±10.2	287.3±4.3	10.0±1.7
6061	T6	196.8±3.0	201.5±3.7	1.1±0.4
6061+1Ti	T6	238.3±3.9	273.3±3.8	12.6±1.2
6061+4Ti	T6	176.7±2.1	241.0±1.0	15.9±0.2

The as-built and heat-treated alloys exhibited initial elastic deformation and clear strain hardening until final failure. This investigation revealed that despite the general perception of the AA6061 alloy being weldable, it is prone to experiencing significant solidification cracking and/or the development of pores under different LPBF conditions. For the as-built alloys, the tensile results show that with the addition of Ti particles, the stress increases compared to that of the bare AA6061 sample. Additionally, with increasing Ti addition from 1% to 4%, the stress increases, which suggests that the

mechanical performance is improved by strength hardening. The tensile performance of the as-built 6061 Al alloy with a 4% Ti addition surpasses that of the as-cast 6061 AA. The yield strength of the heat-treated 6061 alloys with 1% Ti content met the standards of forged AA6061, and the elongation reached 12.6%. The Al alloys exhibited serrations corresponding to the Portevin–Le Chatelier (PLC) effect [37]. The PLC effect is caused by unstable dislocation motion during plastic flow because of the dislocation solute-drag mechanism. The PLC effect has been observed in the tensile behavior of conventionally produced 6061 alloys.

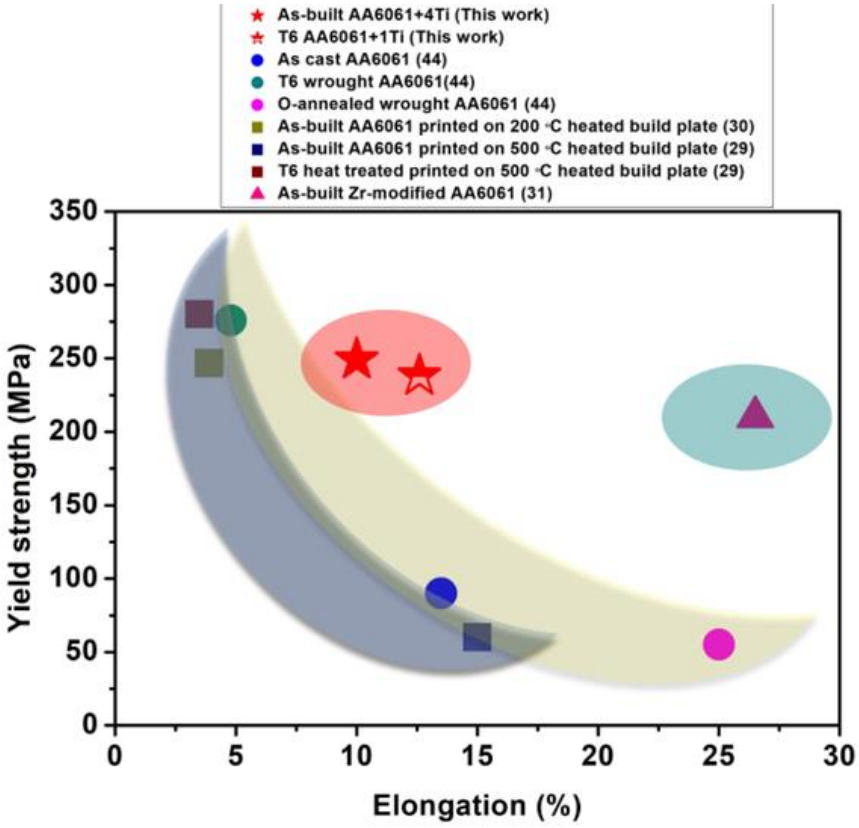

Fig 3.24 Comparison of the mechanical properties of AA6061[38-42].

Fig. 3.24 shows a comparison of the mechanical properties of AA6061. The as-built AA6061+4%Ti and As-built AA6061+1%Ti alloys in this work exhibited relatively high yield strength and relatively high elongation, indicating optimized strength and ductility.

3.3.8 Fracture test

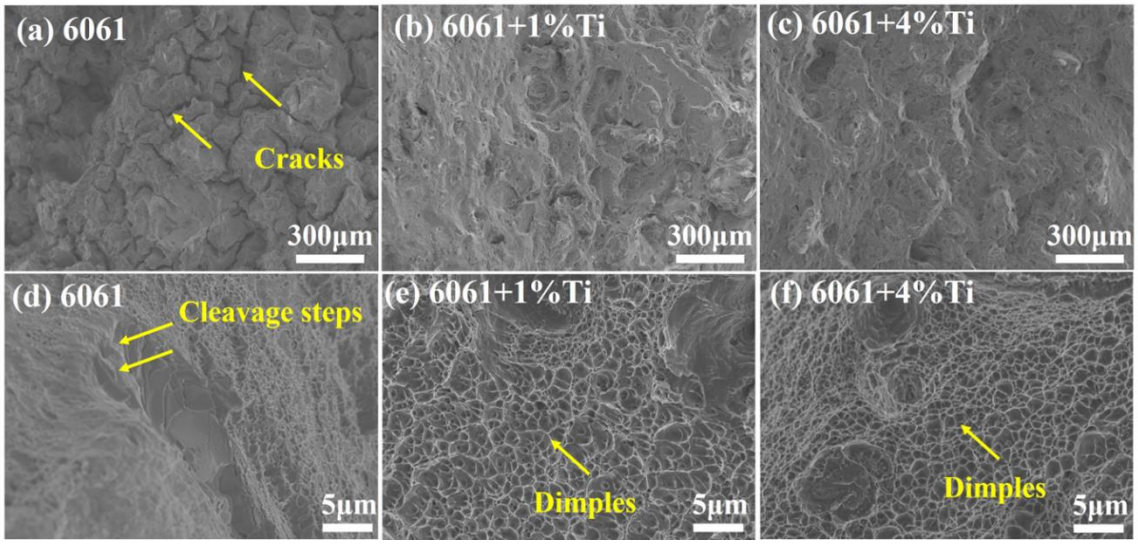

Fig 3.25 Fracture morphologies of As-built samples after fracture: (a) AA6061, (b) AA6061+1%Ti, (c) AA6061+4%Ti, (d) AA6061, (e) AA6061+1%Ti, (f) AA6061+4%Ti.

A fracture test was performed to test the fracture morphologies after fracture. As shown in Fig. 3.25, the as-built AA6061, AA6061+1%Ti, and AA6061+4%Ti samples can be observed. For the AA6061 samples, many cracks and cleavage steps can be observed at the fracture surface. However, for the AA6061+1%Ti and AA6061+4%Ti samples, there were no cracks or many finer dimples. After the addition of Ti particles, the cracks were eliminated. After adding 1% and 4% Ti particles to the 6061aluminum alloy, no cracks were observed on the tensile fracture surface. After adding titanium particles, the titanium can react with elements in the aluminum matrix to form Al_3Ti phases. These Al_3Ti particles act as heterogeneous nucleation sites, refining the grains during the solidification process. The refined grain structure effectively enhances the material's toughness, reducing the formation and propagation of cracks. During fracture, the Al_3Ti particles within the alloy serve as nucleation sites for micropores. As tensile stress is applied, stress concentration causes these micropores to gradually form around the particles. The growth and coalescence of these micropores eventually lead to the formation of a dimpled fracture surface. The addition of titanium and the formation of Al_3Ti particles allow the alloy to undergo more plastic deformation under stress. This enables the material to absorb more energy in localized areas, leading to the generation and expansion of micropores and, consequently, the formation of numerous dimples. This increase in plastic deformation significantly enhances the alloy's ductility and impact resistance. The broken surfaces of both the as-built and heat-treated alloys exhibited similar characteristics, specifically a ductile mode of fracture, after heat

treatment, the dimpled fracture surface becomes more pronounced. During the heat treatment process, precipitates in the alloy, such as Mg_2Si, re-precipitate and enhance the material's strength and toughness. This precipitation strengthening increases the material's plastic deformation capacity, leading to the formation of more dimples during tensile testing. Al_3Ti particles effectively impede the movement of dislocations and provide a pinning effect during the crack propagation process. This pinning effect becomes more pronounced during heat treatment, further promoting the formation of dimples. Finer grain structures help the material absorb more plastic deformation under stress, leading to the formation of more pronounced dimpled fracture surfaces, Therefore, the fracture surface with 4% titanium particles exhibits more and smaller dimples.

3.3.8 Heat treatment microstructure observation

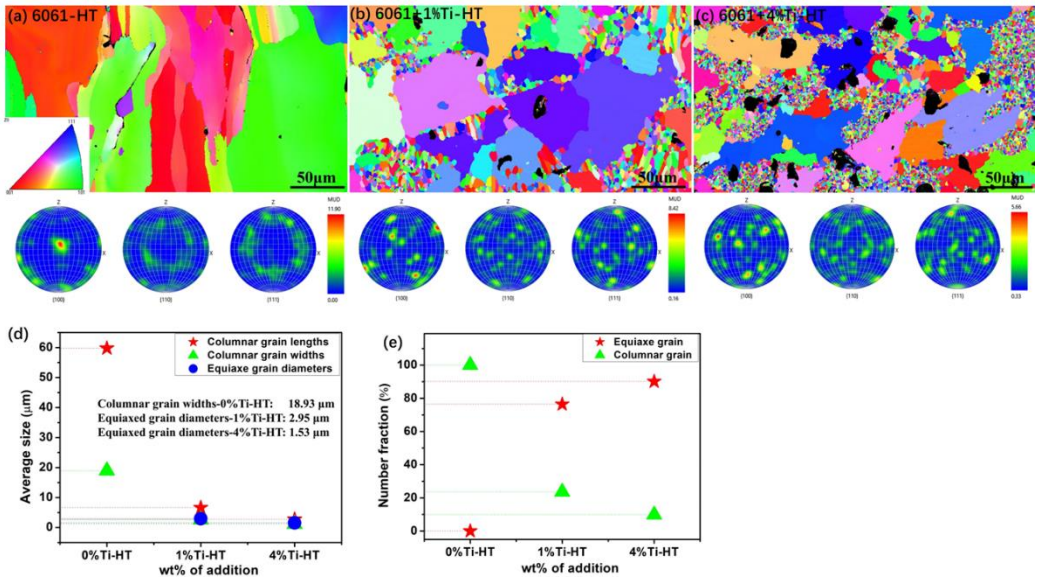

Fig 3.26 EBSD map of heat-treated As-built sample (a) HT-AA6061, (b) HT-AA6061+1%Ti, (c) HT-AA6061+4%Ti, (d) average grain size, and (d) equiaxed-columnar grain fraction.

Figure 3.26 shows the EBSD map of the heat-treated as-built sample. Heat treatment was employed to examine the microstructure performance. Fig. 3.26 (a-c) shows the EBSD results for the AA 6061 and Ti addition samples. For the AA 6061 sample, the columnar grain size was 18.93 μm, and the fiber texture was oriented in the <100> direction. For the 1% Ti-HT sample, the equiaxed grain diameter is 2.95 μm, and the maximum intensity of the texture is 8.42. For the 4% Ti-HT samples, the equiaxed grain diameter is 1.53 μm, and the maximum intensity of the texture is 5.66. With increasing Ti addition, the columnar grain length decreases, which indicates grain

refinement and proves the strengthening effects of To addition. On the other hand, equiaxed grains gradually dominate the microstructures. The replacement of columnar grains by equiaxed grains indicates grain refinement.

Titanium particles act as nucleation agents during the solidification process, promoting grain refinement. However, during heat treatment at high temperatures, the nucleation effect of these titanium particles diminishes, causing the originally refined grains to coarsen during recrystallization. In the high-temperature environment of heat treatment, titanium particles may further react with the aluminum matrix to form larger Al_3Ti particles. The growth of these particles can influence the nucleation and growth of grains, leading to the enlargement of the initially refined grains. Additionally, equiaxed grains may be replaced by columnar grains or other types of grains formed during recrystallization. As observed in Fig. 3.26(e), compared to the as-built sample, there is a noticeable change in the fraction of columnar and equiaxed grains, with an increase in columnar grains and a decrease in equiaxed grains.

During the heat treatment process of 6061 aluminum alloy, the precipitates in the alloy, such as Mg_2Si and Al_3Ti, reprecipitate and form within the matrix. These precipitates effectively impede the movement of dislocations, thereby increasing the material's strength and hardness. This precipitate strengthening enhances the tensile strength of the material. However, the presence of these precipitates can also negatively affect toughness. When the precipitates are large or unevenly distributed, they can serve as initiation points for cracks, thereby reducing the material's toughness. The aggregation of precipitates at grain boundaries or within the grains can also lead to localized stress concentrations, further impacting toughness[44].

T

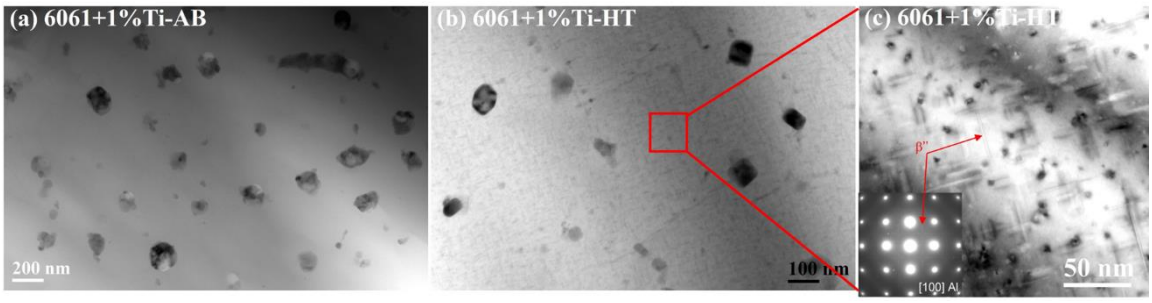

Fig 3.27 Comparison of the TEM results for as-built and heat-treated AA 6061+1% Ti

Fig. 3.27 shows the TEM comparison results of the as-built and heat-treated AA 6061+1%Ti. For the as-built (AB) samples, no needle-like nanosized β'' particles precipitated. Instead, for the HT samples, a large amount of needle-like nanosized β'' particles precipitated. A fast cooling rate during solidification leads to the formation of a supersaturated Ti matrix in the AA6061+Ti alloy. Consequently, the formation of Al_xTi_y occurred during the following heat treatment. The reinforcement provided by the Al_xTi_y precipitates may take place via a shearing mechanism, where the dislocations cut through the precipitates, or an Orowan bypassing mechanism, where the dislocations form loops around the precipitates [55–57]. Coherency and modulus mismatch strengthening occur when the dislocation is in proximity to the Al_xTi_y precipitate, but order strengthening occurs after the dislocation has sheared the ordered Al3Zr precipitate [45].

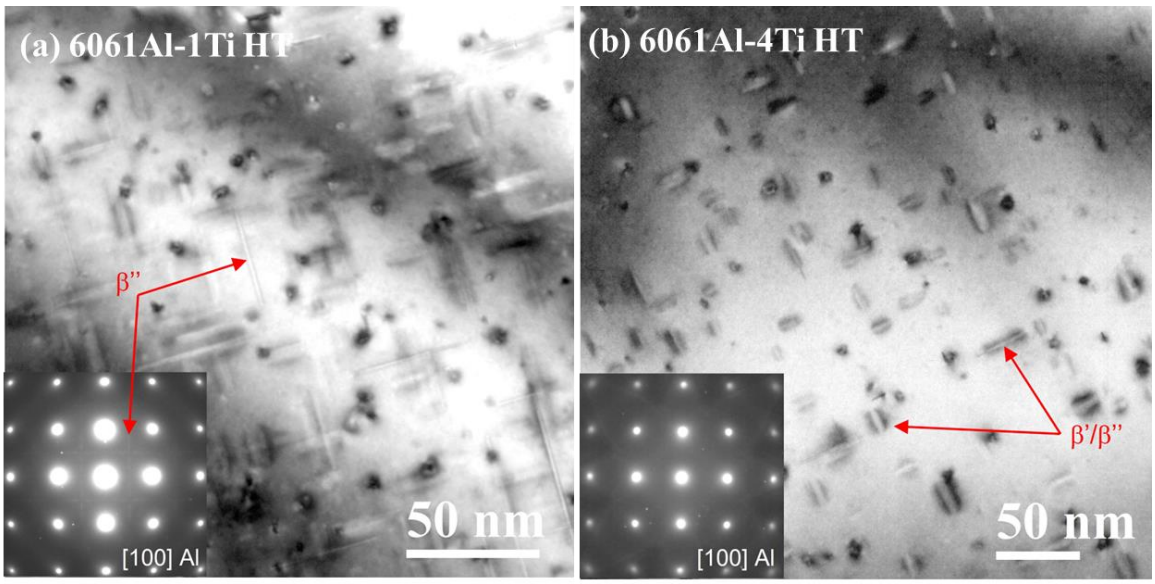

Fig 3.28 Comparison of the TEM results for heat-treated samples: (a) AA 6061+1%Ti and (b) AA 6061+4%Ti

Fig. 3.28 shows the TEM images of the HT AA 6061+1%Ti and AA 6061+4%Ti samples. The nucleation and growth of needle-like nanostructured precipitates were substantially suppressed, which partially accounts for the diminished tensile strength observed in the heat-treated 6061Al-4Ti alloy samples.

3.3.9 Heat treatment fracture test

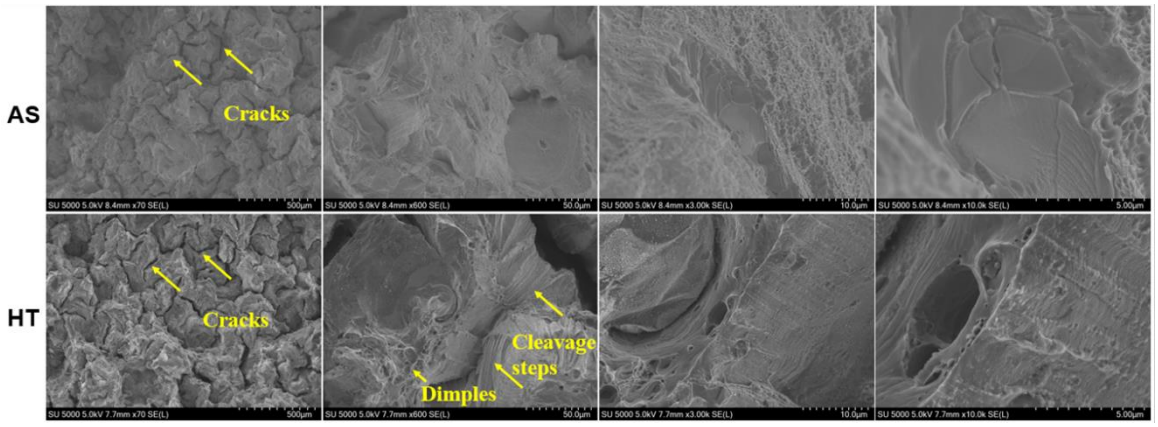

Fig 3.29 Fracture morphologies of the as-built and HT 6061Al alloys.

The fracture morphologies and EDS results of the as-built and HT 6061Al samples are shown in Fig. 3.29. There are numerous cracks present, and the fracture mode is cleavage fracture. Following heat treatment, Mg_2Si phase formation occurs.

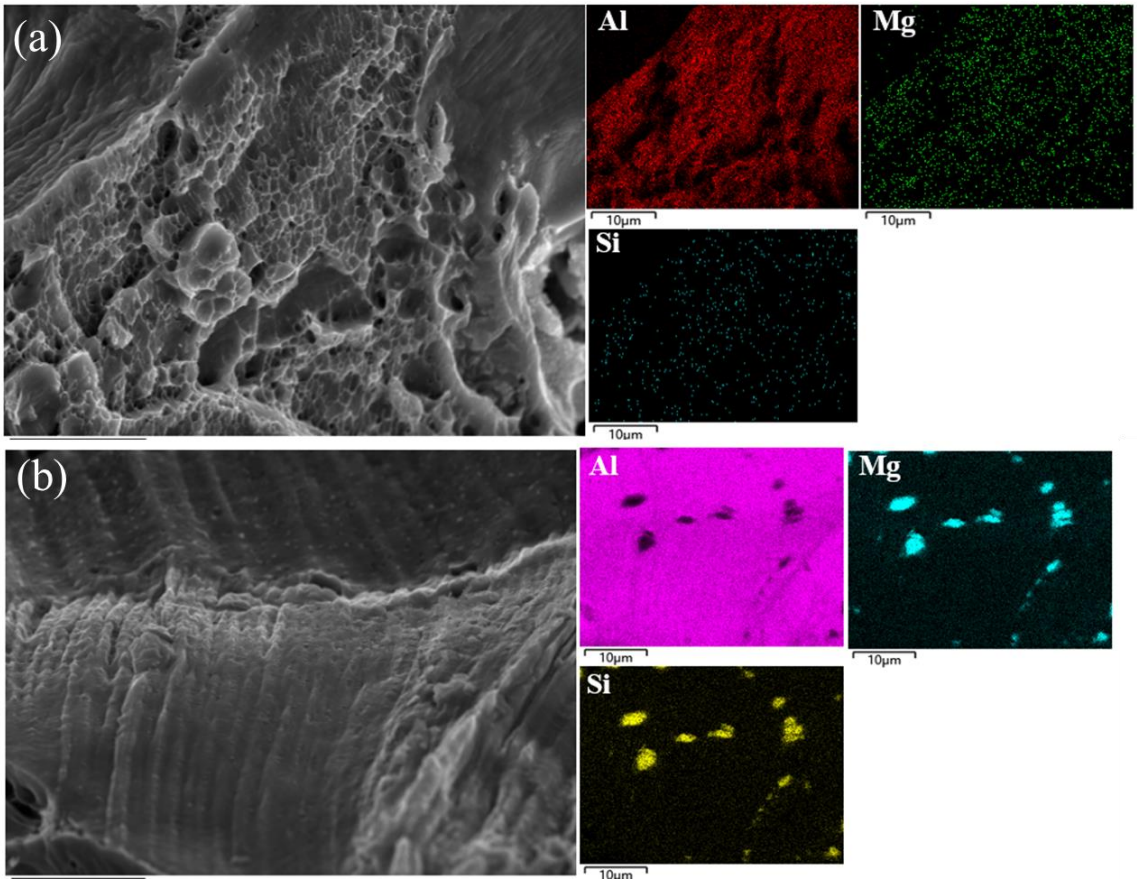

Fig 3.30 Fracture morphologies and EDS results of the as-built and HT-6061Al alloys.

Fig. 3.30 shows the fracture morphologies and EDS results of the as-built and HT-6061Al alloys. From the fractured surface, we detected the Al matrix along the fracture crack. Mg_2Si phase formation was not as obvious on the AB samples, while Mg_2Si phase formation was strongly indicated at the HT surface.

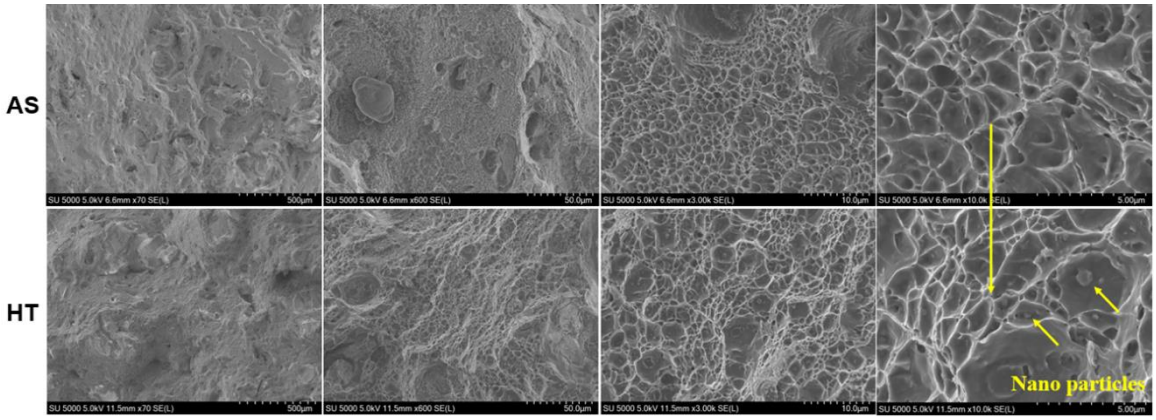

Fig 3.31 Fracture morphologies of the as-built and HT 6061Al+1%Ti alloys

Fig. 3.31 shows the fracture morphologies of the as-built and HT 6061Al+1%Ti alloys. No cracks were present, and the fracture mode was ductile dimple fracture.

Following heat treatment, Mg_2Si phase formation occurs at the bottom of the dimples. Compared with those of the as-built samples, the dimples significantly increase due to the Ti addition. Additionally, inside the dimples, nanoparticles can be found, and their elemental distribution can be observed in Fig. 3.32.

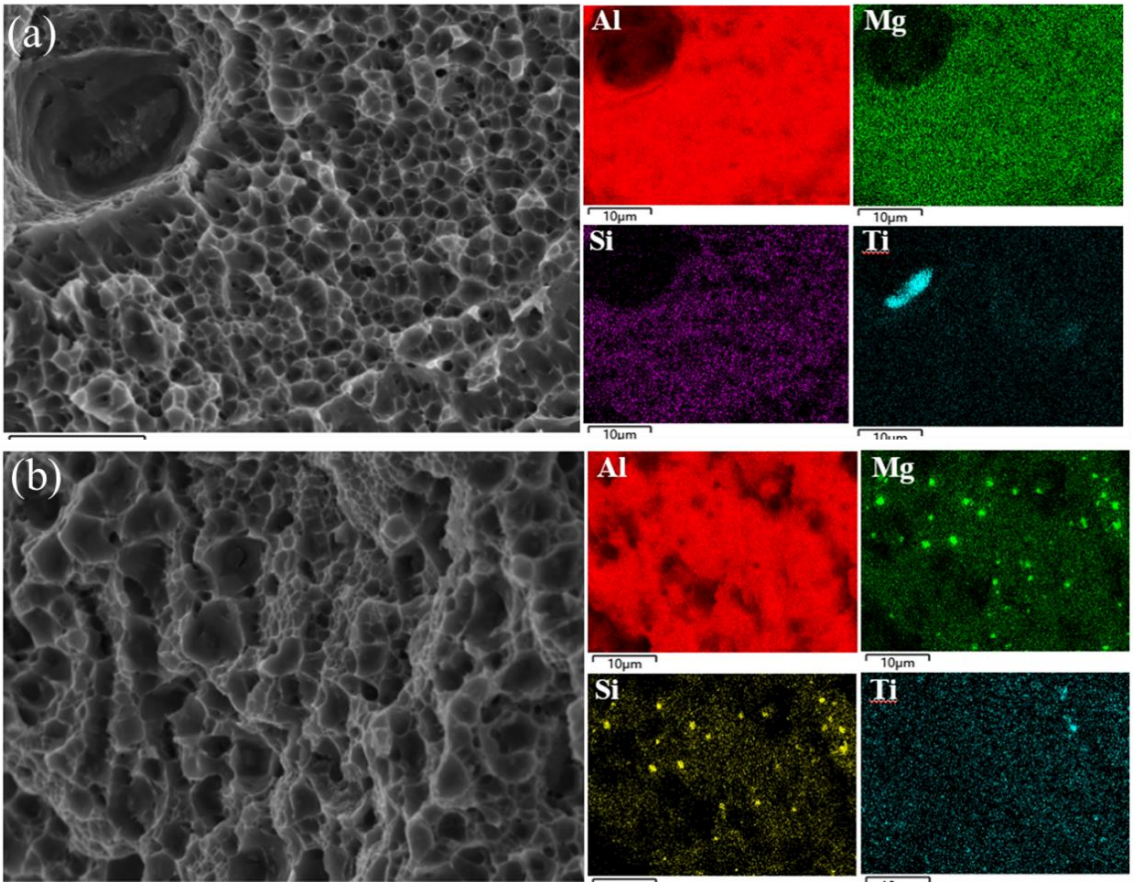

Fig 3.32 Fracture morphologies and EDS results of the as-built and HT 6061Al+1%Ti alloys

Fig. 3.32 shows the fracture morphologies and EDS results for the as-built and HT 6061Al+1%Ti alloys. Nanoparticles inside the dimples were detected here. Mg_2Si phase formation occurs at the bottom of the dimples, and for the HT samples, the nanoparticles can also be the Mg2Si phase.

Additionally, nano-Ti particles can be found inside the dimples, which indicates the strengthening mechanism of Ti particles in the formation of Ti_xAl_y. Based on this work and the findings of others, it has been shown that primary Ti_xAl_y particles are likely to develop along the border of the melt pool during the solidification process. The Ti_xAl_y particle acts as a heterogeneous nucleation site for the liquid melt, resulting in the formation of a band of tiny equiaxed grains along the edge of the melt pool. After this, the liquid melt formed nuclei on the tiny grains during the process of solidification.

As a result, small columnar grains form inside the melt pool. The reduced size of the grains in the SLMed AA6061+1%Ti alloys enhances their resistance to solidification cracking, resulting in a decreased occurrence or absence of cracks.

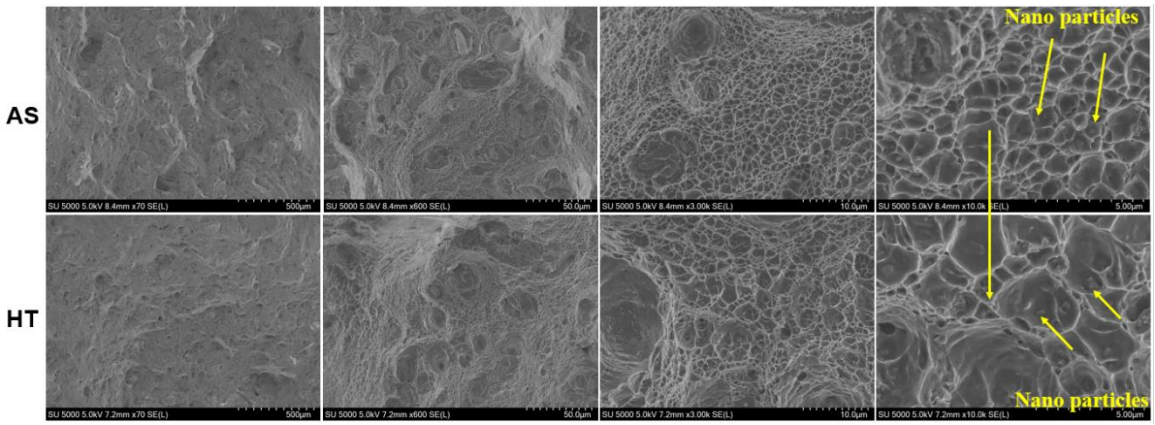

Fig 3.33 Fracture morphologies of the as-built and HT 6061Al+4%Ti alloys

Fig. 3.33 illustrates the fracture morphologies of the as-built and HT 6061Al+4%Ti alloys. No cracks were present, and the fracture mode was ductile dimple fracture. The addition of 4% Ti may inhibit the precipitation of Mg_2Si during heat treatment. The strengthening caused by precipitation is controlled by either the Orowan dislocation bypassing mechanism or the dislocation shearing mechanism [46]. The Orowan process leads to an increase in yield strength as the mobile dislocation is compelled to form a loop around the coherent precipitate that blocks its path.

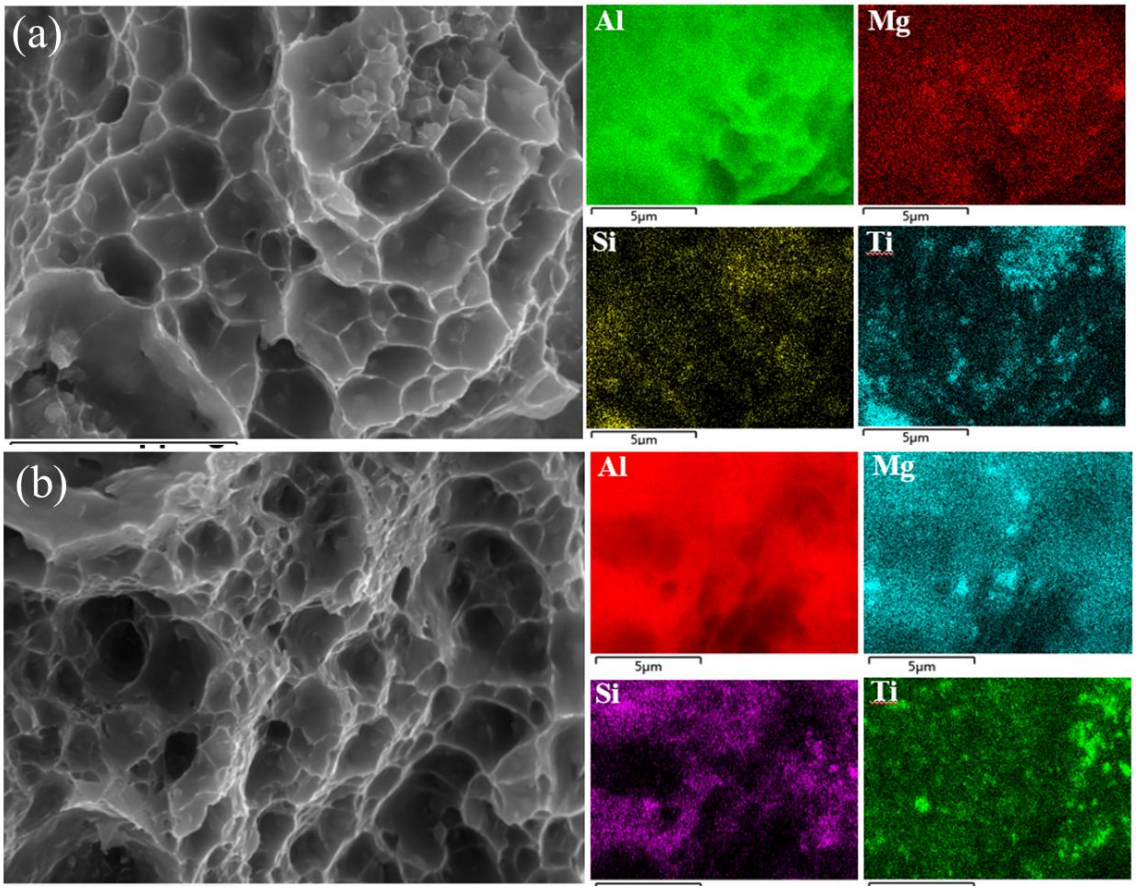

Fig 3.34 Fracture morphologies and EDS data of the as-built and HT 6061Al+4%Ti alloys

Fig. 3.34 shows the fracture morphologies and EDS results of the as-built and HT 6061Al+4%Ti alloys. With increasing Ti addition, Ti is distributed among the fractured structures. After HT, only a small amount of Mg2Si phases were observed, indicating that the addition of 4% Ti particles suppressed the formation of Mg2Si phases. This is consistent with the results in Figure 3.58, which shows a reduction in Mg2Si phases in heat-treated 6061+4%Ti samples. High concentrations of titanium particles may affect the precipitation of Mg2Si phases in 6061 alloys through various mechanisms, including competition for precipitation sites, chemical reactions, lattice distortion, changes in solubility, and alterations in phase transformation mechanisms. This, in turn, impacts the mechanical properties and structural stability of the alloy.

Conclusion

AA 6061 was manufactured by an SLM process with crack and pore defects. For better mechanical performance and crack-free, pore-free structures, Ti particles were added to feedstocks to explore the strengthening mechanism. Additionally, the HT was employed to evaluate additional methods for determining strength improvement. Some key conclusions obtained in this study can be summarized as follows:

1. The optimal parameters are a laser power of 250 W, a scanning speed of 1000 mm/s, and a corresponding energy density of 52.1 J/mm3, which are much lower than those of conventional printing equipment. Adding Ti can significantly inhibit the formation of thermal cracks and increase the relative density within a wide processing window. The remaining titanium particles combine with the aluminum matrix to form aluminum-titanium compounds.
2. When more Ti is added, the grain refinement becomes more obvious, and the anisotropy is greatly weakened. As the titanium content increases, the structure changes from columnar crystals to equiaxed crystals, with the average grain size decreasing from 57 μm to 2 μm. The content of fine equiaxed crystals also increases from 0% to 90%. Among these, the equiaxed crystals and fine columnar crystals are formed by Mg2Si and CuxFey compounds.In the equiaxed crystals of the 6061+Ti sample, the presence of Al3Ti is noted
3. After heat treatment of the Ti particle-added sample, a substantial amount of the reinforcing phase, Mg2Si, can be observed.The addition of 4% Ti may inhibit the precipitation of Mg2Si during heat treatment.
4. Adding Ti can significantly improve the tensile properties, and the yield strength after heat treatment reaches the standard of forged AA6061.

References

[1] S.D. Nath, H. Irrinki, G. Gupta, M. Kearns, O. Gulsoy, S. Atre, Microstructure-property relationships of 420 stainless steel fabricated by laser-powder bed fusion, Powder Technol. 343 (2019) 738–746. 2018.11.075.

[2] D. Herzog, V. Seyda, E. Wycisk, C. Emmelmann, Additive manufacturing of metals, Acta Mater. 117 (2016) 371–392. 2016.07.019.

[3] L. Xi, D. Gu, K. Lin, S. Guo, Y. Liu, Y. Li, M. Guo, Effect of ceramic particle size on densification behavior, microstructure formation, and performance of TiB-reinforced Al-based composites prepared by selective laser melting, J. Mater. Res. 35 (2020) 559–570.

[4] J.R. Davis, Corrosion of Aluminum and Aluminum Alloys, ASM INTERNATIONAL, Ohio, 1991.

[5] Y. Ding, J.A. Muñiz-Lerma, M. Trask, S. Chou, A. Walker, M. Brochu, Microstructure and mechanical property considerations in additive manufacturing of aluminum alloys, MRS Bull. 41 (2016) 745–751.

[6] D. Brackett, I. Ashcroft, R. Hague, Topology optimization for additive manufacturing, Solid Free. Fabr. Symp. Austin, TX, 2011, pp. 348–362.

[7] C.E. Roberts, D. Bourell, T. Watt, J. Cohen, A novel processing approach for

additive manufacturing of commercial aluminum alloys, Phys. Procedia 83 (2016) 909–917.

[8] B.A. Fulcher, D.K. Leigh, T.J. Watt, Comparison of AlSi10Mg and Al 6061 processed through DMLS, Proc. 25th Solid Free. Fabr. Symp. (2014), pp. 404–419.

[9] C.E. Cross, On the origin of weld solidifcation cracking, Hot Crack. Phenom. Welds, Springer-Verlag, Berlin/Heidelberg, 2005, pp. 3–18.

[10] L. Katgerman, D.G. Eskin, In search of the prediction of hot cracking in aluminium alloys, Hot Crack. Phenom. Welds II, Springer Berlin Heidelberg, Berlin, Heidelberg, 2008, pp. 11–26, http://dx.doi.org/10.1007/978-3-540-78628-3_1.

[11] E. Cicală, G. Duffet, H. Andrzejewski, D. Grevey, S. Ignat, Hot cracking in Al–Mg–Si alloy laser welding – operating parameters and their effects, Mater. Sci. Eng. A 395 (2005) 1–9, http://dx.doi.org/10.1016/J.MSEA.2004.11.026.

[12] T. Böllighaus, H. Herold, C. Cross, J.C. Lippold, Hot Cracking Phenomena in Wels II, (2008), http://dx.doi.org/10.1017/CBO9781107415324.004.

[13] W.S. Pellini, Strain theory of hot tearing, Foundry 80 (1952).

[14] S. Kou, A simple index for predicting the susceptibility to solidifcation cracking, Weld. J. 94 (2015) 374s–388s.

[15] J.P. Bergmann, M. Bielenin, T. Feustel, Aluminum welding by combining a diode laser with a pulsed Nd:YAG laser, Weld. World 59 (2015) 307–315, org/10.1007/s40194-014-0218-8.

[16] A. El-Batahgy, M. Kutsuna, Laser beam welding of AA5052, AA5083, and AA6061 aluminum alloys, Adv. Mater. Sci. Eng. (2009) (2009) 1–9, 1155/2009/974182.

[17] E. Louvis, P. Fox, C.J. Sutcliffe, Selective laser melting of aluminium components, J. Mater. Process. Technol. 211 (2011) 275–284, jmatprotec.2010.09.019.

[18] L. Loh, C. Chua, W. Yeong, J. Song, et al., Numerical Investigation and an Effective Modelling on the Selective Laser Melting (SLM) Process With Aluminium Alloy 6061, Elsevier, 2015.

[19] L.E. Loh, Z.H. Liu, D.Q. Zhang, M. Mapar, S.L. Sing, C.K. Chua, W.Y. Yeong, Selective laser melting of aluminium alloy using a uniform beam profle, Virtual Phys. Prototyp. 9 (2014) 11–16, 869608.

[20] J.H. Martin, B.D. Yahata, J.M. Hundley, J.A. Mayer, T.A. Schaedler, T.M. Pollock, 3D printing of high-strength aluminium alloys, Nature 549 (2017) 365–369, http:// dx.doi.org/10.1038/nature23894.

[21] Chunming Wang, Rui Yi, Gaoyang Mi, Mingyang Zhang, Xiuhui Yan & Xiong Zhang, Formation, microstructure, and performance of laser-welded 6061 Al alloy joint with Ti3AlC2 additive, J. Mater. Sci, 57 (2022), 8978-8986.

[22] Leo Watts, Fiber vs CO2 Lasers: Which is Best For You?.

https://www.cncsourced.com/guides/fiber-vs-co2-laser/

[23] L. Zhou, A. Mehta, E. Schulz, B. McWilliams, K. Cho, Y.H. Sohn, Microstructure, precipitates and hardness of selectively laser melted AlSi10Mg alloy before and after heat treatment, Mater. Charact. 143 (2018) 5–17.

[24] B.A. Fulcher, D.K. Leigh, T.J. Watt, Comparison of AlSi10Mg and Al 6061 processed through DMLS, in: Proceedings of the Solid Freeform Fabrication (SFF) Symposium, Austin, TX, USA, (2014).

[25] L. Thijs, K. Kempen, J.-P. Kruth, J. Van Humbeeck, Fine-structured aluminium

products with controllable texture by selective laser melting of pre-alloyed

AlSi10Mg powder, Acta Mater. 61 (2013) 1809–1819.

[26] Santos-Güemes R, Bellón B, Esteban-Manzanares G, Segurado J, Capolungo L, LLorca J.

Multiscale modelling of precipitation hardening in Al–Cu alloys: Dislocation dynamics simulations and experimental validation. Acta Mater 2020;188:475–85.

[27] Opprecht, Mathieu, et al. Acta Materialia 197 (2020): 40-53.

[28] Mehta, Abhishek, et al. Additive Manufacturing 41 (2021): 101966.

[29] Martin, J.H.; Yahata, B.D.; Hundley, J.M.; Mayer, J.A.; Schaedler, T.A.; Pollock, T.M. 3D printing of high-strength aluminium alloys. Nature 2017, 549, 365–369.

[30] Heiland, S.; Milkereit, B.; Hoyer, K.-P.; Zhuravlev, E.; Kessler, O.; Schaper, M. Requirements for Processing High-Strength AlZnMgCu Alloys with PBF-LB/M to Achieve Crack-Free and Dense Parts. Materials 2021, 14, 7190.

[31] R.D. Doherty, D.A. Hughes, F.J. Humphreys, J.J. Jonas, D. Juul Jensen, M.E. Kassner, W.E. King, T.R. McNelley, H.J. McQueen, A.D. Rollett, Current issues in recrystallization: a review, Mater. Sci. Eng. A238 (1997) 219-274.

[32] C.M. Kamma, E. Hornbogen, Recrystallization mechanism in carbon steels, Can. Metall. Q. 23 (2) (1984) 249-257.

[33] R.D. Doherty, Recrystallization and texture, Prog. Mater. Sci. 42 (1997) 39-58.

[34] C. Hofmeister, L. Zhou, F. Kellogg, A. Giri, K. Cho, Y. Sohn, Metall. Mater. Trans. A (2018) 1–14.

[35] R. Goswami, G. Spanos, P. Pao, R. Holtz, Mater. Sci. Eng. A 527 (4-5) (2010) 1089–1095.

[36] L. Zhou, H. Pan, H. Hyer, S. Park, Y. Bai, B. McWilliams, K. Cho, Y. Sohn, Scr. Mater. 158 (2019) 24–28.

[37] A. Le Chatelier, Revue de métallurgie 6 (8) (1909) 914–917.

[38] Ahmed H. Maamoun, Yi F. Xue, Mohamed A. Elbestawi, Stephen C. Veldhuis. The Effect of Selective Laser Melting Process Parameters on the Microstructure and Mechanical Properties of Al6061 and AlSi10Mg Alloys, Materials. 12-12 (2019).

[39] Mathieu Opprecht, Guilhem Roux, Jean-Paul Garandet, and Camille Flament. A Study of the Mechanical Properties of Al6061-$Zr_{1,2}$ Alloy Processed by Laser Beam Melting, J. Mater. Eng. Perform. 17 (2022).

[40] Abhishek Mehta, Le Zhou, Thinh Huynh, Sharon Park, Holden Hyer, Shutao Song, Yuanli Bai, D. Devin Imholte, Nicolas E. Woolstenhulme, Daniel M. Wachs, Yongho Sohn. Addit Manuf. 41 (2021) 101966.

[41] Syed Z. Uddina, Lawrence E. Murra, Cesar A. Terrazasa, Philip Mortona, David A. Robersona, Ryan B. Wicker. Addit Manuf. 22 (2018) 405–415.

[42] Hu Zhang, Haihong Zhu, Xiaojia Nie, Jie Yin, Zhiheng Hu, Xiaoyan Zeng. Scr. Mater. 134 (2017) 6–10.

[43] J. Liu, S. Kou, Crack susceptibility of binary aluminum alloys during solidifcation,

Acta Mater. 110 (2016) 84–94.

[44] A. Sonawane, G. Roux, J.-J. Blandin, A. Despres, G. Martin, Cracking mechanism and its sensitivity to processing conditions during laser powder bed fusion of a structural aluminum alloy, Materialia 15 (2021), 100976.

[45] D.N. Seidman, E.A. Marquis, D.C. Dunand, Acta Mater. 50 (16) (2002) 4021–4035.

43–46.

[46] K. Ma, H. Wen, T. Hu, T.D. Topping, D. Isheim, D.N. Seidman, E.J. Lavernia, J.

M. Schoenung, Mechanical behavior and strengthening mechanisms in ultrafne grain precipitation-strengthened aluminum alloy, Acta Mater. 62 (2014) 141–155.

Chapter 4 Study on Selective Laser Melting of 7075 Aluminum Alloys Modified with Titanium

4.1 Introduction

Complex metallic components can now be directly manufactured without the need for a mold, thanks to a cutting-edge additive manufacturing technique known as selective laser melting [1,2]. Furthermore, due to the non-equilibrium processing conditions involved, alloy components fabricated through selective laser melting (SLM) often exhibit distinctive microstructures and superior overall mechanical characteristics [3, 4]. Therefore, utilizing SLM for high-strength aluminum alloys is an ideal approach for producing intricate and lightweight structural elements for vehicles and aircraft. Nevertheless, due to their wide solidification range, the majority of SLM-fabricated high-strength aluminum alloys—particularly AA7075 alloys—are prone to hot cracking. [5-8].

Currently, the predominant focus of research on aluminum alloys produced via SLM revolves around castable alloys belonging to the Al-Si family, particularly AlSi10Mg and AlSi12 [6], [7], [8], [9]. The near eutectic composition of these castable Al-Si alloys leads to a narrow solidification temperature range, thereby substantially reducing the risk of cracking during the laser additive manufacturing process. Components made from AlSi10Mg and AlSi12 alloys through selective laser melting (SLM) have demonstrated nearly complete density and moderate strength owing to their fine grains and unique meso-structure [8], [9]. Although the aforementioned Al-Si castable alloys are well suited for SLM they cannot entirely supplant wrought aluminum alloys, which generally exhibit superior mechanical properties. This encompasses the high strength characteristic of the 7000 series and the robust heat resistance of the 2000 series [10]. Nonetheless, wrought aluminum alloys manufactured via additive methods from existing brands often encounter issues related to columnar microstructure formation and severe hot cracking. These challenges stem from the rapid cooling rate and significant temperature gradients inherent in the selective laser melting (SLM) process [2], [7]. Numerous efforts have been made to optimize process parameters for the production of high-performance wrought aluminum alloys using selective laser melting (SLM), employing both 7075 (Al-Mg-Si) [11], [12] and 7075 (Al-Zn-Mg-Mg) alloy powders [13], [14]. Despite these endeavors, the majority of these studies have

been unsuccessful in completely eliminating hot tearing fractures. Zhang et al. [15] successfully developed Al-Cu-Mg alloys without cracks using selective laser melting (SLM) technology, showing exceptional tensile strength. However, these alloys still exhibit a notable susceptibility to cracking due to the narrow range of acceptable process conditions and the formation of a columnar microstructure. The SLM process is fundamentally a non-equilibrium solidification process characterized by rapid and intense melting and cooling. Crack-free components can only be reliably fabricated through the use of alloy compositions that harmonize with the dynamic metallurgical characteristics of SLM [16]. Thus, it is highly advisable to engineer customized aluminum alloys with tailored compositions specifically for Selective Laser Melting (SLM) technology.

Hughes Research Laboratory (HRL) [17] demonstrated the successful suppression of cracks in laser additively manufactured aluminum alloys by introducing additional inoculants to regulate solidification. Using an electrostatic coating method, Al alloy powder particles were coated with ZrH2 nanoparticles. The crack-free fabrication of 7075 and 7075 alloys via SLM was achieved, facilitated by the heterogeneous nucleation effect provided by the in situ formation of Al3Zr particles. This Zr/Sc modification approach serves as a valuable reference for producing highly crack-resistant aluminum alloys. Notably, the 2 wt% Zr-modified Al2024 alloy exhibited crack-free behavior and exhibited a high ultimate tensile strength of ~450 MPa [18]. However, the elongation to failure notably decreased from ~6% to ~3% following Zr modification due to the formation of excessive brittle Al3Zr intermetallics [15]. Subsequently, reducing the Zr content to 0.6 wt% remarkably improved the ductility to over 11% while maintaining a high tensile strength of 495 MPa [19]. Furthermore, SLM-manufactured Zr/Sc-modified Al-Mg (known as Scalmalloy®) [20], [21] and Al-Mn alloys [22] exhibit a favorable combination of high strength and ductility with low Zr/Sc content. However, the low Zr/Sc addition may result in insufficient heterogeneous nucleation and grain refinement, potentially limiting the reduction in hot-cracking susceptibility. Consequently, to address the challenges of high cracking propensity and the formation of columnar grains in SLM-fabricated wrought aluminum alloys, further exploration of novel compositional spaces is imperative to expand the range of printable materials for SLM.

Among aluminum alloys in the 2000 family, both the 2024 (Al-4.3Cu-1.5Mg-0.6Mn) and 2014 (Al-4.3Cu-0.5Mg-0.8Si-0.8Mn) alloys exhibit outstanding mechanical properties at temperatures below 100°C [23]. At elevated temperatures, heat-resistant aluminum alloys often exhibit a reduced copper content. However, alloys

with a moderate copper content (~2 wt%) are markedly more prone to cracking during solidification processes [24]. In conventional aluminum alloy casting, titanium (Ti) is commonly added to facilitate grain refinement. Considering Selective Laser Melting (SLM) as a form of micro-area casting or welding characterized by rapid solidification, the incorporation of Ti into aluminum (Al) alloys holds promise for crack reduction during SLM. Additionally, substituting rare earth elements with Ti offers the advantages of utilizing more readily available resources and reducing manufacturing costs. However, limited research has explored the impact of Ti modification on the microstructural and mechanical properties of Al alloys produced via SLM. This study aimed to develop a Ti-modified Al–2.25Cu–1.8Mg alloy that features a fine equiaxed microstructure and high strength, is free from cracks, and is specifically tailored for SLM applications. Thermodynamic calculations and microstructure characterization were employed to thoroughly investigate the alloy composition design, crack mitigation strategies, and microstructural evolution of the Ti-modified Al alloy.

Al/TiAl3 composites can be manufactured through various techniques, including powder metallurgy methods and different casting processes. One innovative approach involves an in situ powder metallurgical method for producing composites reinforced with particulate TiAl3. Additionally, the fabrication of Al/TiAl3 composites can be achieved by depositing molten Al droplets onto a layer of Ti particles [17]. These methods have improved the mechanical properties of the resulting composites. However, these methods are characterized by complex procedures, prolonged manufacturing cycles, and high costs. Moreover, these techniques face challenges in creating extensive and intricate products with improved qualities.

The mechanical stirring approach has gained widespread popularity in the fabrication of composites due to its numerous advantages. These include enhanced matrix-particle bonding, improved control over the matrix structure, simplicity, cost-effectiveness in processing, closer approximation to the desired shape, and a wide range of material options [18-19]. However, a primary challenge in producing aluminum matrix metal matrix composites (AMMCs) using this method lies in achieving uniform dispersoids and small matrix grains, as these factors significantly influence the mechanical characteristics of the composites.

The presence of rod-like or needle-shaped TiAl3 structures in traditional cast Al–Ti alloys adversely affects their mechanical properties. Therefore, it is essential to determine the optimal quantity of Ti to produce Al-TiAl3 composites, ensuring a

uniform dispersion of tiny TiAl3 particles within the matrix. A comprehensive study has been conducted on the overall impact of grain refiners on the microstructure and mechanical properties of alloys [20-21]. The heterogeneous nucleation process in composites is explained by the modest lattice disregistry between the grain refiners and the matrix [22-23]. Recently, Li et al. [24] discovered that the presence of a primary aluminum phase on MgAl2O4 particles in binary Al-Mg alloys is attributed to the slight difference in lattice structure (1-4%) between MgAl2O4 and α-Al, termed heterogeneous nucleation. A similar phenomenon has been observed in AMMCs strengthened with TiC particles [25]. Aluminum alloy matrix composites were fabricated through the stir casting technique by incorporating TiAl3 particles as reinforcements. In this process, both titanium powder and cryolite powder were employed. Cryolite powder was utilized to augment the volume and fluidity of the powdered mixture, thereby promoting enhanced interaction between the molten substance and the powders. The primary aim of this study was to examine the influence of titanium addition on the microstructure and mechanical properties of 7075 alloys.

4.2 Materials and experimental methods

4.2.1. Powder production and characterization

The raw materials utilized for printing components via the TruPrint 1000 additive manufacturing system consisted of AA7075 powder blended with microscale Ti particles sourced from Sichuan Huomosi Industrial Technology Co., Ltd. Particle size analysis conducted using a laser diffraction powder sizer (Mastersizer 2000, Malvern Instruments Ltd., UK) revealed particle sizes ranging from 15-60 μm for AA7075 and 1-20 μm for Ti. The investigation employed a setup utilizing a green laser, chosen for its distinct wavelength compared to the commonly used fiber laser, resulting in varied absorption rates. The superior absorption efficiency of green light allows for the printing of aluminum alloy components using less energy, thereby reducing the evaporation of magnesium (Mg) and zinc (Zn) in AA7075. The optimized processing parameters included a laser energy of 300 W, a scanning speed of 800 mm/s, and an energy density of 78.1 J/mm^3.

To evaluate the characteristics of the samples, they were ground using SiC sheets with a maximum grain size of 1200. Subsequently, the objects were polished using 200-proof anhydrous ethanol and a 0.05 μm alumina polishing slurry. Tensile testing was conducted using an INSTRON 5967 electronic universal testing machine with a

nominal strain rate of 0.001 mm/mm/second. Following the tensile tests, the fracture surfaces were examined using scanning electron microscopy (SEM). The SEM instrument utilized was a ZEISS Sigma 300 model manufactured in Germany and was equipped with a Schottky field emission electron gun. The resolution capability of this microscope is 1.0 nanometers at an operating temperature of 15 K. Additionally, SEM was performed with energy dispersive spectroscopy (EDS), specifically with a SmartEdX system. The electron backscatter diffraction (EBSD) technique was also employed using the Oxford Nordlys max3 model. Prior to SEM inspection, a gold coating was applied using a Quorum SC7620 for 45 seconds. Vickers hardness measurements were conducted using a microhardness tester from Leiz-Wetzlar, Germany, at various positions on the XY and XZ planes. A load of 100 g was applied under specified conditions with an indentation duration of 25 s. This process was repeated 10 times to ensure precision. Finally, the mechanical test was performed using an American INSTRON 5967 Electronic Universal Testing Machine.

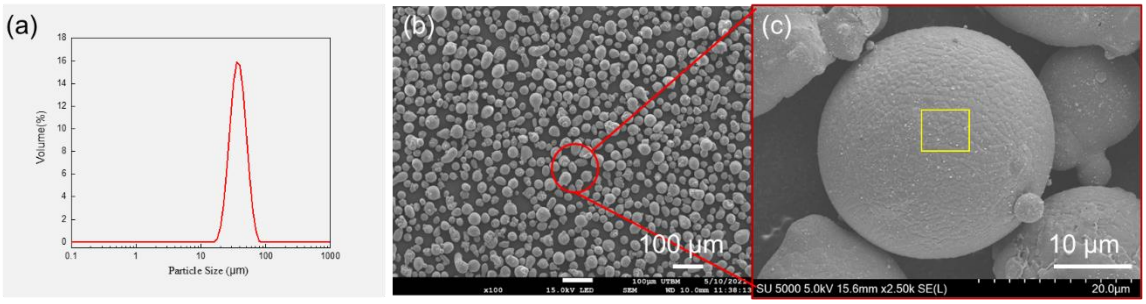

Fig 4.1 Powder morphology and size distribution of the (a) size distribution and (b) 7075 Al powder.

Fig. 4.1 shows the powder size distribution and morphology of the AA 7075 powders. The average powder size is 15 to 55 μm, and the powder is mostly spherical.

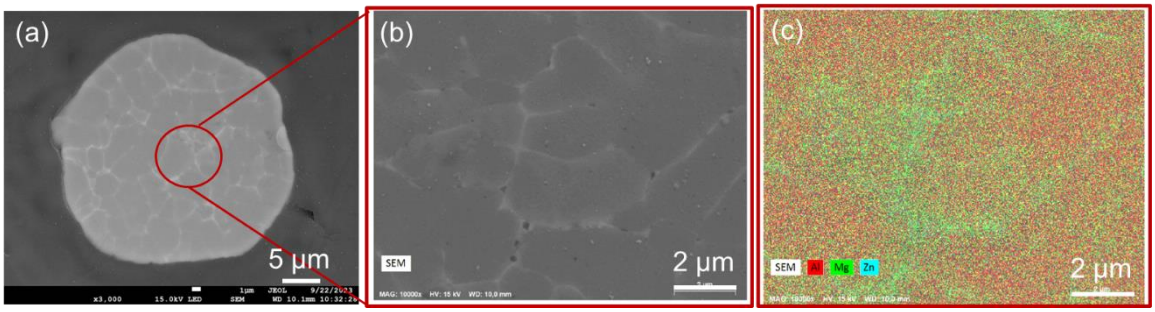

Fig 4.2 Powder morphology and EDX elemental distribution: (a) cross-section of the AA7075 Al powder, (b) enlarged cross-sectional image, and (c) EDX results.

Figure 4.2 shows a cross-sectional image of the AA7075 powder, with the EDX

results indicating the presence of the MgZn2 phase within the powder. The Mg and Zn phases are primarily concentrated at the grain boundaries, while aluminum is predominantly distributed within the grain structure.

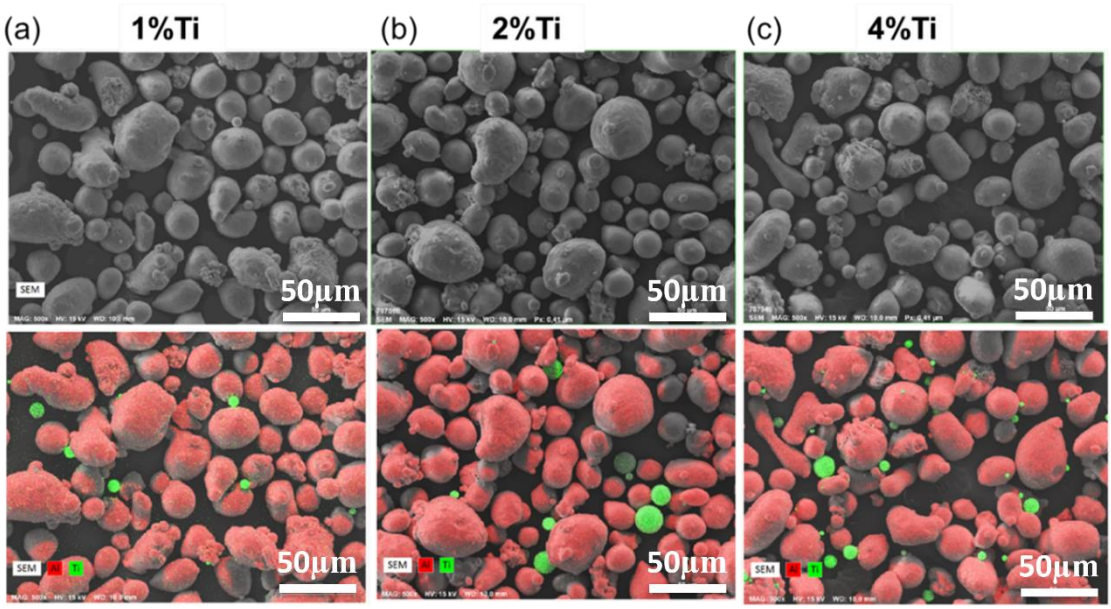

Fig 4.3 Powder morphology with Ti addition: (a) AA7075 Al powder with 1% Ti addition, (b) AA7075 Al powder with 2% Ti addition, and (c) AA7075 Al powder with 4% Ti addition

Figure 4.3 displays the 7075 Al powder with an average size ranging from 15 to 55 μm, alongside Ti particles of approximately 20 μm in size, which are evenly distributed among the AA7075 powders. As the Ti addition increases, there is observable evidence of a uniform distribution of Ti and Al particles following mechanical mixing.

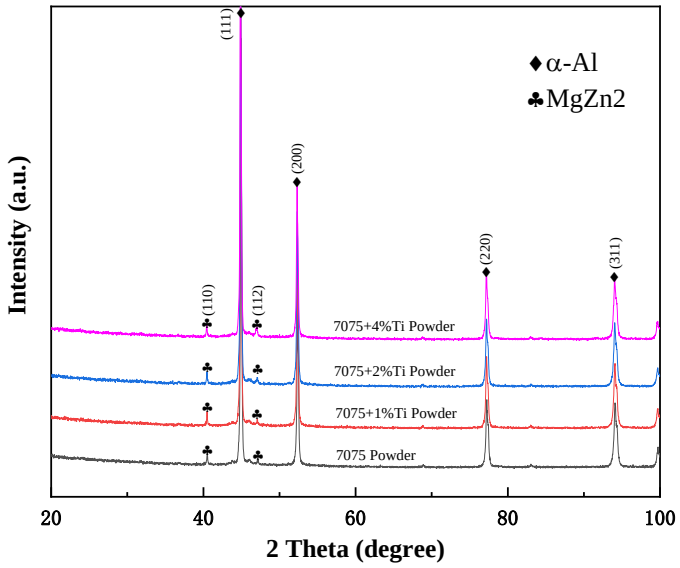

Fig 4.4 XRD patterns of the 7075 Al alloy and 7075/Ti powders.

Figure 4.4 shows the XRD patterns of the 7075 Al alloy and 7075 alloy with 1%, 2%, and 4% added powders. The 7075 powder exhibited favorable phases, prominently featuring the MgZn2 strengthening phase, with no other impurity phases detected. Additionally, due to the low content of Ti particles, no Ti phases were observed.

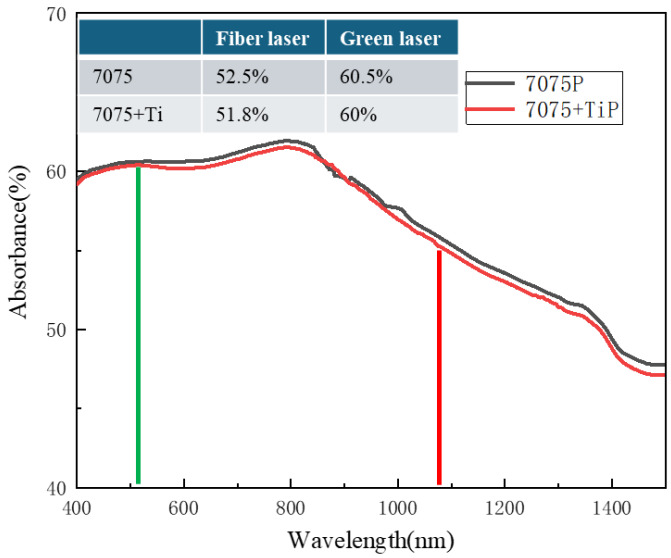

Fig 4.5 Green laser and fiber laser comparison.

Figure 4.5 shows a comparison between the effects of the Green laser and fiber laser on the AA 7075 and AA7075+Ti particles. The laser absorption rates of Ti-added

7075 and unmodified 7075 are nearly identical, given the low quantity of Ti particles present in Ti-added 7075. Upon comparing the absorption of red and green light in the 7075 aluminum alloy, it was observed that the absorption rate for green light was enhanced by 8%.

4.2.2 Experimental details

The SLM tests were conducted using custom-designed equipment equipped with a 1 kW green laser. Cuboid samples measuring 8 × 8 × 8 mm3 were fabricated to optimize the processing parameters and characterize the microstructure. The samples were produced utilizing varying laser powers (ranging from 200 to 300 W) and scan velocities (ranging from 400 to 1800 mm/s). All the experimental details followed the methodology outlined in Chapter 3, as depicted in Fig. 3.5 and Table 3.1. The SLM experiments were carried out using a Truprint 1000 machine from Germany.

As described in Chapter 3, the laser power and scanning velocity were selected as the parameters to optimize the SLM experiment. Eighteen experiments with varying parameters are listed in Table 4.1. The energy density can be calculated using Equation 3.1.

Table 4.1 Experimental parameters

	P (W)	V (mm/s)	Ed (J/mm^3)
1	200	1200	34.7
2		1000	41.7
3		800	52.1
4		666	62.5
5		533	78.1
6		400	104.1
7	250	1500	34.7
8		1250	41.7
9		1000	52.1
10		833	62.5
11		666	78.1
12		500	104.1
13	300	1800	34.7
14		1500	41.7

15	1200	52.1
16	1000	62.5
17	800	78.1
18	600	104.1

4.3 Materials characterization

4.3.1 Microstructure observation

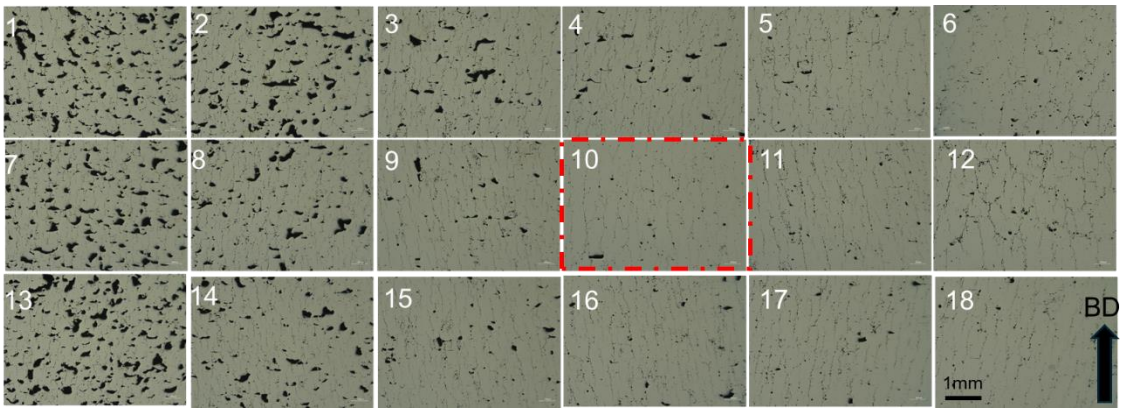

Fig 4.6 **AA7075 microstructure observation**

Figure 4.6 shows the AA7075 sample, revealing the presence of numerous pores and cracks. The experimental findings indicate that low energy density, either through low power or high velocity, results in an abundance of cracks and pores. This phenomenon is primarily attributed to the incomplete melting behavior of the aluminum particles. However, as the energy density increases, the formation of pores and cracks diminishes. As particles undergo full melting and fusion, a denser tissue morphology is expected to form. However, as depicted in the figure, regardless of how the process parameters are optimized, a crack-free microstructure cannot be achieved. This suggests that the cracking in AA7075 cannot be completely eliminated through parameter optimization alone.

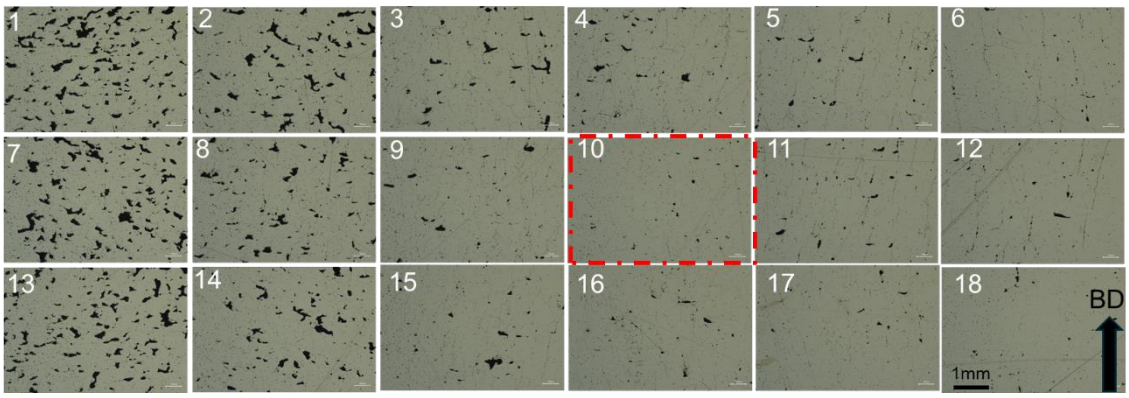

Fig 4.7 AA7075+1%Ti microstructure observation

The microstructure of the as-built AA7075+1%Ti alloy is shown in Fig. 4.7. Similar to the observations in the previous figure, there are not only pores but also a significant number of cracks present. Similarly, a low energy density results in incomplete melting of structures, leading to the formation of numerous cracks and pores. However, with the addition of 1% Ti, the formation of cracks and pores is significantly reduced.

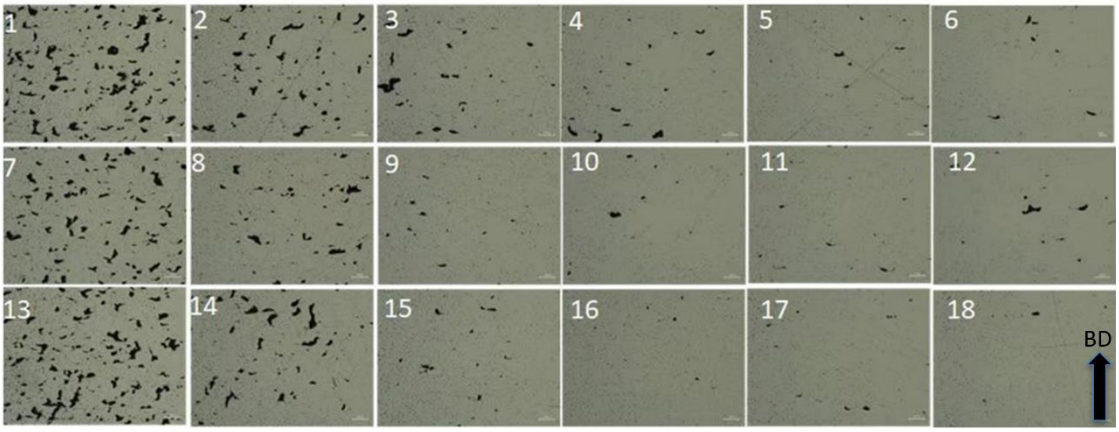

Fig 4.8 AA7075+2%Ti microstructure observation

The microstructure of the as-built AA7075+2%Ti alloy is shown in Fig. 4.8. Unlike in previous observations, only pores are present, and no cracks are detected. The addition of 2% Ti effectively inhibited crack formation. Similarly, a low energy density results in incomplete melting of structures, leading to the formation of numerous cracks and pores. However, with the addition of 2% Ti, both the number of pores and cracks significantly decreased. The addition of more titanium during the production process allows for the elimination of a greater number of pores and cracks, ultimately resulting in improved microstructure quality.

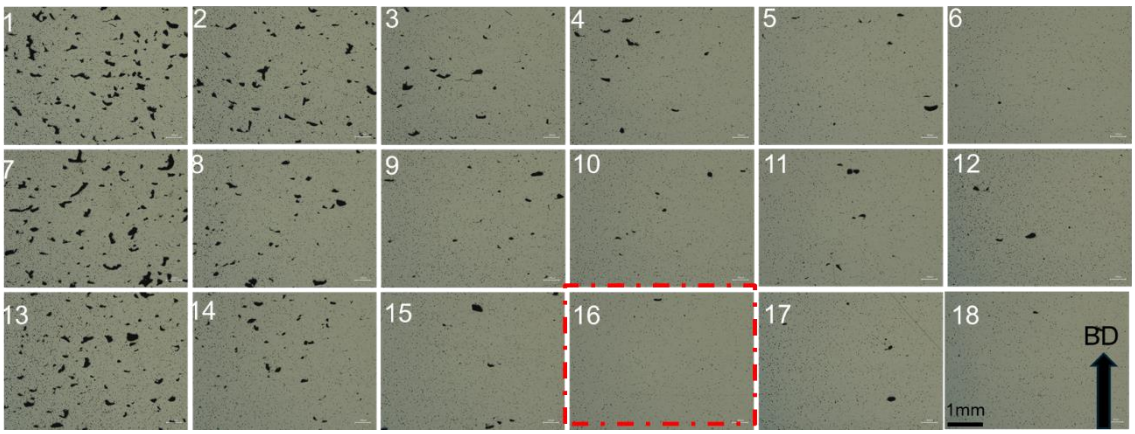

Fig 4.9 AA7075+4%Ti microstructure observation

The microstructure of the as-built AA7075+4%Ti alloy is shown in Fig. 4.9. In contrast to previous observations, only pores are present, with essentially no cracks detected. This effectively enhances the microstructural morphology. Similarly, a low energy density results in incomplete melting of structures, leading to the formation of numerous cracks and pores. However, with the addition of 4% Ti, both the number of pores and cracks significantly decreased. The addition of more titanium during the manufacturing process allows for the elimination of more pores and cracks, further enhancing the microstructural quality.

4.3.2 Elemental distribution

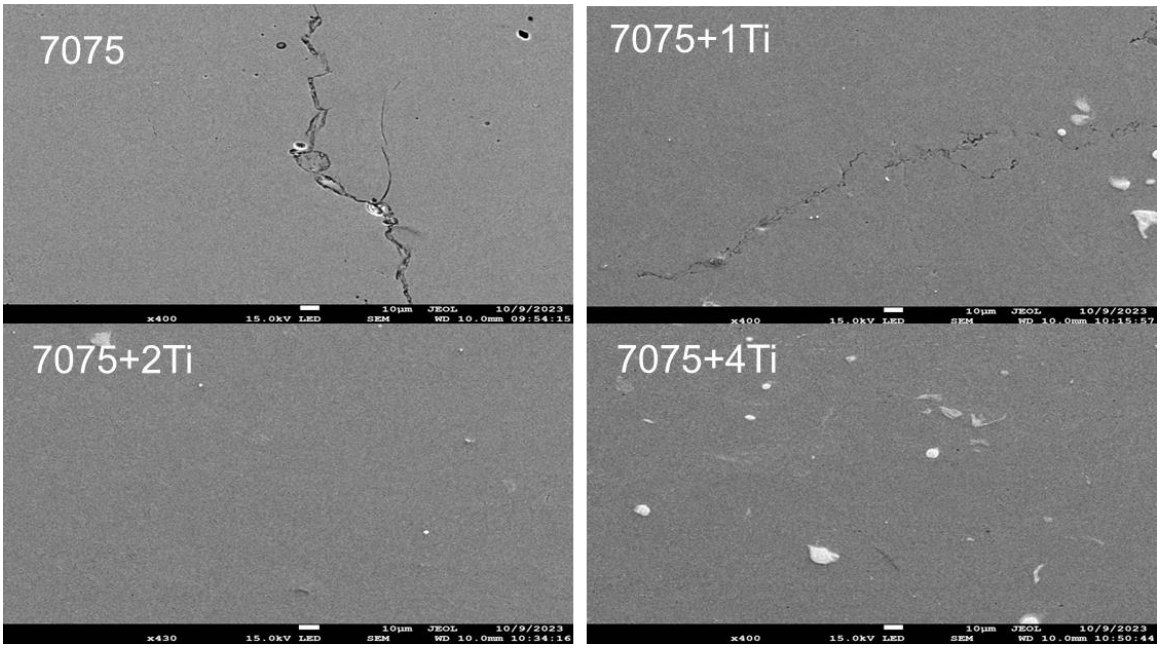

Fig 4.10 As-built sample cross-section images of (a) AA7075, (b) AA7075+1% Ti, (c) AA7075+2% Ti, and (d) AA7075+4% Ti.

Figure 4.10 displays the cross-section morphology of the manufactured AA7075 and mixed powder with optimal process. As previously discussed, cracks and pores are generated during the manufacturing of AA7075 powder due to stress release and solidification. AA7075 exhibited extensive cracking; however, the addition of 2% Ti and 4% Ti particles to AA7075 completely inhibited cracking. A significant amount of residual Ti particles were observed in the samples.

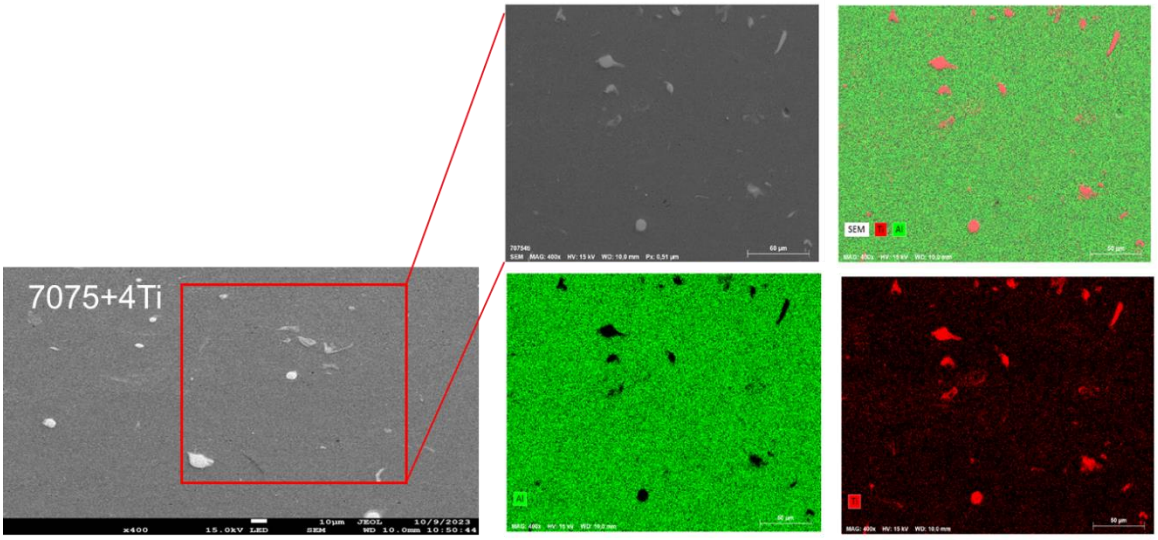

Fig 4.11 As-built cross-sectional images of the AA7075+4%Ti sample.

Figure 4.11 shows a complete cross-sectional image of the AA7075+4%Ti sample. Furthermore, the EDS test confirmed that the residual particles observed on the surface were indeed Ti particles, with no other impurity particles detected. The bonding mechanism between the titanium particles and the aluminum matrix is primarily chemical rather than solely mechanical. This strengthened behavior is substantiated by subsequent mechanical tests.

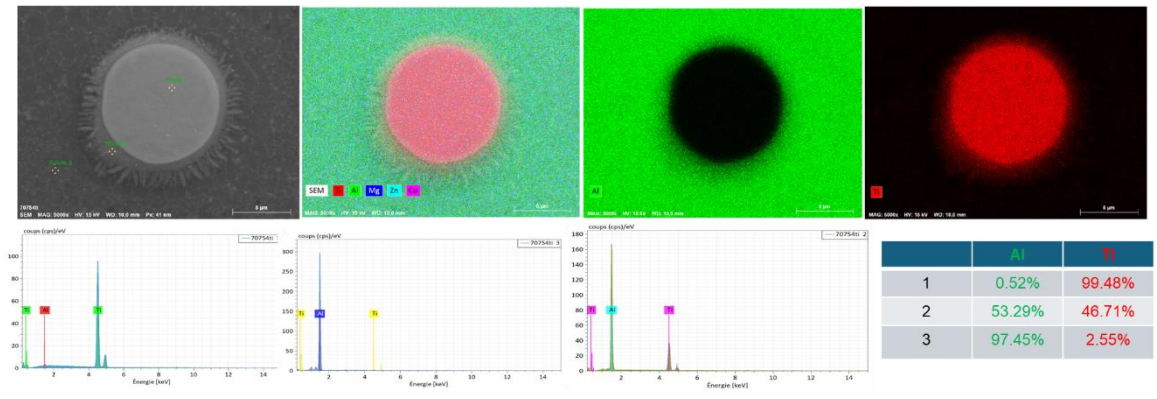

	Al	Ti
1	0.52%	99.48%
2	53.29%	46.71%
3	97.45%	2.55%

Fig 4.12 AA7075+4%Ti elemental distribution: (a) SEM image and (b) enlarged image.

Figure 4.12 shows the elemental distribution of AA7075+4%Ti, which is focused on a single Ti particle. This reveals that a reaction occurs between the Ti particles and the Al matrix in the surrounding area of the particle, resulting in the formation of Al3Ti. This confirms that the bonding mechanism between the titanium particles and the aluminum matrix is primarily chemical rather than purely mechanical.

4.3.3 XRD phase distribution

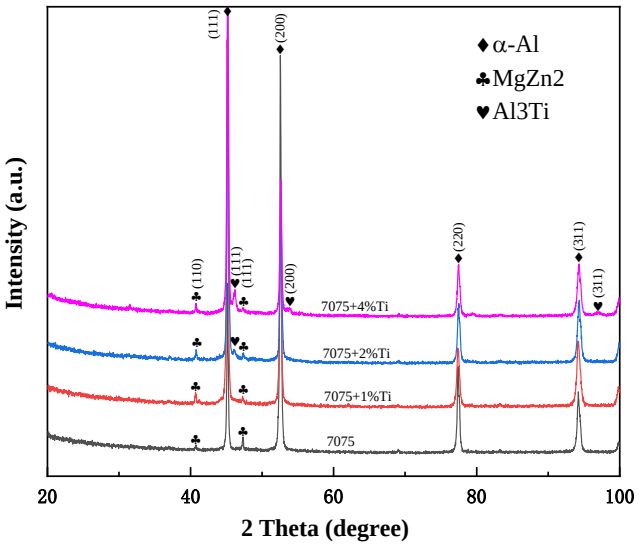

Fig 4.13 As-built sample XRD results for (a) AA7075, (b) AA7075+1% Ti, (c) AA7075+2% Ti, and (d) AA7075+4% Ti.

Comparing the X-ray diffraction (XRD) patterns of the powder and the printed samples, it is evident that Al3Ti was formed during the printing process. In contrast to that of the feedstocks of the original particles, the strength of the Al3Ti peak increases due to the formation of this phase. The formation of Al3Ti significantly enhances the strength of the material and contributes to the elimination of cracks and pores.

4.3.4 Microhardness

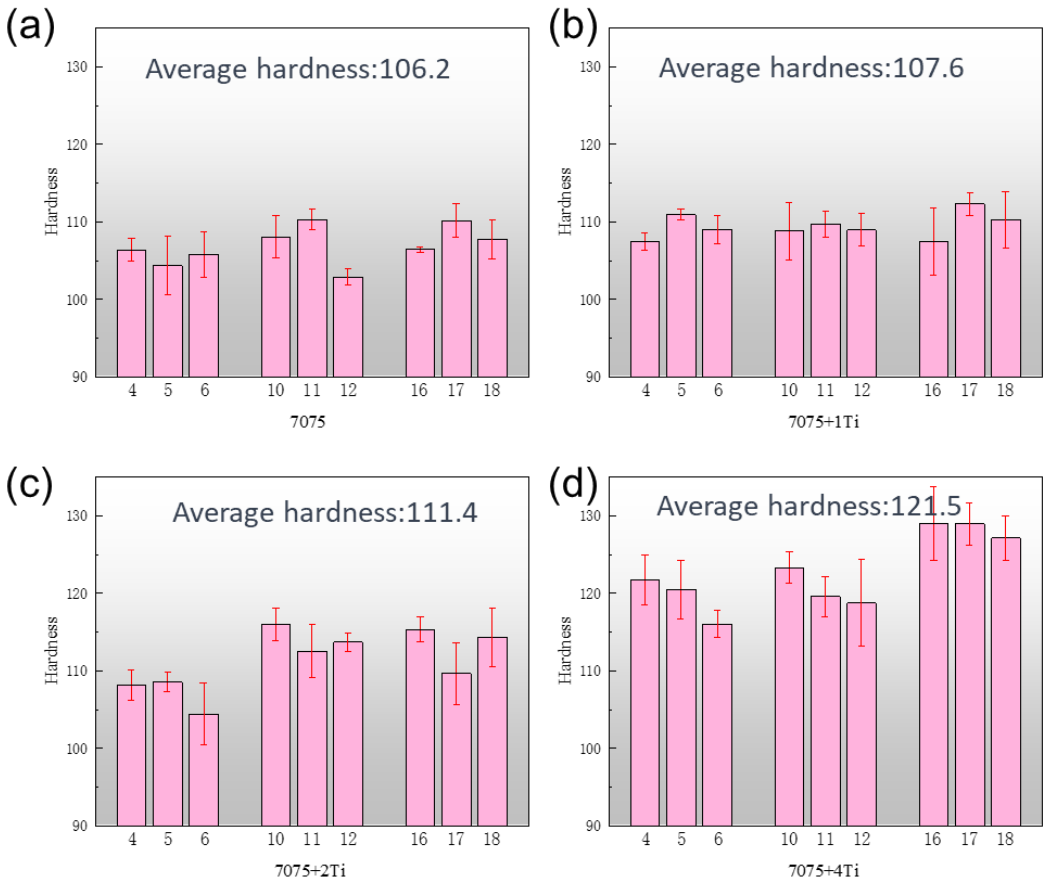

Fig 4.14 As-built sample microhardness results for (a) AA7075, (b) AA7075+1% Ti, (c) AA7075+2% Ti, and (d) AA7075+4% Ti.

Figure 4.14 shows the microhardness results of the as-built AA7075, AA7075+1% Ti, AA7075+2% Ti, and AA7075+4% Ti samples. As the titanium content increased, the microhardness gradually increased. Additionally, at the same energy density, the hardness increases with increasing laser power. The highest hardness is observed for the AA7075+4%Ti sample, reaching 129 HV.

4.3.5 Microstructure evolution corrosion observation

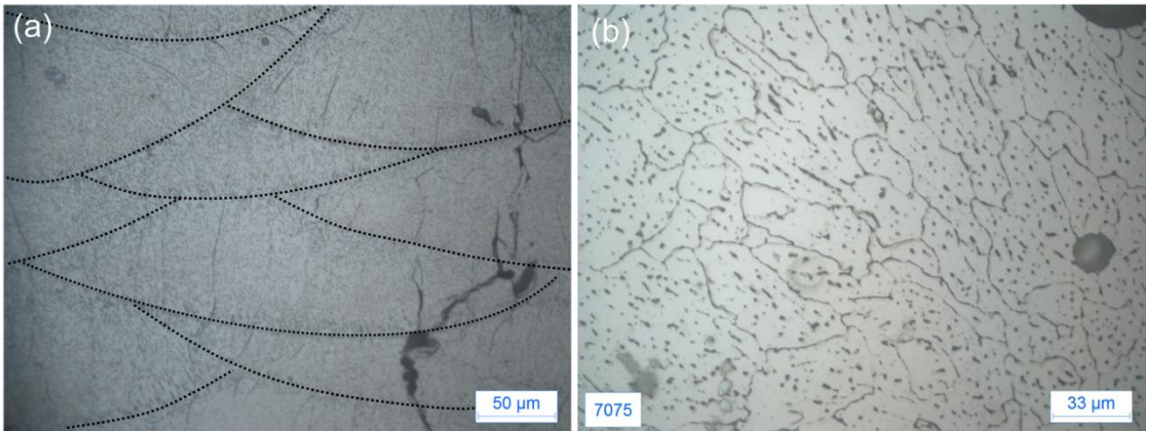

Fig 4.15 As-built morphology: (a) 7075 molten pool morphology and (b) grain morphology of 7075.

After corrosion of the 7075 molten pool, cracks penetrate through several molten pools, and the interior of the pools contains a large number of columnar grains.

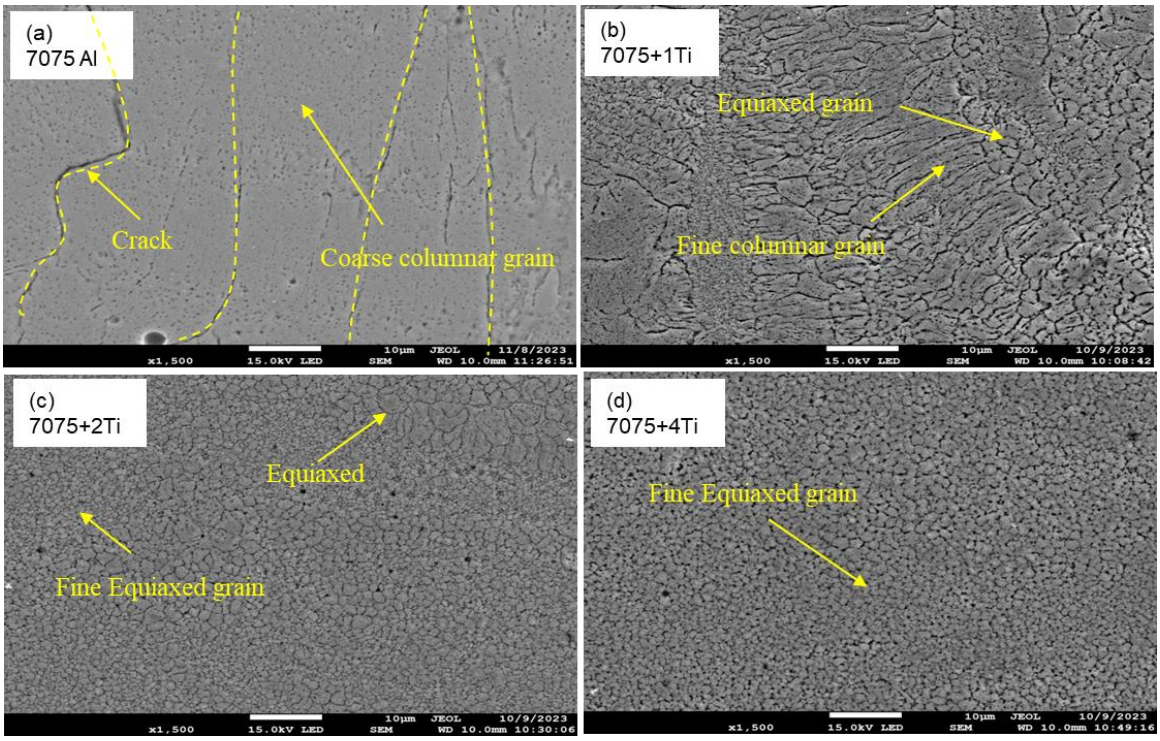

Fig 4.16 As-built sample SEM images of (a) AA7075, (b) AA7075+1% Ti, (c) AA7075+2% Ti, and (d) AA7075+4% Ti.

For the 7075Al samples, coarse columnar grains and hot cracks are visible. However, in the case of 7075Al+1%Ti, the image reveals equiaxed grains and fine columnar grains. Furthermore, for the 7075Al+2%Ti and 7075Al+4%Ti samples, finer equiaxed grains are evident. Figure 4.16 (c-d) shows the transition from columnar grains to equiaxed grains as the Ti% increases. This indicates the occurrence of a refined

crystalline strengthening mechanism during Ti addition in the SLM process. Additionally, as the grain size decreases, the number of cracks and pores gradually decrease. Particularly, in the 4% Ti sample, pores and cracks are barely visible at the same magnification, highlighting the strengthening performance and explaining the increase in microhardness shown in Fig. 4.14.

4.3.6 Microstructure evolution EBSD observation

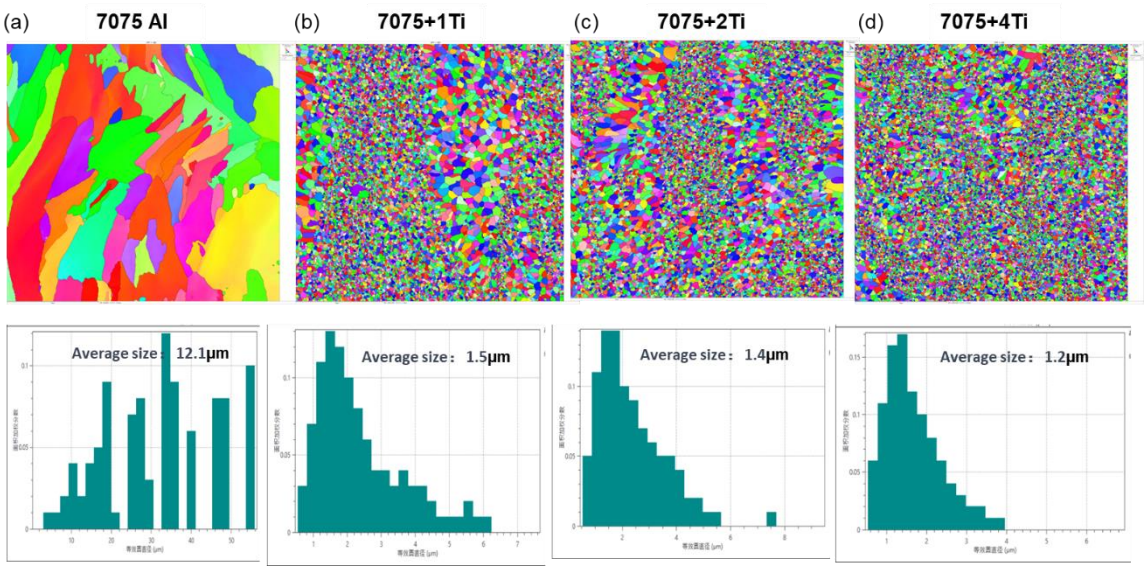

Fig 4.17 As-built sample EBSD IPF results for (a) AA7075, (b) AA7075+1% Ti, (c) AA7075+2% Ti, and (d) AA7075+4% Ti.

In the AA7075 Al samples, coarse columnar grains and hot cracks are evident, with an average grain size of 12.1. However, in the 7075Al+1%Ti samples, fine equiaxed grains and fine columnar grains are observed, with an average grain size of 1.5. Similarly, in the 7075Al+2%Ti and 7075Al+4%Ti samples, finer equiaxed grains and fine columnar grains are observed, with average grain sizes of 1.4 and 1.2, respectively. It is evident that while substrate modification had a negligible effect on the microstructure, the addition of 1 wt% Ti significantly altered the morphology of the Al grains in the SLM-fabricated alloys. The 7075 alloys and the 7075-AS alloy exhibit enormous columnar grains that grow epitaxially along the BD and can extend to lengths up to hundreds of micrometres. The observed IPF color is consistent with recent research on materials with cubic structures that have been additively created. [25–28].

As Fig. 4.17 illustrates, ultrafine and nearly completely equiaxed microstructures were achieved in both 7075 alloys with 1% Ti addition. The equiaxed grains range in size from 0.5 μm to 1.5 μm. Additionally, a noticeable reduction was observed in the small residual columnar grains, which had lengths less than 7 μm. It has often been documented that in SLM-fabricated Al alloys subjected to inoculation treatment,

localized differences in thermal history or composition throughout the melt pool might be the cause of grain size fluctuations in both alloys[29-31].

However, the 7075+2%Ti alloy exhibited an average grain size of 1.4 μm, while the 7075+4%Ti alloy displayed an average grain size of 1.2 μm due to the larger proportion of fine, equiaxed grains. The IPF color indicates that in both alloys, the fine, equiaxed grains are randomly oriented and lack discernible textural characteristics. Nevertheless, despite significant grain refinement, hot cracking cannot be completely eliminated. This suggests that to minimize cracking in this type of alloy during SLM processing, it is necessary to combine both substrate modification and inoculation treatment techniques.

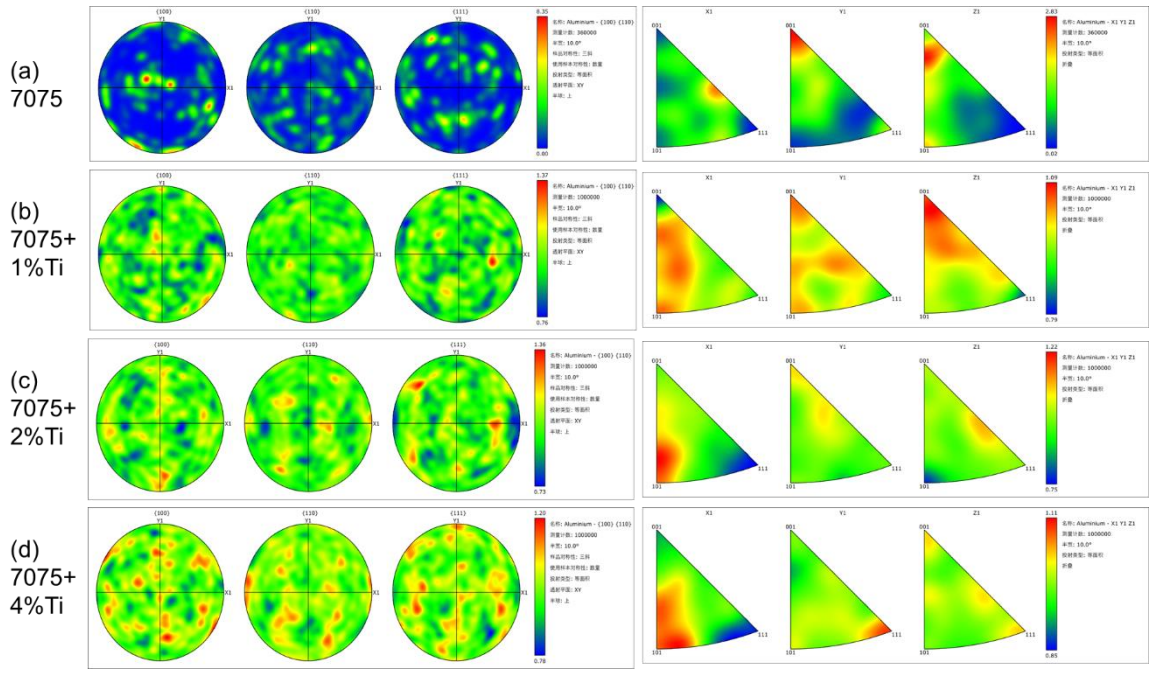

Fig 4.18 EBSD pole figure results for the (a) AA7075, (b) AA7075+1% Ti, (c) AA7075+2% Ti, and (d) AA7075+4% Ti samples.

Fig. 4.18 shows the evolution of the grain size distribution with increasing Ti concentration. The grains demonstrate a parallel growth pattern in the direction of construction. Additionally, Fig. 3.18 presents the electron backscatter diffraction (EBSD) map of the as-built AA7075+1%Ti-XY sample. This map illustrates the 7075Al+1%Ti-XY direction EBSD and polar map. Observations revealed the presence of both fine equiaxed grains and columnar grains, with a maximum texture intensity of 2.05. The significant intensity of the local texture in the {111} plane is attributed to the presence of rather large grains. Furthermore, the black regions correspond to the remaining titanium particles.

The presence of minuscule particles near the titanium particles suggested the occurrence of the aforementioned single-solvent recrystallization phenomenon. Mapping revealed that the refined grains were not uniformly dispersed but were concentrated near the edges of larger grains. This observation also explains the occurrence of recrystallization. Generally, smaller equiaxed grains were observed toward the periphery of the melted region, whereas longer columnar grains were observed within the melted region. It is possible that the AlxTiy phases are formed within the melt pool and help enhance the grain structure in the melt pools.

4.3.7 Mechanical performance

The mechanical characteristics of this alloy were isotropic. Compared to those of 7075 without added Ti particles, the tensile properties were enhanced. Both the as-built and heat-treated alloys exhibited initial elastic deformation and clear strain hardening until final failure. Additionally, with increasing Ti addition from 1% to 4%, the stress increases, suggesting improved mechanical performance through strain hardening.

With increasing Ti addition, the as-built AA7075 alloys exhibited increased tensile strength and elongation. The same trend was observed for the heat-treated (HT) samples, wherein increasing the Ti addition led to a higher tensile strength. However, compared to the as-built and heat-treated samples, the heat-treated samples exhibit better performance. The tensile strength of the as-built sample with 4% Ti is 370 MPa, and the elongation is close to 5%. After heat treatment, the strength increased to 410 MPa, but the elongation decreased.

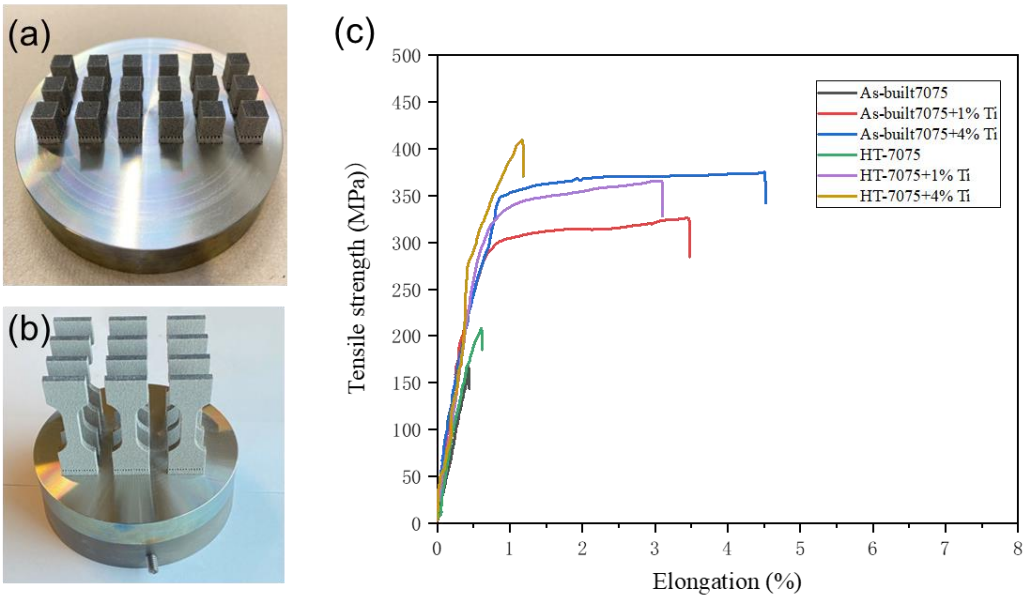

Fig 4.19 Mechanical performance of the (a) as-built samples, (b) tensile test samples, and (c) stress–strain curves

4.4 Fracture test

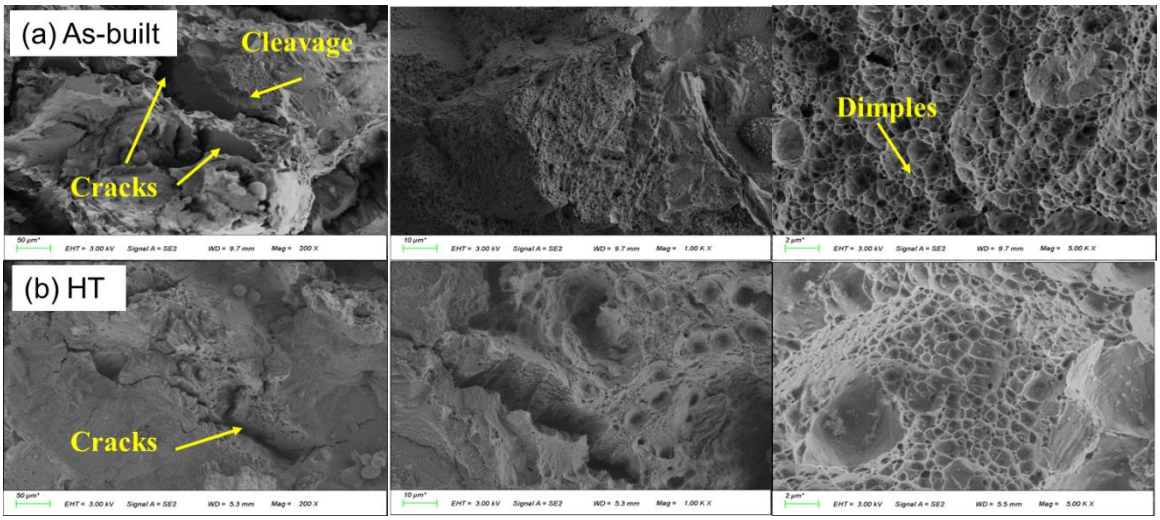

Fig 4.20 Fracture morphologies of the as-built samples after the fracture tests: (a) AA7075 and (b) HT AA7075.

Fig. 4.20 displays the fracture morphologies of the as-built AA7075 and heat-treated (HT) AA7075 samples after fracture testing. Numerous cracks are present, and the fracture mode is cleavage fracture. Equiaxed dimples dominate the rough surfaces of both fractures, indicating ductile fracture behavior. It should be noted that, for the sake of conciseness, the transverse fractographies of the alloy exhibit characteristics

similar to those of their longitudinal counterparts.

After the crash test, the as-built samples show cracks, cleavages, and dimples. These defects are improved after heat treatment, which confirms the strength enhancement after the tensile test. The grain bonding is tightened by heat treatment, which significantly increases the sample strength.

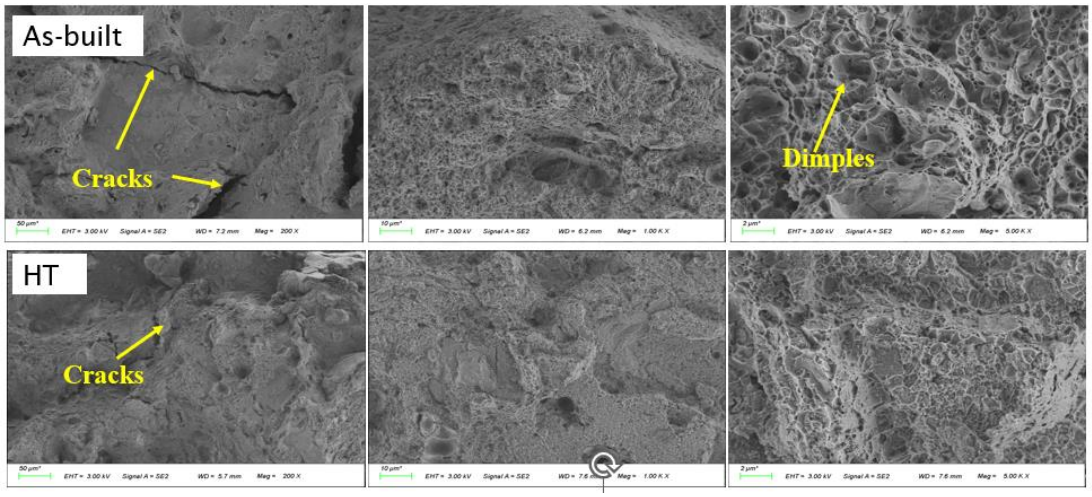

Fig 4.21 Fracture morphologies of the as-built samples after fracture testing: (a) AA7075+1% Ti and (b) HT AA7075+1% Ti.

Fig. 4.21 illustrates the fracture morphologies of the as-built samples after the fracture tests of AA7075+1%Ti and heat-treated (HT) AA7075+1%Ti. Numerous cracks are present, and the fracture mode is cleavage fracture. With an increase in the amount of Ti particles, the number of cracks can be significantly reduced, although slight cracks can still be found on the fracture surface of the as-built samples. After heat treatment, the number of cracks decreases, and the grain structure becomes tighter, which explains the improvement in tensile strength.

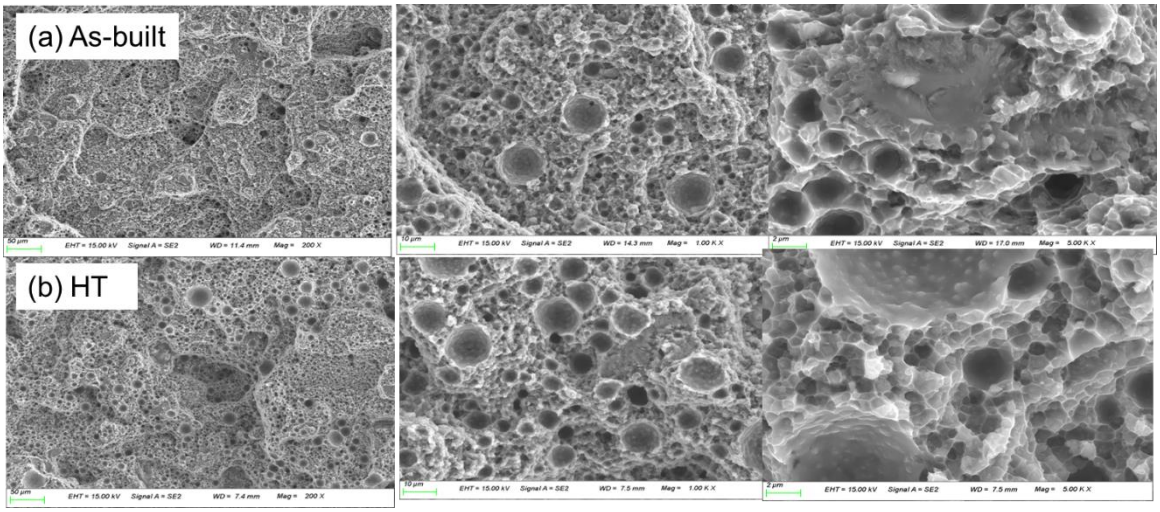

Fig 4.22 Fracture morphologies of the as-built samples after fracture testing: (a) AA7075+1% Ti and (b) HT AA7075+1% Ti.

Figure 4.22 shows the fracture morphologies of the as-built samples after the fracture tests of the AA7075+1%Ti and heat-treated (HT) AA7075+1%Ti samples. In the case of 7075 with 4% Ti added, there are no cracks in the samples. The fracture mode transitioned to ductile dimple fracture. Similarly, with an increase in the Ti particles, cracks can be significantly eliminated, and slight cracks can be found on the as-built samples after the fracture surface. After heat treatment, the cracks are fully eliminated, and the grain structure becomes tight, which explains the improvement in the tensile strength. Unmelted Ti particles can be seen on the fractured surface, and caves become more obvious, which explains the strengthened enhancement trade-off of its ductility. Caves contribute to strength but worsen ductility.

4.5. Element loss

In contrast to findings in other literature where the Mg and Zn contents decrease during the printing process, our results indicate that the loss of Mg and Zn is significantly reduced, as shown in Table 4.2.

Table 4.2 Element loss

Element (wt%)	Zn	Mg	Cu	Ti	Al
7075 powder	5.0±0.07	2.5±0.05	1.7±0.08	-	Balance
7075 as-built	4.83±0.08	2.36±0.06	1.71±0.05	-	Balance

7075+1%Ti	4.77±0.11	2.11±0.06	1.59±0.06	0.89	Balance
7075+2%Ti	4.61±0.08	2.12±0.56	1.60±0.1	1.73	Balance
7075+4%Ti	4.28±0.04	2.00±0.12	1.63±0.08	3.68	Balance

Conclusion

In this study, AA 7075 was manufactured using the selective laser melting (SLM) process, resulting in defects such as cracks and pores. To enhance the mechanical performance and achieve structures free from cracks and pores, titanium (Ti) particles were added to the feedstocks to investigate the strengthening mechanism. Additionally, heat treatment (HT) was utilized to explore additional methods for improving strength. Some key conclusions obtained from this study can be summarized as follows:

1. The optimal parameters are a laser power of 300 W, a scanning speed of 1000 mm/s, and a corresponding energy density of 62.5 J/mm^3, which are much lower than those of conventional printing equipment.
2. Adding 2% Ti can significantly inhibit the formation of thermal cracks, but it cannot completely prevent them. Adding 4% Ti can produce crack-free samples.. Residual titanium particles form AlTi3 at the interface with the aluminum matrix. By comparing the XRD patterns of the powder before printing and the samples after printing, Al3Ti is formed during the printing process, and the residual Ti particles have a good bond with the aluminum matrix.
3. The more Ti is added, the more obvious the grain refinement is, and the greater the weakening of the anisotropy. In the AA7075 Al samples, coarse columnar grains and hot cracks are evident, with an average grain size of 12.1.When added 4% Ti average grain size is 1.2 μm,
4. The loss of Mg and Zn is reduced during the printing process
5. Compared to those of 7075 without added Ti particles, the tensile properties were enhanced. The tensile strength of the as-built sample with 4% Ti is 370 MPa, and the elongation is close to 5%. The primary fracture mode of 7075 is cleavage fracture, and the addition of Ti particles leads to ductile dimple fracture.

Reference

[1] J. Zhang, B. Song, Q. Wei, D. Bourell, Y. Shi, A review of selective laser melting of

aluminum alloys: processing, microstructure, property and developing trends, J. Mater. Sci. Technol. 35 (2019) 270–284, https://doi.org/10.1016/j.jmst.2018.09.004.

[2] D. Herzog, V. Seyda, E. Wycisk, C. Emmelmann, Additive manufacturing of metals, Acta Mater 117 (2016) 371–392, https://doi.org/10.1007/978-3-319-58205-4.

[3] Z. Zhou, Y. Liu, X. Liu, Q. Zhan, K. Wang, Microstructure evolution and mechanical properties of in situ Ti6Al4V–TiB composites manufactured by selective laser melting, Compos. B Eng. 207 (2021) 108567, https://doi.org/10.1016/j.compositesb.2020.108567.

[4] Z. Li, Y. Cui, W. Yan, D. Zhang, Y. Fang, Y. Chen, Q. Yu, G. Wang, H. Ouyang, C. Fan, Q. Guo, D. Xiong, S. Jin, G. Sha, N. Ghoniem, Z. Zhang, Y.M. Wang, Enhanced strengthening and hardening via self-stabilized dislocation network in additively manufactured metals, Mater. Today, 50 (2021) 79–88, https://doi.org/10.1016/j.mattod.2021.06.002.

[5] J.H. Martin, B.D. Yahata, J.M. Hundley, J.A. Mayer, T.A. Schaedler, T.M. Pollock, 3D printing of high-strength aluminum alloys, Nature 549 (2017) 365–369, https://doi.org/10.1038/nature23894.

[6] N.T. Aboulkhair, M. Simonelli, L. Parry, I. Ashcroft, C. Tuck, R. Hague, 3D printing

of Aluminum alloys: additive Manufacturing of Aluminum alloys using selective laser melting, Prog. Mater. Sci. 106 (2019) 100578, https://doi.org/10.1016/j.pmatsci.2019.100578.

[7] S.Y. Zhou, Y. Su, H. Wang, J. Enz, T. Ebel, M. Yan, Selective laser melting additive

manufacturing of 7xxx series Al-Zn-Mg-Cu alloy: cracking elimination by coincorporation of Si and TiB2, Addit. Manuf 36 (2020) 101458, https://doi.org/10.1016/j.addma.2020.101458.

[8] S. Sun, P. Liu, J. Hu, C. Hong, X. Qiao, S. Liu, R. Zhang, C. Wu, Effect of solid solution plus double aging on microstructural characterization of 7075 Al alloys fabricated by selective laser melting (SLM), Opt Laser. Technol. 114 (2019) 158–163, https://doi.org/10.1016/j.optlastec.2019.02.006.

[9] N.T. Aboulkhair, M. Simonelli, L. Parry, I. Ashcroft, C. Tuck, R. Hague, 3D printing of Aluminum alloys: additive Manufacturing of Aluminum alloys using selective laser melting, Prog. Mater. Sci. 106 (2019) 100578, https://doi.org/10.1016/j.pmatsci.2019.100578.

[10] I. Todd, No more tears for metal 3D printing, Nature 549 (2017) 342–343,

https://doi.org/10.1038/549342a.

[11] Q. Tan, Y. Liu, Z. Fan, J. Zhang, Y. Yin, M.-X. Zhang, Effect of processing parameters on the densifcation of an additively manufactured 2024 Al alloy, J. Mater. Sci. Technol. 58 (2020) 34–45, https://doi.org/10.1016/j.jmst.2020.03.070.

[12] A. Hilaire, E. Andrieu, X. Wu, High-temperature mechanical properties of alloy 718 produced by laser powder bed fusion with different processing parameters, Addit. Manuf. 26 (2019) 147–160, https://doi.org/10.1016/j.addma.2019.01.012.

[13] Z. Tian, C. Zhang, D. Wang, W. Liu, X. Fang, D. Wellmann, Y. Zhao, Y. Zhao, Y. Tian, A review on laser powder bed fusion of inconel 625 nickel-based alloy, Appl. Sci. 10 (2020) 81, https://doi.org/10.3390/app1001008.

[14] V. A. Chianeh, H. R. M. Hosseini and M. Nofar: 'Micro structural features and mechanical properties of Al/Al3Ti composite fabricated by in situ powder metallurgy route', J Alloys Compd, 2009, 473, 127–132.

[15] T. Wang and J. S. Zhang: 'Thermoanalytical and metallographical investigations on the synthesis of TiAl3 from elementary powders', Mater. Chem. Phys., 2006, 99, 20–25.

[16] P. Y. Wang, H. J. Li, L. H. Qi, X. H. Zeng and H. S. Zuo: 'Synthesis of Al-TiAl3 compound by reactive deposition of molten Al droplets and Ti powders', Prog. Natl Sci.: Mater. Int., 2011, 21, 153–156.

[17] L. Shen, L. Y. Kong, T. Y. Xiong, H. Du and T. F. Li: 'Preparation of TiAl3-Al composite coating by cold spraying', Trans. Nonferr. Met. Soc., 2009, 19, 879–882.

[18] A. Vencl, I. Bobic, S. Arostegui and B. Bobic: 'Structural, mechanical and tribological properties of A356 aluminum alloy reinforced with Al2O3, SiC and SiCz graphite particles', J. Alloys Compd, 2010, 506, 631–639.

[19] A. Mazahery, H. Abdizadeh and H. R. Baharvandi: 'Development of high-performance A356/nano-Al2O3 composites', Mater. Sci. Eng. A, 2009, A518, 61–64.

[20] N. Iqbal, N. H. Vand and S. E. Offerman: 'In situ investigation of the crystallization kinetics and the mechanism of grain refinement in aluminum alloys', Mater. Sci. Eng. A, 2006, A416, 18–32.

[21] W. W. Ding, T. D. Xia, W. J. Zhao and Y. F. Hou: 'Refining performances of TiC and TiAl3 phases in master alloys on pure aluminum', Trans. Nonferr. Met. Soc., 2009, 6, 1025–1027.

[22] Y. Cai, M. J. Tan, G. J. Shen and H. Q. Su: 'Microstructure and heterogeneous nucleation phenomena in cast SiC particles reinforced magnesium composite', Mater. Sci. Eng. A, 2000, A282, 232–239.

[23] K. Kambakas and P. Tsakiropoulos: 'Solidification of high Cr white cast iron-wc particle reinforced composites', Mater. Sci. Eng. A, 2005, A413–A414, 538–

544.

[24] H. T. Li, Y. Wang and Z. Fan: 'Mechanisms of enhanced heterogeneous nucleation during solidification in binary Al–Mg alloys', Acta Mater., 2012, 60, 1528–1537.

[25] G.P. Dinda, A.K. Dasgupta, J. Mazumder, Texture control during laser deposition of nickel-based superalloy, Scripta Mater. 67 (2012) 503–506, https://doi.org/10.1016/j.scriptamat.2012.06.014.

[26] O. Andreau, I. Koutiri, P. Peyre, J.-D. Penot, N. Saintier, E. Pessard, T. De Terris, C. Dupuy, T. Baudin, Texture control of 316 L parts by modulation of the melt pool morphology in selective laser melting, J. Mater. Process. Technol. 264 (2019) 21–31, https://doi.org/10.1016/j.jmatprotec.2018.08.049.

[27] Y. Yang, X. Li, M.M. Khonsari, Y. Zhu, H. Yang, On enhancing surface wear resistance by rotating grains during selective laser melting, Addit. Manuf. 36 (2020) 101583, https://doi.org/10.1016/j.addma.2020.101583.

[28] S.D. Jadhav, S. Dadbakhsh, L. Goossens, J.P. Kruth, J. Van Humbeeck, K. Vanmeensel, Influence of selective laser melting process parameters on texture evolution in pure copper, J. Mater. Process. Technol. 270 (2019) 47–58, https://doi.org/10.1016/j.jmatprotec.2019.02.022.

[29] H. Zhang, H.H. Zhu, X.J. Nie, J. Yin, Z.H. Hu, X.Y. Zeng, Effect of Zirconium addition on crack, microstructure and mechanical behavior of selective laser melted Al-Cu-Mg alloy, Scripta Mater. 134 (2017) 6–10, https://doi.org/10.1016/j.scriptamat.2017.02.036.

[30] J.H. Martin, B.D. Yahata, J.M. Hundley, J.A. Mayer, T.A. Schaedler, T.M. Pollock, 3D printing of high-strength aluminum alloys, Nature 549 (2017) 365–369,

[31] X. Nie, H. Zhang, H. Zhu, Z. Hu, L. Ke, X. Zeng, Effect of Zr content on formability, microstructure and mechanical properties of selective laser melted Zr modifed Al-4.24Cu-1.97Mg-0.56Mn alloys, J. Alloys Compd. 764 (2018) 977–986, https://doi.org/10.1016/j.jallcom.2018.06.032.

[32] Q. Tan, J. Zhang, Q. Sun, Z. Fan, G. Li, Y. Yin, Y. Liu, M.-X. Zhang, Inoculation treatment of an additively manufactured 2024 aluminum alloy with titanium nanoparticles, Acta Mater. 196 (2020) 1–16, https://doi.org/10.1016/j.actamat.2020.06.026.

[33] S.Y. Zhou, Y. Su, H. Wang, J. Enz, T. Ebel, M. Yan, Selective laser melting additive

manufacturing of 7xxx series Al-Zn-Mg-Cu alloy: cracking elimination by coincorporation of Si and TiB2, Addit, Man (Lond.) 36 (2020) 101458, https://doi.org/10.1016/j.addma.2020.101458.

Chapter 5 Study on Selective Laser Melting 7075 Aluminum Alloys Modified with TiC/SiC

5.1 Introduction

Alloys in the 7xxx class possess superior mechanical properties compared to those of other aluminum alloys. Their exceptional strength, rigidity, corrosion resistance, and weldability render them extensively utilized across various industries, such as aerospace, automotive, and sports equipment. Consequently, extensive research has been conducted on alloys in the 7xxx class for many decades [4]. However, the widespread use of these alloys has been hindered by the need for exceptional wear resistance, superior creep resistance at elevated temperatures, and other similar demands in certain industrial applications. In recent decades, extensive research has been conducted on ceramic-reinforced aluminum metal matrix composites (AMMCs) to investigate their altered mechanical characteristics compared to those of standard aluminum alloys [5–7]. Nonetheless, these materials have certain limitations, including a significant disparity in the coefficient of thermal expansion between the metal matrix and ceramic reinforcements, as well as the intrinsic brittleness of ceramics [8]. Transition metal tri-aluminide intermetallics, such as NiAl3, FeAl3, ZrAl3, and TiAl3, possess a low density, high modulus, and a coefficient of thermal expansion that is significantly closer to that of an aluminum matrix. Considering these factors, these intermetallics might be effectively used in AMMCs. TiAl3 is the most intriguing tri-aluminide due to its low density, high melting temperature (1350°C), and high Young's modulus (217 GPa), which are similar to those of other aluminum-rich intermetallics [9].

Al-Zn-Mg-Cu alloys from the 7 series of aluminum alloys are widely used because of their low weight and high specific strength [10]. However, the occurrence of hot cracking renders AA7075 unsuitable for SLM processing. cracks in AA7075, which originate during the semisolid stage and expand during solidification, pose significant challenges for broad applications [5]. Due to the inherent characteristics of SLM, including notable temperature gradients (~106 K/m) and thermal pressures, substantial, directed dendritic grains may form during solidification, leading to crack propagation along grain boundaries [6]. Eliminating hot cracks in materials with a wide freezing range, such as AA7075, proves to be challenging. The aerospace sector resorts to costly

machining and riveting methods to achieve intricate geometries due to the limited printing and welding capabilities of AA7075.

Recently, powder mixing has gained significance in metallurgy by incorporating ceramic particles into the metal matrix to enhance alloy characteristics. Recent research indicates limited effectiveness in mitigating cracks in aluminum alloys using mixed powders in various production processes. Traditional techniques, such as casting crack-free Al-Zn-Mg-Cu with TiC or TiB2 particles, have been reported [4], and nanotreated welding rods can connect high-strength AA7075 without cracking [7]. The addition of particles may enhance the tribological [8] and thermal performance of 7-series aluminum alloys, rendering them more desirable for diverse applications. This study introduces a novel and successful strengthening method to enhance the anti-crack properties of AA7075 by incorporating SiC and TiC integrated particles manufactured by SLM. Crack-free features with high hardness and tensile strength were achieved by mixing 2% TiC and 2% SiC. This research provides valuable insights into developing powder-mixing aluminum alloy powders for SLM.

In this work, a varying ratio of TiC/SiC added to a powder bed was used to fabricate crack-free and nearly fully dense AA7075 parts via selective laser melting (SLM). Additionally, a green laser was utilized instead of a red laser to reduce the energy density, thereby minimizing the loss of Mg and Zn and further enhancing the mechanical properties. The results indicate that an increased percentage of Ti added to the powder bed decreased the rate of material solidification, resulting in a more uniform solidification process and preventing the occurrence of hot tearing. The micrographs clearly demonstrate the absence of melt pools and melt tracks, which are often observed during SLM. The subsequent passage provides a more comprehensive description of the experimental methods and findings, illustrating the successful production of crack-free AA7075 via SLM with the addition of TiC/SiC

5.2. Materials and experimental methods

5.2.1. Powder production and characterization

The raw material for printing components using the TruPrint 1000 additive manufacturing system comprised AA6061 powder combined with microscale SiC and TiC particles sourced from Sichuan Huomosi Industrial Technology Co., Ltd. The particle sizes were determined to be 15-60 μm for AA7075, 1-5 μm for SiC, and 1-10 μm for TiC using a laser diffraction powder sizer (Mastersizer 2000, Malvern

Instruments Ltd., UK). The investigation utilized a setup employing a green laser. Green lasers and fiber lasers (commonly used) have distinct wavelengths, resulting in varying absorption rates. The absorption efficiency of green light is superior. Aluminum alloys can be printed using less energy, leading to a reduction in the evaporation of magnesium (Mg) and zinc (Zn) in AA7075. The laser energy was set at 300 W, the scanning speed was 800 mm/s, and the energy density was 78.1 J/mm3 for optimized processing.

To evaluate the sample characteristics, the samples were ground using SiC sheets with a maximum grain size of 1200. Subsequently, the specimens were polished using 200-proof anhydrous ethanol and a 0.05 μm alumina polishing slurry. Tensile testing was conducted using an INSTRON 5967 Electronic Universal Testing Machine, with a nominal strain rate of 0.001 mm/mm/second. Following the tensile tests, the fracture surfaces were examined using scanning electron microscopy (SEM). The SEM device used was a ZEISS Sigma 300 model manufactured in Germany with a gold-coated target material and a Schottky field emission electron gun. The microscope has a resolution capability of 1.0 nanometers at an operating temperature of 15 K. Energy dispersive spectroscopy (EDS), specifically the Smartedx system, was integrated into the SEM instrument for additional analysis. Additionally, the electron backscatter diffraction (EBSD) technique was employed using the Oxford Nordlys max3 model SEM. Prior to SEM inspection, a gold coating was applied for 45 seconds using a Quorum SC7620. Vickers hardness measurements were conducted using a microhardness tester (Leiz-Wetzlar, Germany) at various positions on the XY and XZ planes. Under the specified conditions, a load of 100 g was applied with an indentation duration of 25 s. This process was repeated 10 times to ensure precision. The mechanical tests were performed using an American INSTRON 5967 Electronic Universal Testing Machine.

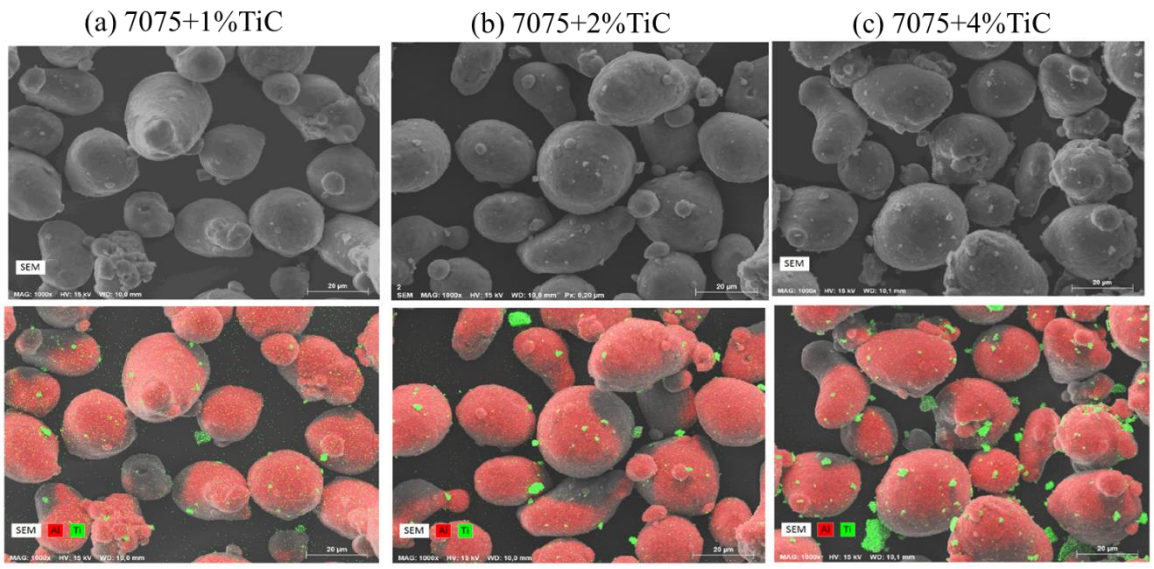

Fig 5.1 Powder morphology and EDX elemental distribution of (a) AA7075+1%TiC, (b) AA7075+2%TiC, and (c) AA7075+4%TiC.

Fig. 5.1 shows the mixed AA 7075 +1%/2%/4% TiC powder morphology and element distribution. AA7075 and TiC powder were distributed in a uniform distribution after ball milling. The AA7075 particles exhibit good sphericity, with the majority being either circular or oval in shape. TiC particles are uniformly distributed around the periphery of the 7075 particles, with a small amount of smaller TiC powder particles adsorbed onto the surface of the 7075 aluminum alloy particles. Adequate powder mixing contributes to the formation of a well-structured microstructure during the printing process.

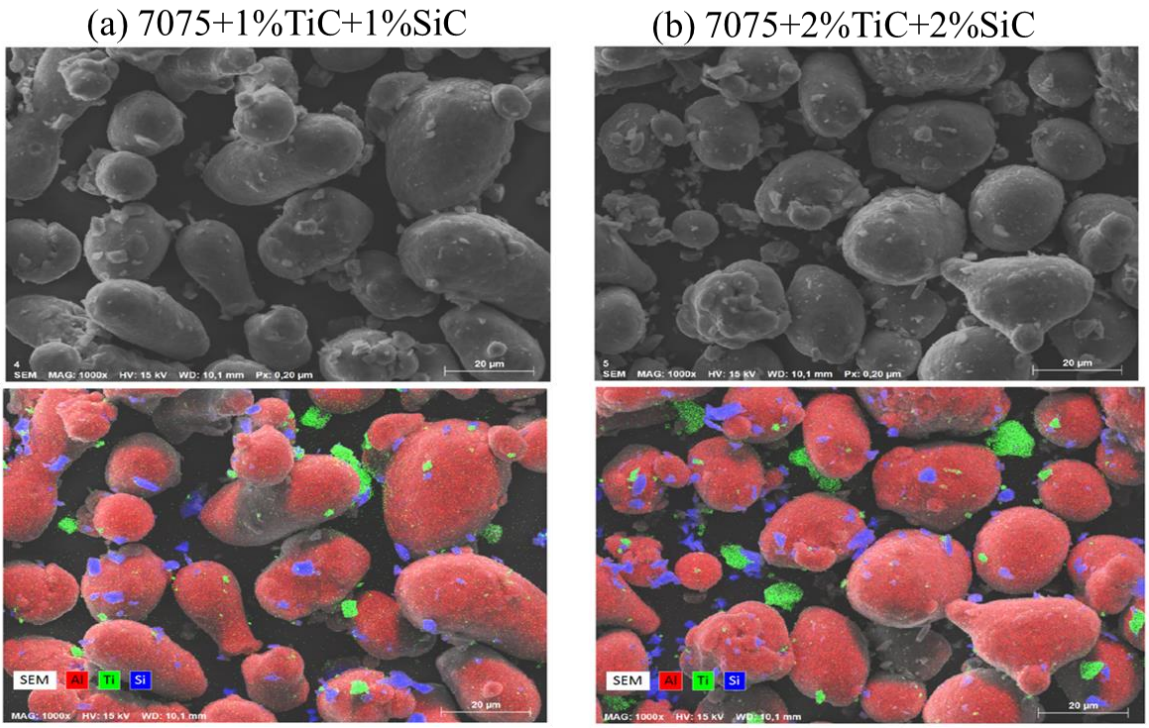

Fig 5.2 Powder morphology and EDX elemental distribution of (a) AA7075+1%TiC+1%SiC and (b) AA7075+2%TiC+2%SiC.

As shown in Fig. 5.2, the morphology of the AA7075 mixed SiC+TiC powder powder was observed, and the microscale TiC and SiC powders were evenly distributed around the 7075 aluminum alloy particles. Compared to the TiC particles, the smaller SiC particles are adsorbed onto the surface of the 7075 powder particles, and no agglomeration phenomenon is observed.

Fig. 5.3 shows the XRD patterns of the 7075 Al alloy and 7075/TiC/SiC powders. The XRD results indicate the presence of alpha-Al, $MgZn_2$, and TiC peaks. Due to the smaller size of the SiC particles and their uniform distribution around the 7075 particles, no peaks corresponding to SiC were observed during the scanning process.

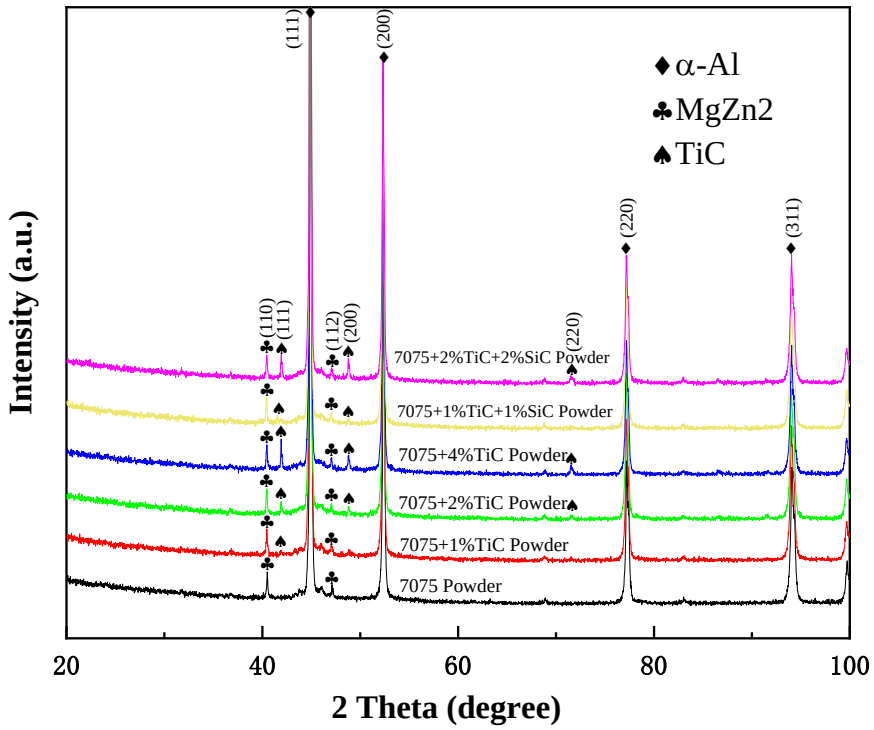

Fig 5.3 **XRD patterns of the 7075 Al alloy and 7075/TiC/SiC powders.**

5.2.2 Experimental details

The same experimental details can be found in the chapter. 3 same section (3.2.3 Experimental details). As mentioned, the laser power and scanning velocity were selected as the parameters to optimize the SLM experiment. Eighteen experiments with varying parameters are listed in Table 5.1. The energy density can be calculated by Eq. 3.1.

Table 5.1 Experimental parameters

	P (W)	V (mm/s)	Ed (J/mm^3)
1	200	1200	34.7
2		1000	41.7
3		800	52.1
4		666	62.5
5		533	78.1
6		400	104.1

7	250	1500	34.7
8		1250	41.7
9		1000	52.1
10		833	62.5
11		666	78.1
12		500	104.1
13	300	1800	34.7
14		1500	41.7
15		1200	52.1
16		1000	62.5
17		800	78.1
18		600	104.1

5.3 Materials characterization

5.3.1 Microstructure observation

After the SLM experiments following the various parameters listed in Table 5.1, AA7075 was characterized, and the as-built microstructure is shown in Fig. 5.4

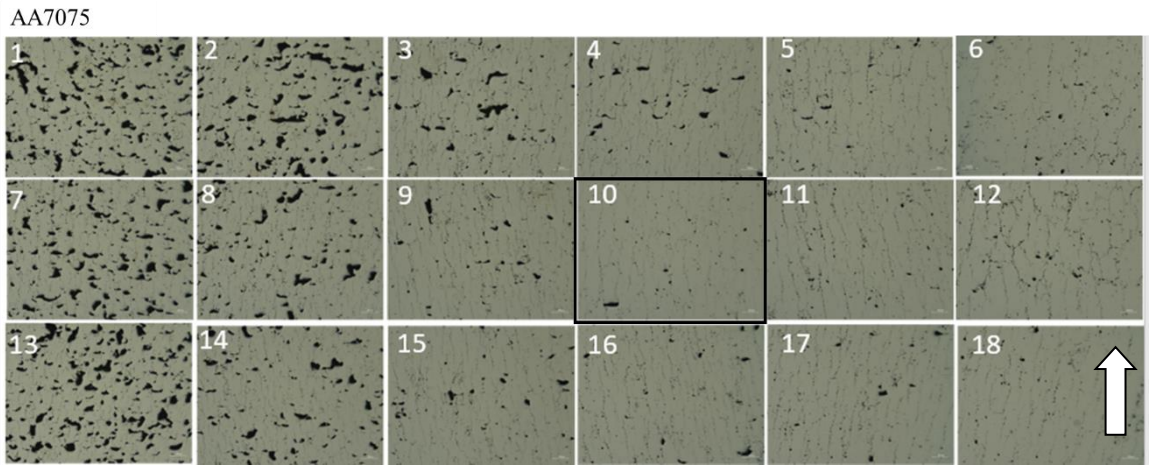

Fig 5.4 AA 7075 microstructure observation (the number can be seen in table 5.1).

According to the information shown in Figure 5.4, the organizational morphology in the build direction (BD) remains consistent under laser powers of 200 W, 250 W, and 300 W. At lower energy densities, ranging from 34.7 J/mm3 to 52.1 J/mm3, a significant number of irregular pores appear in the organizational morphology. Irregular pores, known as process-induced pores, are common defects in SLM processed samples and

are typically attributed to insufficient energy input during the process. As shown in Fig. 5.4, the 1-3, 7-8, and 13-14 samples manufactured at extremely low VEDs exhibit the presence of irregular pores. These irregular pores typically include two types: lack-of-penetration pores, also known as weak bonding defects, and lack-of-fusion pores, also referred to as incomplete fusion holes[11-12]. Fig. 5.4 illustrates the presence of large flat pores with a lack of penetration. These pores, which can reach sizes of hundreds of micrometers, are located between the adjacent tracks and construction layers, indicating inadequate VED to generate sufficient penetration depth of the molten pools. Additionally, the surfaces of the affected areas become uneven, leading to a decrease in the smooth flow of the molten metal and the formation of interlayer faults. As the energy density increases to 62.5 J/mm3, the organizational morphology gradually improves, with only a small number of pores remaining. Among these, at 250 W with a scanning speed of 833 mm/s, as shown in the organizational morphology image labeled as number 10, the fewest pores and cracks are observed. With further increases in energy density, there is minimal change in the organizational structure, indicating that at an energy density of 62.5 J/mm3, the printing requirements of AA7075 are fully met. Notably, regardless of the process, there are numerous cracks in the organizational structure, indicating that it is not possible to suppress cracks when optimizing the printing process parameters.

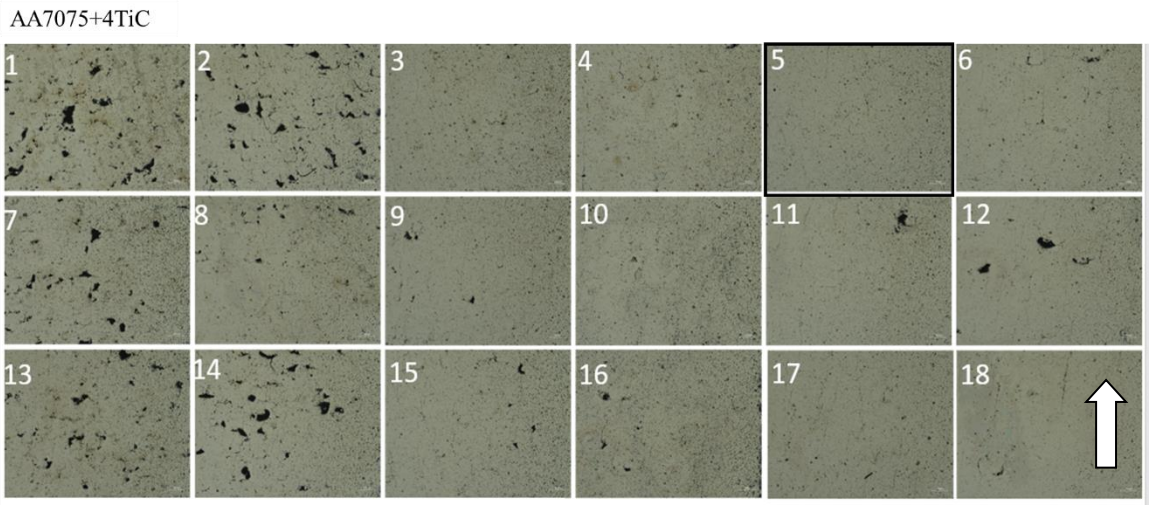

Fig 5.5 AA 7075 +4%TiC densification and microstructure observation.

The addition of 1% TiC and 2% TiC particles did not have significant effects, and the microstructure was similar to that of AA7075, so they will not be discussed individually here. The focus will now be on the microstructure after adding 4% TiC particles. Fig. 5.5 shows the AA7075 +4%TiC microstructure. With increasing power, pores and cracks are significantly eliminated, and the microstructure is significantly

improved, with only a few microcracks and pores observed. Thus, the low melting efficiency and the presence of significant pores in the SLMed Al alloy samples should not be attributed to laser reflectivity, contrary to earlier findings [13]. The current study demonstrated the presence of spherical pores in all the samples. This indicates that it is challenging to eliminate this type of defect in the SLMed AA7075 alloy, even with the optimization of technological parameters. This type of flaw is generally referred to as a gas hole, which is frequently encountered in metallic parts produced using SLM and is difficult to eliminate. This illustrates that these pores had a spherical morphology with smooth and regular boundaries, measuring up to tens of microns in size. In this study, the starting powders and substrate were dried before the SLM process. The trapped gas in the LPBF process can come from different sources. First, nitrogen may be present in the starting powders. Second, argon, which is used as a protective gas, can also be trapped. Finally, low-melting-temperature elements such as Mg, and Zn in the 7075 alloy evaporate and contribute to the formation of gas holes. Some of these dissolved gases were unable to be released from the molten pools, resulting in the retention of gas holes.

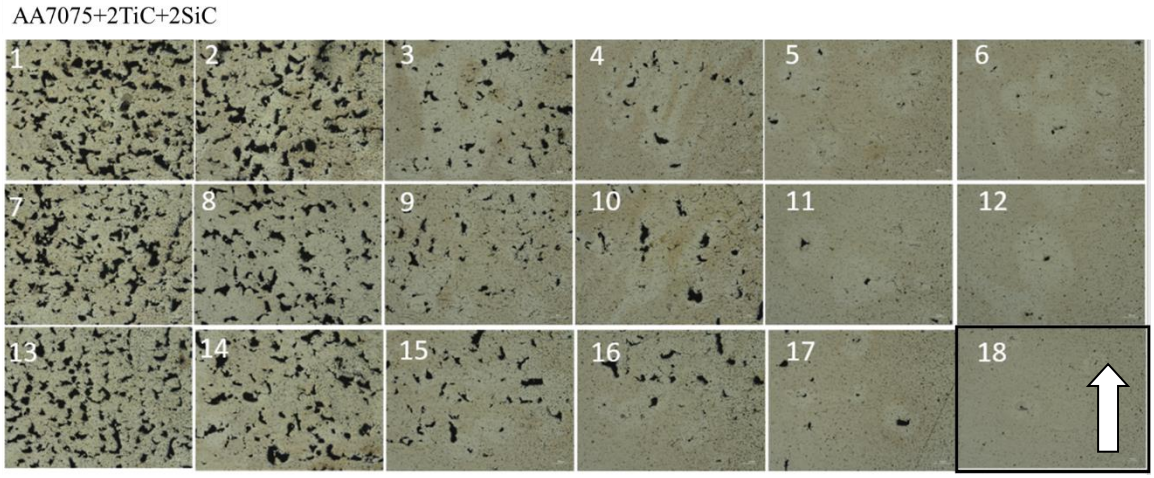

Fig 5.6 AA 7075 +2%TiC+2%SiC microstructure observation.

Fig. 5.6 shows the AA 7075 +2%TiC+2%SiC microstructure. Similar results show that with increasing power, pores and cracks are significantly eliminated. Adding 2% TiC + 2% SiC completely suppressed the cracks. It is noteworthy that achieving a good microstructure morphology after adding 2% TiC + 2% SiC requires a higher energy input, which is related to the mixing of multiple powders. The densest samples were obtained under a laser power of 300 W and a scanning speed of 600 mm/s.

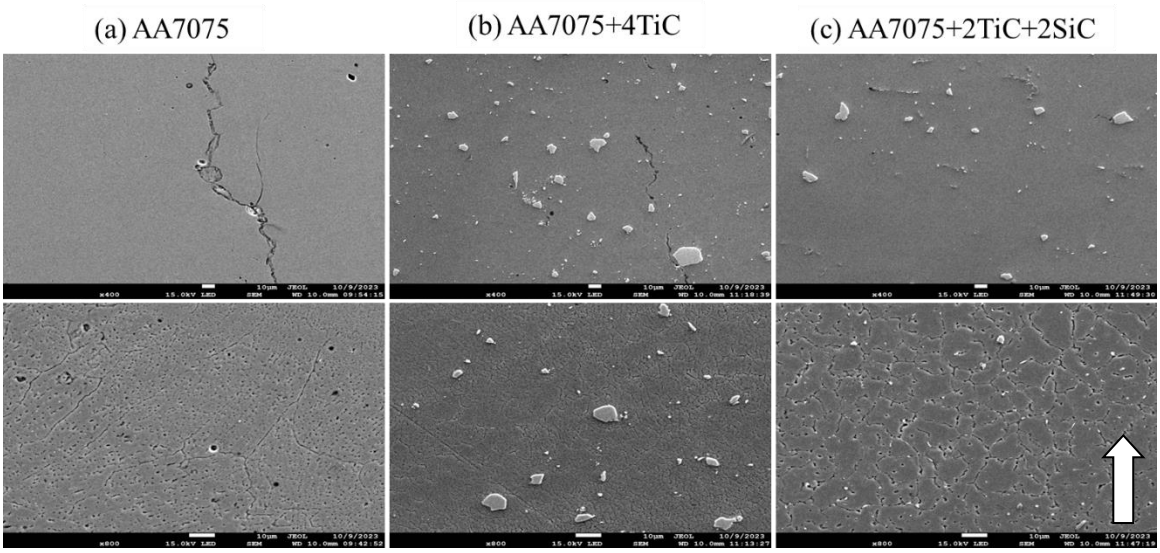

Fig 5.7 As-built microstructure of (a) AA7075, (b) AA7075+4%4TiC, and (c) AA 7075 +2%TiC+2%SiC.

Fig. 5.7 shows the as-built microstructures of AA7075, AA7075+4%TiC, and AA 7075 +2%TiC+2%SiC. We can observe that in the local magnified images of the samples, there are noticeable cracks present in AA7075, running through the entire picture, corresponding to the coarse columnar grains below. In contrast, the AA7075+4%TiC sample only exhibited small microcracks, with the grains transitioning from coarse columnar to fine equiaxed. The cracks in the AA7075+2%TiC+2%SiC sample were completely suppressed, and the grains were also equiaxed. In the cross-sections of the AA7075+4%TiC and AA7075+2%TiC+2%SiC samples, the white particles represent residual TiC and SiC particles.

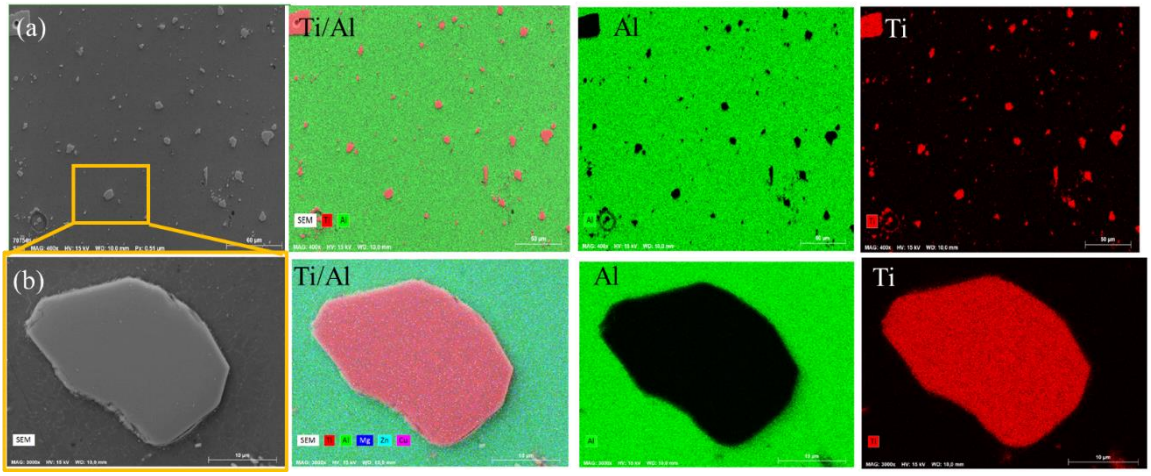

Fig 5.8 As-built AA7075+4%TiC EDX results and elemental distribution: (a) cross-sectional morphology and (b) enlarged image of the added particle.

Fig. 5.8 illustrates the distribution of AA7075+4%TiC elements and their respective contents as determined by EDX characterization. The related data may be found in Table 1. The as-built components of the novel mixed powder have increased levels of Zn and Mg to compensate for vaporization that occurs during SLM, thus confirming our initial predictions. The white particles remaining on the cross-section were also characterized by EDX, confirming that all remaining particles were TiC particles and that the bonding between the TiC particles and the aluminum matrix was mechanical. The TiC and SiC strengthening phases were uniformly dispersed in the as-built samples, without any clustering flaws. This indicates that the strengthening effect is distributed throughout the entire sample, enhancing its overall strength. The exceptional dispersibility of the material ensures remarkable enhancement capabilities [14].

Fig. 5.9 shows the as-built AA7075+2%TiC+2%SiC EDX results and the elemental distribution of the morphology and enlarged particles. Compared with larger TiC particles, SiC particles are smaller. Both the SiC and TiC particles are evenly distributed on the SLMed cross section. Additionally, the EDX results for AA7075, AA7075+TiC, and AA7075+TiC+SiC can be found in Table 4.2.

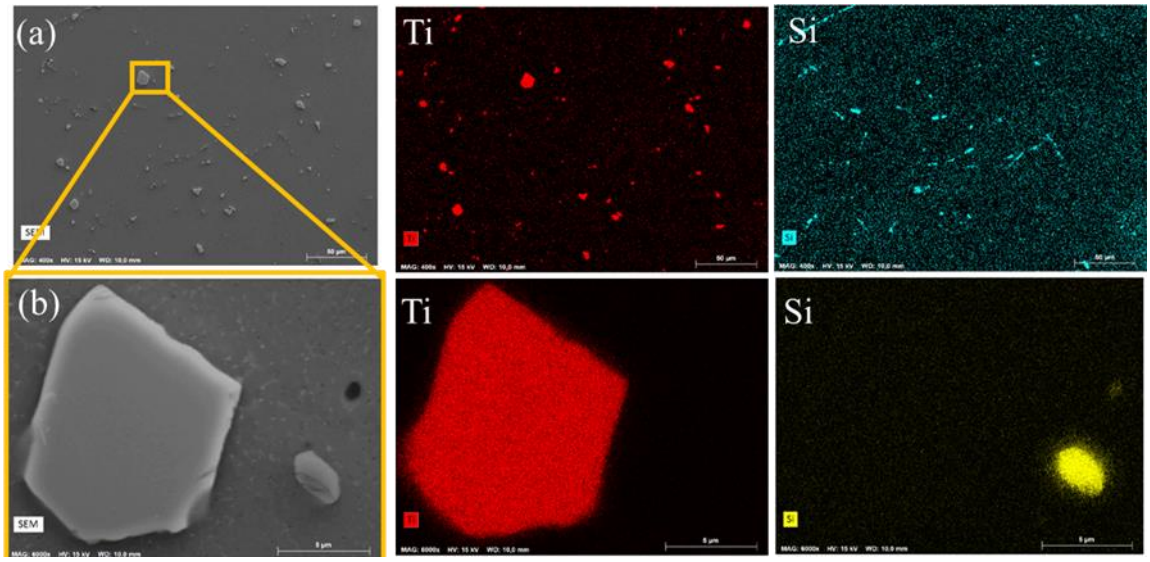

Fig 5.9 As-built AA7075+2%TiC+2%SiC EDX results and elemental distribution: (a) cross-sectional morphology and (b) enlarged image of the added particles.

.

Table 5.2 EDX results of AA7075, AA7075+TiC and AA7075+TiC+SiC

Element (wt%)	**Zn**	**Mg**	**Cu**	**Ti**	**Si**	**Al**
7075 powder	5.0±0.07	2.5±0.05	1.7±0.08	-	-	Balance
7075 as- built	4.83±0.08	2.26±0.06	1.71±0.05	-	-	Balance
7075+4%TiC	4.60±0.09	2.22±0.07	1.55±0.11	3.92±0.12	-	Balance
7075+2%TiC+2% SiC	4.61±0.08	2.12±0.56	1.60±0.1	1.73±0.09	1.39±0.08	Balance

In contrast to findings in other literature [3-4] where the Mg and Zn content experienced some loss during the printing process, our results indicate that the loss of Mg and Zn was significantly reduced.

5.3.2 XRD results

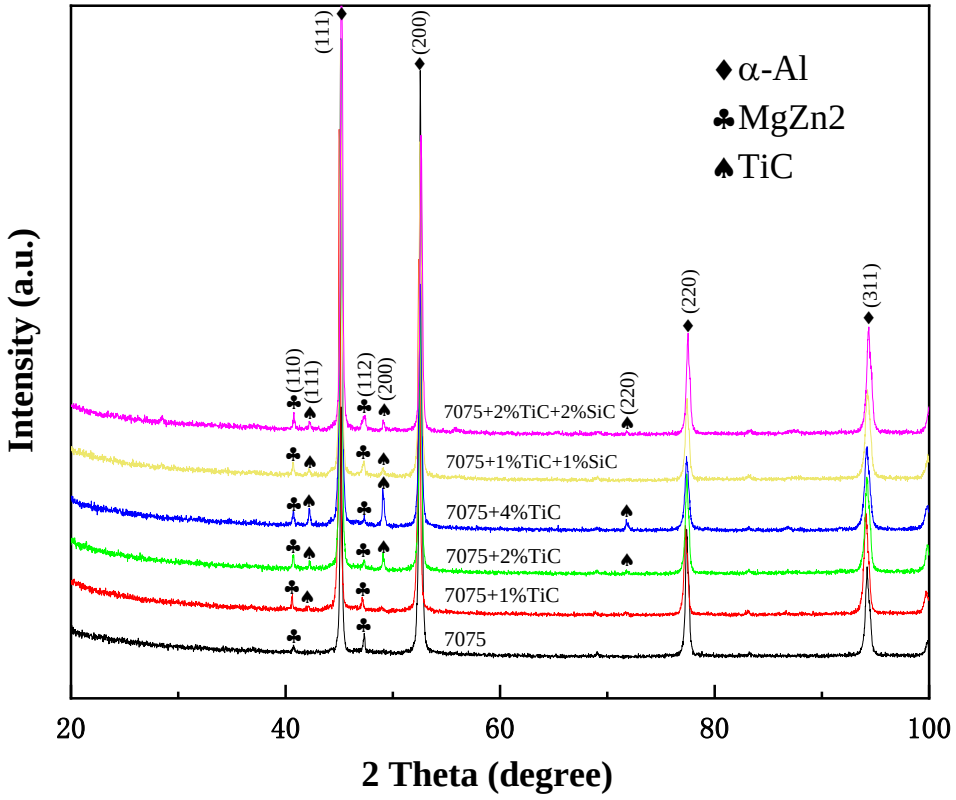

Fig 5.10 **XRD patterns of the as-built 7075 Al alloy and 7075/TiC/SiC.**

Fig. 5.10 shows the XRD patterns of the as-built 7075 Al alloy and 7075/TiC/SiC.

Compared to the powder XRD results shown in Fig. 4.4, the phase peak positions and peak strengths are quite similar. In the as-built samples, Al3Ti was not found, indicating that TiC particles scarcely reacted with the Al matrix. Instead, they serve primarily as nucleating agents to refine the grain structure.

5.3.3 EBSD microstructure evolution

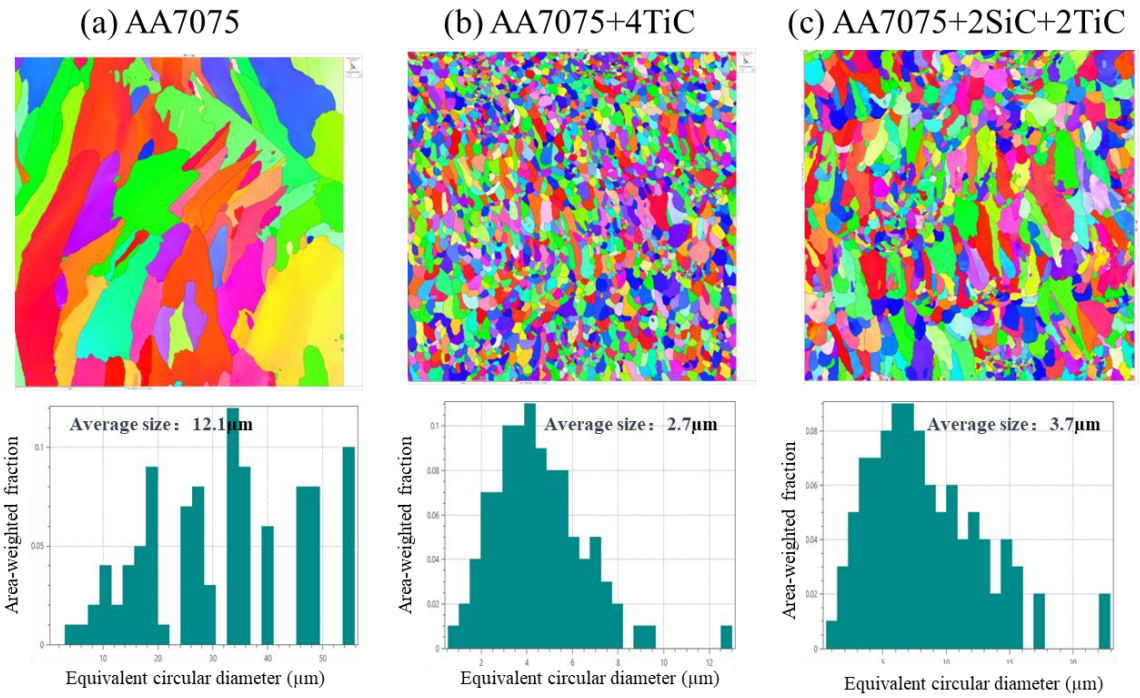

Fig 5.11 IPF EBSD results of (a) AA7075, (b) AA7075+4%TiC, and (c) AA 7075 +2%TiC+2%SiC.

The IPFs in Figure 5.11 compares the microstructures of AA7075, AA7075+4%TiC, and AA7075+2%TiC+2%SiC. The average grain size for AA7075 is 12.1 μm. The SLM process often induces thermal expansion and shrinkage due to the uneven distribution of heat and repeated thermal cycles involving multiple physical and chemical reactions. Consequently, the occurrence of high-level residual stress is inevitable, which is considered the main cause of cracking. In the AA7075 sample, the grains within the columnar structure align in the same direction as in the printing process, while fissures are observed in the spaces between the columns. Thus, it can be inferred that the presence of numerous columnar grains is a significant factor contributing to the formation of cracks when the SLMed 7075 alloy is subjected to high-stress conditions.

Figure 5.11, b and c clearly demonstrate the significant grain refinement effect of

adding TiC and SiC, which transforms coarse columnar grains into equiaxed grains and finer columnar grains. The average grain sizes for AA7075+4%TiC and AA7075+2%TiC+2%SiC were 2.7 μm and 3.7 μm, respectively. Although AA7075+4%TiC exhibited better grain refinement, it still had cracks, and the excessive residual TiC particles also affected its mechanical properties. On the other hand, AA7075+2%TiC+2%SiC shows excellent grain refinement with no cracks in the sample, completely suppressing them. This may be due to the lower melting point of SiC compared to that of TiC. During the printing process, some SiC decomposes, leading to an increase in the silicon content. As previously discussed in the literature review, aluminum-silicon alloys with near-eutectic compositions have lower liquidus line temperatures and a narrower solidification range, providing better fluidity than most aluminum alloys. Therefore, the suppression of cracks is more effective[15,16].

5.3.4 Mechanical performance

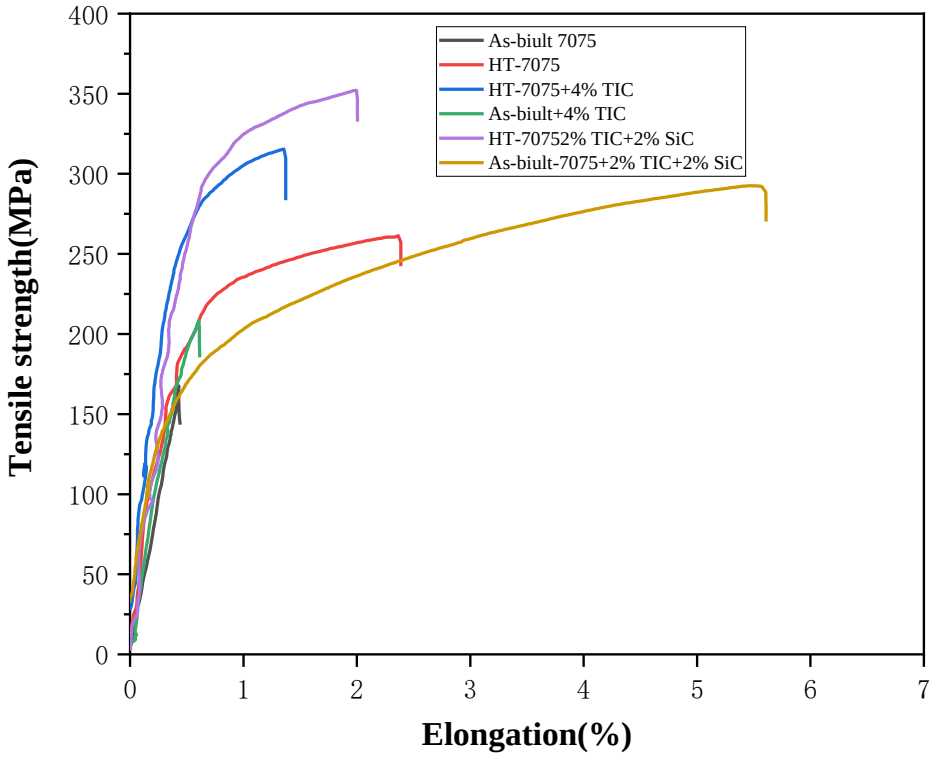

Fig 5.12 Mechanical properties of the as-built samples

Fig. 5.12 illustrates the mechanical performance of the as-built AA7075, HT-AA7075, HT-AA7075+4%TiC, as-built AA7075+4%TiC, as-built

AA7075+2%TiC+2%SiC, and HT-AA7075+2%TiC+2%SiC. Compared to those of 7075 without added Ti particles, the tensile properties were enhanced. Tensile testing was used to further analyze the mechanical properties of the SLMed AA7075. Fig. 4 displays the example curves. The as-built components possess an ultimate tensile strength (UTS) of 208.4 MPa. The as-built components made from AA7075 alloy with 2% TiC and 2% SiC exhibited an ultimate tensile strength (UTS) of 300.8 megapascals (MPa) and a ductility of 5.24%. Due to enhanced particle mixing, the as-built samples demonstrated remarkable tensile strengths (with a 30% increase), and the elongation significantly increased. The strength of the AA7075 alloy with 2% TiC and 2% SiC reached 350 MPa after heat treatment, suggesting the anti-crack strengthening effect of SiC and TiC particles.

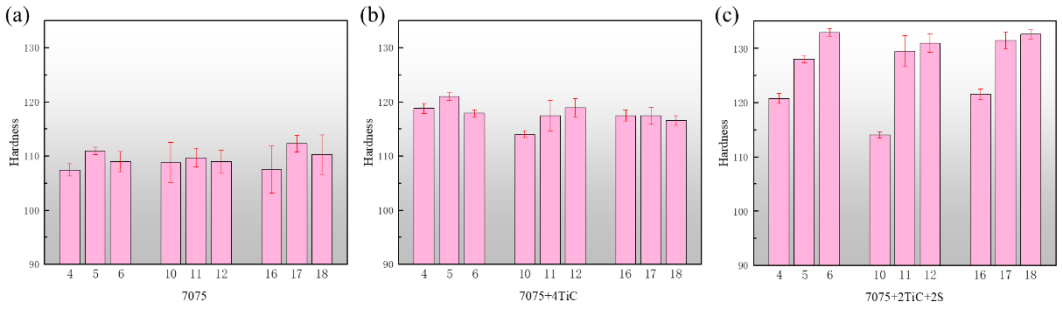

Fig 5.13 Hardness of the as-built samples (a) AA7075, (b) AA7075+4%TiC, and (c) AA 7075 +2%TiC+2%SiC.

Due to the lower energy input, the samples were not fully melted, resulting in larger hardness errors. Therefore, comparisons were made by measuring only the last three sets of each parameter. Fig. 5.13 shows the hardness of the as-built AA7075, AA7075+4%TiC, and AA 7075 +2%TiC+2%SiC samples. AA 7075 has the lowest hardness, and when 4% TiC particles are added, the hardness increases. The AA 7075 +2%TiC+2%SiC had the highest hardness herein. Therefore, the hardness increases due to the addition of particles. Additionally, the strengthening performance of the 2% TiC+2% TiC sample was better than that of the 4% TiC sample.

5.3.5 Fracture performance

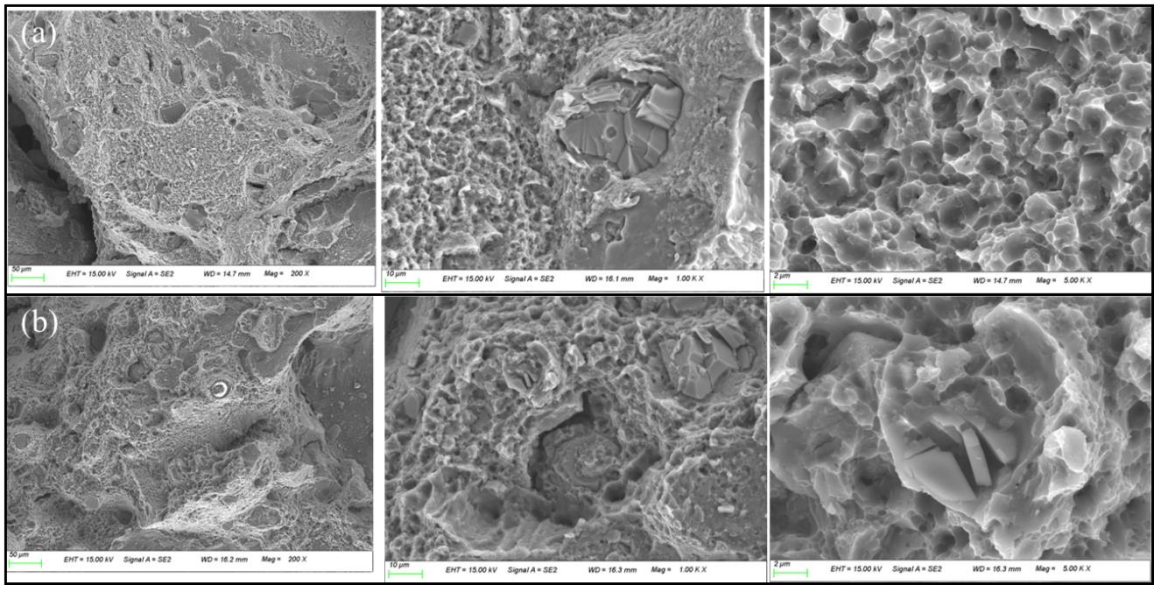

Fig 5.14 Fracture performance of the (a) as-built AA7075+4%TiC and (b) HT-AA7075+4%TiC samples.

Fig. 5.14 shows the fracture performance of the as-built AA7075+4%TiC and HT-AA7075+4%TiC samples. Refinement strengthening is the process by which the presence of TiC particles leads to the refinement of the grain structure in the alloy. This results in an increased number of grain boundaries, which in turn hinders the movement of dislocations and ultimately improves the strength of the alloy [17,18]. From the cross-section, residual TiC particles and numerous dimples can be observed, and cracks can also be seen, while after heat treatment, as the grains grow, the number of dimples decreases.

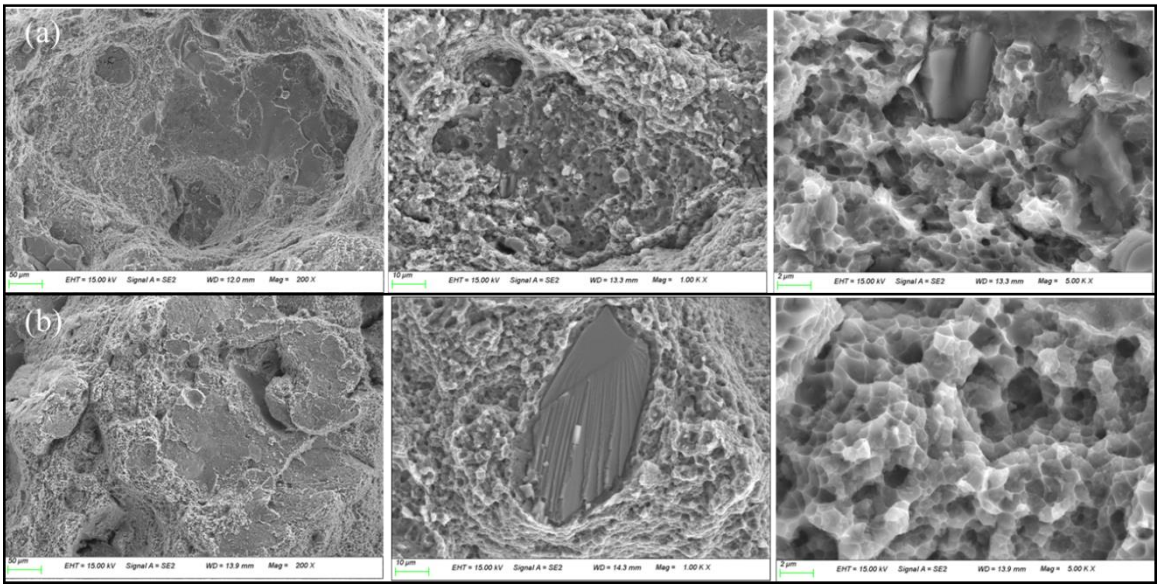

Fig 5.15 Fracture performance of the (a) as-built AA 7075 +2%TiC+2%SiC and (b) HT-AA 7075 +2%TiC+2%SiC samples.

Fig. 5.15 shows the fracture performance of the as-built AA 7075 +2%TiC+2%SiC and HT-AA 7075 +2%TiC+2%SiC samples. In contrast to Fig. 4.16, unmelted SiC particles can also be seen even though their particle sizes are quite small. With the comprehensive strengthening of the SiC+TiC particles, the fracture surface exhibited improved elongation.

The enhancement of elongation and toughness in the alloy through the incorporation of TiC+SiC particles can be categorized into four distinct features. First, the refinement of grains facilitated synchronized and consistent deformation among the grains, hence diminishing the stress concentration and impeding the development of cracks. Simultaneously, an increased number of grain boundaries resulted in a greater torsional fracture propagation route and greater consumption of elastic strain energy in the system. In addition, the presence of SiC+TiC particles resulted in a decrease in the quantity of solid solution precipitates (SPPs) in the alloy following T6 heat treatment. This reduction in the number of SPPs minimized the obstruction of dislocations and hindered the onset of fractures. Furthermore, the inclusion of SiC+TiC particles increased both the dislocation density and the quantity of precipitates in the alloy. The alloy with SiC+TiC particles maintained a dislocation density that was twice as high as that of the alloy without these particles. Additionally, a greater number of smaller precipitates were observed with a uniform distribution of SiC+TiC particles. These features promote the interaction, spread, and buildup of dislocations, leading to a greater rate of work hardening and more consistent deformation of the alloys. As a result, their elongation and toughness are ultimately enhanced. Ultimately, the particles

dispersed at the interfaces between grains might impede the advancement of cracks and induce their diversion in various orientations. This process results in the absorption of additional energy and consequently enhances the toughness of the material.

Conclusions

In this chapter, AA 7075 samples, 4%TiC-added AA7075 samples, and AA 7075 +2%TiC+2%SiC were analyzed to verify the results for the addition of TiC and SiC. This study employed an innovative method to enhance the printability of AA7075, which is often considered unsuitable for printing. The elimination of hot cracking and porosity in the AA7075 alloy during the SLM process was achieved by incorporating microscale TiC and SiC particles into the AA7075 powders. Furthermore, the as-built AA7075+2%TiC+2%SiC samples exhibited substantial increases in both hardness and tensile strength. The remarkable dispersibility of the combined TiC and SiC in the AA7075+2%TiC+2%SiC samples enhances the strengthening process through the formation of fine grains. The unique powders coated with nanotechnology have significant promise for broad use in the selective laser melting (SLM) of high-performance alloys. Additionally, heat-treated samples were investigated to further validate the heat treatment benefits for the mechanical and fracture performance, as well as microstructure evolution. The following conclusions can be drawn:

1. Adding 4% TiC particles can reduce the occurrence of cracks but is unable to completely inhibit them. However, the addition of 2% TiC and 2% SiC particles fully suppressed crack formation.
2. The optimal parameters were a laser power of 300 W and a scanning speed of 600 mm/s. We prepared a crack-free sample of 7075+2%TiC+2%SiC. With the addition of 2% TiC and 2% SiC to 7075, the hardness increased from 112 HV to 132 HV, an improvement of approximately 18%. The addition of 2% TiC and 2% SiC to 7075 resulted in grain refinement, with an average grain size of 3.7 μm.
3. The loss of Mg and Zn is reduced during the printing process，the strength of the AA7075 alloy with 2% TiC and 2% SiC reached 350 MPa after heat treatment.

Reference

[1] G. M. Ludtka and D. E. Laughlin: 'The Influence of microstructure and strength on the fracture mode and toughness of 7xxx series aluminum alloys', Metall. Trans. A, 1982, 13A, 411–425.

[2] T. S. Srivatsan: 'Microstructure, tensile properties and fracture behavior of aluminum alloy 7150', J. Mater. Sci., 1992, 27, 4772– 4781.

[3] D. Y. Lee and J. G. Park: 'High-temperature properties of dispersion-strengthened 7075-T6 aluminum alloy', J. Mater. Sci. Lett., 1997, 16, 158–160.

[4] A. L. M. Carvalho and H. J. C. Voorwald: 'The surface treatment influence on the fatigue crack propagation of Al 7050-T7451 alloy', Mater. Sci. Eng. A, 2009, A505, 31–40.

[5] V. Kalaichelvi, D. Sivakumar, R. Karthikeyan and K. Palanikumar: 'Prediction of the flow stress of 6061 Al–15% SiC–MMC composites using adaptive network based fuzzy inference system', Mater. Des., 2009, 30, 1362–1370.

[6] Y. F. Chen and Y. C. Lin: 'Surface modifications of Al–Zn–Mg alloy using combined EDM with ultrasonic machining and addition of TiC particles into the dielectric', J. Mater. Process. Technol., 2009, 209, 4343–4350.

[7] A. Mandal, B. S. Murty and M. Chakraborty: 'Sliding wear behaviour of T6 treated A356–TiB2 in-situ composites', Wear, 2009, 266, 865–872.

[8] Y. Yang, J. Lan and X. C. Li: 'Study on bulk aluminum matrix nano-composite fabricated by ultrasonic dispersion of nano-sized SiC particles in molten aluminum alloy', Mater. Sci. Eng. A, 2004, A380, 378–383.

[9] J. M. Wu, S. L. Zheng and Z. Z. Li: 'Thermal stability and its effects on the mechanical properties of rapidly solidified Al-Ti alloys', Mater. Sci. Eng. A, 2000, A289, 246–254.

[10] J. Zhang, B. Song, Q. Wei, D. Bourell, Y. Shi, A review of selective laser melting of aluminum alloys: processing, microstructure, property and developing trends, J. Mater. Sci. Technol. 35 (2019) 270–284.

[11] C. Panwisawas, C.L. Qiu, Y. Sovani, J.W. Brooks, M.M. Attallah, H.C. Basoalto, On

the role of thermal fluid dynamics into the evolution of porosity during selective laser melting, Scr. Mater. 105 (2015) 14–17.

[12] N. Read, W. Wang, K. Essa, M. Attallah, Selective laser melting of AlSi10Mg alloy: process optimisation and mechanical properties development, Mater. Des. 65 (2015) 417–424.

[13] D. Buchbinder, H. Schleifenbaum, S. Heidrich, W. Meiners, J. Bültmann,

High power selective laser melting (HP-SLM) of aluminum parts, Phys. Procedia. 12 (2011) 271–278.

[14] J. Yuan, M. Zuo, M. Sokoluk, G. Yao, S. Pan, X. Li, in: Light Metals 2020, Springer International Publishing, Cham, 2020, pp. 318–323.

[15] Kang N, Coddet P, Dembinski L, et al. Microstructure and strength analysis of eutectic Al-Si alloy in-situ manufactured using selective laser melting from elemental powder mixture[J]. Journal of Alloys and Compounds, 2017, 691: 316-322.

[16] Li W Y, Zhang C, Guo X P, et al. Deposition characteristics of Al–12Si alloy coating fabricated by cold spraying with relatively large powder particles[J]. Applied surface science, 2007, 253(17): 7124-7130.

[17] Sokoluk M, Cao C, Pan S, et al. Nanoparticle-enabled phase control for arc welding of unweldable aluminum alloy 7075[J]. Nature communications, 2019, 10(1): 98.

[18] Pan S, Jin K, Wang T, et al. Metal matrix nanocomposites in tribology: Manufacturing, performance, and mechanisms[J]. Friction, 2022: 1-39.

Conclusions and Perspectives

Conclusions

To improve the issues of cracking and low melting point element evaporation in the printing process of high-strength aluminum alloys, this paper conducts an in-depth study on the process and performance of printing Al6061 and Al7075 using green laser through the SLM process. The following conclusions can be drawn:

(1) Using Al6061 powder as the matrix, Ti particles were added to prepare mixed powders with 1wt%, 2wt%, and 4wt% Ti through mechanical mixing. Samples were then fabricated using a green laser SLM device and tested. The experimental results showed that: (I) By optimizing the parameters to explore the process of different Ti particle contents, and by comparing the microstructure, relative density, and element evaporation, the optimal parameters are a laser power of 250 W, a scanning speed of 1000 mm/s, and a corresponding energy density of 52.1 J/mm³.(II) We used the optimal parameters to prepare printed samples of Al6061 and three types of mixed powders for the study. With the increase in Ti particle content, the grain refinement effect becomes more obvious, evolving from coarse columnar crystals to fine columnar crystals and fine equiaxed crystals. By comparing the proportion of columnar and equiaxed crystals, it is known that the Al6061 with 4% Ti particle content has an equiaxed crystal content close to 90%. Among these, the equiaxed crystals and fine columnar crystals are formed by Mg2Si and CuxFey compounds. In the equiaxed crystals of the 6061+Ti sample, the presence of Al3Ti is noted, indicating that the good refinement effect is attributed to the formation of Al3Ti. (III) Mechanical properties tests were conducted on Al6061, Al6061+1wt%Ti, and Al6061+4wt%Ti. Adding Ti can significantly improve the tensile properties, and the yield strength after heat treatment reaches the standard of forged AA6061. This is due to the appearance of nanoscale Mg2Si strengthening phases after heat treatment.

(2) From the above study, it is known that crack-free Al6061 parts with added Ti particles were prepared using green laser equipment, and their mechanical properties were improved. As this chapter mainly focuses on the modification of Al7075 by adding Ti particles, the research results are as follows: (I) The optimal parameters are a laser power of 300 W, a scanning speed of 1000 mm/s, and a corresponding energy density of 62.5 J/mm^3, which are much lower than those of conventional printing equipment. (II) Adding 2% Ti can

significantly inhibit the formation of thermal cracks, although it does not completely eliminate them. However, adding 4% Ti successfully produces crack-free samples. Residual titanium particles form AlTi3 at the interface with the aluminum matrix. By comparing the XRD patterns of the powder before printing and the samples after printing, it is evident that Al3Ti is formed during the printing process, indicating a strong bond between the residual Ti particles and the aluminum matrix. As the Ti content increases, the grain refinement becomes more pronounced, and the anisotropy is significantly reduced. In the AA7075 aluminum samples, coarse columnar grains and hot cracks are initially present, with an average grain size of 12.1 μm. When 4% Ti is added, the average grain size is reduced to 1.2 μm. (III) Comparing literature on infrared laser printing, the reduction in Mg and Zn loss during the printing process is notable. In comparison to AA7075 without added Ti particles, the mechanical properties were improved significantly. The as-built sample with 4% Ti exhibited a tensile strength of 370 MPa and an elongation close to 5%. Whereas the primary fracture mode of 7075 is cleavage fracture, the introduction of Ti particles results in a ductile dimple fracture.

(3) We also conducted new experiments on Al7075. By adding different proportions of TiC and SiC particles to prepare mixed powders and optimizing the process, we produced crack-free printed parts. Using the optimal process, tensile samples were prepared for mechanical performance testing. The specific research results are as follows: (I) Adding 4% TiC particles can reduce the occurrence of cracks but cannot completely prevent them. However, the addition of 2% TiC and 2% SiC particles fully suppressed crack formation. Using optimal parameters of a laser power of 300 W and a scanning speed of 600 mm/s, we prepared a crack-free sample of 7075+2%TiC+2%SiC. (II) With the addition of 2% TiC and 2% SiC to 7075, the hardness increased from 112 HV to 132 HV, representing an improvement of approximately 18%. This combination also resulted in grain refinement, with an average grain size of 3.7 μm. Additionally, the loss of Mg and Zn was reduced during the printing process. The strength of the AA7075 alloy with 2% TiC and 2% SiC reached 350 MPa after heat treatment.

Perspectives

In this thesis, we successfully used green laser equipment for the first time to prepare crack-free modified Al6061 and Al7075 printed parts by designing experiments

and optimizing parameters. The results show significant grain refinement, and improvements in both hardness and strength. However, due to the limitations of my abilities and knowledge, further research and development on green laser printing of high-strength aluminum alloys are necessary. This thesis highlights several ideas for future research improvements, as follows:

(1) Selective Laser Melting (SLM) technology is influenced by a variety of parameters that interact with each other, making the optimization process quite complex. There is a significant gap in research on the process of printing Al alloys using green laser technology, indicating the need for extensive research and experimentation in process optimization. This thesis primarily investigates laser power and scanning speed, using energy density as an indicator for process optimization. Future process optimization efforts can be more specific and detailed. For example investigate a broader range of parameters, such as layer thickness, hatch spacing, and build orientation, to understand their individual and combined effects on the final properties of the printed parts.

(2) In-depth study of the impact of green laser on the melt pool is essential. The difference in wavelength between green and infrared lasers results in varying absorption rates within aluminum alloys. With its shorter wavelength, green laser is more readily absorbed by aluminum, facilitating more efficient energy transfer and localized heating effects. As a result of its higher absorption rate and localized heating, green laser typically forms deeper and narrower melt pools. This can potentially lead to finer microstructural features but also increases the risks of thermal stresses and gradients. Therefore, compared to traditional infrared lasers, detailed investigation into green laser's effects on internal melting, solidification dynamics within the melt pool, and melt pool flow is necessary. Simulation studies may be employed where needed to elucidate underlying principles.

(3) Previous studies have demonstrated improvements in the performance of Al6061 and Al7075 alloys using green laser SLM technology. There exists a research gap regarding the application of green laser printing on other types of aluminum alloys. In comparison to commonly used traditional infrared lasers, alloys like AiSi and other types can be explored for green laser printing feasibility. Additionally, apart from aluminum alloys, research can also encompass other common materials. These studies provide new avenues for advancing additive manufacturing technologies in aerospace, automotive, and other high-performance industries.

Title: Additive manufacturing of 6061 and 7075 aluminium alloy with selective laser melting

Keywords: 6061 Aluminum Alloy, 7075 Aluminum Alloy, SLM (Selective Laser Melting), Green Laser, Grain Refinement, Crack Suppression

With the continuous advancement of Selective Laser Melting (SLM) technology, research into high-strength and medium-strength aluminum alloys using the SLM process has also been deepening. The 7075 aluminum alloy is renowned for its high strength and excellent heat treatment characteristics, and its application in demanding fields such as aerospace is receiving increasing attention. Although the 6061 aluminum alloy has lower strength compared to 7075, it exhibits excellent overall performance, including good weldability, machinability, and corrosion resistance, making it highly suitable for widespread use in the automotive and construction industries. With the help of SLM technology, these high-strength and medium-strength aluminum alloys can be used to manufacture lighter and more complex structural components, thereby enhancing efficiency and performance.

Currently, the challenge facing the SLM process for high-strength or precipitation-hardened aluminum alloys (2xxx, 6xxx, and 7xxx series) is that they are prone to hot tearing during the final stage of solidification. This results in a large number of cracks in the printed samples. Additionally, the low-melting-point elements (Zn, Mg) in these alloys tend to evaporate easily during the process, leading to compositional deficiencies that significantly affect their mechanical properties. Therefore, addressing the issues of cracking and element evaporation during the SLM printing process of medium- and high-strength aluminum alloys is a top research priority.

The purpose of this study is to use green laser SLM equipment to print crack-free 6061 and 7075 aluminum alloy samples and to investigate their mechanical properties. Compared to traditional infrared lasers, aluminum alloy powder has a higher absorption rate for green lasers, which means that lower energy densities can be used for printing. This reduces the evaporation of low-alloy elements. Additionally, Ti particles and TiC/SiC particles are added as nucleating agents to refine grains and reduce cracking. Three types of powders were prepared by mechanical mixing: 6061 +

Ti particles, 7075 + Ti particles, and 7075 + TiC/SiC particles. The samples were printed using green laser equipment, different from the traditional infrared laser. The morphology and phase composition of the powders and printed parts were observed and studied using optical microscopy (OM), scanning electron microscopy (SEM), and X-ray diffraction (XRD). The strengthening mechanisms and mechanical properties of the printed samples were analyzed using high-resolution transmission electron microscopy (HRTEM), electron backscatter diffraction (EBSD), microhardness testing, and tensile testing equipment. By optimizing process parameters (laser power, scanning speed) and the proportion of added particles, crack-free 6061 and 7075 aluminum alloys were ultimately prepared, and their strengthening mechanisms were revealed. 5This provides a new approach for the SLM process to produce crack-free high-performance aluminum alloys.

Experimental results indicate that during the green laser printing process with higher absorption rates, an energy density of 52.1 to 62.5 J/mm³ is sufficient to obtain relatively dense printed samples. The grains in the printed 6061 and 7075 aluminum alloy samples were large columnar grains (12.1-17.9 microns). The addition of titanium particles significantly refined the grains, transforming them into small columnar and equiaxed grains (0.9-1.63 microns). Besides serving as nucleation points, titanium particles reacted with the aluminum matrix to form Al3Ti, which was confirmed in the HRTEM of the 6061 prints and the XRD of the 7075 prints. The addition of titanium particles resulted in crack-free samples for both 6061 and 7075.Compared to the traditional infrared laser, the loss of Mg and Zn elements was reduced with the green laser, and the tensile properties were improved. The yield strength of the heat-treated 6061 alloys with 1% Ti content met the standards of forged AA6061, and the elongation reached 12.6%. The tensile strength of 7075 also approached 400 MPa, though further improvement in elongation is needed. Our attempts with 7075 + TiC/SiC also showed certain effects, indicating that printing aluminum alloys with a green laser is feasible

SPIM

Titre : Fabrication Additive des Alliages d'Aluminium 6061 et 7075 avec Fusion Laser Sélective

Mots clés: Alliage d'aluminium 6061, Alliage d'aluminium 7075, SLM (Fusion Sélective par Laser), Laser Vert, Raffinement des Grains, Suppression des Fissures

Avec l'avancement continu de la technologie de la fusion sélective par laser (SLM), la recherche sur les alliages d'aluminium à haute et moyenne résistance utilisant le procédé SLM s'approfondit également. L'alliage d'aluminium 7075 est réputé pour sa haute résistance et ses excellentes caractéristiques de traitement thermique, et son application dans des domaines exigeants tels que l'aérospatiale reçoit une attention croissante. Bien que l'alliage d'aluminium 6061 ait une résistance inférieure par rapport au 7075, il présente d'excellentes performances globales, notamment une bonne soudabilité, usinabilité et résistance à la corrosion, ce qui le rend particulièrement adapté à une utilisation répandue dans les industries automobile et de la construction. Grâce à la technologie SLM, ces alliages d'aluminium à haute et moyenne résistance peuvent être utilisés pour fabriquer des composants structurels plus légers et plus complexes, améliorant ainsi l'efficacité et les performances.

Actuellement, le défi auquel fait face le procédé SLM pour les alliages d'aluminium à haute résistance ou durcis par précipitation (séries 2xxx, 6xxx et 7xxx) est qu'ils sont sujets à la fissuration à chaud lors de la phase finale de solidification. Cela entraîne un grand nombre de fissures dans les échantillons imprimés. De plus, les éléments à bas point de fusion (Zn, Mg) de ces alliages ont tendance à s'évaporer facilement pendant le processus, entraînant des déficiences de composition qui affectent considérablement leurs propriétés mécaniques. Par conséquent, aborder les problèmes de fissuration et d'évaporation des éléments lors du processus d'impression SLM des alliages d'aluminium de résistance moyenne et élevée est une priorité de recherche majeure. L'objectif de cette étude est d'utiliser un équipement SLM à laser vert pour imprimer des échantillons d'alliage

d'aluminium 6061 et 7075 sans fissures et d'étudier leurs propriétés mécaniques. Comparé aux lasers infrarouges traditionnels, la poudre d'alliage d'aluminium a un taux d'absorption plus élevé pour les lasers verts, ce qui signifie que des densités d'énergie plus faibles peuvent être utilisées pour l'impression. Cela réduit l'évaporation des éléments faiblement alliés. De plus, des particules de Ti et des particules de TiC/SiC sont ajoutées comme agents de nucléation pour affiner les grains et réduire les fissures. Trois types de poudres ont été préparés par mélange mécanique : 6061 + particules de Ti, 7075 + particules de Ti, et 7075 + particules de TiC/SiC. Les échantillons ont été imprimés en utilisant un équipement à laser vert, différent du laser infrarouge traditionnel.

La morphologie et la composition en phases des poudres et des pièces imprimées ont été observées et étudiées à l'aide de la microscopie optique (OM), de la microscopie électronique à balayage (SEM) et de la diffraction des rayons X (XRD). Les mécanismes de renforcement et les propriétés mécaniques des échantillons imprimés ont été analysés en utilisant la microscopie électronique en transmission à haute résolution (HRTEM), la diffraction des électrons rétrodiffusés (EBSD), des tests de microdureté et des équipements de test de traction. En optimisant les paramètres de procédé (puissance laser, vitesse de balayage) et la proportion de particules ajoutées, des alliages d'aluminium 6061 et 7075 sans fissures ont été finalement préparés, et leurs mécanismes de renforcement ont été révélés. Cela offre une nouvelle approche pour le procédé SLM afin de produire des alliages d'aluminium haute performance sans fissures. Les résultats expérimentaux indiquent que pendant le processus d'impression laser vert avec des taux d'absorption plus élevés, une densité d'énergie de 52,1 à 62,5 J/mm³ est suffisante pour obtenir des échantillons imprimés relativement denses. Les grains dans les échantillons d'alliage d'aluminium 6061 et 7075 imprimés étaient de gros grains colonnaux (12,1-17,9 microns). L'ajout de particules de titane a considérablement affiné les grains, les transformant en grains colonnaux et équiaxes de petite taille (0,9-1,63 microns). En plus de servir de points de nucléation, les particules de titane ont réagi avec la matrice d'aluminium pour former Al3Ti, ce qui a été confirmé dans le HRTEM des impressions 6061 et dans le XRD des impressions 7075. L'ajout de particules de titane a donné des échantillons sans fissures pour les deux alliages 6061 et 7075. Comparé au laser infrarouge traditionnel, la perte des éléments Mg et Zn a été réduite avec le laser vert, et les

propriétés de traction ont été améliorées. La limite d'élasticité des alliages 6061 traités thermiquement avec une teneur en Ti de 1% a répondu aux normes de la AA6061 forgée, et l'allongement a atteint 12,6%. La résistance à la traction du 7075 approchait également les 400 MPa, bien qu'une amélioration supplémentaire de l'allongement soit nécessaire. Nos tentatives avec du 7075 + TiC/SiC ont également montré certains effets, indiquant que l'impression d'alliages d'aluminium avec un laser vert est réalisable.